SEARCHING FOR NEUTRON-PROTON EQUILIBRATION AT FERMI ENERGIES

A Dissertation

by

ANDREA MARIA JEDELE

Submitted to the Office of Graduate and Professional Studies of
Texas A&M University
in partial fulfillment of the requirements for the degree of

DOCTOR OF PHILOSOPHY

Chair of Committee,	Sherry Yennello
Committee Members,	Aldo Bonasera
	Charles Folden III
	Daniel Tabor
Head of Department,	Simon North

December 2020

Major Subject: Chemistry

Abstract

The density dependence of the asymmetry term of the nuclear Equation of State (nEoS) has been studied using reactions of ^{70}Zn+^{70}Zn, ^{64}Zn+^{64}Zn and ^{64}Ni+^{64}Ni at 35 MeV/nucleon. The experiment was performed using the NIMROD (Neutron-Ion Multidetector for Reaction Oriented Dynamics), which is a 4π charged-particle array housed inside the TAMU Neutron Ball. The detector was chosen due to its fantastic isotopic resolution and large angular coverage.

Neutron-proton (NZ) equilibration between the two largest fragments originating from the excited projectile-like fragment was used as a probe to study the density dependence of the nEoS. The NZ equilibration was observed to be exponentially decreasing for the second heaviest fragment and exponentially increasing for the heaviest fragment. A mean equilibration lifetime of 0.3zs was extracted for the heaviest and second heaviest fragments in all three reaction systems.

The results were compared to the Constrained Molecular Dynamics (COMD) and Anti-symmetrized Molecular Dynamics (AMD) models in conjunction with the GEMINI statistical model. The results suggest a soft density dependence of the asymmetry energy term.

Additionally, the NIMROD array and the Neutron Ball were recommissioned and upgraded. New detectors were tested, characterized and implemented. The results from the Neutron Ball indicate the background is approximately 1.5 neutrons lower per event than previously measured results.

DEDICATION

"I would like to be remembered as someone who used whatever talent she had to do her work to the very best of her ability"

- (Notorious) RBG

Thanks to my family: Horst, Kerry, Barbara and Erik.

ACKNOWLEDGMENTS

I would like to thank the staff at the Cyclotron Institute for their continual help and support throughout my tenure. In particular, I would like to thank Shane Schmitt, Cory Vickers, Daniel Sherman and Fred Abegglen for ensuring the components of my experiments worked despite whatever else was on their plate and for their great sense of humor. Thank you to Dr. Romauldo de Souza and Dr. Sylvie Hudan for all letting me borrow MASE, and for their advice and assistance throughout the experiment. I would like to thank my committee Dr. Cody Folden, Dr. Aldo Bonasera and Dr. Daniel Tabor. I would like to thank the SJY group for their endless advice and assistance. Thank you to Dr. Mike Youngs for encouraging me to stay in graduate school and for his continued support and life-advice. A massive thank you to Dr. Kris Hagel for his never-ending help with everything NIMROD: from setting up to running to analyzing the experiment. Without his help, willingness to sacrifice holidays and countless weekends, and words of encouragement, I would have never made it to this point. He is truly a man of God. Thank you to my advisor, Dr. Sherry Yennello, for guidance and help throughout my tenure. Thank you to my friends, old and newer. Whether from hockey or else where, they have kept me going. Special thank you to my referee family for helping me grow and balance my life the whole time I was in graduate school. The love and stress-relieve my soccer/referee community provided helped maintain my sanity. Last but not least, the biggest thank you to my parents, Horst and Kerry, and my siblings, Barbara and Erik. Their loving words and (figurative and literal) shoulders to lean on carried me through this journey.

CONTRIBUTORS AND FUNDING SOURCES

Contributors

This work was supported by a dissertation committee consisting of Professor Sherry Yennello, Professor Charles M. Folden III and Professor Daniel Tabor of the Department of Chemistry and Professor Aldo Bonasera of the Department of Physics.

The data presented in Chapter 2 was collected, linearized and calibrated by Dr. Zachary Kohley in collaboration with Dr. John (Kris) Hagel.

The analysis presented in Chapter 3 was done in close collaboration with Dr. Alan McIntosh.

The GEMINI simulations presented in Chapter 3 were simulated by Dr. Alan McIntosh and Dr. Michael Youngs, and the AMD simulations presented in Chapter 4 were run and clusterized by Maxwell Sorensen. The analysis of the neutron capture time distribution was performed by Dr. Michael Youngs.

The data presented throughout this dissertation was collected in collaboration with Dr. Kris Hagel. Dr. Hagel wrote the data acquisition software used for data collection.

The data collection in Chapter 6 was made possible thanks to the MASE modules provided by Professor Romauldo deSouza from Indiana University. The implementation of MASE was achieved with the assistance of Dr. Sylvie Hudan.

All work conducted for the dissertation was completed by the student independently.

Funding Sources

Graduate study was supported by a fellowship from Texas A&M University. Other funding sources include the Welch Foundation (A-1266) and the Department of Energy (DE-FG02-93ER40773).

TABLE OF CONTENTS

Page

LIST OF FIGURES

LIST OF TABLES

TABLE Page

1. INTRODUCTION AND MOTIVATION

The nuclear Equation of State (nEoS) plays a large role in understanding the relationship between many thermodynamic variables such as pressure, temperature and density. The nEoS has implications for many phenomena ranging from understanding of terrestrial nuclear matter to formation of heavy elements in supernova explosions and the composition of the neutron star crusts [18, 19, 20, 21]. Although the nEoS is well constrained near saturation density (ρ = 0.16 nucleons/fm^3) [22], its form is not well understood for asymmetric nuclear matter. To achieve the densities and temperature deviations needed to further constrain the nEoS, experiments with heavy-ion collisions were conducted. This chapter will focus on the nEoS in Section 1.1, neutron-proton equilibration in Section 1.2 and the time dependence of the neutron-proton equilibration in Section 1.3.

1.1 Nuclear Equation of State

In 1935, Weizs*ä*cker proposed a description of atomic nuclei as microscopic liquid drops [23]. The Weisz*ä*cker formula or semi-empirical mass formula (SEMF) successfully describes masses of ground-state nuclides, which are defined as nuclides at low temperature (T=0 MeV) and at saturation density (ρ_0 = 0.16 nucleons/fm^3) [24].

$$BE = a_v A - a_s A^{\frac{2}{3}} - a_c \frac{Z(Z-1)}{A^{\frac{1}{3}}} - a_{asy} \frac{(N-Z)^2}{A} \pm \delta \tag{1.1}$$

The SEMF is shown in Equation 1.1, where BE is the binding energy in MeV, Z is the atomic number, N is the neutron number and A is the atomic mass. The terms, left to right, are the volume term (a_v), the surface area term (a_s), the Coulomb term (a_c), the asymmetry term (a_{asy}) and the parity term (δ). The volume term represents the binding energy per nucleon for an incompressible, spherical nuclide. The surface area, Coulomb and asymmetry terms are correction terms decreasing the binding energy. The affinity for nuclei to be in an even-even neutron-proton configuration is reflected in a positive parity term (δ). The parity term is negative for odd-odd nuclei and is equal to zero for odd-even or even-odd nuclei. The value of the coefficients is determined by fitting the semi-empirical mass formula to experimentally determined binding energies as seen in

Figure 1.1. For ground state nuclides at low temperature, the SEMF is a good approximation for the experimental binding energy.

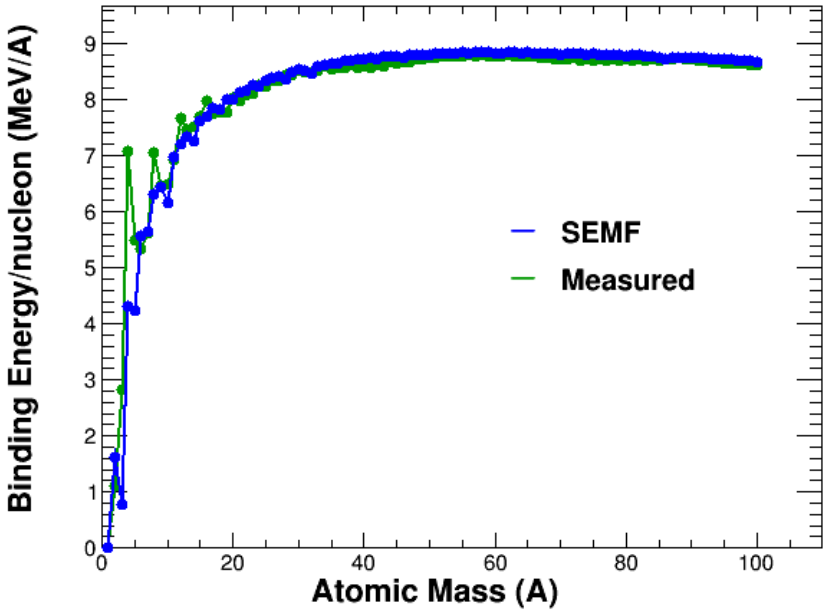

Figure 1.1: Binding energy as a function of mass for most stable nuclides. The green points represent the measured binding energies per nucleon, and the blue points represent the calculated energies per nucleon from the Weizsäcker equation or SEMF. Measured data taken with permission from Ref. [2].

Despite binding energies of ground state nuclei being well understood, understanding of nuclei properties deviating from ground state is incomplete. Specifically, research has been focused on hot nuclear matter, and nuclear matter with sub- or supra-saturation density. For very asymmetric nuclear matter, the nEoS can be expanded around I=0 and expressed in parabolic form (Equation 1.2) [24, 13].

$$E(\rho, I) = E(\rho) + E_{asy}(\rho)I^2 \tag{1.2}$$

Equation 1.2 is a function of both the total nucleon density ($\rho_{total} = \rho_n + \rho_p$) and the isospin concentration ($I \equiv \frac{\rho_n - \rho_p}{\rho_{total}} = \frac{N-Z}{A}$). The first term, $E(\rho)$, is the semi-empirical mass formula (Equation 1.1) for symmetric matter (N=Z) and only depends on the total nucleon density. The second

term, $E_{asy}(\rho)I^2$, compensates for nucleon asymmetry, and depends on both the total nucleon density and the isospin concentration. $E_{asy}(\rho)I^2$ can be viewed as the amount of energy needed to convert all protons in symmetric matter into neutrons.

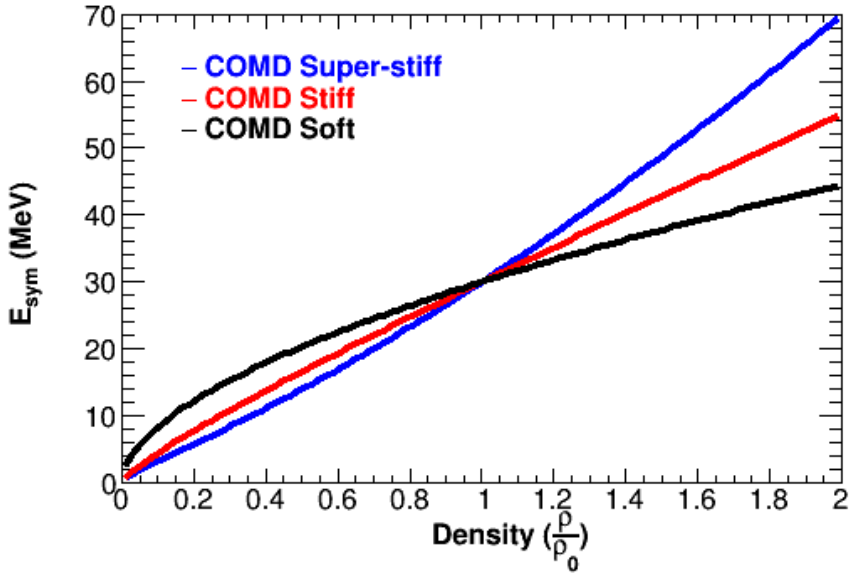

Figure 1.2: Asymmetry energy as a function of density from COMD. The blue line corresponds to the super-stiff dependence, red to a stiff dependence and black to a soft dependence.

The density dependence of the asymmetry term is commonly referred to as "soft" or "stiff". A soft density dependence on the asymmetry energy refers to a contribution from the asymmetry energy that is higher at $\frac{\rho}{\rho_0} < 0$ and lower for $\frac{\rho}{\rho_0} > 0$ relative to the stiff dependence. The soft density dependence is represented by the black line in Figure 1.2. The stiff density dependence has a larger contribution to the asymmetry energy at high density and a smaller contribution at lower density. The stiff contribution is indicated by the blue and red lines in Figure 1.2.

Understanding of the nEoS at sub- and supra-saturation densities is essential to expanding knowledge of nuclear reactions, and astrophysical systems and phenomena. Cluster formation at low-densities, outer crust composition of neutron stars and heavy element formation in supernova explosions are all dependent on the form of the density dependence of the asymmetry term [24]. Terrestrially, sub- and supra- saturation densities are hard to obtain. However, in the laboratory,

these conditions can be reproduced using heavy-ion collisions. Experimental constraints have been placed using various observables as probes. Examples include neutron-proton ratios [25, 26, 27], isoscaling [28, 29, 30, 31, 32, 33], isospin diffusion [6, 22, 34, 35, 36, 37], and neck dynamics and emission [38, 39, 40, 41, 42, 43, 44, 45]. Results point to a stiff density dependence of the asymmetry term. Recently, the time-dependence of neutron-proton equilibration has emerged as an additional probe of the asymmetry energy and will be analyzed within this work.

1.2 Neutron-Proton (NZ) Equilibration

In heavy-ion collisions at Fermi energies, the energy is generally too great for the target and projectile to fuse. Instead, the two heavy-ions graze off each other as they come into contact. During the momentum dampening phase, isospin transport is present, which is defined as the exchange of nucleons from the projectile and target and vice versa. Two processes are present: drift and diffusion. Nucleon drift is responsible for nucleon flow to the low-density, neck region forming between the higher density projectile and target. The neck region is neutron-rich in composition [24, 38, 46] due to the decrease in the asymmetry energy at low densities as seen in Figure 1.2. Nucleon diffusion is the exchange of nucleons through the neck region to minimized the chemical potential difference. If the target and projectile compositions vary, this process plays an important role. However, for symmetric systems, such as the ones studied in this work (Section 2.1), the diffusion component plays a much less significant role. The interplay of these processes can be seen in Figure 1.3b[1].

After the projectile and the target come into contact and exchange nucleons, two competing effects governing the decay dynamics are observed. The velocity gradient causes the projectile-target (PLF-TLF) species to become elongated along its axis of separation. However, the surface tension and nuclear force act to push the PLF-TLF system towards a spherical compound system. Due to the competing interactions, instabilities and deformations arise as are seen in 1.3c. Eventually, the velocity gradient outweighs the surface tension and nuclear force, and the species breaks into an excited target-like fragment (TLF*) and an excited projectile-like fragment (PLF*) (Figure 1.3d). Because the interactions are peripheral or mid-peripheral, the PLF-TLF throughout its formation and decay is rotating along its center of mass. Therefore, the axis of separation may not be the

[1]Drawings courtesy of Anna Poulsen [3].

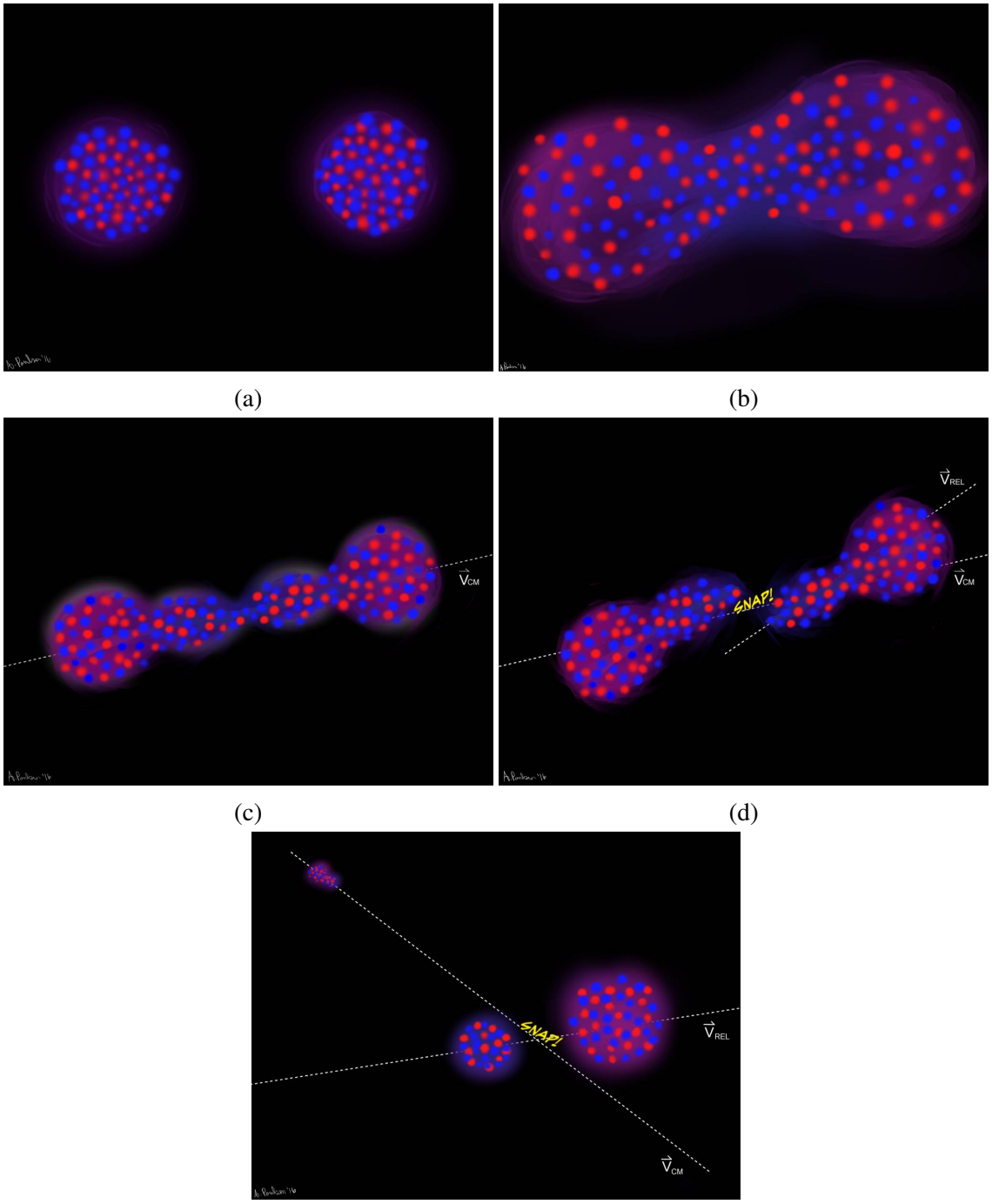

Figure 1.3: Diagrams showing the dynamics of the reaction before, during and after the target and the projectile come into contact and interact. Drawings courtesy of A. Poulsen [3] and reprinted with permission from Ref. [4].

same as the x-axis, but kinematically should be approximately the same.

The PLF* will continue to rotate around its center of mass. Two decay mechanisms are present. The first is the dynamical, aligned break-up of the PLF* referred to as dynamical decay. After the PLF-TLF breaks apart, the PLF* is highly deformed and elongated causing the binary break up of the PLF* on an extremely short timescale. The fragments break apart in the order of size with the heavier fragment (**HF**) decaying forward relative to the lighter fragment (**LF**) [41, 39, 40]. For the second decay mechanism, deformation of the PLF* may also be present after PLF-TLF break up. However, the surface tension is greater than the deformation and velocity forces driving separation. The PLF* becomes spherical and eventually breaks apart due to excess energy. The decay, known as statistical decay, is isotropic in nature and occurs on a longer timescale than dynamical decay [5]. A similar process occurs in the TLF* [45]. However, due to detector limitations [11], it is very hard to study the dynamics of the fragments originating from the TLF*.

For both decay mechanisms present, the neck-region has a differing chemical potential than the end cap or PLF region of the PLF*. Neutron-proton (NZ) equilibration occurs, which is the exchange of neutrons and protons between the two regions to minimize the chemical potential of each fragment. The extent of the NZ equilibration is governed by both the contact time between the two fragments and strength of the driving potential. In the case of dynamical decay, the contact time is very short ($\sim 10^{-21}$ s or $\sim$100 fm/c) [5], and, therefore, the composition of the **LF** remains very neutron-rich and the composition of the **HF** remains relatively neutron-poor [39, 41, 45, 46]. As the contact time increases, the excess neutrons from the neck-region flow to the PLF. For statistical decay, the contact time is significantly longer ($\sim 10^{-20}$-10^{-19} s) [5] and the fragments achieve equilibrium before breaking apart.

1.3 Time-Dependence of Neutron-Proton Equilibration

The first experiments quantifying the interaction lifetime were conducted in the 1970s and early 1980s using lower energy projectiles (E_{beam} $\leq$10 MeV/nuc). Several different observables were probed to restrain the mean equilibration lifetime (τ): kinetic energy distributions [47, 48] neutron-proton ratios [49, 50, 48], orbital angular momentum studies using γ-ray multiplicities [51, 52, 53, 48], and charge distributions [54, 53, 48]. The probes showed a range in the mean equilibration lifetime of 1.3×10^{-22} s$\leq \tau \leq 60 \times 10^{-22}$ s.

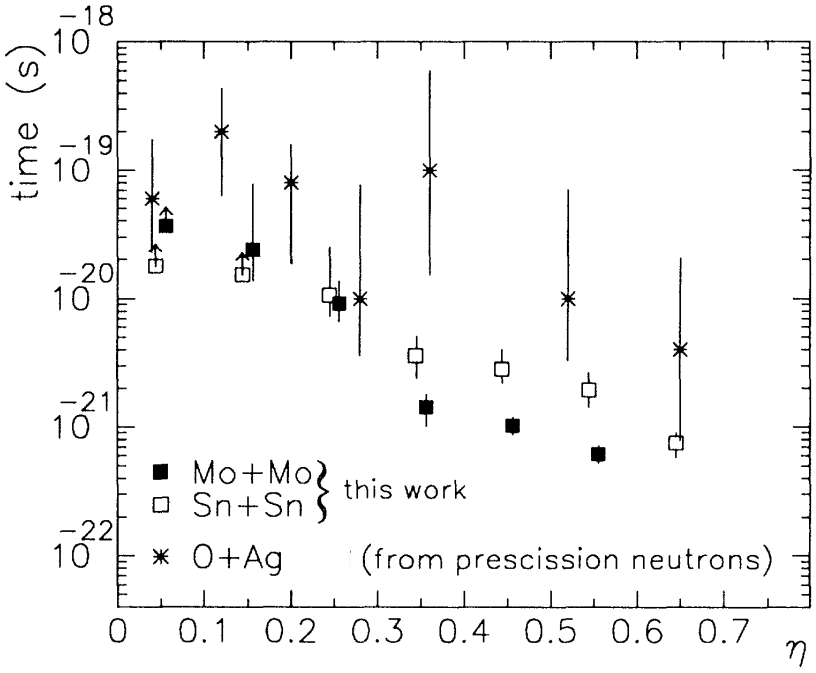

Figure 1.4: Scission times for ^{100}Mo+^{100}Mo (filled square) and ^{120}Sn+^{120}Sn (open squares) as a function of the charge asymmetry. The small charge asymmetry values correspond to more fission-like decay of the TLF-PLF, and the time are consistent with previous fission decay results. The larger charge asymmetry values correspond to a pairing of the PLF and a larger neck fragment. The latter pairing has a scission time approximately 1-2 orders of magnitude faster. Reprinted with permission from Ref. [5]

In the early 1990s, research [55, 5, 38, 56] at approx. 20 MeV/nucleon showed a multi-fragment decay mechanism. Instead of binary decay seen with lower projectile energies, neck emission is present. The scission time for break-up between the neck and PLF was characterized. Results from the timescale as a function of partner asymmetry is shown in Figure 1.4. For events where the charge asymmetry ($\eta = \frac{Z_1 - Z_2}{Z_1 + Z_2}$) is small, the decay times are consistent with fission decay of the projectile and target. However, for events where the charge asymmetry is large, the decay time is much faster. The events with a large charge asymmetry are consistent with the production of an intermediate mass fragment in the neck region. The timescale for the neck and PLF break-up occurs on a timescale of approx. 7×10^{-21} s.

More recently, Boltzmann-Uehling-Uhlenbeck (BUU) simulations[2] were performed measuring the evolution of the composition of ^{124}Sn+^{112}Sn and ^{112}Sn+^{124}Sn at 50A MeV as a function

[2]BUU is a self-consistent meanfield model

of time [6]. The evolution in composition was calculated for two different stiffnesses of the density dependence of the asymmetry term. The stiff interaction (ρ^2) was calculated using the form $E_{sym}/A=C_{sym}(\rho/\rho_0)^2$, where C_{sym}=12.125 MeV. The soft interaction (SKM) was calculated using $E_{sym}/A=38.5(\rho/\rho_0)-21.0(\rho/\rho_0)^2$. The isospin transport ratio, R_i (Equation 1.3), is plotted as a function of time and the results for the evolution of the composition of the PLF* are shown in Figure 1.5.

$$R_i = \frac{2x - x_{124+124} - x_{112+112}}{x_{124+124} - x_{112+112}} \tag{1.3}$$

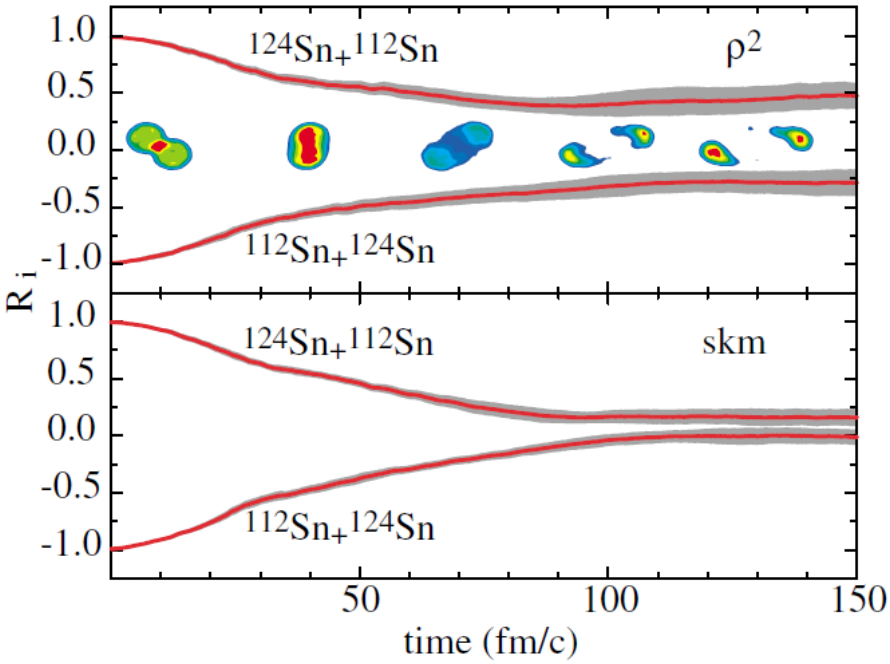

Figure 1.5: BUU simulation of the PLF* isospin transport ratio (R_i) as it evolves with time for ^{124,112}Sn+^{112,124}Sn at 50A MeV. The top panel shows the evolution for the stiffest density dependence and the bottom for the softest. The density profile of the reaction is seen super-imposed on the top panel. Reprinted with permission from Ref. [6].

In Equation 1.3, x is the isospin sensitive observable for the PLF* at time i, $x_{124+124}$ and $x_{112+112}$ is the isospin sensitive observable for the symmetric ^{124}Sn and ^{112}Sn reaction systems, respectively. The NZ composition ($\Delta=\frac{N-Z}{A}$) was used as the isospin sensitive observable.

For the more neutron-rich projectile, the system starts at R_i=1 and decreases as a function of time. The mirror effect is seen for the neutron-rich projectile, where R_0=-1 and increases as a function of time. The compositions of the fragments evolve towards each other with an average lifetime of approximately 100 fm/c (300 fm/c $\simeq$ 1 zs or 10^{-21} s). The extent of the equilibration is dependent on the stiffness of the density dependence. The final state composition is nearly equivalent for the softer dependence. For the stiffer dependence, there is a notable separation between the final state composition values. When comparing results from the model, a stiffer asymmetry energy term is more in agreement with data [6, 34]. Although the model seems to depict the final state values well, the evolution of the equilibration with respect to time is not understood.

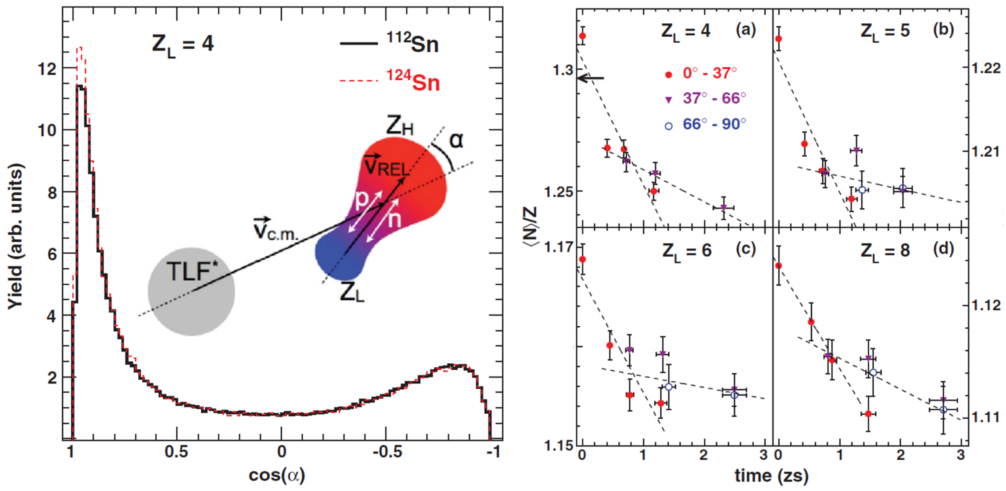

Figure 1.6: Left panel is the α distribution of the heaviest and second heaviest fragment originating from the PLF* for ^{124}Xe+^{112,124}Sn at 50 MeV/nucleon. The red line is the ^{112}Sn projectile distribution and the black one is ^{124}Sn projectile. Emission of the Z_L forward relative to Z_H is equal to cos(α)=1. On the right hand side is the composition of Z_L=4-5,8 (from top left across to bottom right) as a function of time for various angular ranges. The red circles are 0-37°, purple triangles are 37-66° and the blue circles are 66-90°. Both figures reprinted with permission from Ref. [7].

Most recently, Hudan et al. [7] has utilized a clock similar to the one first pioneered in the mid-1970s to determine the timescale of equilibration using the neutron-proton composition of the two heaviest fragments originating from the PLF*. Unlike previous work utilizing the azimuthal

angle (θ, θ_{CM} or θ_{lab}), the angle of rotation, α, used is defined as the dot product between the relative velocity of the heaviest (**HF**) and second heaviest (**LF**) fragment (v_{REL}), and their respective center-of-mass velocity (v_{CM}). Mathematically, the angle of rotation is α=acos($\frac{\vec{v}_{CM}\cdot\vec{v}_{REL}}{\|\vec{v}_{CM}\|\|\vec{v}_{REL}\|}$). The reaction systems are ^{124,136}Xe+^{112,124}Sn at 50A MeV. Due to limits on isotopic identification, only the composition of the second heaviest fragment (Z_L) was analyzed. The angular distributions show a large yield at $cos(\alpha)$=1, suggesting large amounts of dynamical decay in agreement with previous work [40, 41, 43]. The results from the composition ($\langle N\rangle/Z$) versus α is seen in Figure 1.6. For all four cases depicted, the composition of the Z_L starts off relatively neutron-rich for prompt decays ($cos(\alpha)$=1). As the rotation angle increases ($cos(\alpha)$ <1) indicating more time of contact, the composition of the fragments becomes more neutron-poor. The effect is most extreme for Z_L=4 (top, left panel) due to lack of ^{8}Be. The results are converted from angle of rotation to time using the relations $t = \alpha/\omega$ and $\omega = J\hbar/I_{eff}$, where ω is the angular frequency, J is the angular momentum and I_{eff} is the moment of inertia. The angular momentum was assumed to be ~40$\hbar$ and the moment of inertia was calculated assuming two touching spheres. The longest time of equilibration, corresponding to a quarter of a rotation, was calculated to be $\tau_{N/Z} \simeq$3 zs (or 3×10^{-21}s).

Brown et al. [8] followed up with an analysis looking at the effect of the target composition on the equilibration of Z_L. In all three reaction systems analyzed, the projectile was ^{64}Zn at 45A MeV. The targets were ^{209}Bi (N/Z=1.52), ^{64}Zn (N/Z=1.13) and ^{27}Al (N/Z=1.07). Consistent with Hudan et al. [7], the composition of Z_L started neutron-rich for very small angles of rotation and becomes less neutron-rich as $cos(\alpha)$ decreases (Figure 1.7). The target composition affects the composition of Z_L, with the greatest neutron content throughout the entire range of $cos(\alpha)$ seen for the most neutron-rich target, ^{209}Bi. The values for the ^{64}Zn and ^{27}Al target were fairly similar with slightly higher values for the more neutron-rich target (^{64}Zn). The decrease in neutron composition was most stark for smaller angles of rotation, and hence the extent of equilibration and the corresponding timescale was calculated for a quarter of a rotation. The same relationship used in the Hudan et al. work were used to calculated the equilibration timescale. The equilibration timescale was reported to persist up to 3-4 zs corresponding to an exchange of approximately one neutron.

Stiefel et al. [9] compared ^{64}Zn+^{64}Zn results from Brown [8] to Constrained Molecular Dynamics (COMD) simulations for three different stiffnesses of the density dependence of the asymmetry

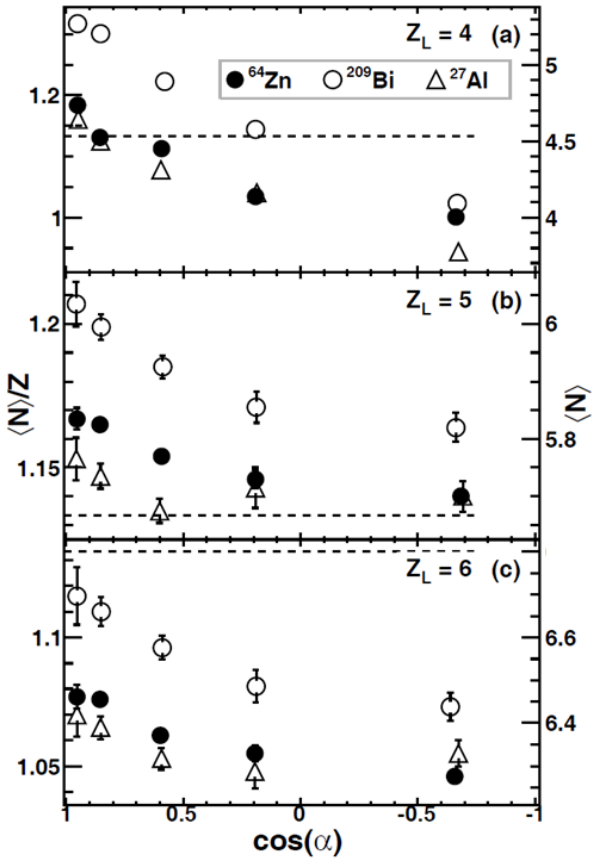

Figure 1.7: Composition versus angle for ^{64}Zn+^{209}Bi, ^{64}Zn and ^{27}Al at 45A MeV for Z_L=4-6 (top to bottom, respectively). The open circles correspond to ^{207}Bi, the close circles to ^{64}Zn and the triangles are ^{27}Al. Reprinted with permission from Ref. [8].

energy term. Simulations replicated the $cos(\alpha)$ distribution and the relationship between $\langle N\rangle/Z$ and $cos(\alpha)$ well. The experimental results and the simulations for the varying density dependences were seen in Figure 1.8. Consistent with the data, the simulation starts off more neutron-rich and decreases as the angle of rotation increases. The slope of the composition was also consistent. However, for all three stiffnesses (soft, stiff and super-stiff), the neutron composition across the entire angular range was underestimated. The ordering also suggests that a soft density dependence of the asymmetry term fits the data best, which was inconsistent with previous heavy-ion collision results. The simulation shows that the composition of the heaviest fragments (Z_H) starts off more neutron-poor and evolves to become more neutron-rich as the angle of rotation increases. Both Z_H and Z_L evolve towards each other in a manner suggesting a similar rate of equilibration for the

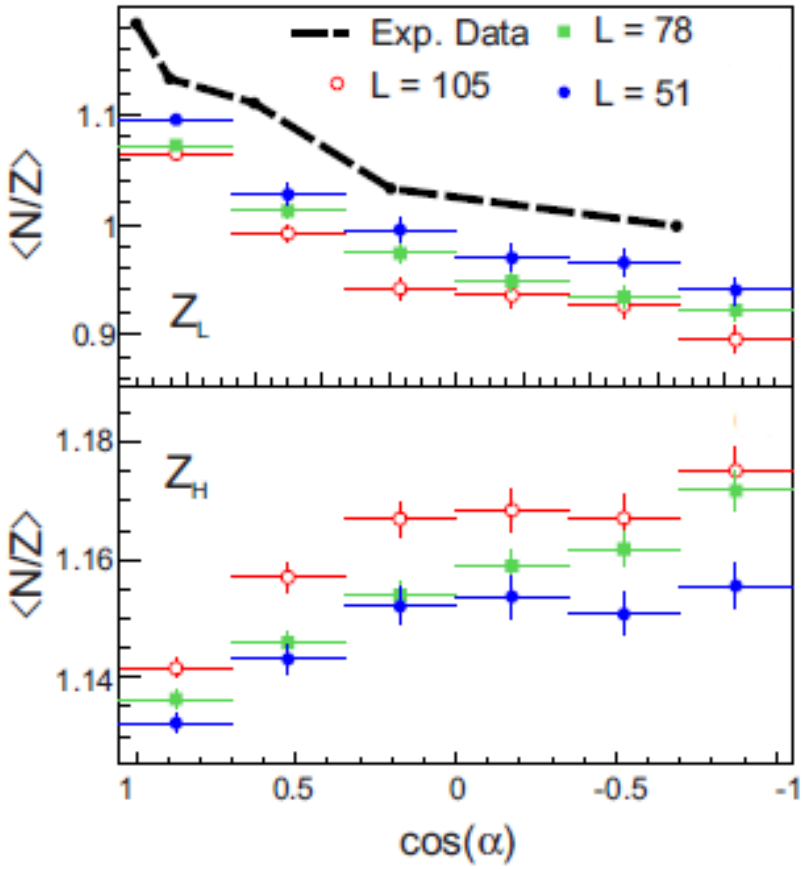

Figure 1.8: CoMD simulations of composition versus angle for ^{64}Zn+^{64}Zn at 45A MeV for Z_L and Z_H (top to bottom). The black line is the experimental data from the closed circles in Figure 1.7. The blue circles are the soft density dependence, the green circles are the stiff dependence and the red circles are the super-stiff dependence. Reprinted with permission from Ref. [9].

two fragments. The ordering of the stiffnesses shows the softest density dependence was the most neutron-poor for all angles of rotation, which was the opposite effect seen for Z_L. However, little can be said about the density dependence, given no comparison to data can be made for Z_H.

1.4 Outline

This dissertation will focus on two main topics. The first four chapters will focus on the experimental results from the reaction of ^{70}Zn+^{70}Zn, ^{64}Zn+^{64}Zn and ^{64}Ni+^{64}Ni at 35 MeV/nucleon. The last chapter will focus on the recommissioning and upgrade of the NIMROD detector array. Chapter 2 will focus on experimental configuration, particle identification and energy calibration for the

reaction systems states above. Chapter 3 will focus on the experimental results and discussion of NZ equilibration. A discussion of the simulations used is found in Chapter 4 and the comparison of the experimental results to simulations is present in Chapter 5. Lastly, the recommissioning and upgrade of NIMROD will be discussed in Section 6. Chapter 7 will summarize the results.

2. EXPERIMENTAL

The ^{70}Zn+^{70}Zn, ^{64}Zn+^{64}Zn and ^{64}Ni+^{64}Ni reaction systems at 35 MeV/nuc were run at Texas A&M University Cyclotron Institute in 2008 by Z. Kohley [10]. The Neutron Ion Multi-detector for Reaction Orientated Dynamics (NIMROD) was used to measure the experimental data due to its large angular coverage and isotopic range. The beam was chosen as a compromise between the isotopic range easily accessible with NIMROD and the large collective effects between the target-like fragment and projectile-like fragment, and its subsequent fragments.

This chapter will cover relevant details regarding the experimental configuration and data collection for the 2008 experiments. The recommission and upgrades of NIMROD will be discussed in Chapter 6. The experimental details ae described in Section 2.1. The configuration of NIMROD, and electronics and data acquisition are discussed in Section 2.2. Particle identification and energy calibrations are discussed in detail in Section 2.3 and Section 2.4, respectively.

2.1 Experiment

The ^{70}Zn, ^{64}Zn and ^{64}Ni beams used in the experiment were produced using the K500 Superconducting Cyclotron at Texas A&M University Cyclotron Institute. The beams were accelerated to 35 MeV/nuc onto a ^{70}Zn, ^{64}Zn and ^{64}Ni targets, respectively. At the end of each experiment, four calibration beams were run using the K500 cyclotron. The details of these beams are shown in Table 2.1. The intent of the calibration beams was to chose well-known calibration points for each detector in NIMROD. More information was provided in Section 2.4.

Calibration Beams	Beam Energy (MeV/u)	Targets
$^{1}H_2$	55	^{nat}Th, ^{28}Si
^{20}Ne	35	^{nat}Th
^{4}He	25	^{nat}Th
^{1}H-^{2}D	30	^{nat}Th, ^{28}Si

Table 2.1: Beam and target combinations used to calibrate the NIMROD detector.

2.2 NIMROD Array

The NIMROD array [57, 11] consists of a 4π charged particle array housed inside the TAMU Neutron Ball [58, 59], which is a neutron calorimeter. The first large upgrade had been implemented in 2006, adding additional silicon detectors in the forward angles, and replacing the backward array with the Indiana Silicon Sphere to increase the angular granularity and isotopic resolution. The thesis experiment presented here falls under the 2006 upgrade.

The NIMROD array was chosen for its large 4π angular coverage and excellent isotopic resolution. This allows one to both charge and mass identify large fragments originating from the projectile-like fragment, as well as ensuring fragments were correctly identified based on size.

2.2.1 Charged Particle Array Configuration

The NIMROD array is broken down into 14 rings ranging from 3.6° to 167.0° shown in Figure 2.1. The forward-most angle corresponds to Ring 2. The last 4 rings correspond to the Indiana Silicon Sphere. Surrounding the charged-particle array is located the neutron ball, which provides an event-by-event neutron multiplicity. The CAD drawing of the entire array is seen in Figure 2.2.

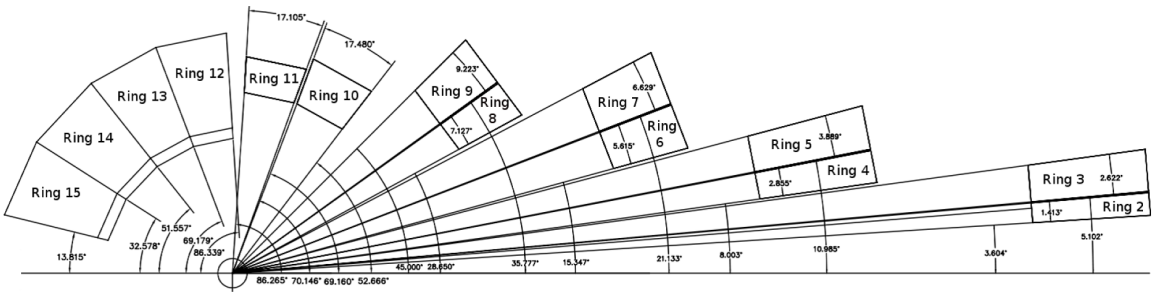

Figure 2.1: CAD drawing of the NIMROD rings. Ring 2-11 correspond to the original NIMROD array and rings 12-15 correspond to the Indiana Silicon Sphere. The detector is designed to include a potential Ring 1.

Rings 2-9 consist of the original NIMROD array covering up to 45°. The Indiana Silicon Sphere covers the back-half of the array and were labeled Rings 12-15. For Ring 10/11, the Indiana Silicon Sphere configuration had been used to construct an intermediate ring covering the angular distribution between the original NIMROD and Indiana Silicon Sphere array.

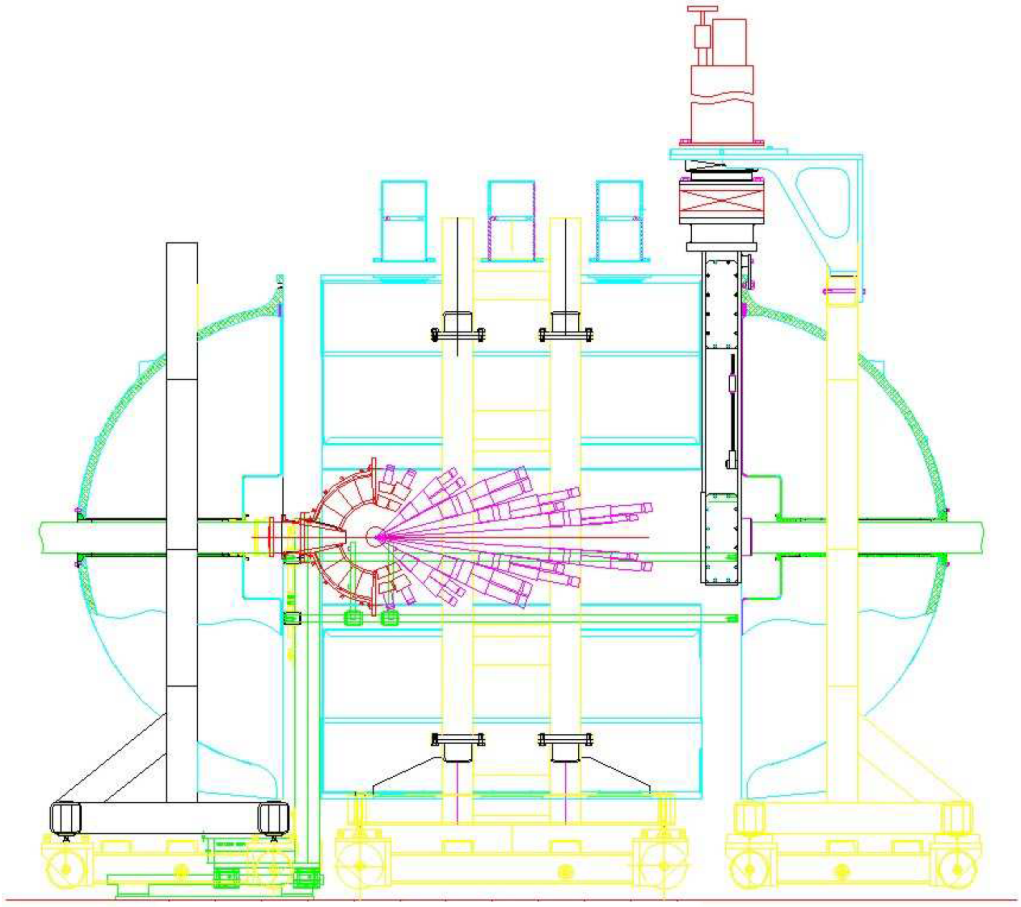

Figure 2.2: CAD drawing of NIMROD housed inside the NBL. The magenta component is the original NIMROD array and the red component is the Indiana Silicon Sphere. The blue and green parts correspond to the neutron ball.

Each detector telescope was designed to be modular as shown in Figure 2.3. Each module has the capability to have an ionization chamber, two silicon detectors (Si) and a thallium-doped cesium iodide crystal (CsI(Tl)). The CsI(Tl) crystals have either a photo-multiplier tube (PMT) or photodiode (PD) attached. For this experiment, the ionization chamber frames were installed, and used as δ-electron shields using 220 μg/cm^2 Mylar foils. There were two modular configurations present, the telescope and supertelescope configurations. For the majority of the array, the modules were in the telescope configuration and have one 300 μm Si detector followed by a CsI(Tl)-PMT detector. One detector in Ring 4/5 and handful of modules in Ring 6/7 and 8/9 contain a 140 μm Si detector followed by a CsI(Tl)-PMT detector. For the supertelescope, two Si detectors were placed

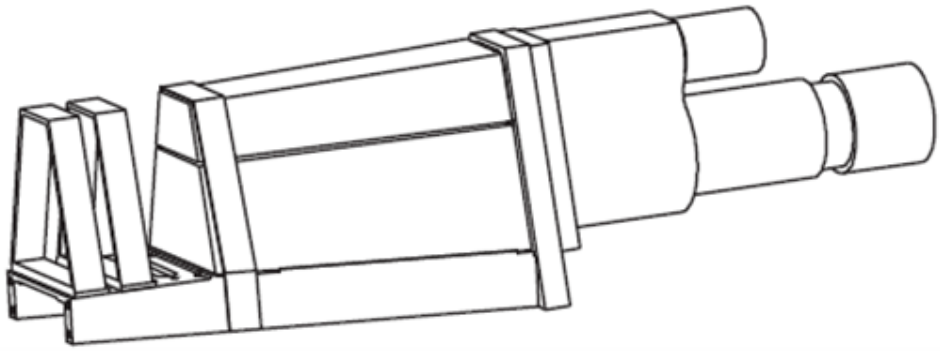

Figure 2.3: CAD drawing of a NIMROD module. The front frames represent the position of the Si detectors. The large trapezoids placed on top of each other represent the CsI crystals. A photomultiplier tube is attached behind each CsI crystal.

in front of the CsI(Tl)-PMT detectors. The two Si detectors were a 140 μm detector followed by a 500 μm detector. Both the telescope and supertelescope configurations provide both a ΔE-E measurement. In the case of the telescope configuration, the energy loss through the Si detector provides a ΔE measurement. The residual energy, which gets deposited in the CsI(Tl) detector, was the E measurement. For the supertelescope configuration, two ΔE-E technique can be applied. In the case where a particle punches through the first Si detector and stops in the second one, the energy of the first detector can be plotted against the residual energy of the second detector. The CsI(Tl) detector energy can be plotted against the energy of the second Si detector if the particle punches through both of the Si detectors and the residual energy was deposited in the CsI(Tl) detector. Further details are provided in Section 2.3.

Additionally, the front plane of the Si wafers are segmented into 4 parts for the Ring 2-9 detectors. An example of the front panel segmentation is seen in Figure 2.4 for a Ring 4/5 detector. The segmentation was chosen to provide an increase in the theta and phi angular granularity. Ideally, all channels in the experiment would have been taken in and analyzed. However, the number of electronic channels was too large. To mitigate this effect, the top two front panels and the corresponding bottom two panels were tied together on the motherboard outside the chamber. For the super-telescope configuration, all four panels were individually taking in. The super-telescope configuration was present in some of the modules in Rings 2-9. Ring 10-15 consists only of the

telescope configuration. The number, position and angular coverage of the telescopes in the 1st 8 rings was seen in Table 2.2.

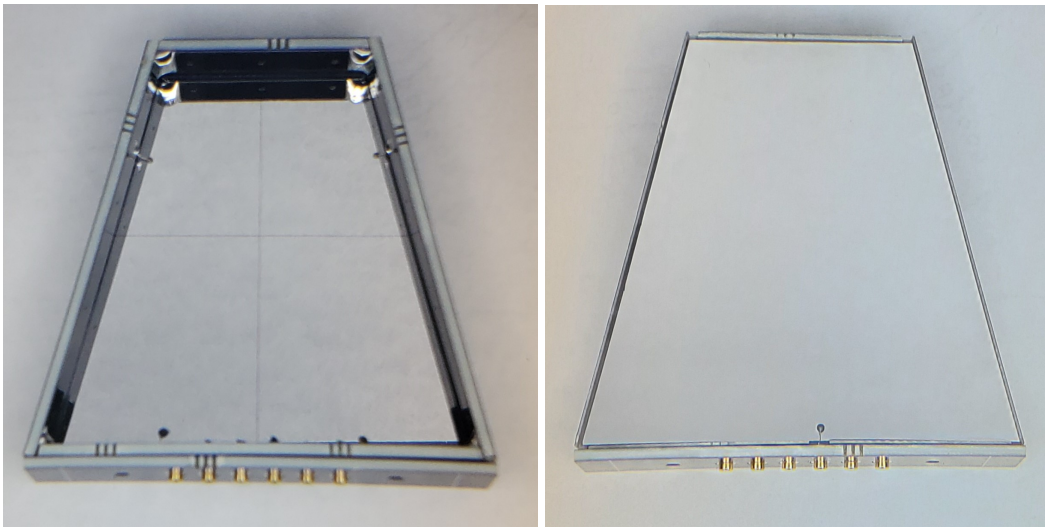

(a) Front panel of NIMROD detector (b) Back panel of NIMROD detector

Figure 2.4: Front and back plane of the NIMROD detectors on the left and right, respectively. The back plane consists of a single segment and the front one is segmented into 4 quadrants.

Ring	$\Delta\theta$	$\Delta\phi$	Telescopes Si (thickness)	Super Telescopes	CsI (Ring 2-11) PD (Ring 12-15)	CsI Length (cm)
2	3.6-5.0°	30°	10 (300 μm)	2	12	10.0
3	5.0-7.6°	30°	10 (300 μm)	2	12	10.0
4	8.0-10.8°	30°	10 (300 μm)	2	12	10.0
5	10.8-14.7°	30°	10 (300 μm)	2	12	10.0
6	15.3-20.9°	30°	10 (300 μm)	2	12	6.5
7	20.9-27.6°	30°	10 (300 μm)	2	12	6.5
8	28.6-35.8°	30°	10 (300 μm)	2	12	6.0
9	35.8-45.0°	30°	10 (300 μm)	2	12	6.0
10	52.7-69.2°	20°	18 (300 μm)	-	18	4.0
11	70.1-86.3°	20°	18 (300 μm)	-	18	3.0
12	93.5-110.8°	20°	18 (500 μm)	-	18	2.8
13	110.8-128.4°	20°	18 (500 μm)	-	18	2.8
14	128.4-147.4°	20°	18 (500 μm)	-	18	2.8
15	147.4-167.0°	20°	18 (500 μm)	-	18	2.8

Table 2.2: List breaking down the number of CsI detectors, telescopes and supertelescopes in each ring. The table also covers the θ and ϕ range of detector. The last column consists of the length of each CsI crystal.

Because the front and back segments were separated, the Ring 2-9 Si detectors were designed to allow charge collection on both the p+, front segments and the n+, back plane. Negative bias was applied to the front-plane segments of each Si detector to ensure the bias was more uniformly distributed. The negative charge or electrons were collected on the front side, and the positive charge or electron holes were collected on the back plane. The ability to collect charge from both planes allows for a greater range of isotope identification. The back plane had a lower gain setting and the front segments had a higher gain setting.

The CsI(Tl) detectors were installed to cover the same θ coverage as the top or bottom segments of the Si detectors. The CsI(Tl) detectors were placed on top of each other within each module. For each half of the module within Ring 2-9, one CsI(Tl) detector with a PMT was present, with the exception of Ring 7 and 9. Two CsI(Tl) detectors with a PMT each were located in Ring 7 and 9. PMTs were also used for the CsI(Tl) detectors in Ring 10-11. Photodiodes were attached to the CsI(Tl) detectors in Ring 12-15. The length of the CsI(Tl) crystals throughout each ring varies as noted in Table 2.2. The length was chosen to fully collect light deposition of the highest energy protons in the Fermi Energy region [11]. More details on the exact position of each CsI and Si detector within NIMROD can be seen the schematics in Appendix A and Appendix B.

Two additional steps were taken in order to minimize the amount of impact on the energy resolution of each particle through free electrons. First, a positive 15 kV bias was applied to the target frame within the NIMROD target ladder. The objective was to capture electrons from leaving the target. For the electrons having left the target, 220 $\mu g/cm^2$ aluminized mylar foils were glued to the front of the ionization chamber frames in front of Ring 2-9 to ensure the entire face of each Si detector was shielded.

2.2.2 Electronics Configuration

The objective of the electronic modules within the NIMROD array was to convert the analog signals from the detectors (silicon, Cesium Iodide and neutron ball) to digital signals. The digital signals were collected by the data acquisition software (DAQ). In this section, a brief overview of the modules use to collect signals is discussed. For additional details and electronics diagrams, refer to Ref. [10].

For the silicon detectors, two different electronic configurations were used. For Rings 2-9,

custom motherboards were designed for data collection. The motherboards functioned to hold the Zeptosystem preamps [60], provide ±12 V, and provide bias to each detector. For Rings 10-15, Zeptosystem motherboards [60] were used.

All detectors were biased with a combination of the Tennelec Voltage Supply modules for the Si detectors and PDs, and the LeCroy 1440 Voltage Supply for the CsI-PMTs. The ±12 V power supply for the Ring 2-11 preamps was supplied using a Topward Dual-Channel DC Voltage Supplies. The Si signals were collected using Pico Systems Shaping Amplifiers [61] and converted to digital signals using Philips peak-sensing ADCs. The Si back-plane signals from Ring 2-7 were also sent through Pico Systems Discriminators, which are leading-edge discriminators providing SUM and OR signals for triggering. All the above mentioned modules are CAMAC modules. For Ring 10/11, the same shaping amplifiers were used. However, VME peak-sensing ADCs were used.

For the Indiana Silicon Sphere detectors, signals from both the silicon detectors and the photo-diodes attached the CsI detectors were amplified and shaped using Zeptosystem [60] pre-amplifiers and the shaper component of the original Indiana Silicon Sphere shaping amplifiers [62].

Passive bases were used to bias the CsI-PMTs in Rings 2-11. The signal from the CsI-PMTs were split into the fast and slow component. The fast component was used to trigger the DAQ using a CFD. A 400 ns gate was used to capture the fast portion. After a 1 μs delay, a 1 μs gate captured the slow component. Both signals were sent to a QDC for pulse-shape analysis.

All of the electronics were triggered using a common triggering signal. Events were triggered using one of three triggers: a minimum bias (min bias), high-multiplicity (high-mult) and pulser trigger. For the min bias and the high-mult triggers, signals from the CsI and Si back-plane were used to start the DAQ. In the case on the min bias trigger, the OR from either source was used. In this case, the DAQ is triggered regardless of event multiplicity. For the high-mult trigger, the SUM output was set to trigger the acquisition when a multiplicity of three was detected. The pulser trigger was used to randomly start the DAQ as a background measurement for the neutron ball. A complete description for the trigger logic can be found in Ref. [10].

2.3 Particle Identification

Three forms of particle identification (PID) were implemented in NIMROD: Si vs. Si, CsI vs. Si and CsI Slow vs. Fast. For the combinations and placements of the modules in NIMROD, refer back to Section 2.2. The wide range of isotopic resolution for particles of Z=1 to Z=17 and the elemental resolution through the beam was achieved using a combination of the three PID methods. PID was achieved by using a linearization method to linearize 2-D plots and utilize the x-projection. The x-projections were fit with Gaussian functions for each isotope, providing a quantitative approach to isotopic identification.

2.3.1 CsI Slow Versus Fast (SlowFast)

As previously mentioned in Section 2.2.2, the fast and slow component of the CsI(Tl)-PMT was collected. Unlike most scintillators that produce a single fast component due to interaction with radiation [63], CsI scintillators were unique because they exhibit a two-component decay [64, 63]. The fast component comes from the excitation of radiative states, where as the slow component comes from the excitation of metastable ones within the CsI crystal. Radiative state production was favored for high ionization density, and the metastable state production was favored for low ionization density [63]. The dE/dX profile governs the ionization density of the radiation [64].

To give an example, a heavy ion stops within the a very short distance within the CsI. As a result, the particle has a high ionization density and the production of radiative states was much larger than the metastable states. For a very light particle such as a proton or alpha particle, it punches further into the CsI lowering the ionization density. The metastable states are more highly produced than in the case of the heavy ion. As a result, the various particles can be identified by comparing the fast and slow components.

The thallium-doping of the CsI detectors was done to enhance the number of energy levels in the semiconductor's forbidden energy gap. The thallium-doping allows for the excited electrons to decay back to the valence band, which also shifts the wavelength of the emitted light. The wavelength shift occurs because the energy difference was lower since the electron decays from the forbidden band and not the conduction band. The new wavelength was within the region where the PMT sensitivity was much higher [64].

Figure 2.5 shows PID by plotting the slow component versus the fast component of the CsI-

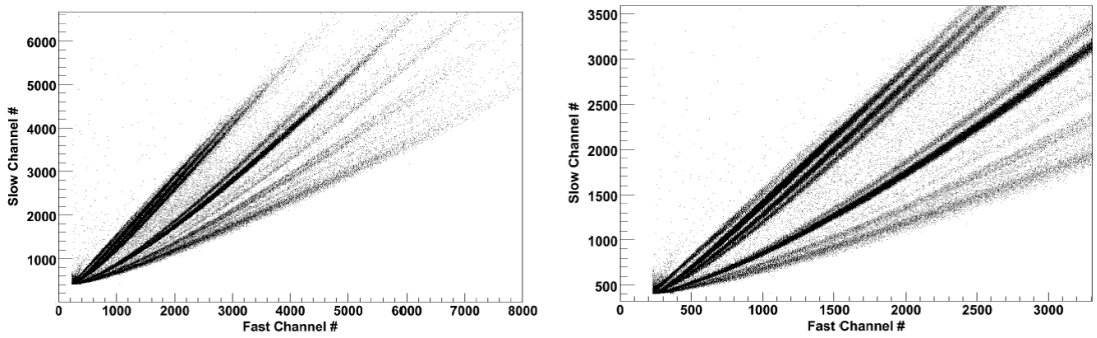

Figure 2.5: Slow vs. Fast component of the CsI signals. The left panel shows the entire QDC range and the right panel shows a zoomed-in version of the same histogram. Reprinted from Ref. [10].

PMT signal. The left panel shows the entire range and the right panel shows a zoomed in version of the left hand panel at the origin. The motivation of the left panel was to show the p, d, t resolution at low energy. The results show isotopic particle identification of Z=1-3. The Z=1 band, which corresponds to the top band, has clear separation between protons, deuterons and tritons. ^{3}He, ^{4}He, ^{6}He and ^{8}He, were seen in the Z=2 band. ^{8}He does not exist and corresponds to 2α particles. For particle with Z>3, the difference in ionization density was not great enough to separate the isotopes and elements.

2.3.2 CsI Versus Silicon (CsISi)

For Z≥3, most particles were identified by plotting the energy lost in the silicon detector (ΔE) versus the residual energy deposited in the CsI crystal (E). The entire detector array consists of Si-CsI modules, as noted in Section 2.2, which maximizes the identification capabilities of the heavy fragments. Two methods exist in Ring 2-9 to identify isotopes using the CsI-Si methods. The front-plane or the back-plane signal can be plotted against the CsI signal, as shown in left and right panels of Figure 2.6, respectively. Using both the front-plane and back-plane allows for the shaping amplifier gains to be set to achieve greater elemental identification.

The energy loss, dE/dX, of a charged particle through material can be described by the Bethe-Bloch equation [63]. The Bethe-Blocke equation was simplified to

$$-\frac{dE}{dX} \propto \frac{Z^2}{v^2} \propto \frac{Z^2 \cdot A}{KE} \tag{2.1}$$

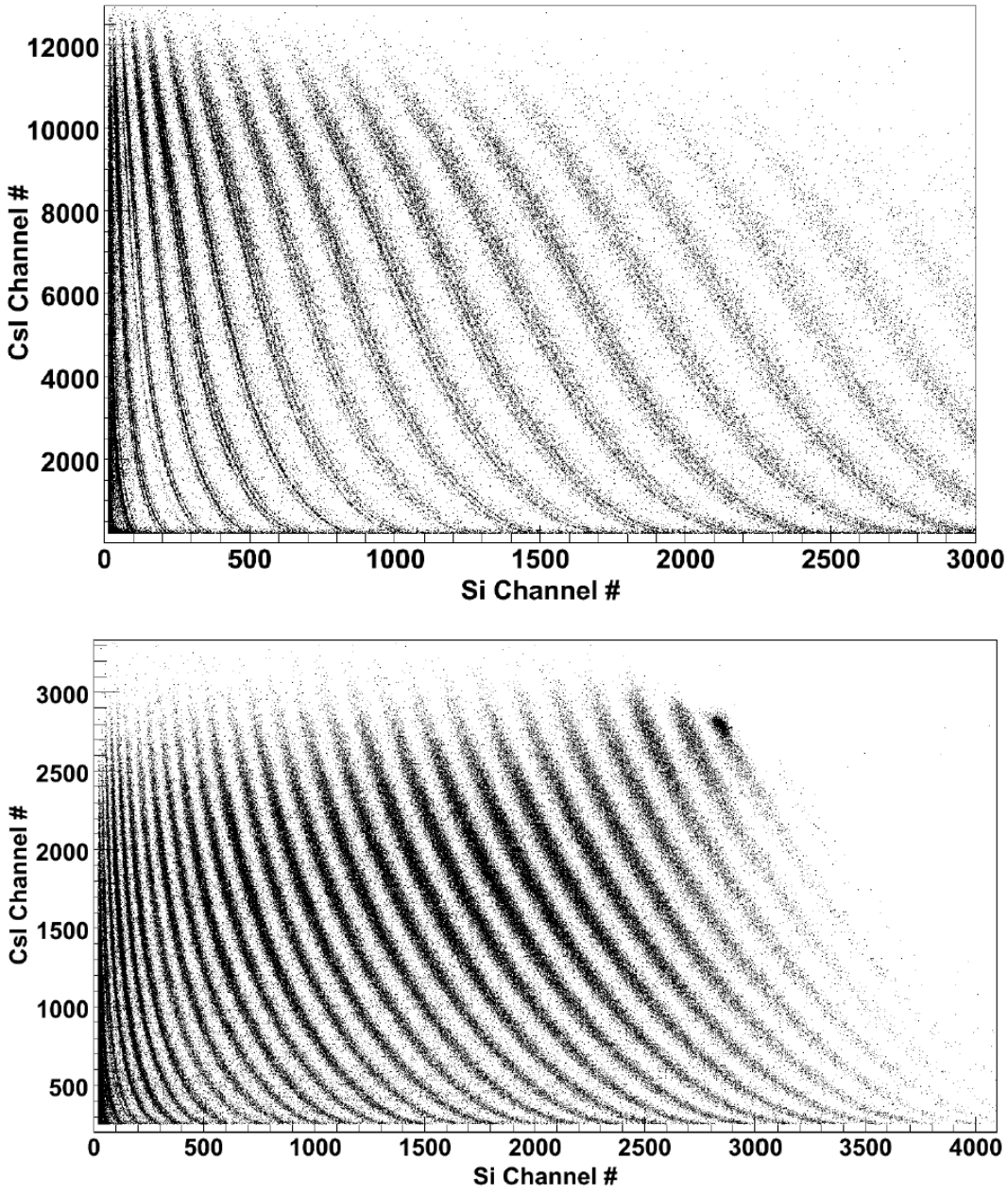

Figure 2.6: CsI total energy in channels vs. Si energy in channels. The top panel corresponds to the Si front signals and the bottom panel corresponds to the Si back signals. Reprinted from Ref. [10].

where Z was the charge, A was the mass and KE was the kinetic energy of the particle [64]. The energy loss of the particle through the silicon detector are dependent on the charge and mass of the particle. Equation 2.1 also explains why the charge bands are easier to separate than the

isotopic bands.

2.3.3 Silicon Versus Silicon (SiSi)

For the supertelescopes, additional PID capabilities exist in the form of Si versus Si plots in addition to the Si vs CsI plots. The signal of the second silicon (500 μm) detector was plotted against the signal of the first silicon (150 μm) detector. The results were shown in Figure 2.7. The Si vs. Si plots allows for greater isotopic identification due to the lower energy threshold requirement to punch through the 1st silicon detector. In addition, the energy resolution of the silicon detectors is greater than the energy resolution of the CsI detectors.

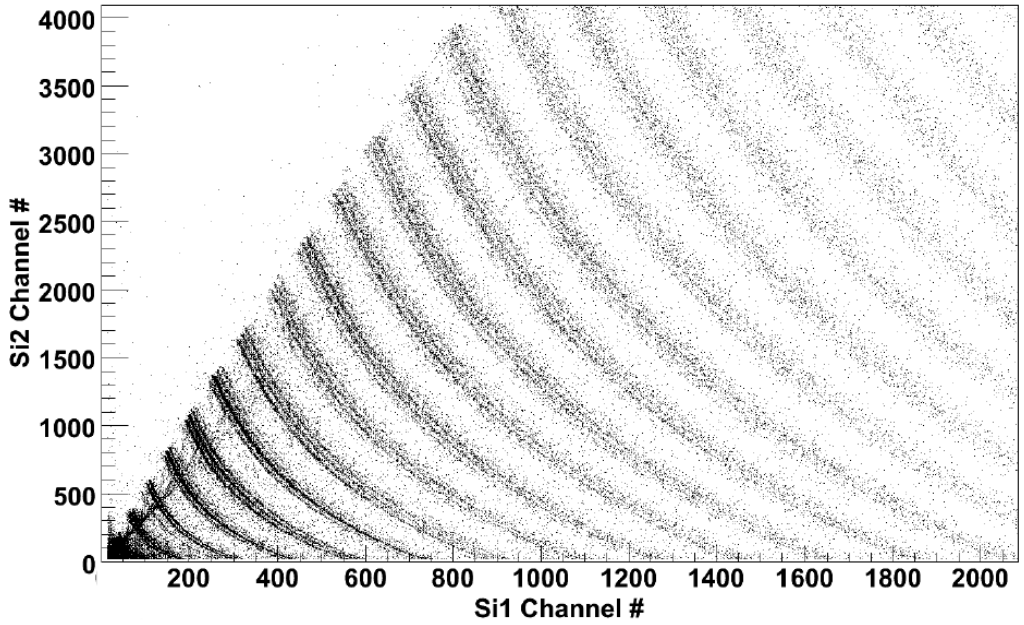

Figure 2.7: Second Si detector signal vs. first Si detector in channel number. Reprinted from Ref. [10].

2.3.4 Linearization Method

A linearization method was utilized to determine the Z and A of each particle. The method allows for conversion of the 2-D plots to 1-D projections of the data. The first step consists of hand-picking the data along the curvature of each elemental line. A spline fit was applied using a

100 points evenly spaced and were used to linearize the experimental data.

The linearization method works by calculating the relative distance of an experimental data point to the two closest lines. As an example, if a point was located $\frac{2}{3}$ of the way between Z=5 and Z=6, the assigned linearization value, or LinZ, would be 5.67. The value for LinZ was calculated using Equation 2.2- 2.4, where Line1 and Line2 were the Z lines, and dist1 and dist 2 were the distance from the data point to the Z line. Which equation gets chosen depends on where the data point falls relative to the Z line. For data points to the left and right of the first and last Z line, Equation 2.2 and Equation 2.4 were used, respectively. For all other data, Equation 2.3 was used.

$$LinZ = \frac{dist2}{|dist2 - dist1|}Line1 - \frac{dist1}{|dist2 - dist1|}Line2 \tag{2.2}$$

$$LinZ = \frac{dist1}{|dist1 + dist2|}Line2 + \frac{dist2}{|dist1 + dist2|}Line1 \tag{2.3}$$

$$LinZ = \frac{dist1}{|dist1 - dist2|}Line2 - \frac{dist2}{|dist1 - dist2|}Line1 \tag{2.4}$$

Line1 and Line2, which were utilized in Equations 2.2- 2.4, came from the 99 line segments between each of the 100 spline fit points. The LinZ value calculated was plotted in a 2-D plot against the original 2-D plot y-value. Additional information regarding the linearization method can be found in Ref. [11, 65].

The last step before taking the 1-D projections of the data was to incorporate limits. For each elemental line, left and right limits were added to help define the charge and limit noise contribution. A lower limit was also applied to minimize the noise contamination level in the data set. The values that fall within the 2-D limits were projected onto the x-axis. For the linearized experimental data, it was subsequently possible to assign isotopic identification. The details will be further discussed in Section 2.3.5.

2.3.5 Gaussian Fits for PID

The next step in the PID process was to fit each of the 1-D projections discussed in Section 2.3.4 with Gaussian functions. The Gaussian functions allow one to define the Z and A for each peak. Each Gaussian fit represents a different elemental and isotopic combination. The form of the Gaussian function is

$$G(x) = C \cdot \exp^{-0.5\cdot(\frac{x-\mu}{\sigma})^2} \tag{2.5}$$

where C was the height, μ was the mean, σ was the width of the Gaussian distribution. The Gaussian distribution was fit for each of the isotope for a given element. The parameters were then adjusted to minimize the total errors for the sum of the Gaussians. Most of the Gaussian distributions have partial overlap with neighboring Gaussian distributions. Because of the overlap, the contamination factor for each isotope can be calculated for each isotope using the equation

$$Contam\% = \frac{\left(\sum_{i=0}^{N_{Gauss}} G_i(LinZ)\right) - G_{Max}(LinZ)}{G_{Max}LinZ} \tag{2.6}$$

where N_{Gauss} was the number of Gaussian fits per element, G_i(LinZ) was the value of the i^{th} Gaussian at LinZ, and G_{Max}(LinZ) was the maximum value of G_i(LinZ) for all the Gaussians. The contamination factor used in the analysis discussed in Chapter 3. Another tool to determine the accuracy of the Z and A assignment was the fraction of sigma, which was defined as

$$FracSigma = \frac{|LinZ - \mu|}{\sigma} \tag{2.7}$$

where μ and σ were the same parameters using in Equation 2.5 for G_{Max}(LinZ). The fraction of sigma represents the distance of a data point from the center of the Gaussian, and a value of 2.0 was using in the analysis in Chapter 3. For details about how the contamination percentage and the fraction of sigma were used to accept the isotopic identification of a particle refer to Ref. [10].

The exact assignment of the A for each Gaussian distribution was determined based on previous work. For lighter fragments, the experimental yields were compared to natural abundances. For higher Z fragments, the A assignment was done based on previous NIMROD experimental assignment [11] and comparing isotopic yield distributions from MARS experiments [31]. If the particle was not isotopically identified, a value of A=0 was assigned. A "GuessA" value was later assigned based on most likely A.

The linearization process was applied for all types of detectors in the ^{70}Zn+^{70}Zn, ^{64}Zn+^{64}Zn, and ^{64}Ni+^{64}Ni reaction systems at 35 MeV/nuc.

2.4 Energy Calibration

All experimental data is collected in the form of electronic module channel number. In order to convert the data from channel number to energy, calibration beams (Table 2.1) were used to scatter particles of a given energy into each detector.

The calibration beams were scattered off ^{nat}Th. ^{nat}Th was chosen due to its large atomic charge (Z=90), which maximizes the scattering cross-section at large angles. The calibration points and the punch-through points were used to calibrate the NIMROD detectors.

The silicon detectors were calibrated using the punch-through energy points, the 25 MeV/nucleon ^{20}Ne calibration beam and the ^{228}Th source for larger rings. The punch-through point corresponds to the energy needed for each isotope to pass through and exit a silicon detector. The punch-through points are shown on the top-left of each line in the Si-Si plots and the top of the CsI-Si plots. Each plot has a different means to calculate these points. For the CsI-Si plots, the value was determined by taking the minimum energy from the silicon detector coming in coincidence with a CsI signal. For the Si-Si plots, two punch-through points can be calculated. The 1st is the energy needed to punch through the 1st, 150 μm thick silicon detector, and the 2nd is the energy needed to punch through the 2nd, 500 μm thick detector. The punch-through points on the Si-Si plot are very visible. The corresponding energy for each isotope was calculated using energy loss tables [66].

Assuming a linear relationship between the particle energy and the silicon signal [63], a calibration was established of the form

$$Energy = m \cdot SiChannel + b \tag{2.8}$$

where m is the slope and b is the y-intercept.

For the CsI calibration, the calibration beams and previous experimental data [67] was used. Unlike the silicon detectors, the light output from the CsI detectors is not linearly related to the particle energy and depends on the particle charge and mass. To calculate the relationship, Equations 2.9- 2.11 from Ref. [68] was used. The equation is based on the Birk's formula. The 3 equations related the CsI energy E to the light output h and ρ.

$$E = \sqrt{h^2 + 2\rho h\left(1 + \ln\left(1 + \frac{h}{\rho}\right)\right)} \tag{2.9}$$

$$\rho = \eta Z^2 A \tag{2.10}$$

$$h = \frac{chan - ped}{scal} \tag{2.11}$$

Chan is the slow signal from the CsI-PMT signal, *ped* is the pedestal for each detector, *scal* and η are fitting parameters, Z is the charge and A is the mass of the particle. Further details and examples of the Si and CsI energy calibration can be seen in Ref. [10].

The total energy was calculated based on the CsI-PMT and silicon detector calibrations. For a particle with Z≥4, the silicon calibration was used to determine the energy loss in the silicon detector. The silicon detector energy loss and energy loss tables [66] were used to determine the CsI residual energy. The process using the silicon detector calibration was not applied to Z=1 and Z=2 particles because the gains in the Ring 2-11 silicon detectors were set too high to detect or the energy of the particle was too low to distinguish from the noise. Further details are discussed in Ref. [10].

3. NEUTRON-PROTON EQUILIBRATION CHRONOMETRY

The neutron-proton (NZ) equilibration between the two heaviest fragments (**HF** and **LF**) produced in binary decay of the excited projectile-like fragment (PLF*) was investigated. The reaction systems studied were ^{70}Zn+^{70}Zn, ^{64}Zn+^{64}Zn and ^{64}Ni+^{64}Ni at 35 MeV/nucleon. All Sections, except for the last one will focus on the ^{70}Zn+^{70}Zn reaction systems due to the greater statistics. Section 3.1 will discuss how the two heaviest fragments of the PLF* were identified. Section 3.2 will discuss the angular distribution, and the composition as a function of rotation angle will be in Section 3.3. Section 3.4 will focus on the conversion from rotation angle to time. The effects of secondary decay will be talked upon in Section 3.5. Lastly, the results from the ^{64}Zn+^{64}Zn and ^{64}Ni+^{64}Ni reaction system will be compared to the ^{70}Zn+^{70}Zn reaction system in Section 3.6. The results for the analysis discussed in this Chapter have been published in Ref. [1] and Ref. [4].

3.1 Determination of the Source

To focus on the dynamical decay of the PLF*, events were chosen where at least two heavier charged particles were measured in NIMROD. The charged particles were sorted by atomic number with charge-equivalent particles sorted by mass number. The heavier of the two fragments was labelled as heavy fragment (**HF**) and required to have an atomic number of $Z_H \geq 12$. The lighter fragment was labelled as light fragment (**LF**) and an atomic number requirement of $Z_L \geq 3$ was implemented. Both **HF** and **LF** were required to be isotopically identified. A total measured charge (Z_{tot}) condition of $21 \leq Z_{tot} \leq 32$ was applied. The total measured charge includes Z_H, Z_L and all other charged particles measured.

The Z_H, Z_L and Z_{tot} requirements maximize the possibility the fragments originated from the PLF*. The $Z_L \geq 3$ requirement ensures fragments are mostly produced dynamically. Due to their low binding energy, α, helion, triton, deuteron and proton fragments are commonly emitted during the secondary decay or evaporation phase. Therefore, the dynamic decay signature of the the $Z = 1 - 2$ fragments is highly suppressed relative to the statistical decay one. Because the Z_L atomic number requirement is very low, the $Z_H \geq 12$ requirement was implemented to guarantee the combined Z_H and Z_L consists of at least 50% of the total atomic number of the projectile ($Z_{projectile}$=30). Additionally, in the process of the analysis, concerns arose whether or not a $Z_H < 12$

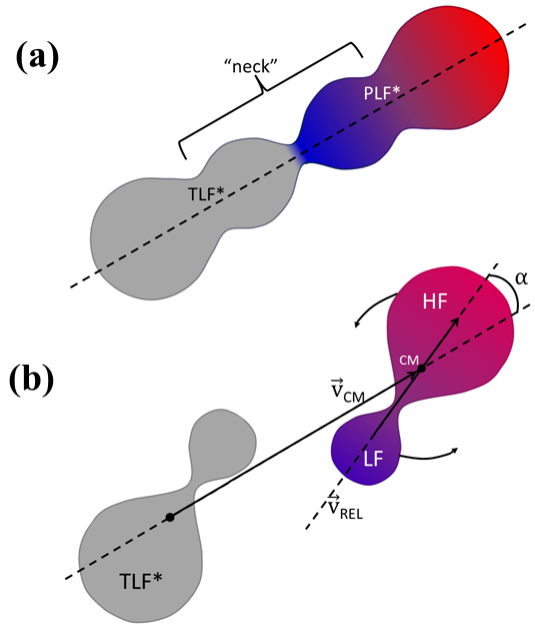

Figure 3.1: Schematic of the deformation and decay in dynamical decay. Panel a shows the elongation between the TLF* and PLF* along the axis of separation (dotted line) before the neck rupture. Panel b shows the subsequent time where the neck has ruptured and the TLF* and PLF* has separated. The PLF* has rotated relative to the PLF*-TLF* axis of separation ($\vec{v}_{CM}$). The PLF* is about to break into the **HF** and **LF**, and the angle α is proportional to the contact time between the two fragments. The coloring corresponds to the composition where blue indicates relative neutron richness and red indicates relative proton richness.

actually corresponds to the heaviest fragment. Further details of this will be discussed in Section 3.3.

Figure 3.2 shows the charge of the **LF** versus the charge of the **HF**. The z-axis corresponds to the yield plotted in log scale. The largest enhancement in the yield is seen at small Z_H,Z_L pairings. A hard cut-off in the yield at Z_H >21 is seen on the right side of Figure 3.2. The hard cut off is due to the isotopic limitations of the supertelescopes in the NIMROD array.

Lastly, the 21≤ Z_{tot} ≤32 cut was added to ensure the fragments generating from the PLF*, as well as the heaviest fragment originating from the PLF*, were analyzed. The neck formation between the TLF* and PLF* results in the flow of protons and neutrons from one species to the other [38, 10, 34]. However, the flow is limited to a few neutrons and/or protons. Events where Z_{tot} >32 most likely correspond to cases where at least one larger fragment originating from the TLF* is identified in NIMROD. While NIMROD has a very large angular coverage, the lack of coverage between 0.0° < θ <3.6° can result in the heaviest fragment missing the NIMROD detector. In

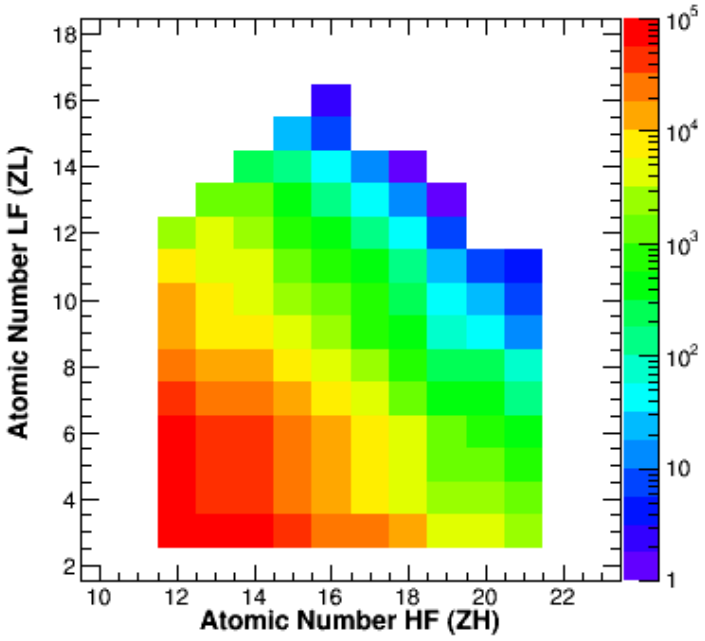

Figure 3.2: Atomic number of the **HF** vs. the atomic number of the **LF**.

order to reject these events, the minimum total charge multiplicity of Z_{tot} ≥21 was applied.

The parallel velocity (v_Z) distribution of the **HF** and **LF** can be used to verify the source of the **HF** and **LF**. The distribution is seen in Figure 3.3. The distributions are for Z_H=14, Z_L=7 (top, left) Z_H=14, Z_L=5 (top, right) Z_H=12, Z_L=7 (bottom, left) Z_H=12, Z_L=5 (bottom, right). The red line represents the **HF** velocity distribution, and the blue line represents the **LF** velocity distribution. The dashed lines, right to left, correspond to the beam velocity (0.27c) and mid-velocity (0.13c), with the target located at 0.00c in this frame. Both the **HF** and **LF** distributions are peaks above the mid-velocity. The distribution for the **HF** is peaked just below the beam velocity, which is consistent with the **HF** being a slightly velocity-dampened projectile-like fragment. The **LF** velocity distribution is peaked between the mid-velocity and the **HF** peak. The **LF** peak location indicates the particle is formed in the neck region, but dynamically decays from the PLF*. These results further support the picture illustrated in Figure 3.1.

The four Z_H, Z_L combinations shown in Figure 3.3 are a representative set of pairings. Focus will be paid to these pairings throughout Chapter 3 with an understanding that similar effects are

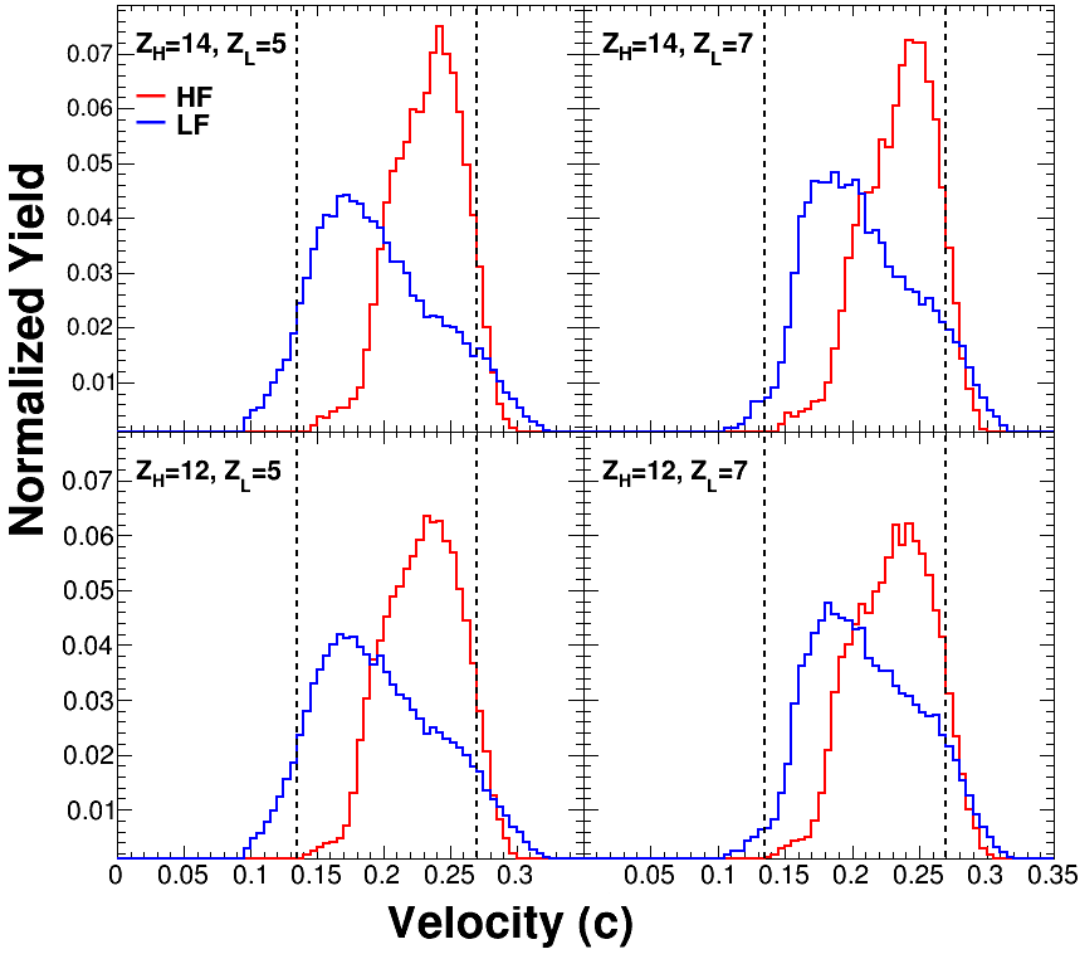

Figure 3.3: Parallel velocity distribution of **HF** (red) and **LF** (blue). The dashed lines correspond to the beam velocity (0.27c, right) and mid-velocity (0.13c, left). The target, in this frame, is at rest (0.00c). The majority of the distribution is located above mid-velocity.

seen and characterized in 39 other pairings.

3.2 α Angular Distribution

The alignment angular distribution can give insight into the dynamics of the PLF* decay. The alignment angle, α is defined in Equation 3.1.

$$\alpha = acos\left(\frac{\vec{v}_{CM} \cdot \vec{v}_{REL}}{||\vec{v}_{CM}||||\vec{v}_{REL}||}\right) \tag{3.1}$$

The two velocity vectors are the center-of-mass velocity ($\vec{v}_{CM}$) of the **HF** and **LF**, as shown in

Equation 3.2, and the relative velocity, as shown in Equation 3.3.

$$v_{CM} = \frac{m_{HF}\vec{v}_{HF} + m_{LF}\vec{v}_{LF}}{m_{HF} + m_{LF}} \tag{3.2}$$

$$v_{REL} = \vec{v}_{HF} - \vec{v}_{LF} \tag{3.3}$$

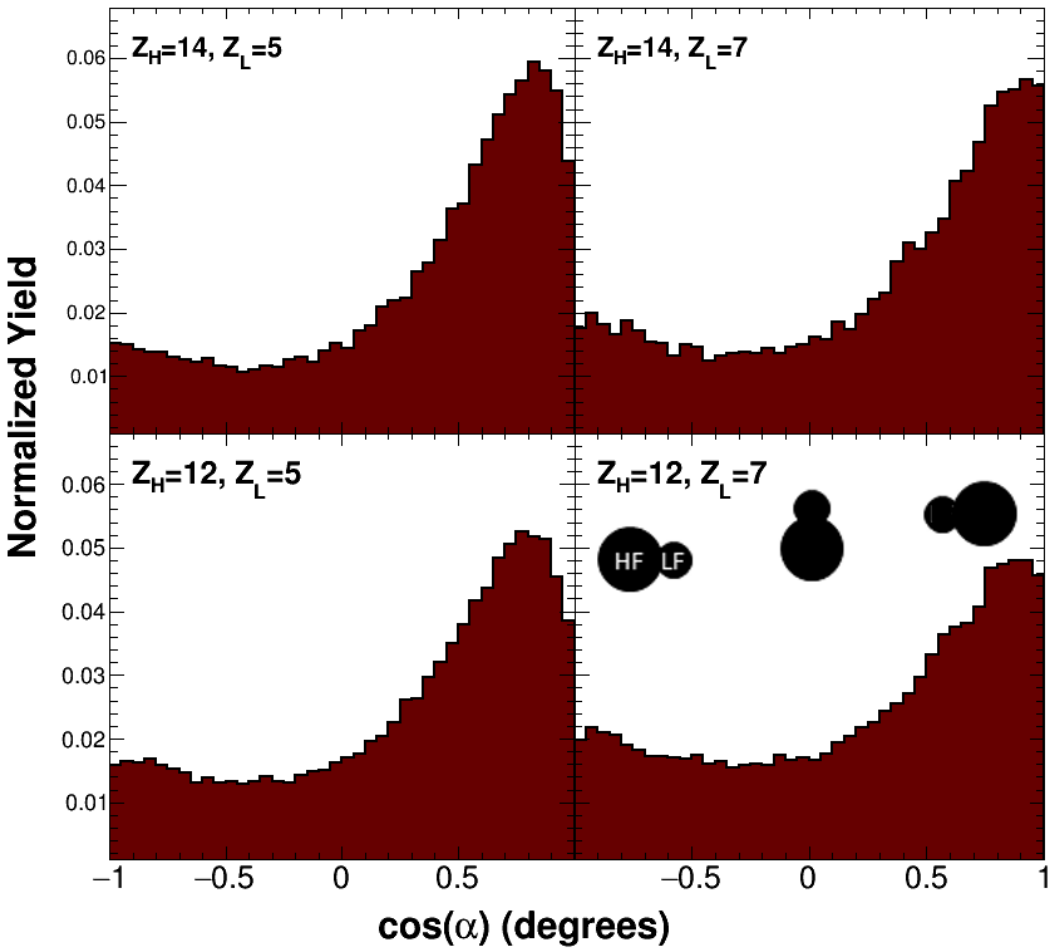

Figure 3.4: The cosine alpha distributions for four select Z_H, Z_L pairing. The large yield enhancement is seen at cos(α)=1 is consistent with dynamical decay sitting on top of an isotropic statistical background.

Figure 3.4 shows the $cos(\alpha)$ distributions for the four Z_H, Z_L combinations featured. For each

pairing, there is a strong yield enhancement at $cos(\alpha)$=1. The enhancement represents a preference for decay of the **HF** forward relative to **LF**. As $cos(\alpha)$ decreases, the yield falls off quickly reaching a minimum around $cos(\alpha)$=-0.5. The $cos(\alpha)$ distribution is flat between -1.0< $cos(\alpha)$ <-0.5 with a slight increase as $cos(\alpha)$ reaches -1.

The features in the angular distribution discussed above are indicative of the two different production mechanisms. For statistical decay from a non-rotating source, the $cos(\alpha)$ distribution should be flat. If the source is rotating, an enhancement in the yield is seen at the edges of the $cos(\alpha)$ distribution ($cos(\alpha)=\pm1$) [48, 5, 39] and the enhancement is symmetric around $cos(\alpha)$=0. The greater the angular momentum, the larger the enhancement at the edges due to a preference for fragments to decay in the plane perpendicular to the angular momentum vector [69, 70]. Therefore, the yield at $cos(\alpha)$ <0 is primarily due to statistical decay.

To verify the contribution to the angular distribution from the statistical mechanism, GEMINI++ [71] simulations were performed. A ^{58}Fe nucleus was inputted into GEMINI. A reasonable angular momentum of l=22$\hbar$ was chosen and an excitation energy per nucleon range of 0-3.0 MeV/nucleon was randomly assigned. The decaying fragments were boosted in velocity in the lab frame assuming the inital PLF* was at approx. 90% of the beam velocity (v_{beam}=0.27c). All Z_H, Z_L pairings were combined due to limited statistics. Minimum energy or double hit requirements were not applied.

Since GEMINI++ is a statistical decay simulation, the results should give insight into the shape of the angular distribution. Simulated particles were passed through minimum energy cuts to replicate the NIMROD environment. Results from the GEMINI++ simulation are shown in Figure 3.5. For each angular momentum and excitation energy per nucleon combination, the symmetry around $cos(\alpha)$=0 was preserved. The excess yield at $cos(\alpha)=\pm1$ was also present.

The GEMINI++ simulations did not produce the anisotropy at $cos(\alpha)$=1, which implies the enlargement is not solely due to the statistical production mechanism. Rather, the excess yield at $cos(\alpha)$ >0 is consistent with dynamical decay. Dynamical decay occurs when the PLF* is strongly deformed and breaks apart promptly into two large fragments along the PLF*-TLF* separation axis. Therefore, the most aligned configuration, $cos(\alpha)$=1, has the greatest yield. The yield decreases as the break up configuration becomes less aligned. The location of the $cos(\alpha)$ distribution peak depends on the mass asymmetry of the **HF** and **LF**. The peak is closer to $cos(\alpha)$=1 for sys-

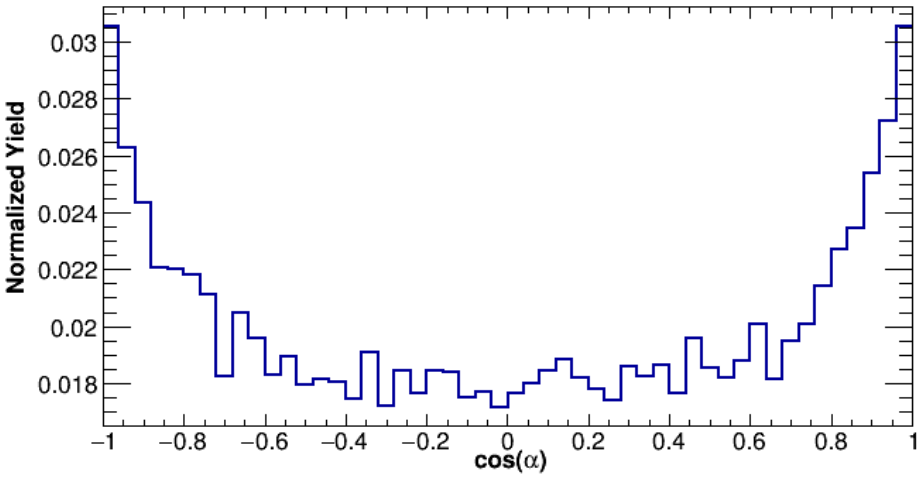

Figure 3.5: Cosine angular distribution for all combined Z_H,Z_L pairings. All pairings were combined due to a limited statistics. Results show a flat distribution with a small enhancement at cos(α)=±1 due to the presence of spin.

tems where the difference in **HF** and **LF** is the greatest. This effect is notable for the peak of the $cos(\alpha)$ distribution for the four Z_H, Z_L combinations shown in Figure 3.4. The peak moves from left to right for Z_H=12 and Z_L=5, Z_H=14 and Z_L=5, Z_H=12 and Z_L=7, and Z_H=14 and Z_L=7, respectively, where Z_H=14 and Z_L=5 and Z_H=12 and Z_L=7 are similar. The shift in the $cos(\alpha)$ peak is due to collectivity and a larger potential barrier. These effects slow down symmetric breaks and decrease their likelihood of occurring.

Because the dynamical contribution to the angular distribution is very **HF**-forward focused relative to **LF**, the timescale of the dynamical decay production mechanism is much shorter than the PLF* period of rotation. Less alignment in the PLF* break up indicates a longer time of contact between the **HF** and **LF**, which is the basis for using the rotation angle as a clock.

3.3 Average Composition Versus Rotation Angle ($\langle\Delta\rangle$ Vs. α)

This section is divided into two subsections. The first subsection (Section 3.3.1) will focus on the results from plotting $\langle\Delta\rangle$ versus α. The second subsection (Section 3.3.2) will discuss the exponential fits that were applied.

3.3.1 $\langle\Delta\rangle$ Versus α

The average composition $\langle\Delta\rangle = \left\langle\frac{N-Z}{A}\right\rangle$ for **HF** and **LF** is calculated for each Z_H, Z_L pairing. The $\langle\Delta\rangle$ is plotted as a function of α as shown in Figure 3.6 for the four pairings seen in the previous figures in Chapter 3. The results for all 43 pairings analyzed is shown in Figure 3.7 for $12 \leq Z_H \leq 15$ and Figure 3.8 for $16 \leq Z_H \leq 19$. The detector configuration of NIMROD provides for larger angular binning than previous experimental results [7, 8, 72], which allows for more detailed examination of the evolution of $\langle\Delta\rangle$ vs α.

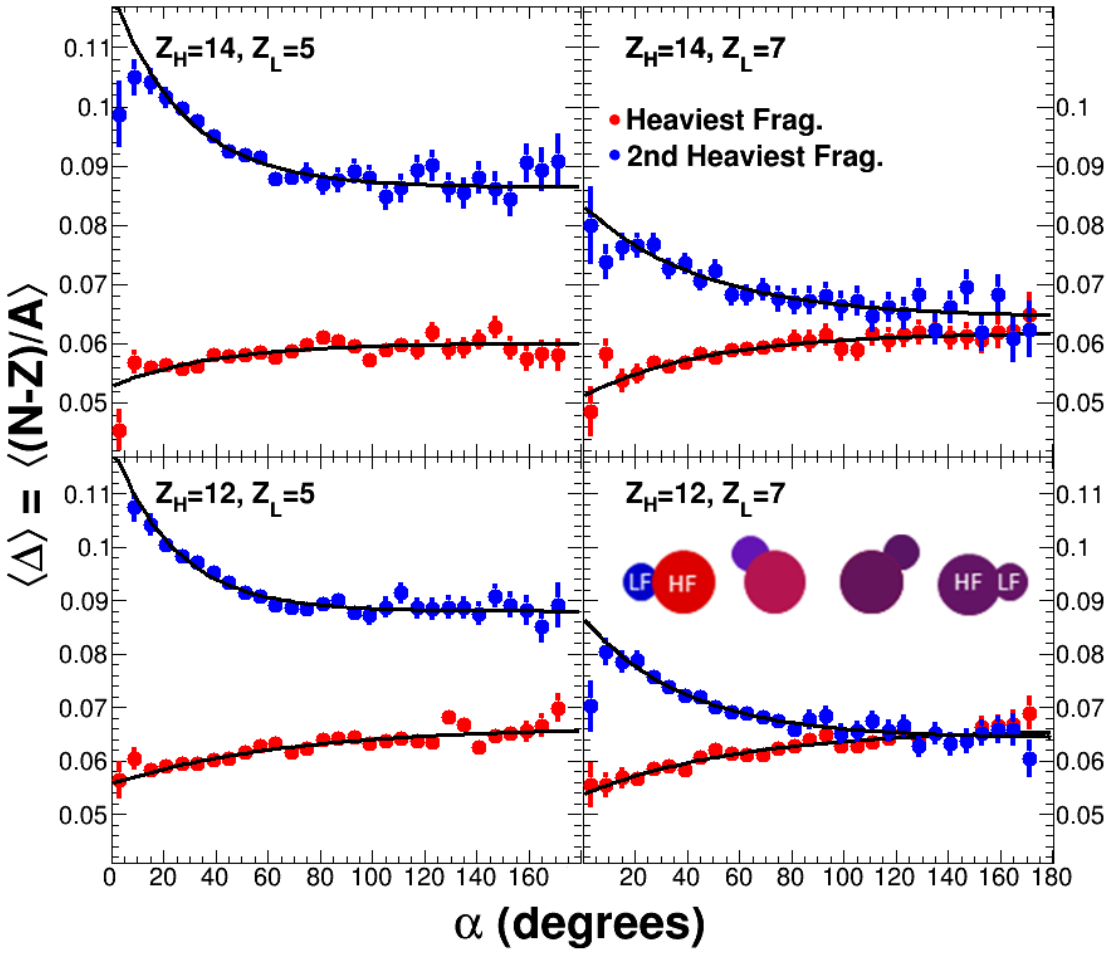

Figure 3.6: Composition as a function of decay alignment showing equilibration. As the angle of rotation increases (α increases from 0° to 180°), the $\langle\Delta\rangle = \langle\frac{N-Z}{A}\rangle$ initially decreases rapidly for Z_L and increases for Z_H before plateauing. The majority of equilibration occurs between 0° and 80°.

For **LF**, the initial composition (at α=0°, t=0) starts off relatively neutron rich. As the angle of rotation increases, $\langle\Delta_L\rangle$ falls off rapidly for small changes in α. The $\langle\Delta_L\rangle$ starts to level off as α increases, eventually plateauing. Most of the equilibration occurs within α <80°. Similarly, $\langle\Delta_H\rangle$ starts off neutron-poor and evolves to be more neutron-rich as α increases. The evolution of both $\langle\Delta_H\rangle$ and $\langle\Delta_L\rangle$ is exponential as a function of rotation angle indicating first-order kinetics. The inset in Figure 3.6 illustrates the change in composition. The coloring is consistent with the schematic in Figure 3.1 with blue indicating relative neutron abundance and red indicating relative neutron deficiency.

The dependence of $\langle\Delta\rangle$ on α is understood when examining the dynamical production mechanism. As discussed in Section 3.2, the PLF* tends to break apart quickly due to the strong deformation and velocity gradient. The **HF** has its origin as the projectile-like fragment and the **LF** has its origin in the neck region. The neck region is characterized as being neutron-rich due to a preferential flow of neutrons to the low-density region [46]. This preferential neutron flow occurs to minimize the asymmetry energy. The projectile and target are both at saturation density. After they collide, the low density neck is formed between the two species, while the projectile-like and target-like ends remain at saturation density. Because the asymmetry of both the projectile and target is large, the target and the projectile pays an energetic price due to their asymmetry. The asymmetry energy contribution below saturation density is lower, therefore the neutrons preferentially flow to the low density region. As a result, if the **HF** and **LF** break apart immediately, the **LF** is relatively neutron-rich and the **HF** is closer to symmetric (N=Z).

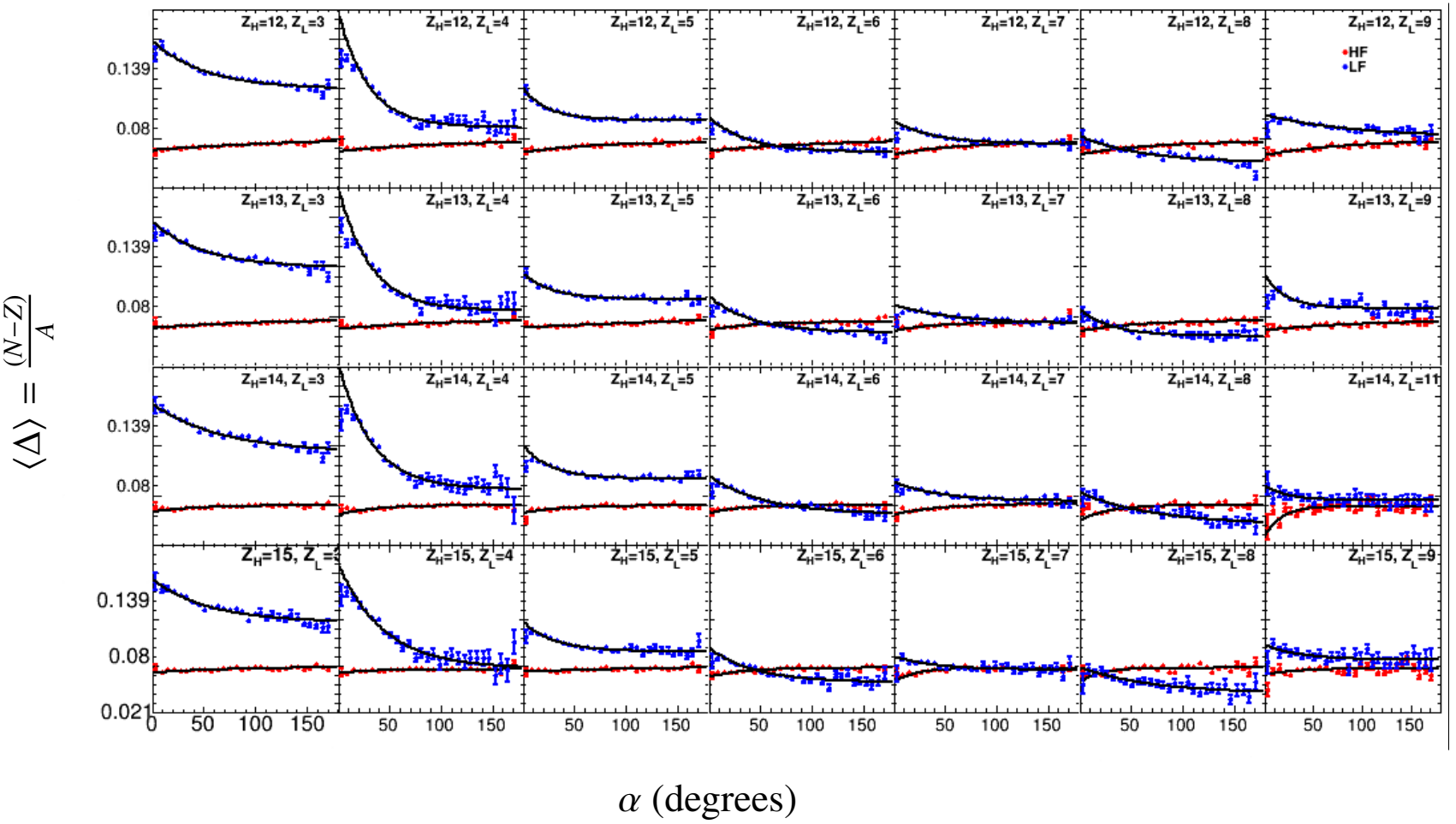

Figure 3.7: $\langle\Delta\rangle$ vs α for combinations of $12 \leq Z_H \leq 15$ and the corresponding Z_L pairing where both the $\langle\Delta_H\rangle$ and $\langle\Delta_L\rangle$ fits converged with the exception of Z_H=13,Z_L=5. Reprinted from Ref. [4].

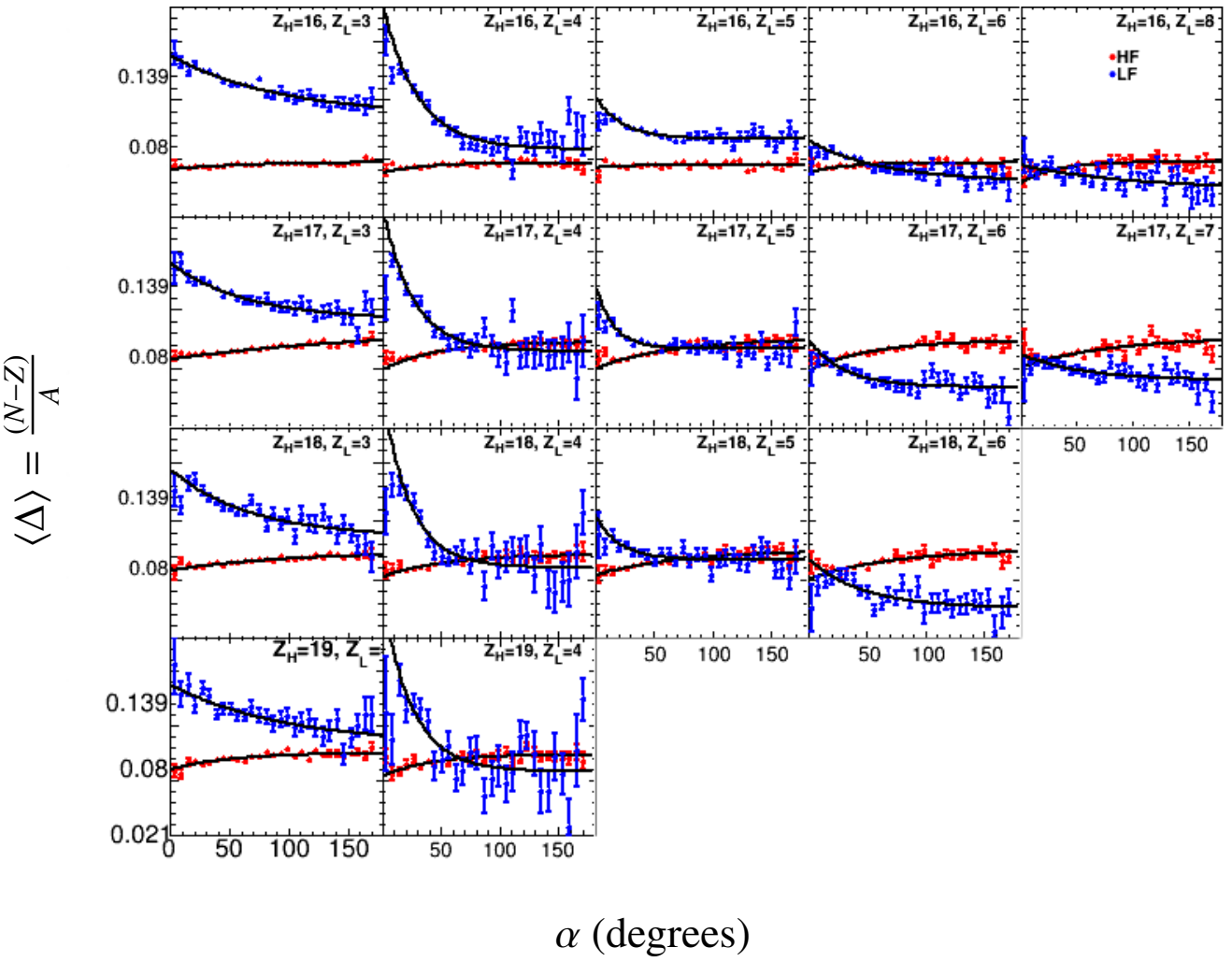

Figure 3.8: $\langle\Delta\rangle$ vs α for combinations of 16$\leq Z_H \leq$19 and the corresponding Z_L pairing where both the $\langle\Delta_H\rangle$ and $\langle\Delta_L\rangle$ fits converged. Reprinted from Ref. [4].

The nuclear attractive forces can delay the PLF* decay or even prevent the PLF* from decaying dynamically. The surface tension acts as an opposing force driving the deformed PLF* towards sphericity. The longer the **HF** and **LF** stay in contact before breaking apart, the more their densities evolve towards each other. The asymmetry also changes likewise, therefore the slower the decay (α >0), the more similar the $\langle\Delta_H\rangle$ and $\langle\Delta_L\rangle$ values should be. However, the plateau values are not necessarily equal, which will be discussed in further detail in Section 3.3.2.

Originally, the **HF** requirement was less constrained with a $Z_H \geq 7$ cut. However, while the **LF** still showed the exponentially decreasing effect in $\langle\Delta_L\rangle$, $\langle\Delta_H\rangle$ evolved linearly as a function of α. Two reasons have been proposed for the difference in the shape of the $\langle\Delta_H\rangle$ as a function of α: missing the **HF** and collision dynamics. Due to the angular coverage of NIMROD, mostly notably the lack of coverage at $0.0^\circ < \theta < 3.6^\circ$, there is a possibility the **HF** will not be detected. If the **HF** is very forward focused and The **HF** detected could actually be the **LF** due to the Z_H requirement being smaller than the Z_{tot} minimum ($21 \leq Z_{tot} \leq 32$).

For the collision dynamics, mid-peripheral and peripheral collisions produce the dynamical mechanisms focused on in this work. Central collisions cause the PLF* to "shatter" apart, which produce many fragments with smaller atomic numbers. As a result, the different types of collisions are more likely to mix and may impair the signature of interest.

3.3.2 Δ Versus α Exponential Fit

Each of the Z_H, Z_L combinations, the exponential trend was parameterized using a fit seen in Equation 3.4,

$$\langle\Delta\rangle = a \pm b \cdot e^{-c\alpha} \tag{3.4}$$

where a is the asymptotic value, b is the pre-exponential factor and c is the rate constant. The exponential fits were only fitted between $12^\circ \leq \alpha \leq 168^\circ$. The exponential fit is limited to this α range due to the angular granularity of NIMROD. Only pairing where the fit for both Z_H and Z_L converged were analyzed. In total, 43 pairings were analyzed. The next series of plots looks into detail at the a and c parameter.

The asymptotic value, a, for each $\langle\Delta_H\rangle$ versus α and $\langle\Delta_L\rangle$ versus α fit corresponds to the average final composition ($\alpha \simeq 180^\circ$). Figure 3.9 shows the asymptotic values for each Z_H, Z_L

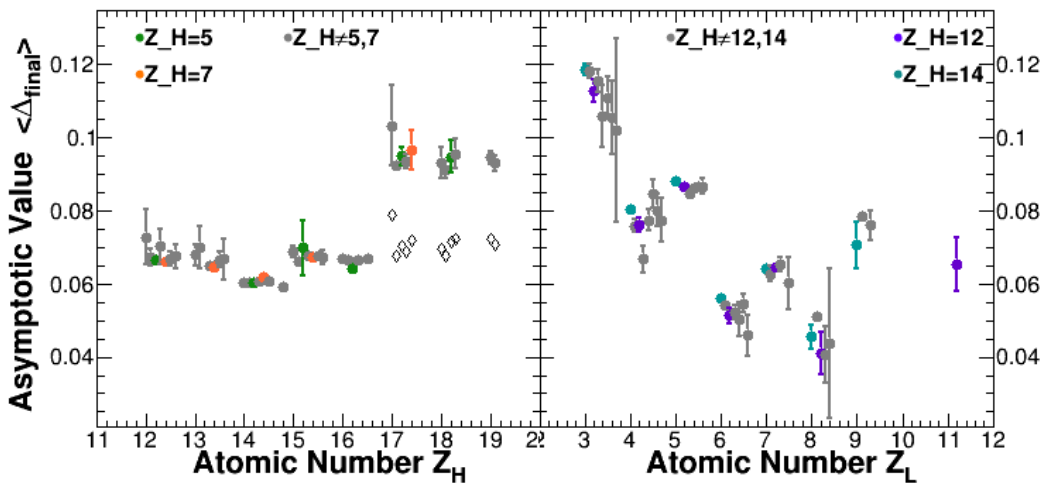

Figure 3.9: Asymptotic value of $\langle\Delta\rangle$ plotted from the $\langle\Delta\rangle$ vs. α fit. The rate constants for **HF** are plotted as a function of Z_L in the left panel and the rate constants for **LF** as a function of Z_H are in the right panel. The green and orange points correspond to the Δ_H values for Z_L=5 and Z_L=7, respectively, and the teal purple and teal points correspond to the Δ_L values for Z_H=12 and Z_H=14, respectively. The asymptotic values for Z_H >16 were recalculated for $\frac{(N-1)-Z}{A-1}$, and the new values are plotted with open, black triangles. Reprinted from [4].

combinations. The left panel shows the values for $\Delta_{final,H}$ as a function of Z_L and the right panel shows the values for $\Delta_{final,L}$ as a function of Z_H. The color is used to highlight the Z_H and Z_L values focused upon in this work. Green and orange represent the $\Delta_{final,H}$ values as a function Z_L=5 and Z_L=7, respectively. Similarly, teal and purple represent the $\Delta_{final,L}$ values as a function Z_H=12 and Z_H=14, respectively. The grey values represent all other Z_H, Z_L pairing combinations. All values have been slightly offset in x as a function of their partner to help distinguish them. The error bars are consistent with the statistical errors from the fit.

When examining the left panel of Figure 3.9, a sudden jump is seen in the asymptotic composition from approx. Δ_{final}=0.07 to Δ_{final}=0.10 for Z_H >16. The effect appears to be an artifact of the particle identification assignment discussed in Section 2.3. The asymptotic values were recalculated assuming the isotopic assignment is off by one neutron (A_{new}=$A_{previous}$-1). The recalculated asymptotic values are plotted as open, black triangles. The open, black triangles are more consistent with the asymptotic values for Z_H ≤16, indicating the isotopic assignment is most likely over-predicted by a neutron. While this affects the asymptotic values, it should not significantly change the shape of the Δ_H vs. α distribution. Hence, the rate constants should remain consistent.

As stated in Section 3.3.1, the asymptotic values for **HF** and **LF** for a given Z_H, Z_L combination are not necessarily equal. Thermodynamically, the asymptotic chemical potential for **HF** and **LF** should be equivalent rather than the composition. The chemical potential is governed by several factors including the internal energy, density and ground-state binding energies. The effect of the ground-state binding energies can be seen in Figures 3.7, 3.8 and 3.9. Final plateau values are greater for Z_H and Z_L with an odd atomic number. This effect makes sense when looking at the nuclear equation of state. The parity term exists as a correction for the preference of nuclei to be in an even-even neutron-proton configuration. Because the **HF** and **LF** nuclei are small in atomic number and mass number, the N=Z configuration is preferred for even atomic number nuclei and N=Z+1 is preferred for odd atomic number nuclei. This explains why some of the $\langle\Delta_H\rangle$ and $\langle\Delta_L\rangle$ plateau values cross.

The asymptotic values are higher for smaller **LF** (Z_L <6) and decrease as Z_L increases. The decreasing trend is prevalent because of the choice of Δ for the composition. For smaller nuclei, less isotopes are available to populate. For example, for Z_L=3, the mass number can be A_L=6,7 and 9, whereas for Z_L=10, the mass number can be A_L=18-24. However, because the difference in neutron and proton number ($N - Z$) is divided by the mass number, a difference of 1 or 2 neutrons represents smaller change in Δ_{final} for larger atomic number nuclei. The one exception to this case is Z_L=4. The absence of the $N = Z$ decay (Z_L=4, A_L=8) artificially boosts the $\Delta_{final,Z_L=4}$ value.

Next, the c parameter, or the rate constant, was examined. Figure 3.10 shows the c parameters for **HF** and **LF**. The **LF** values as a function of the atomic number Z_L is plotted in the left panel and the **HF** values as function of the atomic number of the Z_H is plotted in the right panel. The coloring is consistent with Figure 3.9, where the green points represents Z_L=5 and the orange ones represents Z_L=7. The **LF** values are plotted on the right panel. The teal points in the right panel represent the Z_H=12 points and the purple ones represent Z_H=14 ones as a function of **LF**. All other points are plotted in grey. All points are offset in x as a function of Z_L for **HF** and as a function of Z_H for **LF**. The offset was included to assist in seeing the points. The error bars are consistent with statistical error bars, and the systematic error bars are negligible at this point in the analysis.

Results for the **HF** rate constants are consistent, which indicates the rate constants are not dependent on the Z_L the **HF** is paired with. The same trend is seen for the **LF** rate constants, where

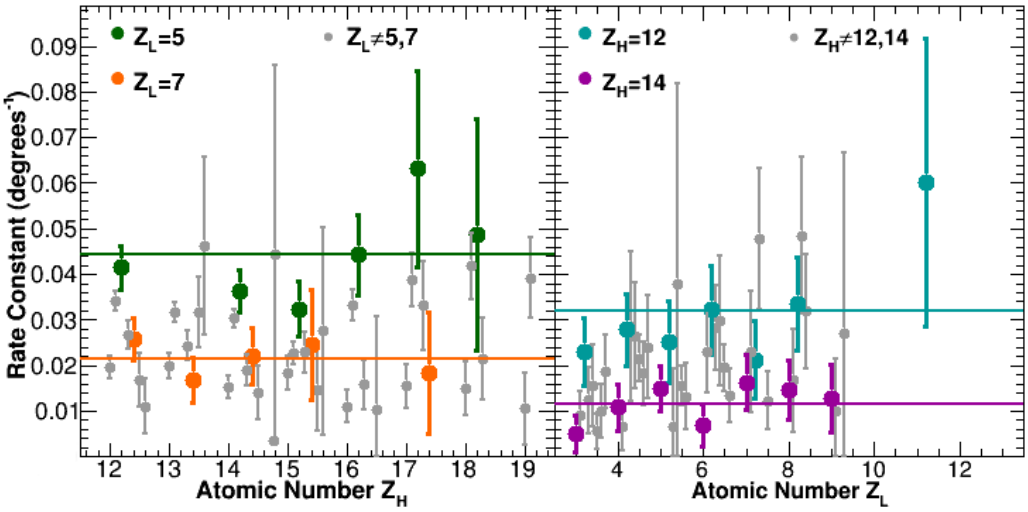

Figure 3.10: Exponential rate constant parameters plotted in units of inverse degrees from the $\langle\Delta\rangle$ vs. α fit. The rate constants for **HF** are plotted as a function of Z_L in the left panel and the rate constants for **LF** as a function of Z_H are in the right panel. The green and orange points correspond to the rate constants for **HF** paired with Z_L=5 and Z_L=7, respectively, and the teal purple and teal points correspond to the rate constants for **LF** paired with Z_H=12 and Z_H=14, respectively. Reprinted with permission from Ref. [1].

there is a lack of dependence of Z_H on **LF**.

The average rate constant was 0.02±0.02 per degree for **HF** and 0.03±0.04 per degree for **LF**. The average of **HF** and **LF** are in agreement within statistical errors. The equivalency correlates to the force driving the equilibration being independent of the size of the two species, and only depending on the difference in chemical potential.

3.4 Conversion from α to Time

The angle of rotation, α, provides an internal clock to measure the decay timescale. In conversing from α to time, two assumptions are applied. The first assumption is the correlation between α and the decay time being monotonic. This implies the decay time is short relative to the rotation period, evidence of which is present in Figure 3.4. The large excess yield at $cos(\alpha)$ >0 supports the short decay time. The second assumption is the rotation angle and the decay time is linear. If both of these conditions hold, then the c parameter from the $\langle\Delta\rangle$ vs. α exponential fits can be converted from inverse angle to inverse time. Equation 3.5 is the basis for the conversion,

$$t = \frac{\alpha}{\omega} \tag{3.5}$$

where t is the time and ω is the angular frequency. Equation 3.6 correlates ω to the angular momentum (J) and moment of inertia (I_{eff}).

$$\omega = (J\hbar)/I_{eff} \tag{3.6}$$

Although Equation 3.6 looks rather simple, the moment of inertia (I_{eff}) and angular momentum (J) are not well understood for multi-fragmentation reactions. Three approaches (Hudan et. al, Brown et al. and Jedele et. al) have been taken in the time conversion differing in the approach towards calculating J and I_{eff}. The varying approaches will be discussed in the following subsections.

3.4.1 Hudan et al. Approach

Hudan et al. [7] determined the moment of inertia of the dinuclear complex assuming two touching ellipsoids with a ratio of 0.6 between the minor and major axis. The angular frequency is taken to be 0.6-0.7$\times 10^{21}$ rad/s, which comes from previous experimental observation [5] and assumed an angular momentum of l=40$\hbar$. Instead of calculating α to time on a bin by bin basis, the $\langle v_{REL} \rangle$ dependence on $cos(\alpha)$ was used due to the angular restrictions for the given experimental setup. Results showed most of the equilibration occurred within 0.25 rotations and equilibration persisted for 2-3 zs.

3.4.2 Brown et al. Approach

Several changes were made in the Brown et al. [8] analysis, most notably the calculation of the angular momentum. For the moment of inertia, the following equation was used:

$$I_{eff} = \frac{2}{5} M R^2 F_l \tag{3.7}$$

where $R^2 F_l$ is the effective radius and M is the mass. The radius is $R = r_0 A^{1/3}$. F_l is a sphericity correction term and is extracted from ^{149}Tb data [73]. The mass is defined as M=$m_0 c^2 A_{PLF^*}$, where m_0 is the rest mass of the nucleon and A_{PLF^*}=$(\frac{A}{Z})_{projectile} Z_{PLF^*}$.

The angular momentum is calculated using a statistical fission model [74, 56]. The model

shows the width of the out-of-plane (ϕ) angular distribution is proportional to the angular momentum of the system through the equation:

$$J^2 = (2k^2 I_{eff} T)/\hbar^2 \tag{3.8}$$

where T is the temperature. k is the width of the $sin(\phi)$ distribution and is extracted using a Gaussian fit of the form: $P(sin\phi) = A\ddot{e}xp(-k^2 sin^2\phi)$, where A is a pre-exponential factor. The value is calculated for cases where the second heaviest fragment is emitted forward of the heaviest ($\alpha < 90°$). The restriction is applied because of the angular limitations of the experimental setup. T is assumed to be 3-5 MeV. Plugging the values into the angular momentum equation, one gets $J = 6 \pm 1\hbar$.

3.4.3 Jedele et al. approach [1]

The above approaches give a good framework for the calculation of the moment of inertia (I_{eff}) and the angular momentum (J). For the moment of inertia, the value is calculated assuming two touching spheres rotating around their common center of mass:

$$I_{eff} = m_H r_{CM,H}^2 + \frac{2}{5} m_H r_H^2 + m_L r_{CM,L}^2 + \frac{2}{5} m_L r_L^2 \tag{3.9}$$

where r_H is the radius of **HF**, r_L is the radius of **LF**, $r_{CM,H}$ is the distance from the center of **HF** to the two-fragment center-of-mass, and $r_{CM,L}$ is the distance from the center of **LF** to the two-fragment center-of-mass. The masses of **HF** and **LF** are denoted by m_H and m_L respectively. The moment of inertia range is 2.8-9.9$\times 10^{-42}$MeV$\cdot$s^2.

The angular momentum is determined using the same assumption as Brown et al. [74] discussed in Section 3.4.2: the width of the out-of-plane angular distribution is proportional to the angular momentum. However, there are a few problems with the statistical fission model approach. The model examines the out-of-plane angular distribution for the binary fission fragments produced in the reaction of α on ^{238}U reactions at 63.5 MeV. The reaction dynamics at these low energies are significantly different than the reactions being studied in this analysis. Most notably, the fission fragments are produced through statistical decay. For the data present in this analysis, the statistical contribution cannot be easily detangled from the dynamical decay mechanism.

Additionally, the angular granularity in NIMROD does not allow for a good understanding of the behavior of the two heaviest fragments at sin(ϕ)=0, where ϕ is the out-of-plane angle.

In order to still use the statistical decay method to understand the angular momentum of the products, the fission fragments are replaced with α fragments. α fragments are commonly produced in secondary or evaporation decay, which is emitted isotropically. All α particles produced in coincidence with an **HF**,**LF** pairing were included in the out-of-plane distribution. The out-of-plane angle (ϕ) is defined as the spin axis perpendicular to the reaction plane, which is constructed from the beam axis and the **HF**-**LF** center-of-mass velocity ($\vec{v}_{CM}$).

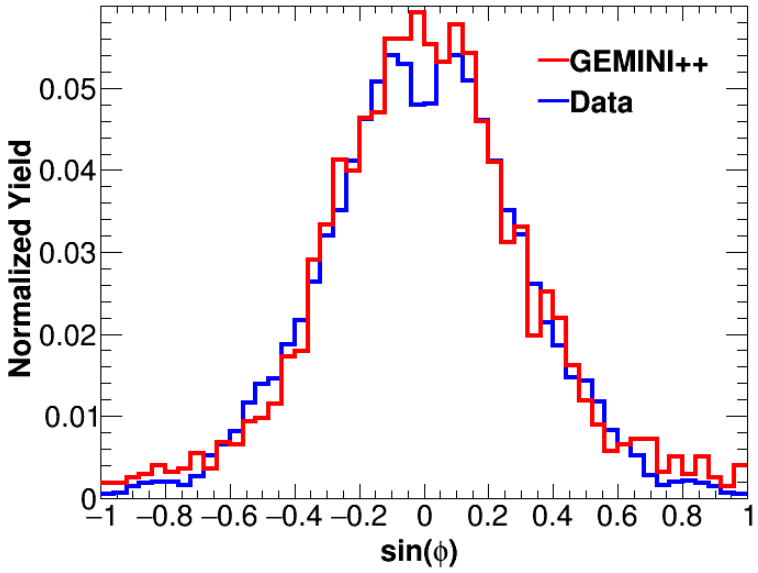

Figure 3.11: Out-of-plane distribution for α particles. Experimental results are in blue and GEMINI++ results for a spin of J=22$\hbar$ are in red.

The out-of-plane distribution widths were compared for different Z_H, Z_L combinations and the differences were negligible. Therefore, the α-particles from all Z_H, Z_L pairings were combined. The distribution was fit with a Gaussian distribution and a σ width of k=0.28 was extracted.

The angular momentum cannot directly be determined from experimental data. Therefore, GEMINI++ [70] is used to reproduced the $sin(\phi)$ distribution and extract the angular momentum.

Z_H,Z_L Pairing	Period (zs)	k_H (zs^{-1})	k_L (zs^{-1})	τ_H (zs)	τ_L (zs)
12,5	$2\pm^{5}_{1}$	$3\pm^{3}_{1}$	$7\pm^{9}_{4}$	$0.4\pm^{0.5}_{0.2}$	$0.1\pm^{0.2}_{0.1}$
12,7	$3\pm^{6}_{1}$	$2\pm^{3}_{1}$	$4\pm^{4}_{2}$	$0.5\pm^{0.6}_{0.3}$	$0.3\pm^{0.3}_{0.2}$
âĂČ 14,5	$2\pm^{5}_{1}$	$4\pm^{5}_{3}$	$6\pm^{7}_{3}$	$0.3\pm^{0.3}_{0.2}$	$0.2\pm^{0.2}_{0.1}$
14,7	$3\pm^{7}_{1}$	$3\pm^{3}_{2}$	$3\pm^{3}_{2}$	$0.4\pm^{0.5}_{0.3}$	$0.4\pm^{0.5}_{0.2}$
Average	$3\pm^{6}_{1}$	$3\pm^{4}_{2}$	$4\pm^{4}_{2}$	$0.3\pm^{0.5}_{0.3}$	$0.3\pm^{0.3}_{0.2}$

Table 3.1: Rotational period, rate constants for **HF** (k_H) and **LF** (k_L), and the mean lifetime for **HF** (τ_H) and **LF** (τ_L). The values shown correspond to the select (Z_H,Z_L) pairings shown throughout the analysis, and the average of all 43 pairings.

The width of the angular distribution is sensitive to the angular momentum of the parents. A ^{61}Fe nucleus was used as the input. For varying excitation energies and angular momentum, the width of the distribution is replicated. The angular momentum ranges from $10\hbar$ for E*/A=0.8 MeV/nucleon to $50\hbar$ for E*/A=1.2 MeV/nucleon. The geometric mean of $22\hbar$ is used for the analysis, giving the final result a factor of 2.2 systematic uncertainty. The out-of-plane angular distributions for GEMINI++ and experimental data are seen in Figure 3.11. The experimental results are plotted in blue and the GEMINI++ results are in red.

The final results are shown in Table 3.1 for the rotational period, rate constant for **HF** (k_H) and **LF** (k_L) in zs^{-1}, and the mean equilibration lifetime for **HF** (τ_H) and **LF** (τ_L) in zs. The values correspond to the Z_H, Z_L pairings featured in the analysis and the average of all 43 pairings. The mean equilibration time for both fragments was τ=0.3 zs (0.3×10^{-21} s), further reinforcing the equilibration is driven by the chemical potential gradient between the **HF** and **LF**.

The mean equilibration lifetimes are consistent with previous experimental results [48]. Four probes were explored in the 1970s and 1980s extracting mean equilibration times. The first probe used an exponential fit of the kinetic energy versus θ to extract a mean equilibration time of τ_{KE}=0.3 zs [75]. The neutron-proton ratios near and past the grazing angle can be used to measure a $\tau_{N/Z}$=0.13 zs [76, 50]. An upper limit of τ_l=1.5 zs was extracted from orbital angular momentum studies using γ-ray multiplicities [51]. Lastly, charge and mass distributions at a variety of angles were used to extract a τ_Z=6 zs [77]. The results for the 4 probes were all measured in the deep-

inelastic energy range ($E_{projectile}$ ≤12 MeV/nucleon). The extracted average mean equilibration lifetime for **HF** and **LF** (τ_{MF}) is within the range of τ_{KE}, $\tau_{N/Z}$ and τ_{l}. The results indicate the forces driving the equilibration are independent of the reaction dynamic mechanism and dependent on the chemical potential difference.

3.5 Effects of Secondary Decay on NZ Equilibration

One particular area to explore in this analysis is the role secondary decay plays on the composition ($\langle\Delta_L\rangle$) as a function of angle (α). Secondary decay occurs when fragments break up a second time due to high excitation energy. Commonly, the initial fragment will "shed" α, ^{3}He, t, d, p and n particles. A statistical model, in this case GEMINI++ [71], can be used to explore these effects.

For the initial GEMINI++ inputs, an angular momentum of J=5$\hbar$ and a $Z_{L,initial}$=7-10 was chosen. Only nuclei that decay to Z_L=7 were used in the final calculation of $\langle\Delta_L\rangle$. The initial α was randomly chosen from an exponential distribution with a mean angle of 30°. The $\langle\Delta_L\rangle$ distribution was an exponential distribution and a Gaussian distribution with a width of 0.01 $\langle\Delta\rangle$ was used to reproduce the experimental fluctuations.

Two factors are analyzed in detail: the input excitation energy per nucleon (E*/A) and the initial composition distribution. The excitation energy input was E*/A=1 MeV/nucleon and E*/A=2 MeV/nucleon. the asymptotic composition was changed from $\langle\Delta_{final}\rangle$=0.08 to $\langle\Delta_{final}\rangle$=0.1. Figure 3.12 shows the input excitation results in the top panel and the initial composition distribution in the bottom one. The solid points represent the primary decay and the open points represent the secondary decay. The initial distribution was chosen to mimic the distributions seen in the experimental results.

Results show the larger the input excitation energy, the greater the decrease in the composition throughout all α values. The asymptotic composition and magnitude of the pre-exponential factor from the exponential fit both decrease. However, the rate constant remains constant within statistical errors. A similar effect is seen for the difference in initial asymptotic composition. The final composition for both initial configurations shows a decrease in asymptotic composition and the pre-exponential factor, but no noticeable change in the rate constant.

The results from both factors explored show, the rate constant does not change when secondary effects are implemented. This implies that while secondary decay may flatten out and decrease the

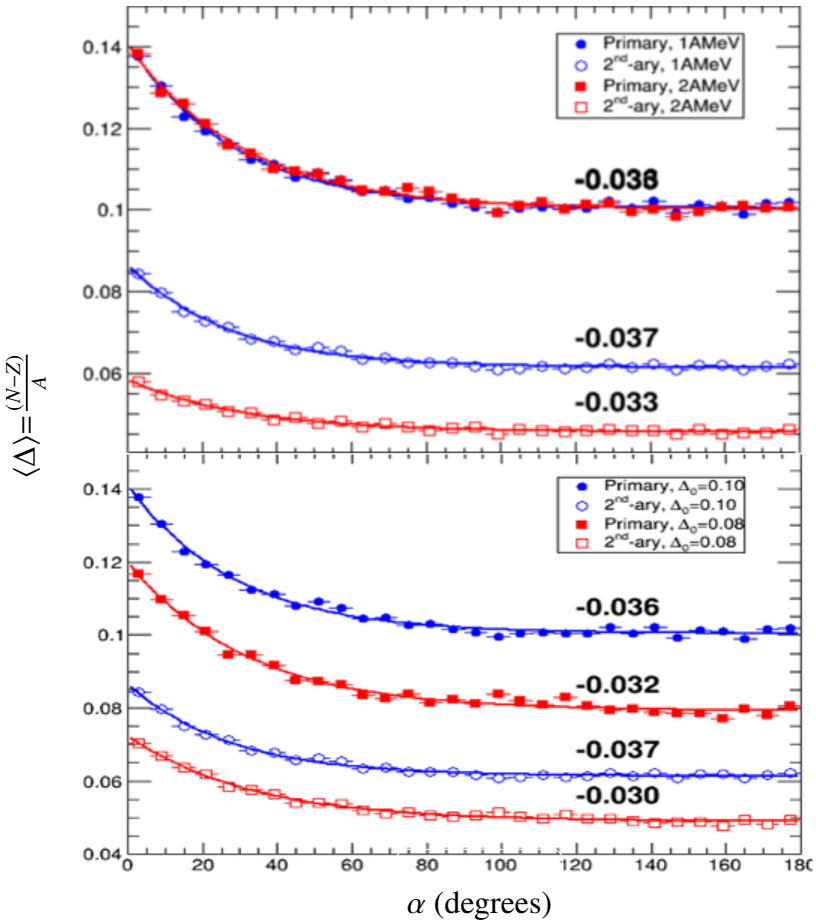

Figure 3.12: Effects of secondary decay effects studied through plotting the composition $\langle\Delta\rangle$. The top panel shows the effects of changing the initial excitation energy per nucleon (E*/A) and the bottom panel shows the effects of changing the asymptotic composition ($\langle\Delta_{final}\rangle$). Reprinted with permission from Ref. [4].

composition, it cannot manufacture the effects seen.

3.6 Comparison to symmetric ^{64}Zn and ^{64}Ni Reaction Systems

All discussion within this Chapter so far, has focused on the ^{70}Zn+^{70}Zn reaction system. This section will focus on comparing the results to the ^{64}Zn+^{64}Zn and ^{64}Ni+^{64}Ni reaction systems. The comparisons for all plots focus on the Z_H=12, Z_L=7 pairing. All figures shown in this section are plotted with the ^{70}Zn+^{70}Zn in the top panel, ^{64}Zn+^{64}Zn in the middle panel and ^{64}Ni+^{64}Ni in the bottom one.

First, the velocity distributions will be observed. The velocity distribution gives insight into the

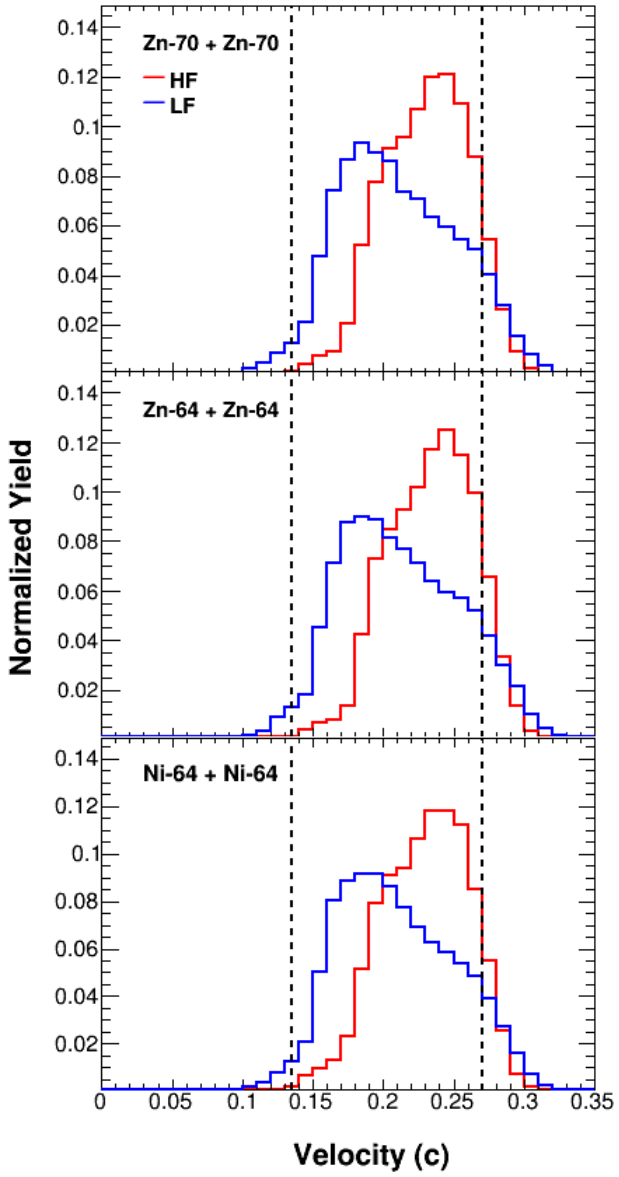

Figure 3.13: Average velocity for Z_H=12 (plotted in red) and Z_L=7 (plotted in blue). The reaction systems plotted from top to bottom are ^{70}Zn+^{70}Zn, ^{64}Zn+^{64}Zn and ^{64}Ni+^{64}Ni. The left dotted line corresponds to the mid-velocity and the right dotted line correpsonds to the beam velocity. All reaction systems show an average v_L approximately the same and above the mid-velocity. The average v_H for all reaction systems is above the v_L and close to the beam velocity. Since both fragments have an average velocity above the mid-velocity, the fragments originate from the PLF*.

source of the **HF** and **LF**. Figure 3.13 shows the velocity distributions. The red line corresponds to the **HF** and the blue line corresponds to the **LF**. The dotted lines represent the mid-velocity (left) and beam velocity (right). For all three reaction systems, the peaks of the **HF** and **LF** distributions

are above mid-velocity. The **HF** peak is close to the beam velocity, consistent with the **HF** being the projectile-like fragment. The **LF** is peaked between the mid-velocity and the **HF**. Because the peak for all reaction systems is above the mid-velocity, the majority of the fragments are coming from the PLF*, not the TLF*.

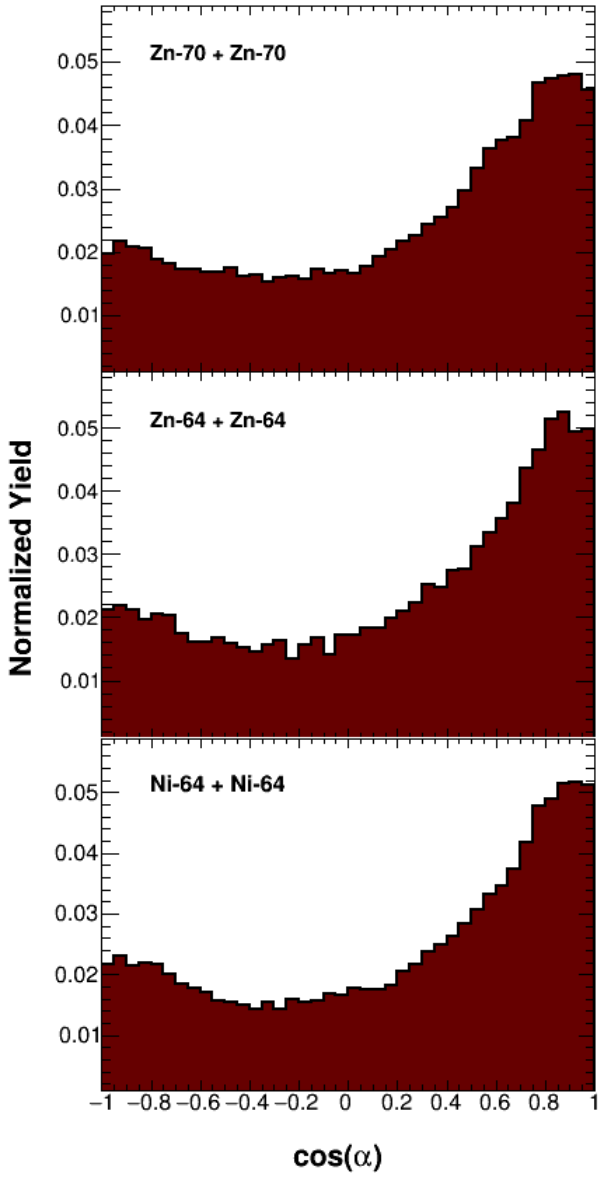

Figure 3.14: Cos(α) distributions for ^{70}Zn+^{70}Zn (top), ^{64}Zn+^{64}Zn (middle), ^{64}Ni+^{64}Ni (bottom) reaction systems. The plotted values correspond to the Z_H=12, Z_L=7 pairings. For each reaction system, there is a large yield enhancement at cos(α)=1 indicating large dynamical yield contribution.

The $cos(\alpha)$ distributions are plotted in Figure 3.14. For all three reaction systems, a large enhancement in the yield is seen at $cos(\alpha)$=1. The distribution falls off quickly, reaching a minimum around $cos(\alpha)$=-0.3. The distribution flattens out between -1.0≤ $cos(\alpha)$ ≤-0.3, with slight upturning in the yield is seen at $cos(\alpha)$=-1. The upturning is consistent with a spinning source. Because the $cos(\alpha)$ distribution trends are consistent across all three reaction systems, the reaction dynamics are consistent.

The composition as a function of rotation angle is examined in Figure 3.15. In all three cases, $\langle\Delta_L\rangle$ starts off relatively neutron-rich and evolves to be less neutron-rich with increasing α. $\langle\Delta_H\rangle$ mirrors this effect starting off neutron-poor and evolving to be more neutron-rich. The evolution in all three panels is exponential in nature. The statistics in the ^{70}Zn+^{70}Zn reaction system is greater than in the other reaction systems, which explains why the error bars on the top panel are smaller than in the other panels. The data was fit with the same exponential fit applied in Section 3.3.2.

There are some notable differences in the $\langle\Delta\rangle$ versus α plots. The asymptotic compositions are different for both **HF** and **LF**. The symmetric reaction systems with the asymptotic compositions from least to greatest for **HF** and **LF** are ^{70}Zn, ^{64}Ni, and ^{64}Zn, respectively. The differences in asymptotic compositions make sense when examining the initial Δ of the reaction systems. The initial compositions are Δ_{Zn-70}=0.143, Δ_{Zn-64}=0.057 and Δ_{Ni-64}=0.125 for the symmetric ^{70}Zn, ^{64}Zn, and ^{64}Ni reaction systems, respectively. While neutrons can flow to the neck region after the projectile and target collide, limitations are imposed due to the number of neutrons. For a more neutron-rich system, more neutrons are available to flow to the neck region, making the **LF** more neutron-rich. The projectile-like fragment will remain more neutron-rich too. The PLF*-TLF* contact time and the forces driving the neutron flow limit the number of neutrons that can be pushed from the PLF* to the neck region.

The pre-exponential factor, b parameter, for the reaction systems is also different. The pre-exponential factor corresponds to the difference in composition from the initial to the final composition. Similar to the asymptotic composition, the magnitude of the pre-exponential factor for both **HF** and **LF** is largest for the ^{70}Zn+^{70}Zn and smallest ^{64}Zn+^{64}Zn reaction system. Again, the effect makes sense when looking at the dynamics of the reaction. After the PLF* and TLF* break apart, the neutron-rich neck component of the deformed PLF* (**LF**) pushes the neutrons back into the neutron-poorer component (**HF**). Because the available number of stable, neutron-rich isotopes

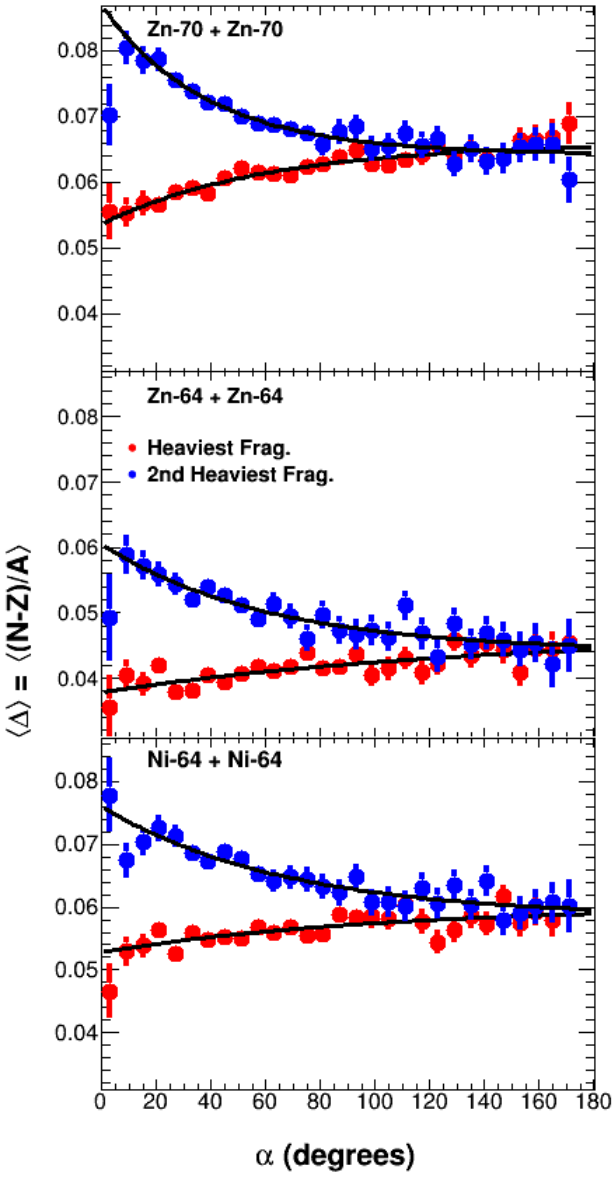

Figure 3.15: Average composition ($\langle\Delta\rangle$) versus rotation angle (α) for ^{70}Zn+^{70}Zn (top), ^{64}Zn+^{64}Zn (middle), ^{64}Ni+^{64}Ni (bottom) reaction systems. The plotted values correspond to the Z_H=12, Z_L=7 pairings.

is greater for the **HF** than the **LF**, the **HF** acts as a sponge absorbing the excess neutrons. Since the neck region in the more neutron-rich reaction systems starts off more neutron-rich, the neck region needs to drive more neutrons to the projectile-like fragment region to achieve a more stable configuration.

The rate constants of the **HF** and **LF** for all three reaction systems are consistent within statis-

Reaction System	Z_H,Z_L Pairing	k_H (zs^{-1})	k_L (zs^{-1})	τ_H (zs)	τ_L (zs)
^{70}Zn+^{70}Zn	12,7	$2\pm^{3}_{1}$	$4\pm^{4}_{2}$	$0.5\pm^{0.6}_{0.3}$	$0.3\pm^{0.6}_{0.1}$
âĂČ ^{64}Zn+^{64}Zn	12,7	$1\pm^{2}_{1}$	$2\pm^{3}_{2}$	$1\pm^{2}_{1}$	$0.4\pm^{0.5}_{0.3}$
^{64}Ni+^{64}Ni	12,7	$1\pm^{2}_{2}$	$2\pm^{3}_{1}$	$0.7\pm^{1}_{0.8}$	$0.5\pm^{0.3}_{0.6}$
^{70}Zn+^{70}Zn	Average	$3\pm^{4}_{2}$	$4\pm^{4}_{2}$	$0.3\pm^{0.5}_{0.3}$	$0.3\pm^{0.3}_{0.2}$
^{64}Zn+^{64}Zn	Average	$4\pm^{5}_{3}$	$4\pm^{5}_{3}$	$0.3\pm^{0.4}_{0.2}$	$0.3\pm^{0.3}_{0.2}$
^{64}Ni+^{64}Ni	Average	$4\pm^{5}_{3}$	$4\pm^{5}_{3}$	$0.3\pm^{0.4}_{0.2}$	$0.3\pm^{0.3}_{0.2}$

Table 3.2: Rate constants for **HF** (k_H) and **LF** (k_L), and the mean lifetime for **HF** (τ_H) and **LF** (τ_L). The values shown correspond to the Z_H=12 and Z_L=5 pairing for ^{70}Zn, ^{64}Zn and ^{64}Ni symmetric reaction systems, which are shown throughout Section 3.6. The average of all pairings for each reaction system is also shown.

tical errors. The equivalence indicates that the forces driving the neutron-proton equilibration are the same and independent of the initial composition of the reaction system.

Results for the conversion of α to time are shown in Table 3.2. The first three rows compare Z_H=12, Z_L=7, which is the pairing shown in each of the figures in this section. The latter three rows are the results for the average of all pairings analyzed in each reaction system. The number of pairings for each symmetric reaction system is 43 for ^{70}Zn, 43 for ^{64}Zn and 32 for ^{64}Ni. The number of pairings for ^{64}Ni+^{64}Ni is less due to the overall statistics of the reaction system compared to the ^{70}Zn+^{70}Zn reaction system.

When looking at the **LF** for the Z_H=12, Z_L=7 pairing, the mean equilibration time for all three reaction systems is consistent within error bars. The mean equilibration time values for the Z_H,Z_L pairing shown are also consistent with the mean equilibration time for the average of all three reaction systems. The consistency furthermore verifies that the mechanism driving the equilibration is independent of the size of the projectile or the asymmetry of the reaction system.

For the **HF**, the mean equilibration times for the Z_H=12, Z_L=7 pairing are greater than the mean equilibration times for the average value. Although, the values are still consistent within error bars. The higher value indicates the rate neutrons are flowing from the neck region (**LF**) to the **HF** is slower than for other pairings. The effect may be due to competing effects such as neutron flow from a secondary source. For the ^{64}Zn+^{64}Zn and ^{64}Ni+^{64}Ni reaction systems, the data

set is smaller, hence the lack of statistics when determining the mean equilibration lifetime plays a larger role than in the ^{70}Zn+^{70}Zn reaction system. The values are consistent with each other and with the **LF** values for the average mean equilibration times across all three reaction systems. The results again reiterate the neutron-proton equilibration between the **HF** and **LF** is governed by the forces driving the equilibration independent of the size of the projectile or initial asymmetry of the system.

Comparisons were made between experimental results and simulations. Two simulation codes were used to compare results: Constrained Molecular Dynamics (COMD) and Antisymmetrized Molecular Dynamics (AMD). Both codes are dynamical codes that model the collision over a preset time period.

Molecular dynamic codes are a semiclassical approach to treating N-body interactions. The codes provide a means to model large fluctuations seen in multifragmentation collisions at Fermi energies. Both AMD and COMD solve wave functions using N wave packets. This section will discuss the details and differences of AMD and COMD.

4.1 Constrained Molecular Dynamics (COMD)

The Constrained Molecular Dynamics (COMD) simulations [78, 79] model heavy-ion collisions using wave functions. The one-body distribution function is represented by

$$f_i(\mathbf{r},\mathbf{p}) = \frac{1}{(2\pi\sigma_r\sigma_p)^3}\cdot\exp\left[-\frac{(\mathbf{r}-\langle\mathbf{r}_i\rangle)^2}{2\sigma_r^2}-\frac{(\mathbf{p}-\langle\mathbf{p}_i\rangle)^2}{2\sigma_p^2}\right] \tag{4.1}$$

where $\langle\mathbf{r}_i\rangle$ and $\langle\mathbf{p}_i\rangle$ are the centers of the position and momentum of the ith nucleon, and σ_r and σ_p are widths of the position and momentum space, respectively. The widths are used as free parameters constrained by the uncertainty principle $\sigma_r\sigma_p \geq \hbar/2$ to reproduce basic ground state properties of the nuclei. The time-dependent variational principle is used to derive the equations of motion as seen in Equation 4.2

$$\langle\dot{\mathbf{r}}_i\rangle = \frac{\delta H}{\delta\langle\mathbf{p}_i\rangle}, \qquad\qquad \langle\dot{\mathbf{p}}_i\rangle = -\frac{\delta H}{\delta\langle\mathbf{r}_i\rangle)} \tag{4.2}$$

H is the total energy. A Skyrme interaction was used with an incompressibility of 200 MeV to describe the equation of state.

One of the key differences between COMD and other dynamical models is the implementation of the Pauli exclusion principle. The Pauli exclusion principle prevents two nucleons with the same isospin and spin to occupy the same phase space. In order to uphold the Pauli exclusion principle,

the occupation density ($\bar{f}_i$) is calculated at each time step as seen in Equation 4.3.

$$\bar{f}_i \equiv \sum_j \delta_{\tau_i,\tau_j}\delta_{s_i,s_j}\int_{h^3} f_j(\mathbf{r},\mathbf{p};\langle\mathbf{r}_j\rangle,\langle\mathbf{p}_j\rangle)d^3rd^3p \tag{4.3}$$

τ_i, τ_j represents the isospin projection quantum number and s_i, s_j are the spin projection quantum number of the ith and jth particles, respectively.

At each time step, an ensemble of particles is chosen within $3\sigma_r$ and $3\sigma_p$ in phase space. If the occupation density of the particle within the ensemble has the condition $\bar{f}_i \leq 1$, the particle configuration is accepted. Otherwise, the momenta of the particles within the ensemble is changed randomly until $\bar{f}_i \leq 1$. Special attention is paid to make sure the total momentum and total kinetic energy is preserved. The occupation density requirement acts to preserve the Fermionic nature of the system.

Finally, the final system needs to also meet the $\bar{f}_i \leq 1$ condition. If a nucleon-nucleon collision does not meet this requirement, the collision is rejected. Comparison of COMD to quantum molecular dynamics (QMD) was performed in Ref. [78] for ^{40}Ca+^{40}Ca at 35 MeV/nuc. Results indicate the Pauli exclusion principle treatment using the occupational density constraint utilized in COMD shows a much better agreement with experimental distributions than QMD. Additional constraints were imposed to further improve the COMD model, such as the conservation of angular momentum. Details are found in Ref. [79].

One motivation for choosing the COMD model is the computational time scale. Due to the general condition for the Pauli exclusion principle treatment, the computational time scales as N^2, where N is the number of nucleons. Therefore, COMD allows one to run for much longer interaction times without utilizing large amounts of computational resources. In this analysis, 10M heavy-ion collisions were run to 1000 fm/c. Previous simulations had been run to 3000 fm/c. However, recent research [80] has shown the dynamics of interest occur within the first 1000 fm/c. At the end of the reaction, the collisions were de-excited 10 times using GEMINI [69], which will be discussed shortly. The charge and mass distributions were compared for de-excited and non-de-excited events and are shown, left to right, in teal in Figure 4.1. The COMD particles were passed through an experimental software filter to recreate the experimental conditions. The black line corresponds to the experimental distribution. The zigzagging effect seen in the experimental mass

distribution is due to the NIMROD isotopic limitations. A triangular distribution for the impact parameter was chosen.

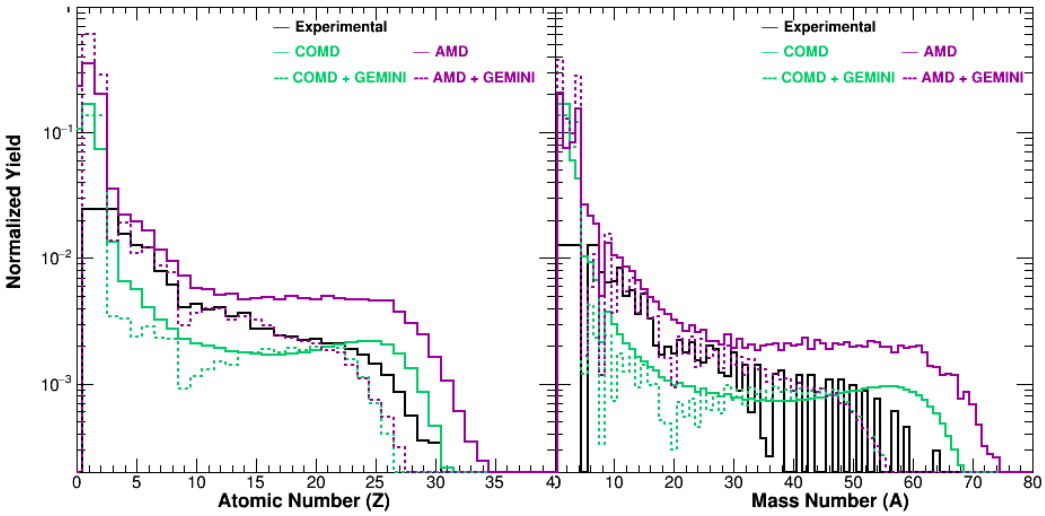

Figure 4.1: Charge (left) and mass (right) distribution for all fragments produced in the experiment and in simulations. The black line is the experimental results. The solid, blue line is the AMD distribution and the dotted, blue line is the AMD + GEMINI results. The COMD results are shown using the solid, red line and the COMD + GEMINI results are shown with the dotted, red line.

4.2 Anti-Symmetrized Molecular Dynamics (AMD)

Anti-symmetrized molecular dynamics (AMD) uses Gaussian wave packets to solve a single Slater Determinant of the form

$$\langle \mathbf{r}_1 ... \mathbf{r}_A | \Phi(Z) \rangle = \det_{ij} [\phi_{\mathbf{Z}_i}(\mathbf{r}_j) \chi_{\alpha_i}(j)] \tag{4.4}$$

where χ_{α_i} is the spin-isospin wave function and $\chi_\alpha = p\uparrow, p\downarrow, n\uparrow, n\downarrow$, where n is neutrons, p is protons and the arrows indicate the spin assignment in accordance to Hund's rule. The nucleons are represented with a spatial wave function of form

$$\langle \mathbf{r} | \phi(\mathbf{Z}) \rangle = \left(\frac{2\nu}{\pi}\right)^{3/4} exp\left\{ -\nu \left(\mathbf{r} - \frac{\mathbf{Z}}{\sqrt{\nu}}\right)^2 + \frac{1}{2}\mathbf{Z}^2 \right\} \tag{4.5}$$

$Z \equiv Z_{ii=1,...,A}$ is a set of complex variables defined as

$$Z = \sqrt{\nu}\frac{\langle\phi_{\mathbf{Z}}|\mathbf{r}|\phi_{\mathbf{Z}}\rangle}{\langle\phi_{\mathbf{Z}}|\phi_{\mathbf{Z}}\rangle} + \frac{i}{2\hbar\sqrt{\nu}}\frac{\langle\phi_{\mathbf{Z}}|\mathbf{p}|\phi_{\mathbf{Z}}\rangle}{\langle\phi_{\mathbf{Z}}|\phi_{\mathbf{Z}}\rangle} \tag{4.6}$$

The time-dependent variational method equations of motion for $\mathbf{r}$ and $\mathbf{p}$ correspond to the centroids of the position and momentum, respectively, if the anti-symmetrization effect is ignored. The width parameter ν in Equation 4.4 and Equation 4.6 is set to 0.16 fm^{-2}.

The equation of state was calculated using a momentum-dependent Gogny and Gogny-AS force interaction. The Gogny interaction produces a soft density dependence and the Gogny-AS interaction produces a stiff density dependence. The equation of state calculated an incompressibility of 228 MeV and an appropriate saturation point of the nuclear matter for symmetric matter. Due to the parameterization of both the Gogny and Gogny-AS interactions, the values calculated for the symmetric component of the equation of state are identical. Therefore, the density dependence of the asymmetry term can be examined. The ground state nuclei properties were reasonably well described.

Because AMD is anti-symmetrized, the Fermionic nature of the nucleus or Pauli principle is preserved. In order to ensure Pauli blocking was properly implemented, the Slater Determinant was examined before and after a collision. However, in a two-body collision, the wave packet centroids, $\mathbf{Z}$ does not have a physical meaning. Instead, a new set of coordinates W=$\mathbf{W}_1, ..., \mathbf{W}_A$ corresponding to the centroids of the nucleon wave packet distribution is introduced. W is related to Z through Equation 4.7,

$$\mathbf{W}_i = \sum_{j=1}^{A}\left(\sqrt{Q}\right)_{ij}\mathbf{Z}_j \qquad\qquad Q_{ij} = B_{ij}B_{ij}^{-1} \tag{4.7}$$

where B_{ij} is the single-particle states overlap matrix in the AMD wave function and Q_{ij} is the matrix defined by Q_{ij}=$B_{ij}B_{ij}^{-1}$. To understand the implementation of W more, two wave packets with the same spin and isospin can be close in phase space, but the two nucleons can be far away physically in order to maintain the Pauli principle. The nucleon-nucleon collision is calculated in the physical space W before being transformed back to the Z coordinates. If W cannot be transformed back to Z, then the Pauli principle is violated and the collision is not allowed.

The anti-symmetrization conditions discussed above cause AMD to be very computationally

demanding. Only 25,000 events were simulated and were stopped after 300 fm/c. The hot fragments were de-excited 10 times using GEMINI. The filtered simulated charge and mass distributions are shown in purple in Figure 4.1. The black lines are the experimental distributions.

4.3 GEMINI

The GEMINI++ (GEMINI) code is a statistical decay code. For this experiment, GEMINI is paired with AMD and COMD to de-excite hot fragments. GEMINI uses a Monte Carlo technique to determine the compound nuclei decay chains. Sequential binary decays occur until the products are unable to undergo further decay. Decay widths of the light charged particles are calculated using the Hauser-Feshbach formulism. A light fragment in GEMINI is defined as n, p, ^{3}He, α, ^{6}He, $^{6-8}$Li. For the heavier fragments or fission channel, the Bohr-Wheeler formalism is used to calculate the decay widths. The inputted values required for each fragment are excitation energy, angular momentum, mass and charge. The decay-width of the gamma-ray decay is also calculated, which is important at low excitation energies since gamma-ray and particle decay width may be similar.

There are some limitations of the GEMINI code. GEMINI assumes the source is spherical and at nuclear saturation density (ρ_0=0.16 fm^{-3}). These assumptions are not completely valid since most fragments produced after COMD or AMD decay are strongly deformed and the density is below ρ_0; the data of which is lost when GEMINI is applied. No further nuclear or Coulomb forces are applied to the fragments after GEMINI decay. While the concerns mentioned are valid, there is good reasonable agreement with previously studied experimental observables [67, 81].

5. COMPARISON OF EQUILIBRATION CHRONOMETRY RESULTS TO SIMULATIONS

Results from Chapter 3 showed an exponential change in composition between the two heaviest fragments originating from the PLF*. In order to determine how equilibration chronometry can be used to constrain the nuclear equation of state, the results are compared to simulations. This chapter will mirror Chapter 3, focusing specifically on the ^{70}Zn+^{70}Zn results at 35 MeV/nucleon. Section 5.1 will discuss the PLF* source. The angular distribution will be discussed in Section 5.2. Section 5.3 will focus on the composition as a function of time, followed by the equilibration rate constants and final asymptotic values. Finally, an overview comparing the experimental and simulated results will be presented in Section 5.4.

5.1 Determining the Source for Simulated Data

In order to make direct comparisons between the simulated and experimental results, experimental conditions needed to be reproduced. To achieve this, all COMD and AMD particles were passed through a simulation experimental filter at the end of either the simulation or after GEMINI was applied. The filter reproduces the geometric efficiency of NIMROD, energy thresholds for each individual detector and angular granularity. Only particles that passed the above mentioned requirements were analyzed.

After the particles were filtered, they were sorted based on their atomic number, with charge-equal particles sorted by mass number. The heaviest fragment (**HF**) was required to have a charge of $Z_H \geq 12$, and the second heaviest fragment (**LF**) was required to have a charge of $Z_L \geq 3$. Unlike the experimental data, where both fragments had to pass isotopic identification requirements, all simulated particles are automatically isotopically identified. A total "measured" charge of $21 \leq Z_{tot} \leq 32$ was applied.

Figure 5.1 compares the experimental and simulated charge distributions for the **HF** (left) and **LF** (right). The simulation distribution for the **LF** follows the experimental data fairly well. In all cases, the simulations slightly under-predict the relative yield at higher Z_L except for the AMD without GEMINI de-excitation. The under-prediction of the yields after GEMINI is due to high excitation energies after the COMD and AMD simulation. If the excess energy after COMD or AMD is large relative to the experimental values, GEMINI will over-de-excite the fragments. For

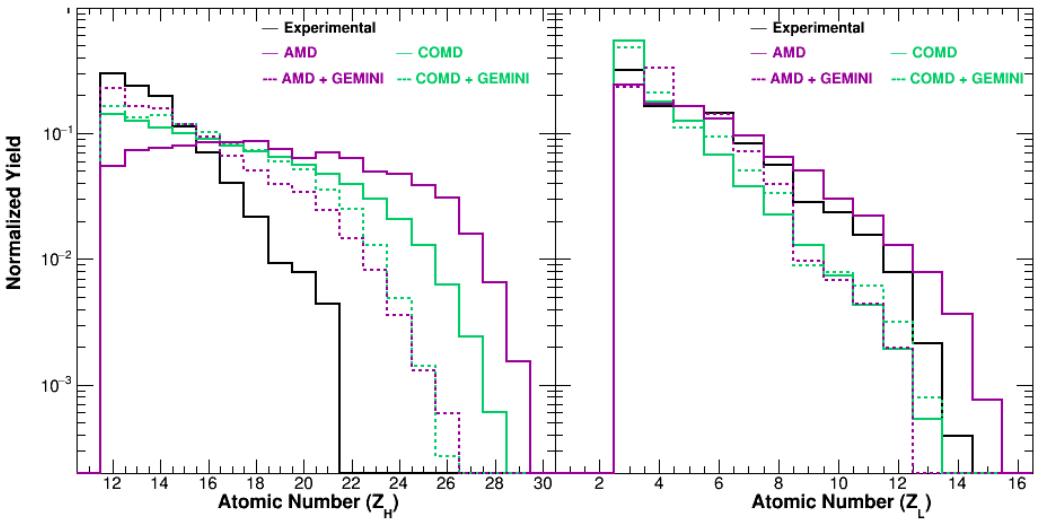

Figure 5.1: Charge distribution for the **HF** (left) and **LF** (right). The black line is the experimental results. The solid, blue line is the AMD distribution and the dotted, blue line is the AMD + GEMINI results. The COMD results are shown using the solid, red line and the COMD + GEMINI results are shown with the dotted, red line. The simulated results for the **LF** are consistent with the experimental distributions. For the **HF**, the simulated distributions, the data over-predicts the charge of the heavy fragment. The experimental data is cut off at Z>21 due to the isotopic identification capabilities of NIMROD [11].

the **HF**, AMD and COMD over-predict the relative yield at higher Z_H. Despite still over-predicting the yields at higher Z_H, de-exciting better replicates the shape of the distribution. However, the experimental distribution does not exceed Z_H=21, unlike the simulation distributions. The cut at Z_H=21 is due to the isotopic requirement applied to the experimental analysis. The experimental isotopic identification achievable in NIMROD is limited to $Z_H \leq 21$.

The charge distributions for Z_H and Z_L are plotted against each other. In Figure 5.2, the left panel shows the COMD results and the right panel shows the AMD results. In both cases, the results are post-GEMINI. The largest yield is seen for small Z_H, Z_L pairings. The yield falls off quickly as the sum of Z_H and Z_L increases, with few statistics seen for pairings at $Z_H + Z_L$=30. In comparison to the experimental data, the distribution has a larger relative yield at small Z_H, Z_L pairings. However, the AMD distribution under estimates the Z_L=3 yield.

To examine the origin of the **HF** and **LF**, the velocity distribution of the fragments was examined. Due to the low statistics in the simulation data set, all **HF** and **LF** fragments were combined and the total distribution is shown in Figure 5.3. The velocity of the **HF** is plotted in red and the

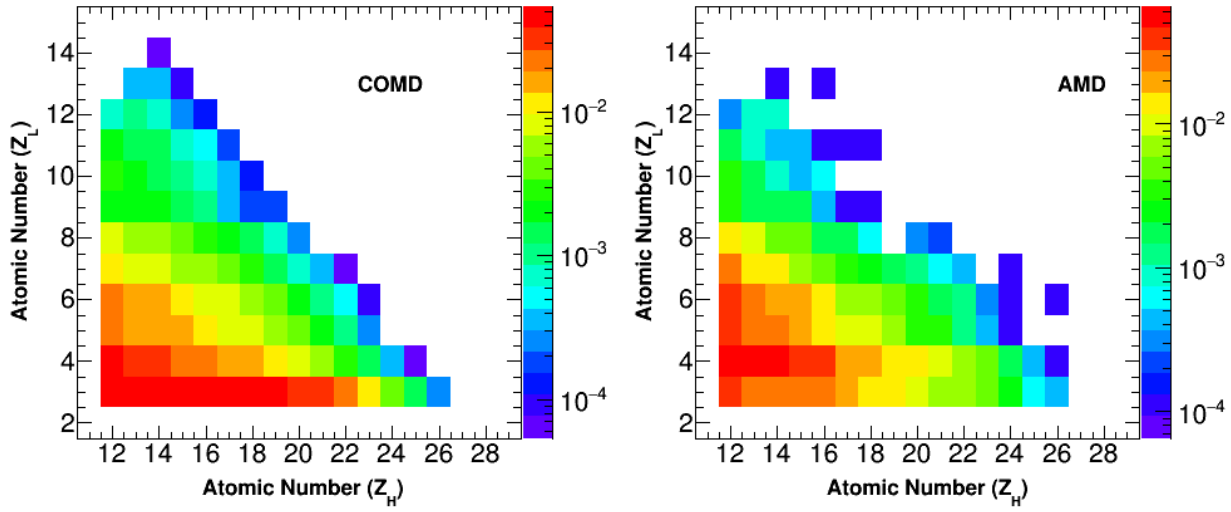

Figure 5.2: Atomic number of **HF** vs the atomic number of **LF**. The left panel shows the results for COMD + GEMINI results and the right one shows the AMD + GEMINI results. For both simulations, the yield is greatest for small Z_H, Z_L pairings.

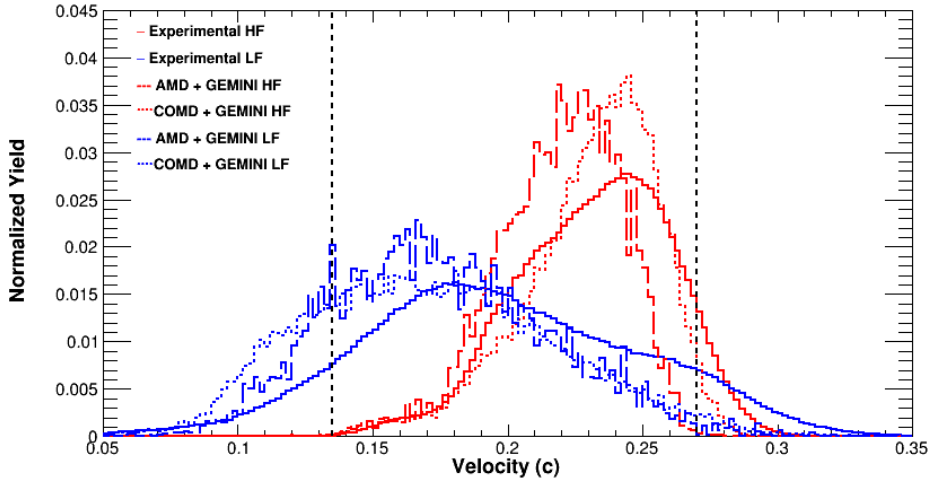

Figure 5.3: Velocity distribution for **HF** and **LF**. The red lines indicated the **HF** and the blue ones indicated the **LF**. The solid lines correspond to the experimental data and the simulations are plotted using dotted lines. The mid-velocity and beam velocity are represented with the dotted black lines from left to right, respectively.

velocity of the **LF** in blue. The solid lines show the experimental data and the dotted lines represent the simulation data. The black, dotted lines correspond to the mid-velocity (left) and beam velocity (right). The peak of the distribution for both the **HF** and the **LF** is peaked above the mid-velocity indicating the fragments originate from the PLF*. In all cases, the fragments are also ordered with the $\langle v_H \rangle > \langle v_L \rangle$. The ordering is consistent with the idea of dynamical decay of the PLF*.

5.2 Simulated Angular Distributions

More insight into the dynamics of the reaction is explored by examining the alignment angle. The alignment angle is defined based on the dot product between the center of mass ($\vec{v}_{CM}$) and relative velocity ($\vec{v}_{REL}$) of the **HF** and **LF** as seen in Equation 5.1.

$$\alpha = acos\left(\frac{\vec{v}_{CM} \cdot \vec{v}_{REL}}{||\vec{v}_{CM}||||\vec{v}_{REL}||}\right) \tag{5.1}$$

The cos(α) distribution for the combination of all **HF** and **LF** pairings is shown in Figure 5.4. The experimental results are shown in black, the AMD results are in teal and the COMD results are in purple. The dotted lines show the simulated data after GEMINI. For both simulations and the experimental data, the distribution is peaked toward $cos(\alpha)$=1, indicating a preference for decay of the **HF** forward relative to the **LF**. The distribution falls off quickly as $cos(\alpha)$ decreases and reaches a minimum toward $cos(\alpha)$=-0.3. A flattening effect is seen for -1< $cos(\alpha)$ <-0.3.

Since both the experimental and simulation results show the same features, the two decay mechanisms discussed in Section 3.2 are present. The symmetric decay around $cos(\alpha)$=0 is due to the statistical mechanism since statistical decay is isotropic. Interestingly, when comparing the experimental results to each of the simulated results, the experimental enhancement in the yield at $cos(\alpha)$=-1 relative to $cos(\alpha)$=-0.3 is either not present or strongly suppressed for the simulated data. The lack of enhancement at the edges suggests the simulated angular momentum is lower than experimental results. For the **HF**, the total angular momentum is peaked at approx. 8-10$\hbar$ for both COMD and AMD. The total angular momentum for **LF** is approx. 2-5$\hbar$. The experimental angular momentum is not well characterized for reactions at Fermi energies.

The large yield toward $cos(\alpha)$=1 indicates the presence of dynamical decay. The dynamical decay occurs when the PLF* breaks apart into the **HF** and **LF** along the PLF*-TLF* separation axis due to strong deformation. Kinematically, the PLF-TLF axis of separation is most likely to be

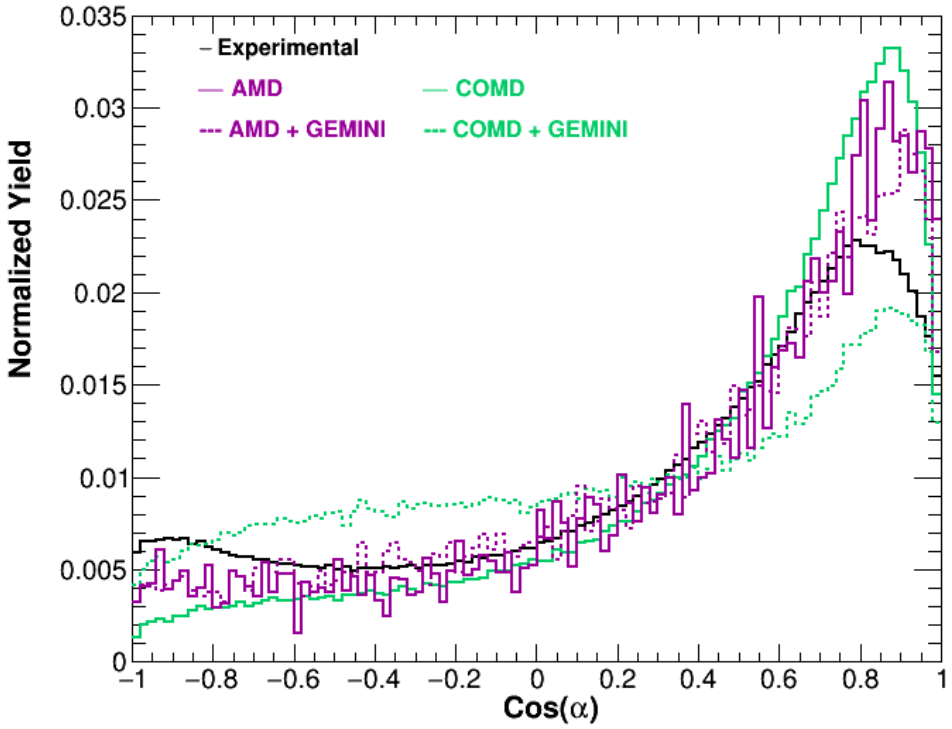

Figure 5.4: Cosine α distributions for the experimental and simulated data. The experimental results are shown in black. The AMD results and in purple and the COMD results are in teal. The results without GEMINI are plotted using solid lines and the results using GEMINI are shown using dotted lines. A large enhancement in the yield is shown at cos(α)=1, which is consistent with the presence of dynamical decay. The flattening of the distribution for cos(α)<0 is due to the statistical contribution.

the beam axis. Therefore, the decay at $cos(\alpha)$=1 is strongly favored. The longer the PLF* stays intact, the less aligned the system becomes.

The two decay mechanisms can be further explored by examining the distribution from COMD and AMD pre- and post-GEMINI. Since the simulation times are fairly short (1000 fm/c for COMD and 300 fm/c for AMD), reactions that produce an **HF** and a **LF** before GEMINI de-excitation are most likely to be produced dynamically. For the rest of this analysis, these reactions are referred as having a different source. In the case where the PLF* is still intact after AMD or COMD has finished running, the **HF** and **LF** is produced by GEMINI de-excitation and is statistical. These reactions will be referred to as having the same source.

Figure 5.5 shows the contribution to the total $cos(\alpha)$ broken down by the same and different

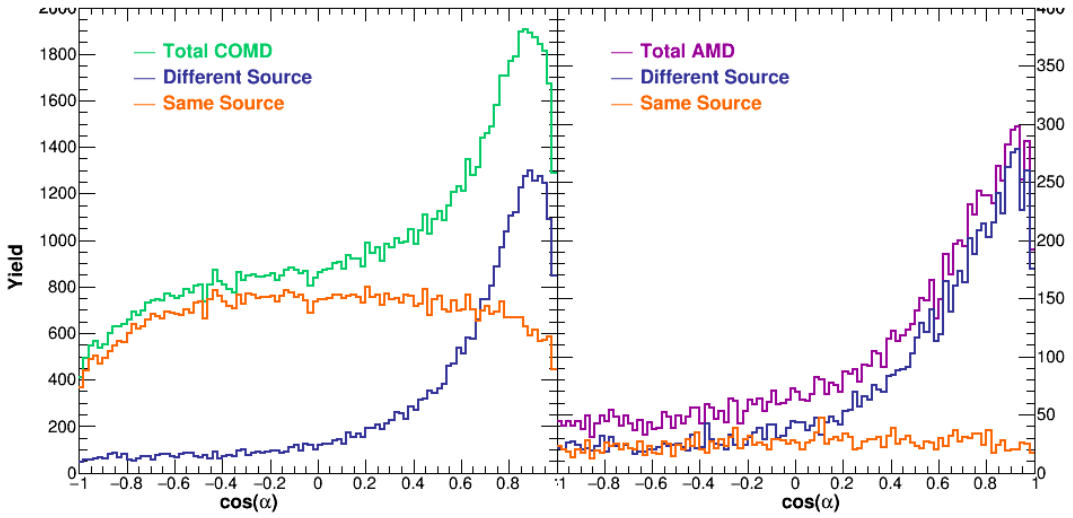

Figure 5.5: Cosine α distribution broken down by the source pre-GEMINI. The left panel shows the COMD simulations and the right panel shows the AMD simulations. Events where the PLF* broke up before de-excitation are labelled as having a different source, and events where the PLF* remains intact are labelled as having the same source. The blue line represents the total distribution. The green line represent events from a different source, and the purple line represents events from the same source.

source pre-GEMINI. The left panel shows the COMD results and the right panel shows the AMD results. The teal and purple lines are the combination of the two sources and are consistent with the de-excitation results shown in Figure 5.4 (dotted lines of the same color). The orange lines are for events with the same source, and the blue lines are for events with a different source.

For both simulations, the results for the same source show a symmetric distribution around $cos(\alpha)$=0, consistent with statistical decay. Excess yield is observed at $cos(\alpha)$=1 followed by an exponential drop in yield. The behavior exhibited is consistent with dynamical decay with a small statistical contribution at $cos(\alpha)$ <0. The source breakdown for COMD and AMD shows a much greater contribution from the same source for the COMD results. The same source percentage contribution is 69% for the COMD simulations and 25% for the AMD simulations. An exact comparison to the experimental source contribution cannot be made. However, an estimate can be made if one assumes the contribution for $cos(\alpha)$ <0 is predominantly statistical and isotropic. By subtracting the yield for $cos(\alpha)$ <0 from the yield at $cos(\alpha)$ > 0, the statistical contribution can be estimated to be 57%.

The greater same source contribution for the COMD is due to the clusterization parameters

used to define a fragment. Nucleons whose center of mass is within 2.76 fm of each other are defined as the same fragment. For a great number of events, many nucleons are still within the clusterization radius at 1000 fm/c and are identified as one large fragment. Because GEMINI assumes a spherical initial source, the PLF* deformation present is not preserved, and the **HF** and **LF** are emitted isotropically.

Because GEMINI washes out the dynamics of the fragments from the molecular dynamic codes for same source, the remainder of the analysis will focus on events where the **HF** and **LF** are produced from different primary sources.

5.3 Simulated Equilibration Chronometry Results

The average composition $\langle\Delta\rangle = \frac{\langle N-Z\rangle}{A}$ was calculated for each **HF** and **LF**. Due to the limited statistics, no requirement was made on the charge of the **LF** when calculating the $\langle\Delta_H\rangle$, and vice versa for the COMD and AMD data. For all simulation results presented throughout this chapter, the results shown post-GEMINI are gated on events with a different source. Sections 5.3.1 and 5.3.2 will focus on the raw results from the COMD and AMD simulations, respectively, and Section 5.3.3 will focus on the fits.

5.3.1 $\langle\Delta\rangle$ Vs. α for COMD Simulations

For the COMD results, Figure 5.6 shows the results for the softest interaction for the density dependence on the asymmetry energy for **LF**. The composition for $3\leq Z_L \leq 9$ is plotted, which is consistent with the Z_L values shown in the experimental analysis in Chapter 3. The top panel shows the results without GEMINI de-excitation and the bottom panel shows the results after de-excitation.

For the COMD only results (top panel), the initial composition starts off relatively neutron-rich and decreases quickly for small α. As the angle of rotation increases, the decrease in composition lessens, eventually plateauing. When comparing the initial $\langle\Delta_L\rangle$ compositions to the initial experimental compositions (Figure 3.7 and Figure 3.8), a clustering of the $\langle\Delta_{init,L}\rangle$ in the COMD data is observed for $5\leq Z_L \leq 9$ particles. The simulated compositions start off at approx. the same value ($\langle\Delta_{init,L}\rangle$=0.11-0.14) relative to the experimental ones, which range from $\langle\Delta_{init,L}\rangle$=0.08-0.19. The lack of difference in the initial composition for the COMD data as compared to the experimental data appears to be an artifact of the molecular dynamics code. The odd-even effect of the asymp-

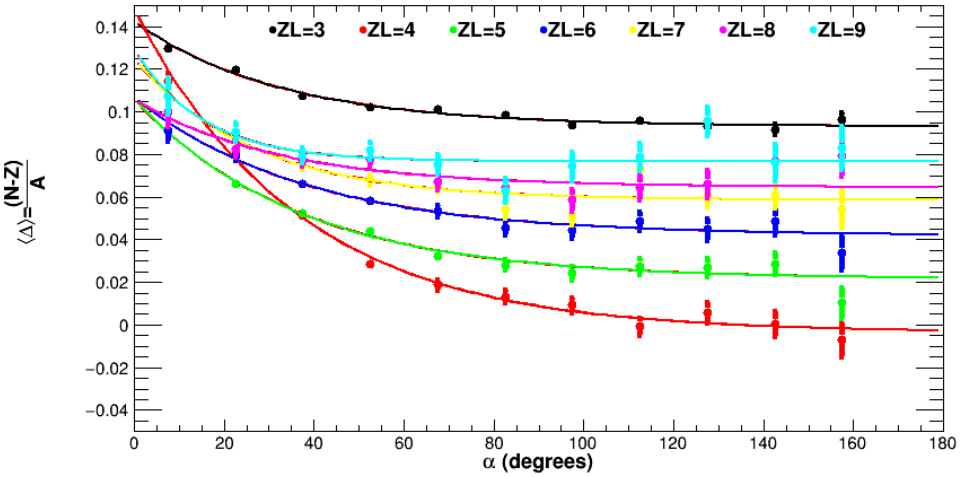

(a) No GEMINI de-excitation

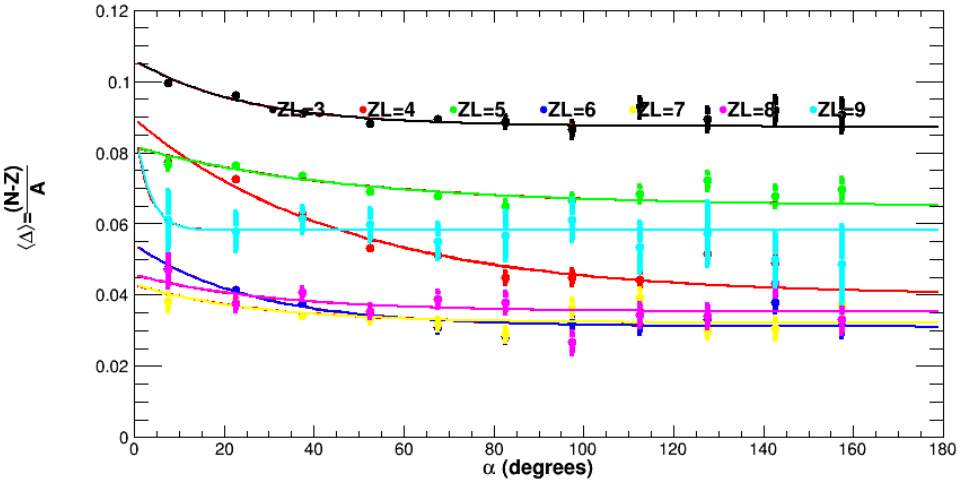

(b) 10 GEMINI de-excitations

Figure 5.6: COMD Δ_L vs. α for the softest density dependence of the asymmetry energy.

totic values is not observed in the COMD data. Rather, the asymptotic values from smallest to largest are sorted by increasing atomic number.

When GEMINI is applied to the data, as shown in the bottom panel of Figure 5.6, the initial composition for each Z_L starts off less neutron-rich relative to the data without GEMINI. The initial composition of each Z_L is relatively neutron-rich and decreases slightly in the composition for small values of α. The greatest change in composition between the initial and final composition

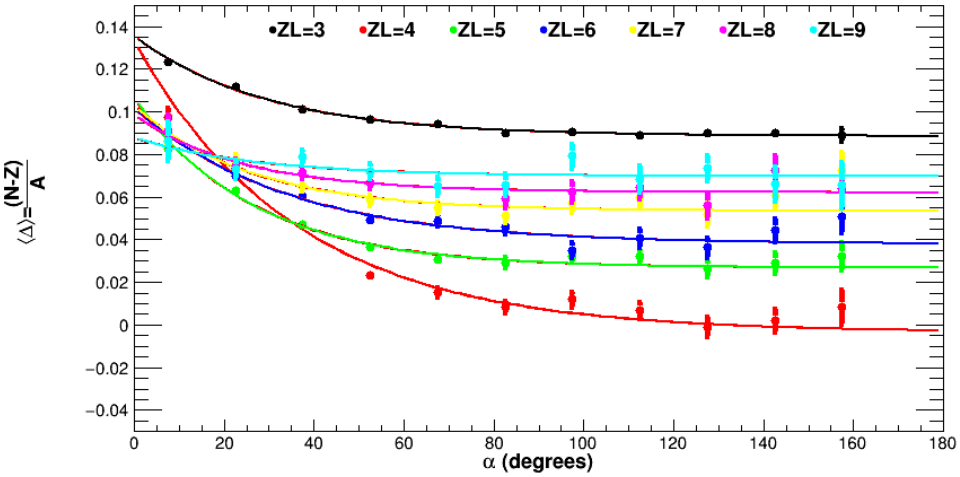

(a) No GEMINI de-excitation

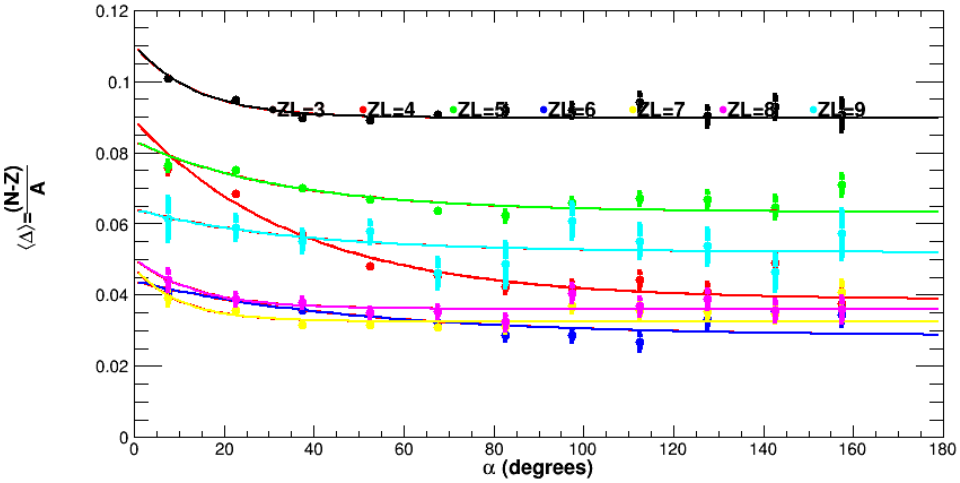

(b) 10 GEMINI de-excitations

Figure 5.7: COMD Δ_L vs. α for the stiff density dependence of the asymmetry energy.

is seen for the Z_L=4, which is almost certainly due to the lack of ^{8}Be. The exponential change in composition is preserved. However, it is significantly reduced relative to the results pre-GEMINI.

The results for the composition as a function of time are shown for the stiff and super-stiff interactions in Figure 5.7 and 5.8, respectively. All $\langle\Delta_L\rangle$ vs. α plots have the same y-range for all COMD results and all COMD+GEMINI results, respectively. The exponential trend discussed for the soft interaction is also present for the stiff and super-stiff interactions in the data with and

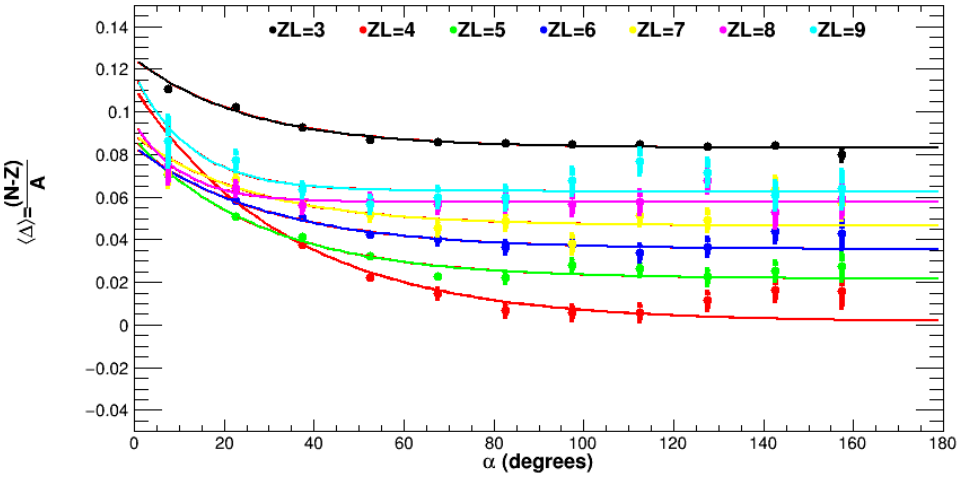

(a) No GEMINI de-excitation

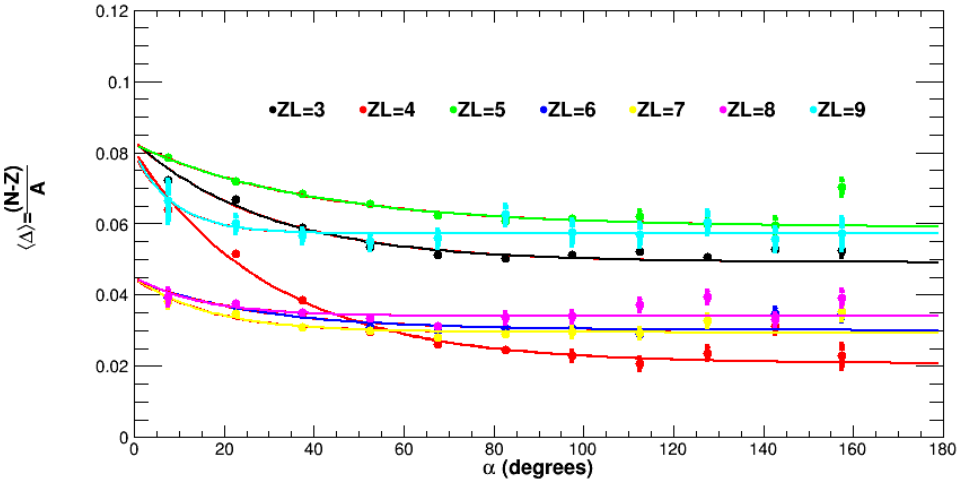

(b) 10 GEMINI de-excitations

Figure 5.8: COMD Δ_L vs. α for the super-stiff density dependence of the asymmetry energy.

without GEMINI.

In comparing the different stiffnesses, several features emerge for the systems without GEMINI. The initial composition of the **LF** decreases as the interaction becomes stiffer. For example, the composition for Z_L=3 starts at approx. $\langle\Delta_{L,init}\rangle$=0.14 for the softest systems. The initial composition decreases to approx. $\langle\Delta_{L,init}\rangle$=0.135 for the stiff system and $\langle\Delta_{L,init}\rangle$=0.125 for the super-stiff system. During the nucleon drift phase of the projectile and target interaction, the difference in

the symmetry energy compared to saturation energy for the soft interaction is less than for the stiffer ones. As a result, the potential barrier for the enhanced neutron flow is lower for the soft interaction, producing an excess of neutrons in the neck region relative to the other, stiffer ones.

The extent of the equilibration is also dependent on the density dependence of the asymmetry energy. The greatest change in composition between the initial and asymptotic values is seen for the softest interaction. Because the asymmetry energy penalty for the softest interaction is the smallest, the neutrons from the neck region (**LF**) are more likely to flow to the PLF region (**HF**). Therefore, the extent of the equilibration is the greatest. The details about the equilibration and the fit will be discussed in Section 5.3.3.

When examining the composition after GEMINI is applied, the initial compositions and asymptotic values for all **LF** across the three interactions start and end at approximately the same $\langle\Delta_L\rangle$ with the exception of Z_L=3,4. For Z_L=3,4, the composition starts off the most neutron-rich for the softest interaction, and the asymptotic values are also the most neutron-rich. However, the difference between the initial and asymptotic value is the same for all three interactions.

The composition of the **HF** for the softest interaction is plotted in Figure 5.9. The composition is shown for $12 \leq Z_H \leq 18$, focusing on the Z_H results shown in the experimental chapter. The top panel shows the results for no GEMINI de-excitation and the bottom panel shows the results after the GEMINI de-excitation was applied.

Focusing on the events with no de-excitation, the results show an overall increase in the composition of each **HF**. For most **HF**, the composition evolves in a S-shape as the angle of rotation increases. While the initial composition starts off slightly more neutron-poor and increases for α <30°, the composition across the entire α distribution is linear within error bars. A slight increase is seen again for α >100°. The increase in the composition is not exponential and the evolution in composition is not well understood for the parameters applied in this analysis.

After the events were de-excitated, the composition of the **HF** is observed to be fairly flat. Overall, the initial composition is much less neutron-rich, with a $\langle\Delta_{H,init}\rangle$ composition about half the initial composition without de-excitation. A slight decrease in composition is seen at $60° \leq \alpha \leq 120°$. The statistics for α >120° are too poor to conclusively say anything about the evolution of the composition.

The $\langle\Delta_H\rangle$ vs. α results are shown for the stiff and super-stiff interaction in Figure 5.10 and 5.11,

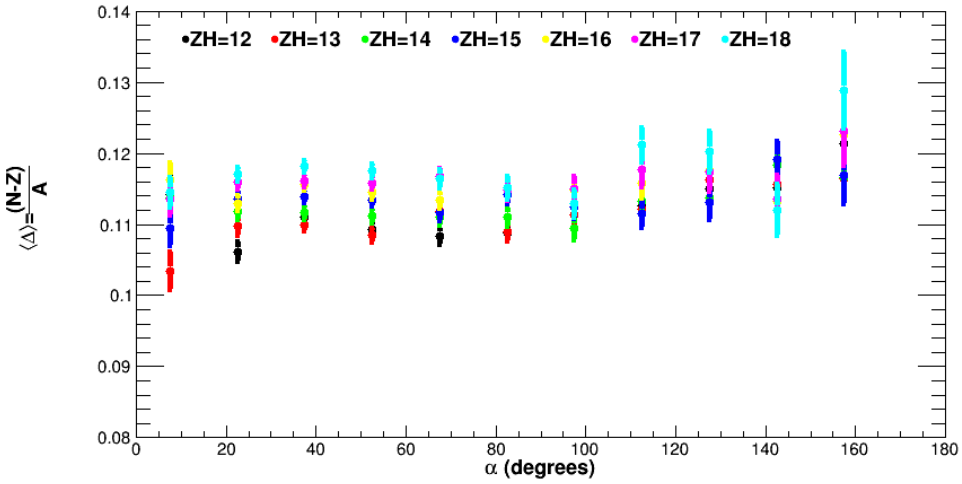

(a) No GEMINI de-excitation

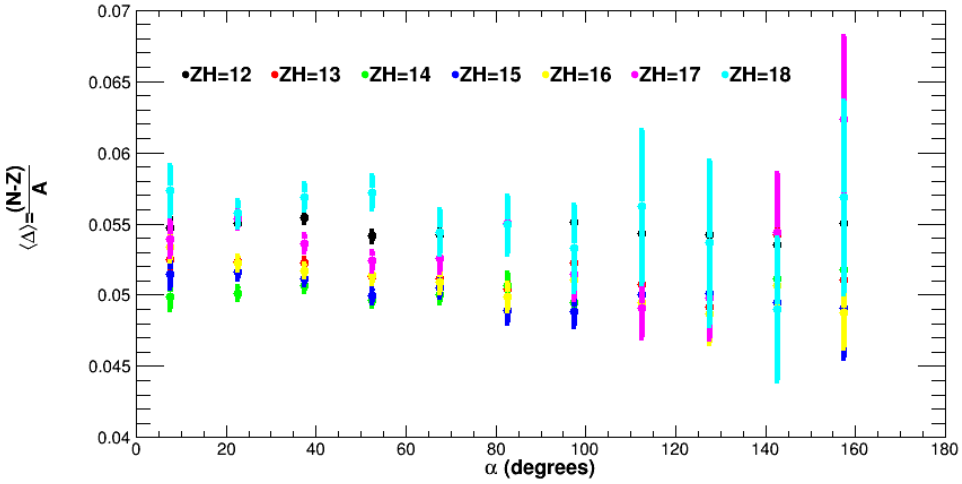

(b) 10 GEMINI de-excitations

Figure 5.9: COMD Δ_H vs. α for the softest density dependence of the asymmetry energy.

respectively. The y-range for the top panels of Figure 5.9-5.11 and also consistent for the bottom panels of the same figures.

First, the results without GEMINI (top panel Figure 5.10 and 5.11) are examined. The initial composition for the softest interaction is the most neutron-rich followed by the stiff and super-stiff interactions, respectively. The results are in contradiction to the dynamics discussed for the light fragment. Since the asymmetry energy barrier for the soft interaction is lower, not only should the

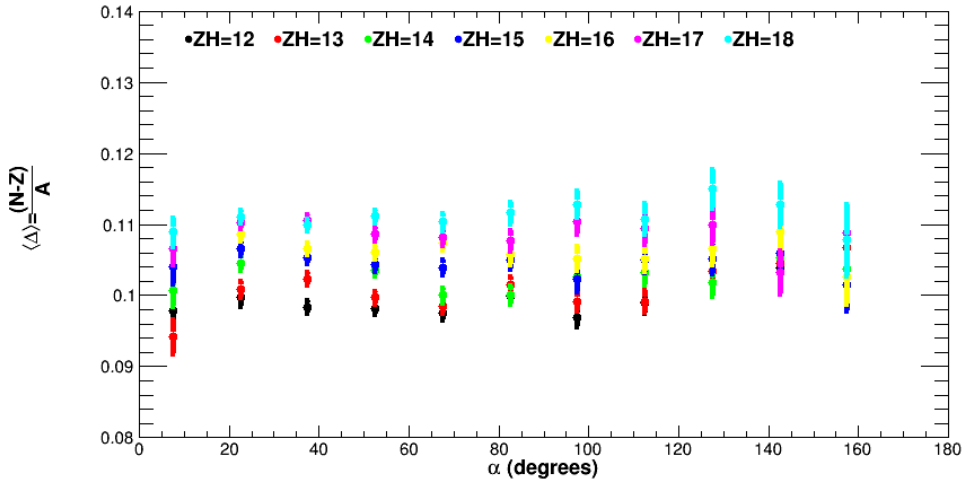

(a) No GEMINI de-excitation

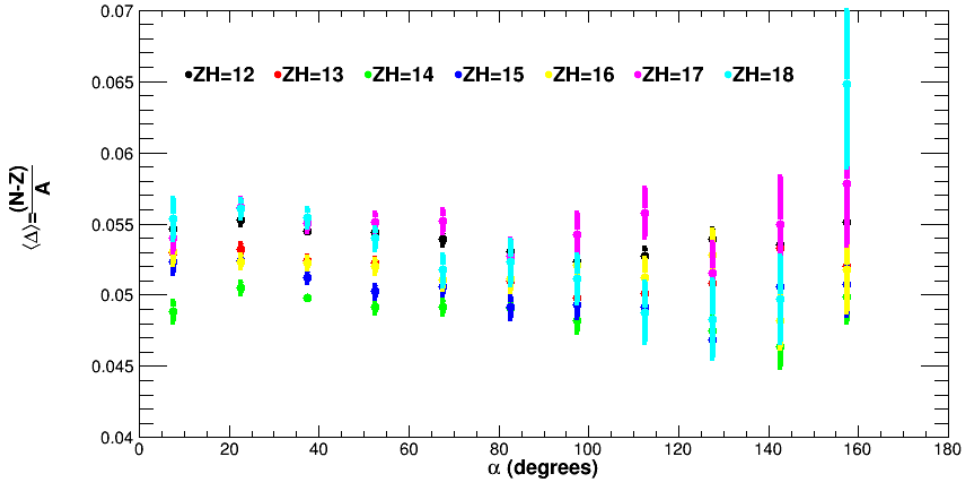

(b) 10 GEMINI de-excitations

Figure 5.10: COMD Δ_H vs. α for the stiff density dependence of the asymmetry energy.

neutron content in the neck region be higher, the neutron content in the PLF should be lower.

For the stiff interaction (Figure 5.10), an increase in the **HF** composition is seen across all Z_H. Similar to the soft interaction, the first point has a lower composition. However, between $20^\circ \leq \alpha \leq 120^\circ$ the composition is flat. The composition increases slightly for $\alpha > 120^\circ$, which is also consistent with the soft interaction results. The difference in the initial and asymptotic composition for the stiff interaction is less than the soft interaction.

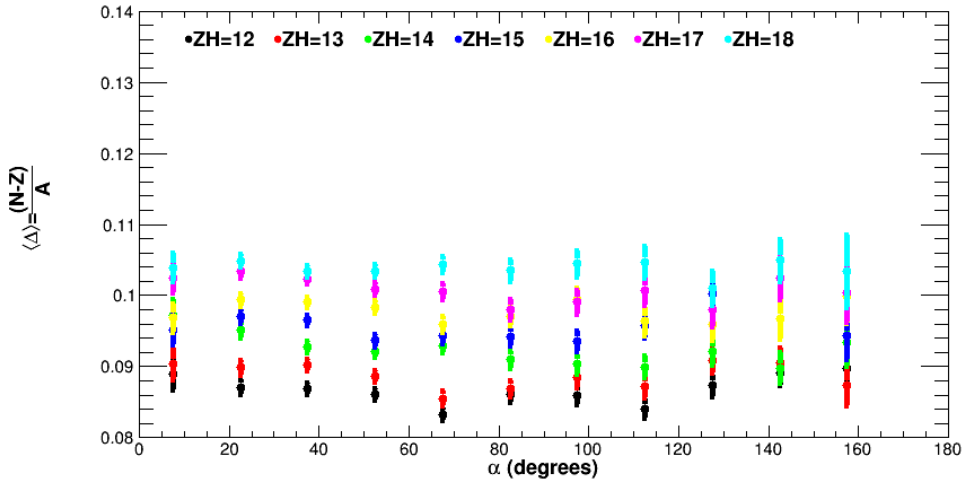

(a) No GEMINI de-excitation

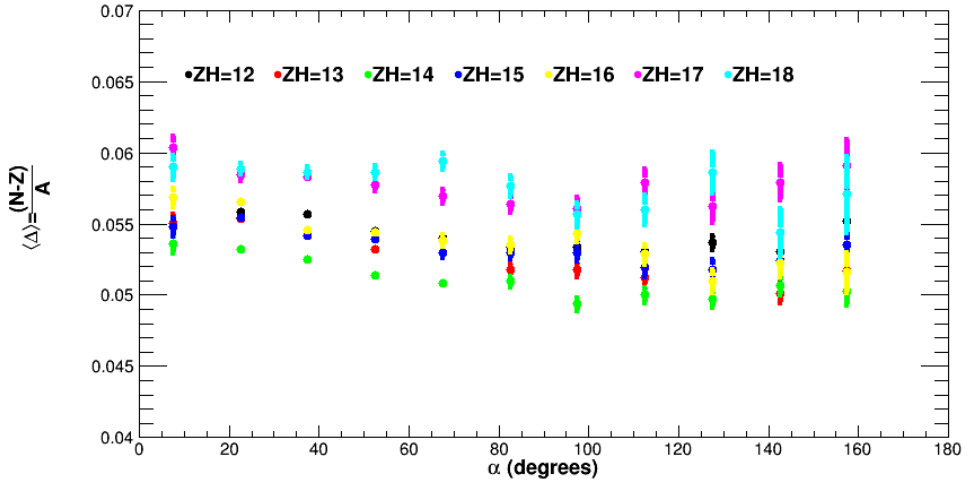

(b) 10 GEMINI de-excitations

Figure 5.11: COMD Δ_H vs. α for the super-stiff density dependence of the asymmetry energy.

For the super-stiff interaction, a flat distribution is seen. For α <80°, a small decrease in the composition is seen followed by a small increase at α >120°. The results do not exhibit the experimental trends discussed in Chapter 3.

Next, the events after GEMINI de-excitation were analyzed. For all three symmetry energy interactions, the initial composition is lower. The initial values are the highest for the stiffest interaction and lowest for the softest interaction. A decrease in the composition is seen as a function of

α for all three interactions. While this may seem in contradiction to the results seen pre-GEMINI, the results are in agreement with how GEMINI works. The fragments produced pre-GEMINI in the soft interaction are further from the line of stability. As a result, GEMINI is more likely to de-excite the fragment more, causing the final $\langle\Delta_H\rangle$ to be lower for the soft interaction than for the stiffer interactions.

5.3.2 $\langle\Delta\rangle$ Vs. α for AMD Simulations

For the AMD results, Figure 5.12 shows the Δ versus α results of the **LF** for the soft (Gogny) interaction. The top panel shows the results without GEMINI de-excitation and the bottom panel shows the results after 10 GEMINI de-excitations. Each color corresponds to a different Z_L ranging from $3\leq \Delta_L \leq 9$. The Z_L range was chosen to reproduce the experimental range.

The composition of the **LF** starts off relatively neutron-rich. The composition decreases more severely for small angles of rotation before plateauing at large angle of rotation (α >100°). The statistics for α >80° are low, making the details hard to examine. However, the points are overall consistent and lower for α >80° than for smaller α. The change in composition is exponential in nature, which is consistent with the results seen in the experimental data.

For the GEMINI de-excitation, the $\langle\Delta_L\rangle$ starts off relatively neutron-rich for Z_L <6 and decreases linearly for α <60°. A bump in the data is seen between 60° < α <140°, indicating secondary effects present. For Z_L >6, a linear increase is seen in the composition for α <60°. The change in the trend observed for the AMD+GEMINI data for large Z_L is due to the stability of the fragments. For Z_L=9, the initial $\langle\Delta_L\rangle$=0.14 corresponding to an A=21 or N=Z+3. Small-Z fragments are most stable in a N=Z configuration. Therefore, fragments the further from stability will be de-excited the most by GEMINI.

For the stiff interaction, as shown in Figure 5.13, an exponential effect is also present in the $\langle\Delta_L\rangle$ data as a function of α for Z_L <7. For Z_L=8,9, the statistics are too low to analyze in detail. As the composition decreases, $\langle\Delta_L\rangle$ does not reach its plateau, unlike the data for the soft interaction. The lack of plateauing indicates the equilibration continues past α=180°.

The $\langle\Delta_L\rangle$ vs. α trends shown for the GEMINI results are consistent with the soft interaction. A linear decrease is seen for Z_L <5 and a linear increase is seen for Z_L >5 at α <60°. A wave effect in the composition is seen for α >60°.

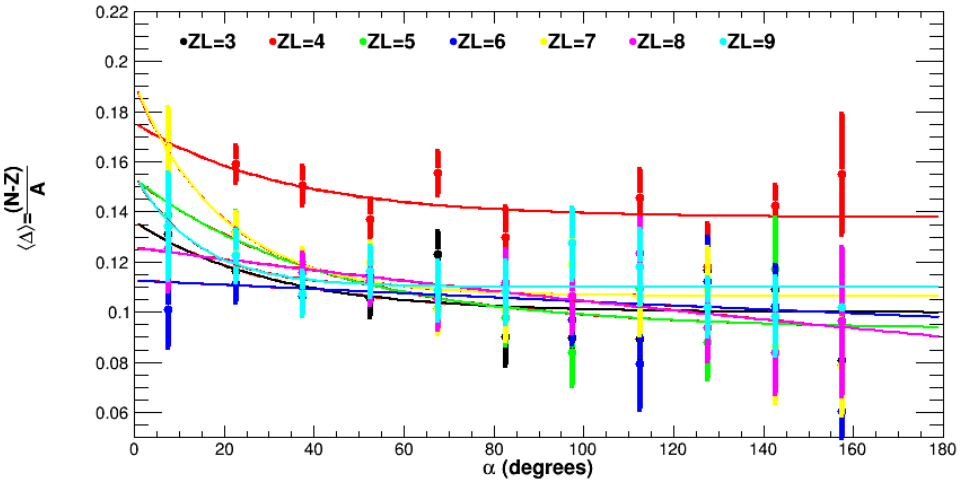

(a) No GEMINI de-excitation

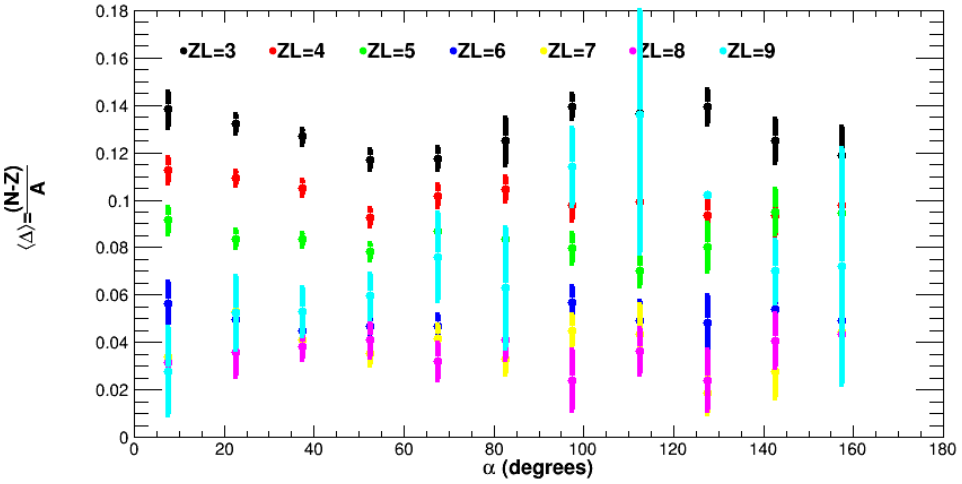

(b) 10 GEMINI de-excitations

Figure 5.12: AMD Δ_L vs. α for the soft Gogny interaction. The colored points correspond to each Z_L between $12 \leq Z_L \leq 18$. The lines correspond to the individual fits and the color matches the color of the fitted points.

When comparing the two interactions, the composition for most Z_L is slightly higher for the stiff interaction. This contradicts the idea that the neck region should be more neutron-rich for the softer interaction. The energy required to donate neutrons to the neck region is less for the soft interaction, indicating the initial composition should be higher. The final values at α=180° for both interactions are approximately the same ($\langle\Delta_L\rangle \simeq 0.1$) for all Z_L except for Z_L=4. The combination of similar final compositions and the slower rate of change in composition for the stiff interaction

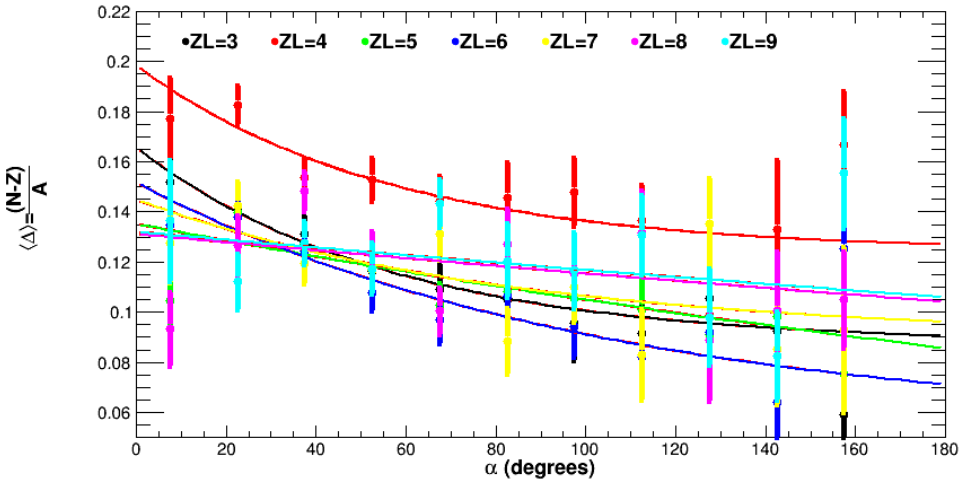

(a) No GEMINI de-excitation

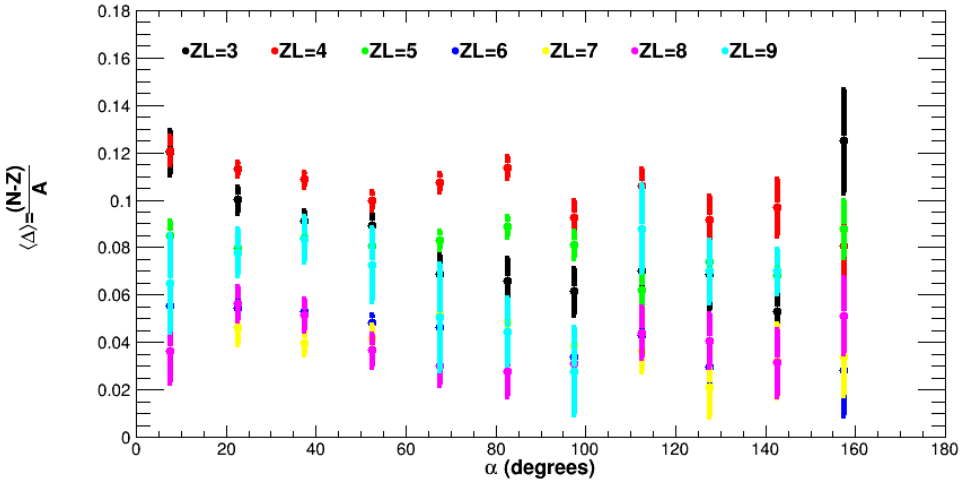

(b) 10 GEMINI de-excitations

Figure 5.13: AMD Δ_L vs. α for the stiff Gogny interaction. Each color corresponds to a each Z_L ranging from Z_L=3 to Z_L=9. The colored lines are the fits and are shown in the same color as the fitted points.

indicates the form of the density dependence has an impact on the equilibration. Specially, the lower energy penalty for the softer interaction causes the neutrons to be driven back into the PLF faster.

For the GEMINI results, the composition for Z_L=4-8 is consistent within error bars. The consistency is due to the similar initial and final compositions of those fragments in the soft and stiff interaction. For example, in the case of Z_L=5, $\langle\Delta_{L,init}\rangle$=0.15 for the soft interaction and $\langle\Delta_{L,init}\rangle$=0.14 for

the stiff interaction. The final composition is approx. $\langle\Delta_{L,final}\rangle$=0.10 for both interactions. Because the initial composition, angular momentum and excitation energy are similar, the composition after GEMINI should be consistent. The only Z_L values that are not consistent are Z_L=3,9. The difference in Z_L=9 is due to the low statistics in the AMD only data, which shows an increase in the composition at small angles for the stiff interaction, unlike the soft interaction. For Z_L=3, the $\langle\Delta_L\rangle$ is systematically lower for the soft interaction than the stiff one. The $\langle\Delta_L\rangle$ after GEMINI is much lower for the stiff interaction due to more N, Z unstable fragments present before de-excitation in the stiff interaction.

The composition of the **HF** is shown for the soft interaction in Figure 5.14. The initial composition starts off relatively neutron-poor. As the angle of rotation increases, the composition evolves exponentially to be more neutron-rich. The composition eventually plateaus around α >100°, which is consistent with where $\langle\Delta_L\rangle$ flattens out. The statistics overall are fairly low. However, the trends are still present throughout all Z_H.

The GEMINI de-excitation results show a fairly flat distribution with a decrease at α >120°. The decrease in $\langle\Delta_H\rangle$ is most likely due to the composition being furthest from stability.

For the stiff interaction, Figure 5.15 shows an exponential evolution in composition for **HF** is not observed. Rather, the initial composition starts off relatively neutron-rich and decreases linearly between 0° $\leq \alpha \leq$80°. The composition increases for 90° $\leq \alpha \leq$180°. The overall trend is more consistent with a V-shape than the exponential shape seen for the soft interaction. For the GEMINI results, the composition is also fairly flat. The same trends seen in the soft interaction is also present, yet the extend of the change is smaller.

Additionally, the initial composition is lower for the soft interaction, which is consistent with the greater neutron contribution from the PLF to the neck region during the momentum dampening phase. The asymptotic values are consistent for the soft and stiff interaction.

The post-GEMINI composition for all Z_H is consistent within error bars across the entire range of α. Given how close the initial and final compositions are for the pre-GEMINI results, it makes sense that the post-GEMINI results are equivalent.

Because the AMD simulations are statistically limited, all **HF** and **LF** fragments were combined and the results are shown in Figure 5.16. The results for the **HF** are plotted in red and the **LF** results are plotted in blue. The soft interaction is shown in the top panel and the stiff interaction is

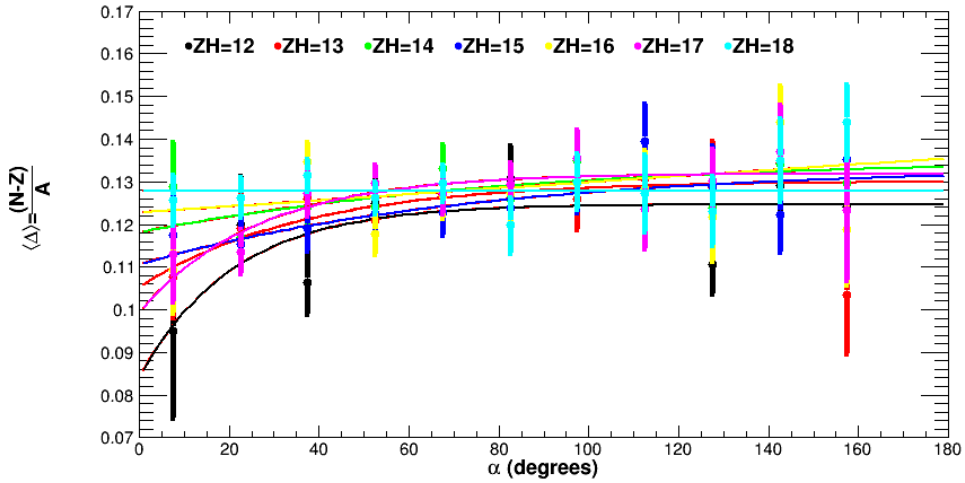

(a) No GEMINI de-excitation

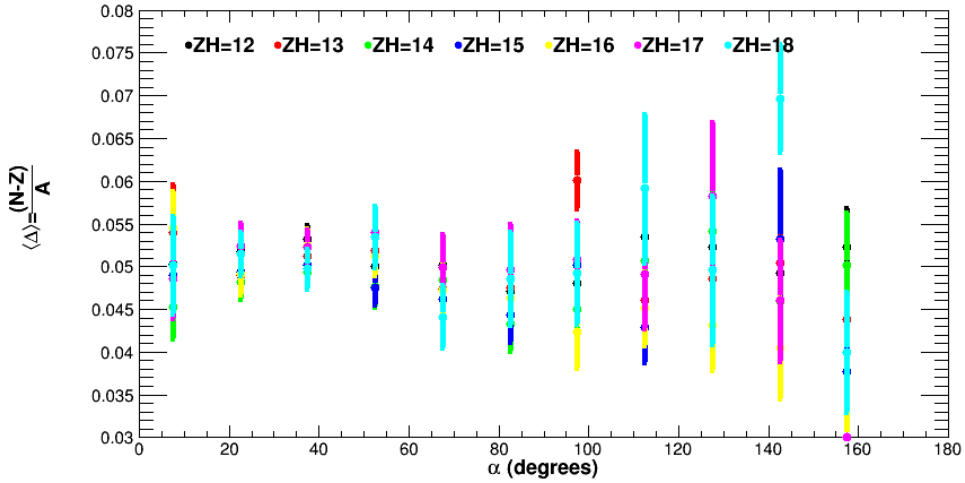

(b) 10 GEMINI de-excitations

Figure 5.14: AMD Δ_H vs. α for the soft Gogny interaction. Each color corresponds to a each Z_H ranging from Z_H=12 to Z_H=18. The colored lines are the fits and are shown in the same color as the fitted points.

shown in the bottom panel. The exponential trend seen in the experimental data is reproduce in the combined AMD simulations for the **HF** and **LF** using both interactions. The equilibration is much faster for the soft interaction than the stiff interaction. For the soft interaction, the equilibration approaches the asymptotic value at α=180°, which is more consistent with the experimental trends seen.

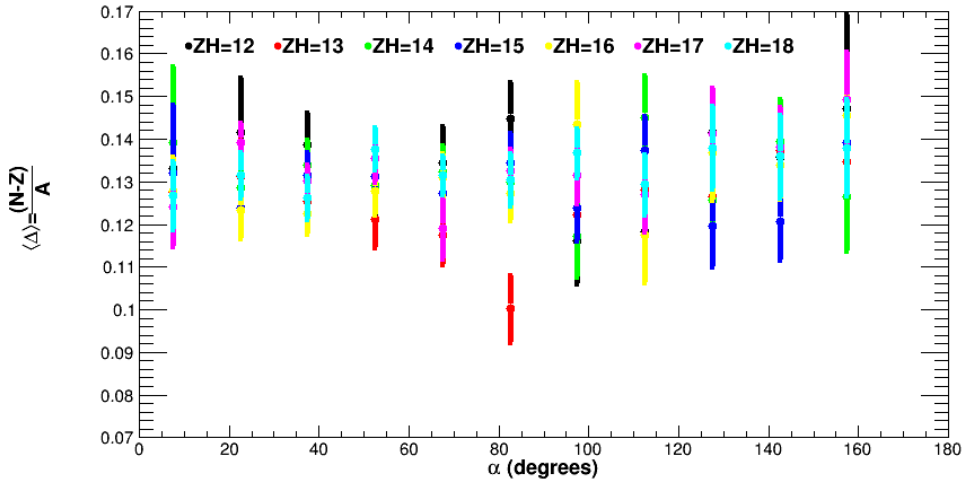

(a) No GEMINI de-excitation

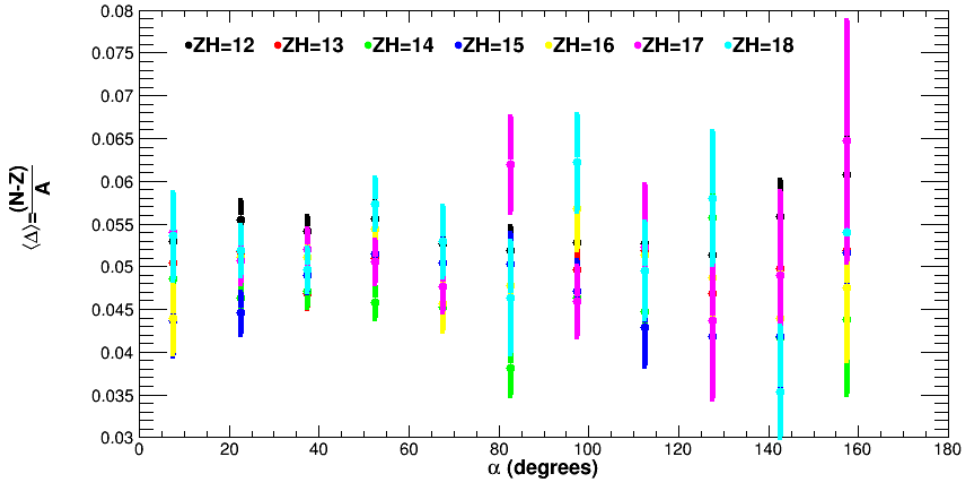

(b) 10 GEMINI de-excitations

Figure 5.15: AMD Δ_H vs. α for the soft Gogny interaction. The colored points correspond to each Z_H between $12 \leq Z_H \leq 18$. The lines correspond to the individual fits and the color matches the color of the fitted points.

5.3.3 Simulated $\langle\Delta\rangle$ Vs. α fits

The $\langle\Delta_H\rangle$ and $\langle\Delta_L\rangle$ versus α plots were fit using an exponential form. The fit was applied to all Z_L results from both molecular dynamics simulations. However, for the **HF**, only the AMD Z_H results from the softest interaction are fit. The exponential trend was not observed for the stiff interaction in AMD and all interactions in COMD. The form of the fit is shown in Equation 5.2,

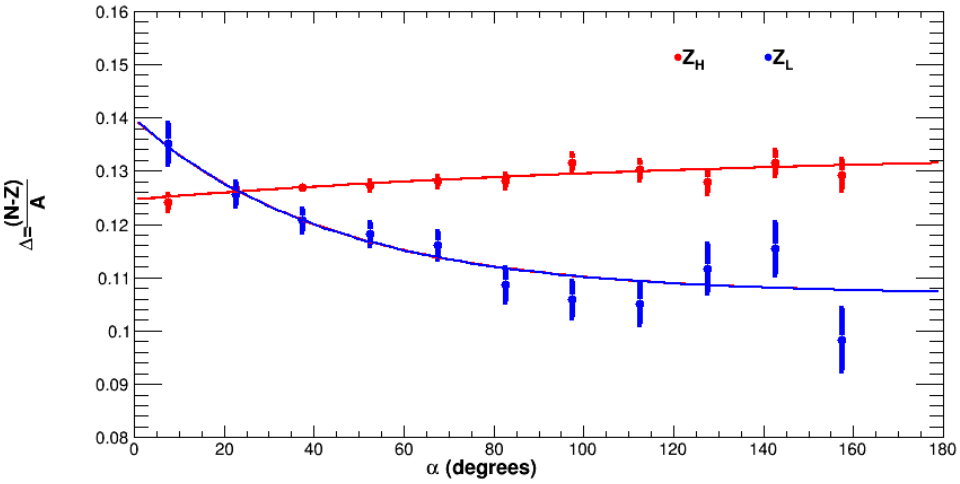

(a) Soft (Gogny) interaction

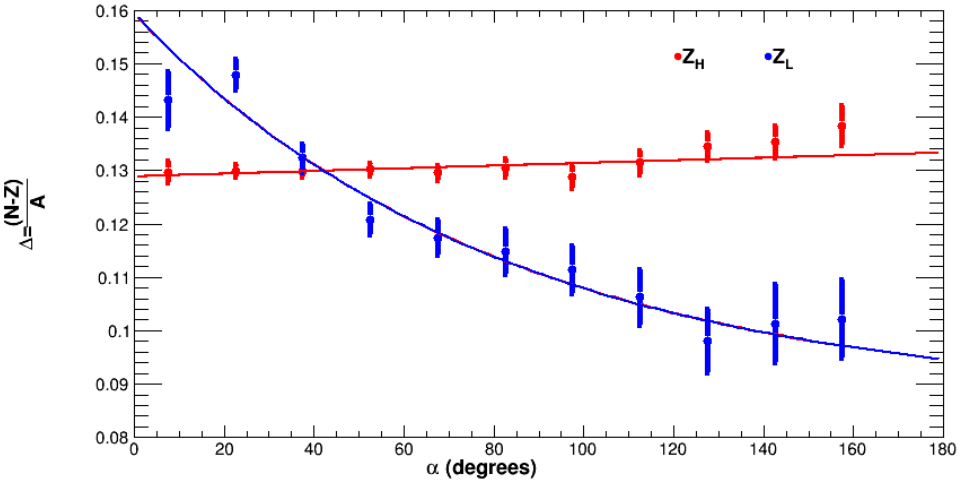

(b) Stiff (GognyAS) interaction

Figure 5.16: AMD Δ vs. α for all combined **HF** (red) and **LF** (blue). The soft interaction is plotted on the top panel and the stiff interaction is plotted on the bottom panel. The exponential trend exhibited the experimental data is preserved. However, the soft interaction approaches the asymptotic value much faster than the stiff interaction, which is more consistent with the experimental results.

where a is the asymptotic value, b is the pre-exponential factor and c is the rate constant in degrees.

$$\langle \Delta \rangle = a \cdot \exp(-c\alpha) \tag{5.2}$$

The exponential was fit between $0^\circ \leq \alpha \leq 156^\circ$, which is different from the range chosen for

the experimental data. The COMD and AMD data was more coarsely binned, which allows for the first data point to be included. The data past α >156° was not included since they exhibited behavior deviating from the exponential trend. The fits are shown in Figure 5.6-5.8 and 5.12-5.14.

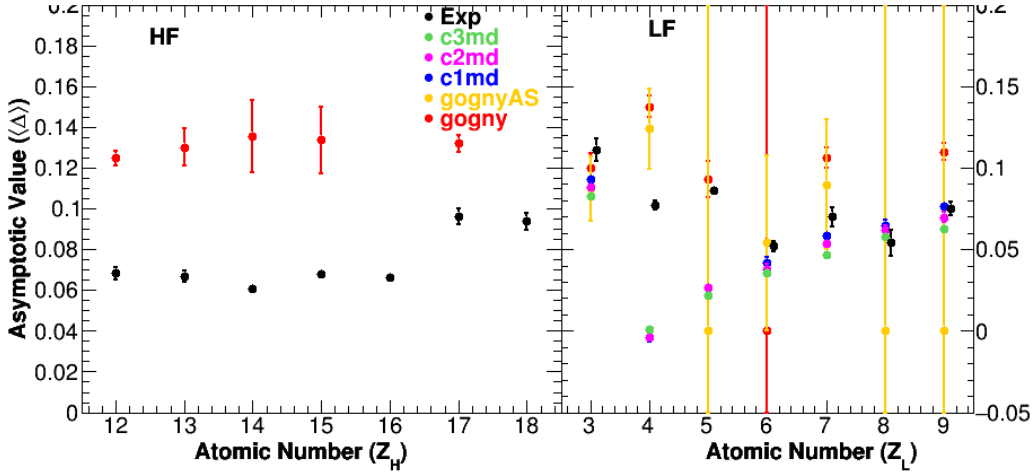

Figure 5.17: Experimental, and AMD and COMD simulation results of the asymptotic values for **HF** and **LF** with no GEMINI applied. The **HF** results as a function of Z_H are plotted on the left and the **LF** results as a function of Z_L are plotted on the right. The black points are the experimental and the colored points are from the simulations. Only the soft (Gogny) interaction from AMD showed an exponential trend in the composition as a function of time for the **HF**. Therefore, those are the only results compared to the experimental one. The **HF** values for the simulation over-predicts the neutron content. The composition for the **LF** from the simulations does not exhibit the even-odd trend expected from the binding energies.

First, the asymptotic values are examined. Figure 5.17 shows the asymptotic values for the AMD, COMD and experimental data. The results post-GEMINI were not included in this figure. The experimental results are plotted in black and the colored points represent the simulated data. The AMD results are plotted in red (soft) and yellow (stiff). The COMD results from softest to stiffest are blue, pink and green. The left panel shows the **HF** results as a function of atomic number and the right panel shows the **LF** results as a function of atomic number.

Focusing on the **HF** results, the simulation systematically over-predicts the neutron composition. Considering the AMD fragments still have excitation energy and have not undergone much evaporative decay by the time the simulation is stopped (1000 fm/c), an over-estimation of the

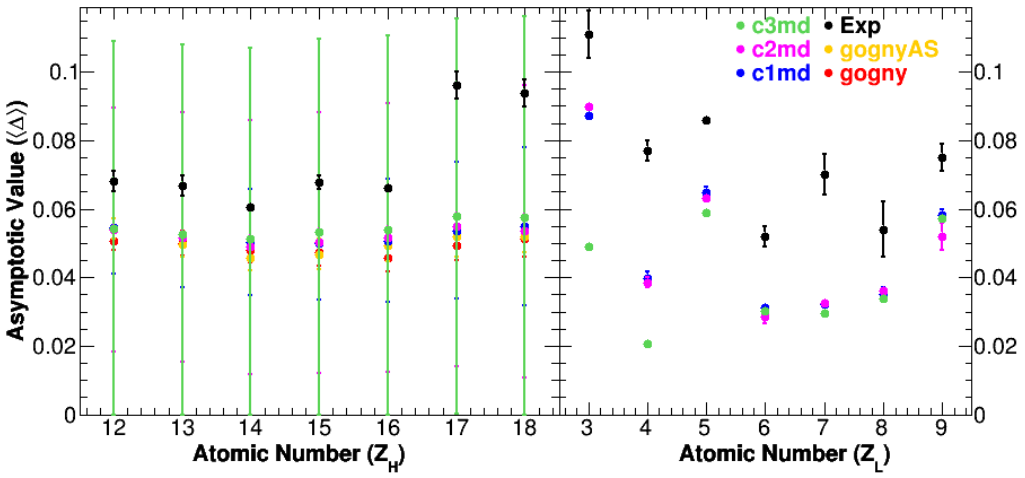

Figure 5.18: Experimental, and COMD and AMD simulation results of the asymptotic values for **HF** and **LF** after GEMINI de-excitation. The **HF** results as a function of Z_H are plotted on the left and the **LF** results as a function of Z_L are plotted on the right. The black points are the experimental and the colored points are from the simulations. The values shown for the COMD Z_L results are the asymptotic values extracted from an exponential fit. The other asymptotic values were calculated from a linear fit. The results for both **HF** and **LF** across all combinations of stiffnesses and simulations under-predict the neutron composition relative to the experimental values. The odd-even effect is reproduced.

neutron content is expected. Additionally, the odd-even effect due to the parity term in the binding energy, is not present.

The **LF** results show effects that are inconsistent with experimental data. For $Z_L \leq 6$, the asymptotic composition for both the AMD and COMD results are consistent with the experimental data. The asymptotic composition for $Z_L < 6$ is consistent for AMD, but not for COMD. For COMD, the asymptotic composition decreases linearly as the **LF** decreases. This indicated COMD is under-producing neutron-rich neck fragments. The only exception is Z_L=3, where A_L=4,5 were broken apart is the experimental code.

A better indication of the final asymptotic values is given by looking at the final compositions of the GEMINI results. For the **LF**, the COMD results still preserved the exponential effects (refer to bottom panels of Figures 5.6-5.8). Therefore, the distribution was fit with the same exponential form as the pre-GEMINI results. For the **HF** and the AMD results, the exponential signature was not preserved. Therefore, a linear fit was applied and what is referred to as the asymptotic value for GEMINI de-excitation results corresponds to the average.

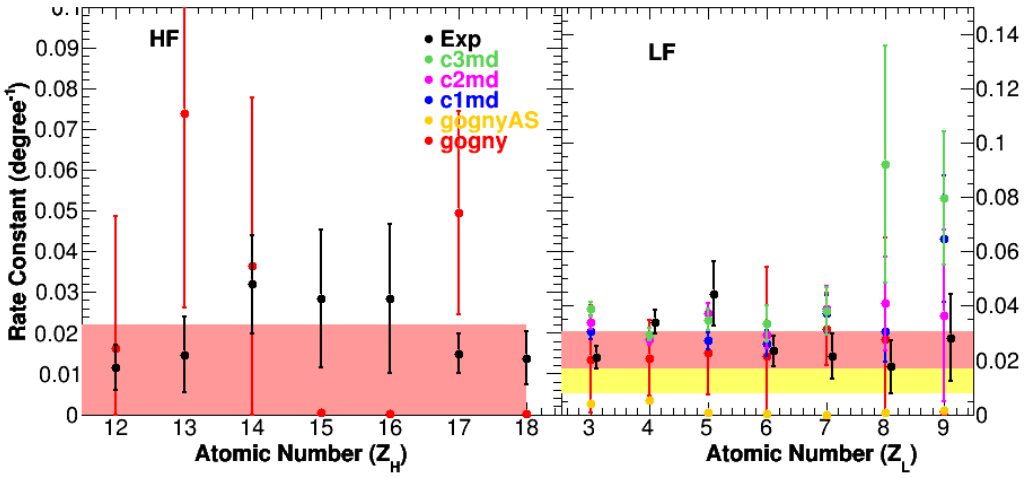

Figure 5.19: Experimental, and AMD and COMD simulation results of the rate constants for **HF** and **LF** without any GEMINI afterburner. In the left panel are the **HF** results as a function of Z_H and in the right panel are the **LF** results as a function of Z_L. The black points are the experimental and the colored points are from the simulations. The red and yellow shaded regions correspond to the rate constants extracted from the combined AMD soft and stiff interactions, respectively. Only the results from the soft (Gogny) interaction from AMD are shown, since it was the only data to exhibit an exponential trend. The **HF** values for the simulation are consistent with the experimental ones. The **LF** values are also consistent with the experimental values, with the exception of Z_L=17, 18. The AMD stiff interaction (GognyAS) systematically underpredicts the rate of change in composition.

The asymptotic values after GEMINI de-excitation are shown in Figure 5.18. The left panel also corresponds to the **HF** and the right panel corresponds to the **LF**. The coloring is consistent with Figure 5.17. For both the **HF** and the **LF**, all simulation and stiffness combinations exhibit a lower neutron content than the experimental results. The results indicate GEMINI is de-exciting the fragments too much. The odd-even effect seen in the experimental data is present for the **LF**, except for Z_L=7. For the **HF**, the odd-even effect is not as strongly seen.

Figure 5.19 shows the rate constants for **HF** in the left panel and **LF** in the right panel. The coloring is consistent with Figure 5.17. The red and yellow bars show the rate constant with error bar for the AMD soft (red) and stiff (yellow) interaction for all combined **HF** and **LF**. In addition, the average rate constant per degree was calculated, and the values are shown in Table 5.1.

The rate constants for the **HF** for both the AMD soft interaction and the experimental results are consistent within statistical error bars for all Z_H. The average rate constant was calculated to be k_H=0.02±0.01 per degree for the experimental data and k_H=0.03±0.01 per degree for the simulated

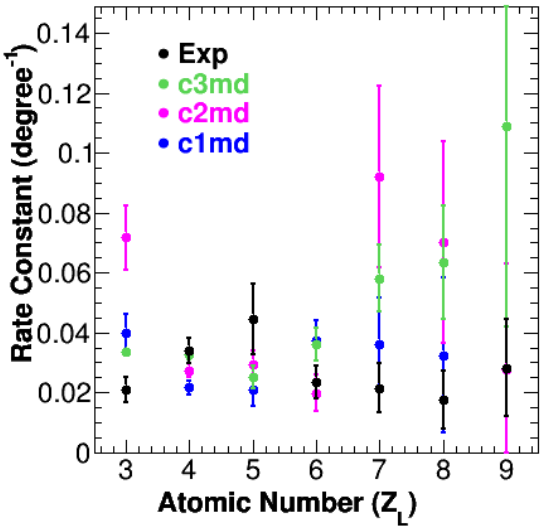

Figure 5.20: Experimental and COMD simulation results of the rate constants for **LF** after GEMINI was applied. Only the **LF** results from the COMD simulations were retained after GEMINI. The colored points correspond to the COMD simulations and the experimental points are the black ones. The rate constants for Z_L=4-6 for all simulation interactions are consistent with the experimental results. Deviation is seen for Z_L=3 and Z_L >6.

data. The soft interaction rate constant value for the combined **HF** and **LF** is also consistent with experimental results. However, the stiff interaction rate constant for all combined pairings is not.

The rate constants for the **LF** are also in fairly good agreement with the exception of the AMD stiff interaction. Deviation from the experimental data is seen for Z_L >7 in some cases. However, this may be due to the limited statistics for larger Z_L. Several features arise when comparing the interaction stiffness. For the AMD results, the rate constant for the soft interaction is consistent within error bars with the experimental results for both the individual Z_H pairings and the combined **LF** results. As shown in Table 5.1, the average rate constant for the AMD soft interaction is 0.03±0.01 per degree and the experimental average rate constant is 0.03±0.01 per degree. The rate constant for the soft interaction is systematically higher than the stiff one. The average rate constant of the stiff interaction (0.009±0.004 per degree) does not agree with the experimental data. The rate constant for the combined pairings for the stiff interaction is higher than the individual values. However, the results are still systematically lower than the experimental results and are only consistent with a select number of experimental k_L values. The results indicate the equilibration is

Interaction	k_H (degrees^{-1})	k_L (degrees^{-1}) No GEM.	k_L (degree^{-1}) GEM.
Experimental	0.02±0.01	0.03±0.01	0.03±0.01
AMD soft (gogny)	0.03±0.01	0.03±0.01	-
AMD stiff (gognyAS)	-	0.009±0.004	-
COMD soft (c1md)	-	0.035±0.004	0.03±0.01
COMD stiff (c2md)	-	0.034±0.005	0.05±0.02
COMD super-stiff (c3md)	-	0.043±0.005	0.04±0.01

Table 5.1: Average rate constants for **HF** (k_H) and **LF** (k_L). The top row shows the experimental values. The soft (gogny) interaction for the AMD data was the only interaction fit with and exponential for the **HF**. The third column shows the rate constant for the **LF** before GEMINI de-excitation and the last column shows the rate constants for **LF** after GEMINI de-excitation.

much slower than the experimentally observed rate.

For the COMD results, the difference between the rate constants is not as extreme as for the AMD results. The difference between the softest and stiffest interactions is approx. 0.01 per degree. The rate constants systematically falls in order, with the fastest rate is seen for the super-stiff interaction. The ordering is in contraction with the results seen from AMD. In all three cases, the average rate constant is greater than the experimental one. The results for the soft and stiff interaction are consistent with the experimental results.

The effects of the GEMINI de-excitation can be examined by comparing the rate constants for Z_L from the COMD simulations. Figure 5.20 shows the results for the rate constants post-GEMINI de-excitation and the average rate constant is presented in the last column of Table 5.1. The results show consistency with the experimental data for Z_L=4-6. For Z_L=3 and Z_L >6, the rate constants are larger than the experimental results for stiffer interactions. However, the error bars are also considerably large for the Z_L >6 case.

When comparing the average rate constants, k_L for the soft and super-stiff interaction are equal within error bars. Only the stiff interaction shows significant deviation between the pre- and post-GEMINI results. The final results for all three interactions are consistent with the experimental data within error bars. The k_L from the soft interaction is the closest.

5.4 Comparison of the Simulated Results to Previous Experimental Results

The simulation results from Section 5.3 indicate the soft interaction for both the COMD and AMD results reproduce the data best. For the **HF**, the soft interaction for both the COMD and AMD results showed an increase in the composition as a function of rotational angle. The AMD results were able to reproduce the exponential increase in composition observed in the experimental results. The rate constant was in agreement the experimental results. Neither the super-stiff interaction from COMD nor the stiff interaction from AMD were able to reproduce the trend. Instead, a flat or V-shaped change in composition was observed.

When considering the **LF** composition as function of rotational angle, all interactions reproduced the exponential decrease in composition. However, the average rate constant extracted for the AMD stiff and COMD super-stiff interactions was not in agreement with the experimental rate constant. The results from the soft interaction for both the AMD and COMD simulations is in the best agreement with the experimental data. However, the stiff COMD interaction cannot be ruled out as a possible form for the density dependence of the asymmetry energy term either.

The simulated results from this dissertation can be compared to other simulated and experimental results. Specifically, the same equilibration analysis was performed using COMD and AMD by Stiefel [9] and Piantelli [12], respectively. For the Stiefel results, as discussed in Section 1.3, COMD simulation were performed and based through a software simulation replica of the FIRST detector array. The motivation was to directly compare the COMD simulations to the experimental results from Brown [8]. The trends seen in the composition of the **LF** are consistent with the results presented in this chapter. However, the **HF** shows an evolution of the composition more consistent with the **LF** trends seen. The composition starts off relatively neutron-poor and evolves to be more neutron-rich at a rate similar to the **LF**. For each of the stiffness inputs for the asymmetry energy, the results were consistent. The only difference between the stiffnesses in the interaction was the ordering, where the softest interaction produced the most neutron-rich **LF**s and the most neutron-poor **HF**s. All three interaction under-predicted the neutron content of the **LF**. Due to the angular limitations of the FIRST array, the data was fairly coarsely binned and plotted as a function of $cos(\alpha)$ instead of α. Therefore, a direct comparison to the rate constant was not made.

Recently, Piantelli [12] utilized FAZIA data to look at the composition as a function of α.

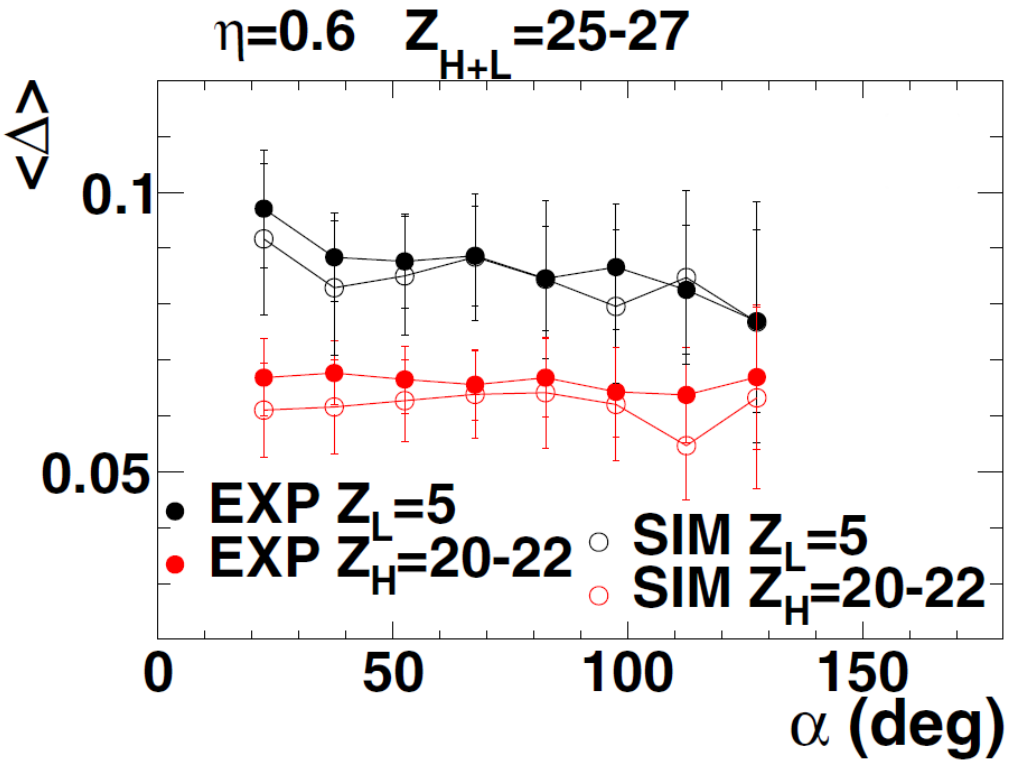

Figure 5.21: Δ vs. α for FAZIA results [12] for Z_L=5 (black) and Z_H=20-22 (red). The closed points are experimental results and the open circles are AMD simulation results. While a small decrease in the composition may be present for Z_L=5 at small α, the error bars are large. Therefore, the results are consistent within error bars. The results for the **HF** are uniform as a function of α. Reprinted with permission from Ref. [12].

The results were compared to AMD simulations. Figure 5.21 shows the results for Z_H=20-22 in red and Z_L=5 in black, where the closed points are experimental results and the open one are simulated results. The AMD simulations shown are using the stiff (gognyAS) interaction. For the **LF**, the composition seems to decrease slightly for small α. However, due to limitations in statistics, the results could be described as uniform within error bars. The simulations reproduce the experimental results well. For the **HF**, the composition is uniform across α within error bars for both the experimental and simulation results. The experimental trends presented in the Piantelli work are not consistent with the experimental trends presented in the work in this dissertation. The difference in results may be due to the difference in experimental configuration and the statistics present in each data set. For the FAZIA data, only 64 detectors were used in their configuration

covering θ=2.5°-17.5°.

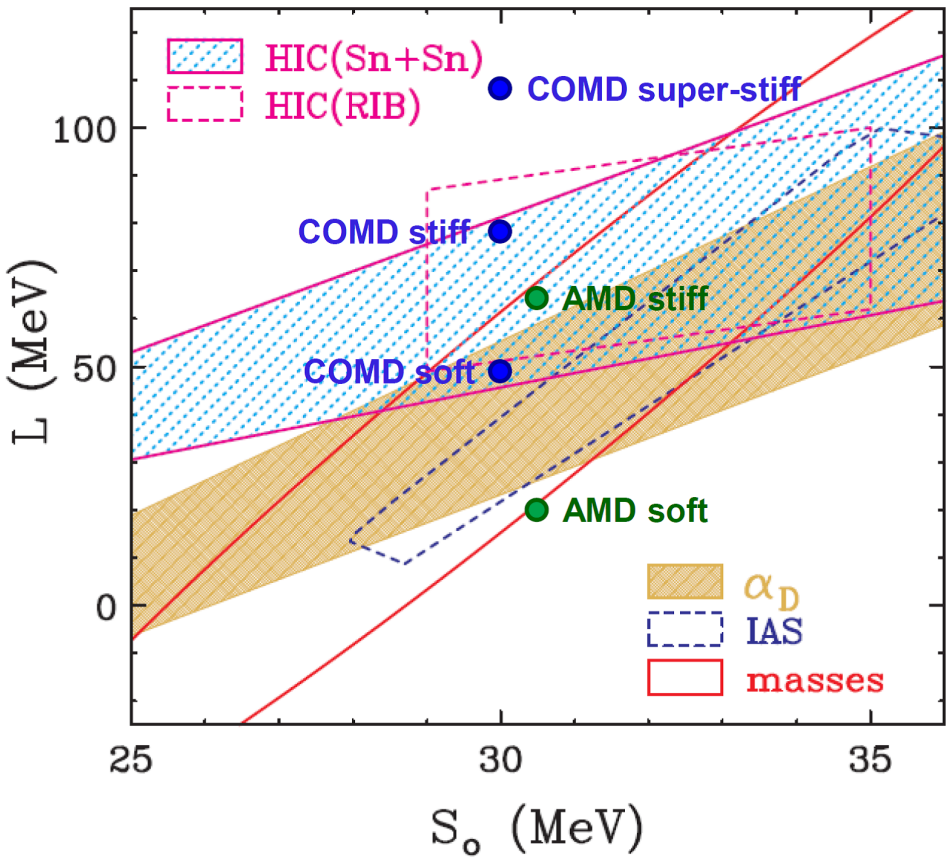

Figure 5.22: The input slope (L) plotted against the saturation asymmetry energy (S_0). Reprinted with permission from Ref. [13].

While the results in this dissertation do not directly constrain the nuclear equation of state (nEoS), the results can be compared to previous work which does. Previous results have constrained the density dependence of the asymmetry energy mostly through nuclear structure probes [82, 83, 13] and heavy-ion collisions [26, 10, 84, 13]. The varying probes are shown in Figure 5.22, where the pink boxes are constraints from heavy-ion collisions, and the gold, blue and red boxes are the constraints from nuclear structure probes. The blue points correspond to the COMD input slopes and saturation asymmetry energy, and the green points correspond to the respective AMD values. The results from this dissertation are consistent with the experimental constraints

applied by both the nuclear structure and heavy-ion collision probes.

6. RECOMMISSION AND UPGRADE OF NIMROD

Recently, the NIMROD array was recommissioned and upgraded. This chapter will focus on the new experimental conditions in Section 6.1. The detector upgrades including silicon testing will be discussed in Section 6.2 and the electronics and data acquisition will be discussed in Section 6.3. The particle identification will be discussed in Section 6.4. Lastly, the neutron ball configurations, electronics and results from new testing will be discussed in section 6.5.

6.1 Experiment

Several experiments were run to recharacterize NIMROD and the neutron ball. All experiments involved either a ^{22}Ne or ^{40}Ar beam, with varying beam energies depending on which cyclotron was utilized to perform the experiment. In the cases where the K150 cyclotron was used, the ^{22}Ne beam was at 19 MeV/nucleon and the ^{40}Ar beam was at 16 MeV/nucleon. The experiment to characterize the NIMROD detector energy and particle identification resolution was run on the K500 cyclotron using an ^{40}Ar beam at 40 MeV/nucleon. The target for all experiments, with the exception of some NBL testing, was a 500 μg thick ^{58}Ni target.

6.2 Detector Upgrades and Studies

The first phase of upgrades to NIMROD involved replacing and adding additional Si detectors. During the last NIMROD experiment in 2012, the silicon detectors in Ring 2 were radiation damaged. Because Ring 2/3 are physically attached to the same detector and share a back plane, the detectors in Ring 2/3 were replaced. Additionally, more 140 μm and 500 μm Si detectors were added to enhance the number of supertelescopes. Table 6.1 shows the θ range, and number of telescopes and supertelescopes in the new configuration per ring. The additional supertelescopes allow for a greater range of isotopic resolution and identification, especially in the most forward angles.

One significant change from the last NIMROD campaign was the manufacturer of these Si detectors. Previous detectors were designed and manufactured by Eurisys Mesures Inc. [85], however the company is no longer in existence to produce the INDRA-design Si detectors. The new detectors were manufactured by Micron Semiconductor Ltd. [15]. In this section, testing to

Ring	$\Delta\theta$	Telescopes	Super Telescopes
2	3.6-5.0°	6	6
3	5.0-7.6°	6	6
4	8.0-10.8°	8	4
5	10.8-14.7°	8	4
6	15.3-20.9°	8	4
7	20.9-27.6°	8	4
8	28.6-35.8°	10	2
9	35.8-45.0°	10	2

Table 6.1: Ring number, θ range each ring covers, number of telescopes and number of supertelescopes present.

determine the thickness of the Si detectors and the channelling effects will be discussed.

6.2.1 Silicon Wafer Thickness Testing

Previous experiments [86], showed large discrepancies in the thickness uniformity of the Si detectors purchased from Micron [15]. Fortunately, in the previously mentioned experiment [86], the limited number of Si detectors and the resistive strip design allowed for fairly easy correction. The quad segment design of the NIMROD Si detectors and sheer number of detectors does not allow for an easily implementable correction.

The Si detector thickness uniformity is significant because of the Bethe-Bloch relationship discussed in Section 2.4. The relationship shows the energy loss in each Si detector is dependent on the thickness of the detector. To quantify the thickness uniformity tolerance, SRIM [87] calculations were performed to determine the thickness uniformity for a Si supertelescope. Results indicated that a ±1% thickness uniformity tolerance across the detector is needed to obtain the isotopic separation needed to identify isotopes of Ca.

Specifications for Micron included the ±1% thickness uniformity tolerance. To achieve this, a new polishing company was used. However, Micron does not have the means to measure the thickness at a specific point, and they typically report the thickness at either 5 or 9 points (each corner, the center and, if specified, the center of the edges). Three polished wafers of each thickness (140 μm, 300 μm and 500 μm) were send to the Cyclotron Institute to test the overall thickness uniformity using a mono-energetic beam. The 140 μm and 300 μm thick wafers were 4 inches in

diameter and the 500 μm thick wafers had 6 inch diameters. Each of the wafers had been polished, but not treated.

The experiment was performed at the end of the Momentum Achromat Recoil Separator (MARS) line using a 24.8 MeV ^{22}Ne beam from the K500 cyclotron. The motivation for running in the MARS line was to have a more well-defined beam energy. Each wafer was placed in front of a 5 cm $\times$ 5 cm, 1 mm thick resistive 16-strip Si detector. The energy and beam was chosen to ensure the incident particle punched through the wafer and stopped in the Si detector.

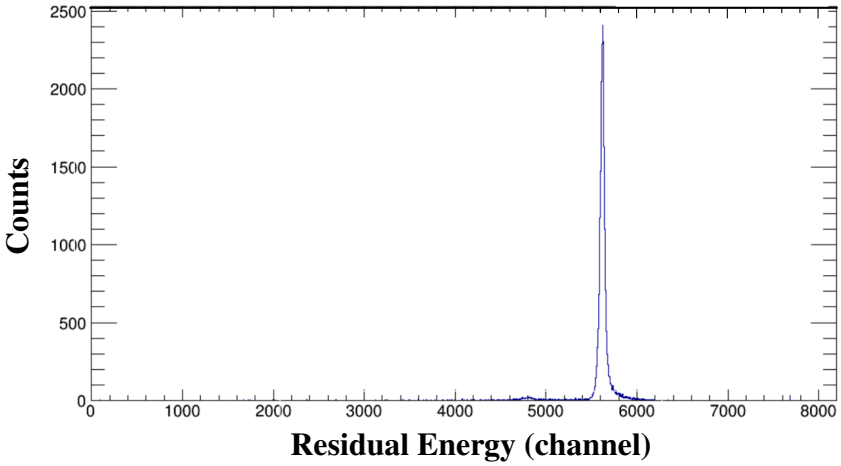

Figure 6.1: Mono-energetic energy beam in the 1 mm Si strip detector without a wafer present. The results show a large, narrow peak at approx. 5600 channels.

Initially, the beam was passed through MARS onto the 1 mm Si detector without a wafer present to verify the beam was mono-energetic and the uniformity across all strips. Figure 6.1 shows the results.

The results for the detector thickness were plotted in channels first, an example for which is shown in Figure 6.2. To convert from channels to energy, several degraders were placed upstream of the 1 mm Si detector. The list of degraders is seen in Table 6.2. LISE++ [88] was used to calculate the energy loss through each degrader.

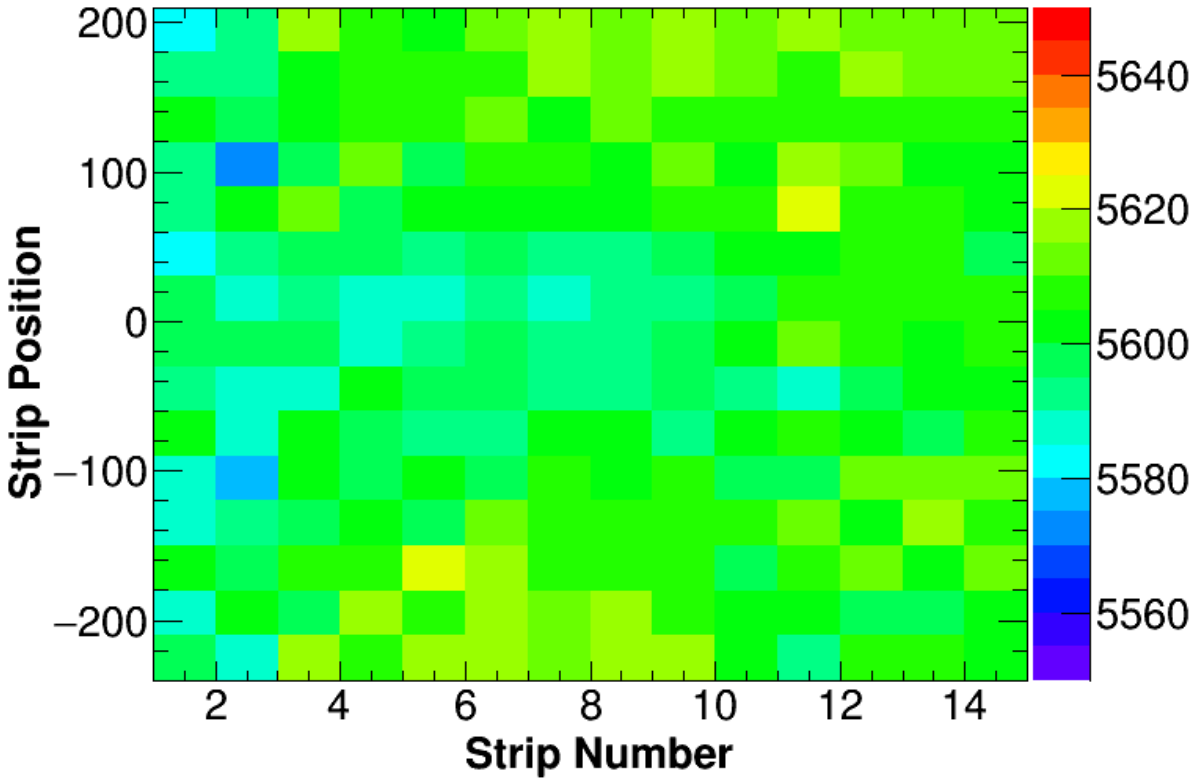

Figure 6.2: Thickness map for a 140µm thick wafer in channels. The x-axis corresponds to the strip the particle hit and the Y-axis corresponds to the resistive position on the strip.

A pulser was used to further calibrate the detector by testing the linearity of the shaper response. The pulser input was set to integer values between 1-9 V and every 0.1 V between 9 V and 10 V to more concretely test the linearity at the limits of the ADC. Figure 6.3a shows the peak location in channels for each pulser voltage. The right-hand panel (Figure 6.3b) shows the voltage to channel conversion. The results from the degraders were used to convert the channel number to the energy in MeV, and the pulser testing was used correct for the linearity. Figure 6.4 shows the same results seen in the pulser testing (Figure 6.3b), but converted from channel space to energy in MeV.

From there, LISE++ [88] was used to calculate the thickness that corresponds to the energy loss in the Si wafer. Figure 6.5 shows the final results for all wafers tested. Nine wafers were tested, however only the 8 with appreciable statistics are shown in Figures 6.5. The central section

Degrader	Energy (Channels)	Pulser Equivalent Voltage (V)	LISE++ Energy (MeV)
Carbon	7290	9.553	545.5
Thin Aluminum	7152	9.303	530.8
Thick Aluminum	4580	5.613	337.5
Nickel	4913	5.647	397.0

Table 6.2: List of degraders placed upstream of the silicon wafers in MARS. The degraders were used to calibrate the energy loss in the wafers. The thick Al target was not used for calibration purposes due to inconsistencies in the predicted and actual energy deposited.

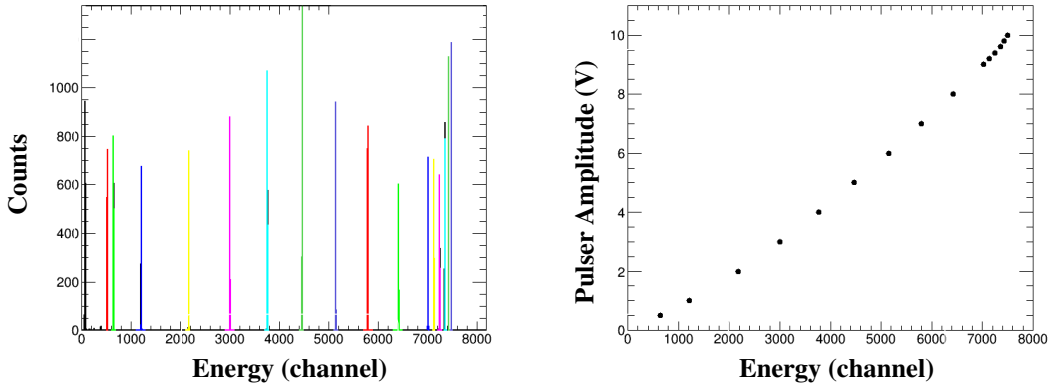

(a) Peak in channels for the pulser input ranging from 1-10V.

(b) Pulser voltage versus channel number

Figure 6.3: Results from the pulser used to examine the linearity of the silicon response. The left panel shows the peaks for every integer voltage between 1V to 9V and every 0.1V between 9V and 10V. The right panel shows the calibration for counts to energy in channel number.

of all the wafers fall within the ±1% tolerance. The edges on some of the detectors do not fall within this limit, but this is believed to be due to limited statistics.

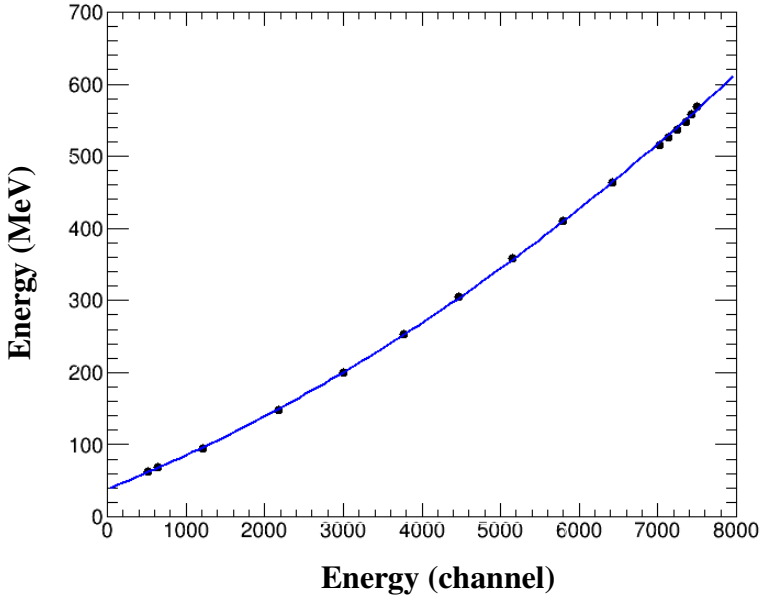

Figure 6.4: Calibration to convert channel number to energy in MeV. The values are the same data points as shown in the pulser testing calibration (Figure 6.3b). The pulser values have been converted to energy using the degrader calibration from Table 6.2.

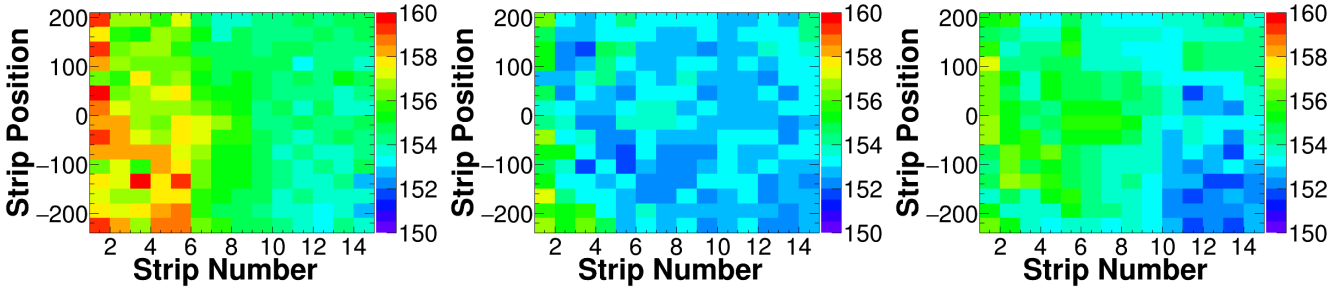

(a) Wafer 3327-1 (150 µm)

(b) Wafer 3327-2 (150 µm)

(c) Wafer 3327-3 (150 µm)

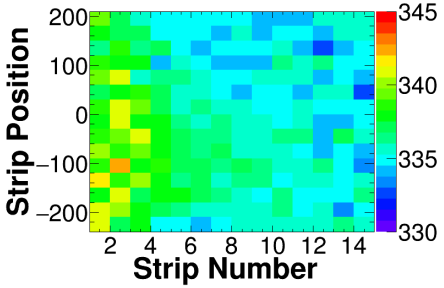

(d) Wafer 3328-1 (300 µm)

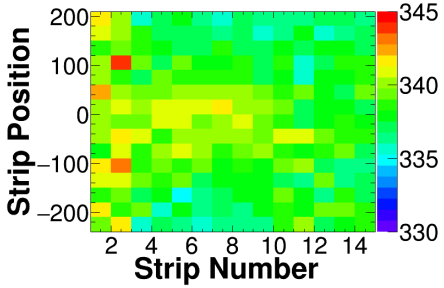

(e) Wafer 3328-2 (300 µm)

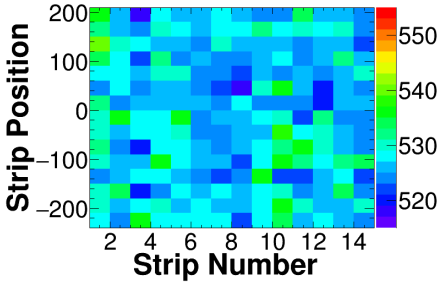

(f) Wafer 3264-19 (500 µm)

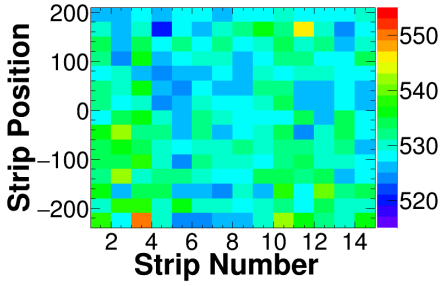

(g) Wafer 3264-20 (500 µm)

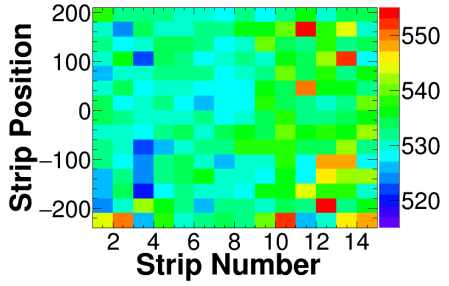

(h) Wafer 3293-21 (500 µm)

Figure 6.5: Thickness map for the 8 detectors tested.

6.2.2 Silicon Detector Channeling Testing

For the new Micron [15] Si detectors, when the energy deposited in the first Si detector was plotted against the energy deposited in the second Si detector, the elastic peak showed a long, narrow band along a line of constant energy above the elastic point (x~1700 channels, y~1800 channels) as shown in Figure 6.6. Several features of the detector can be contribute to this effect, mainly detector thickness uniformity issues as discussed in Section 6.2.1 and channeling effects.

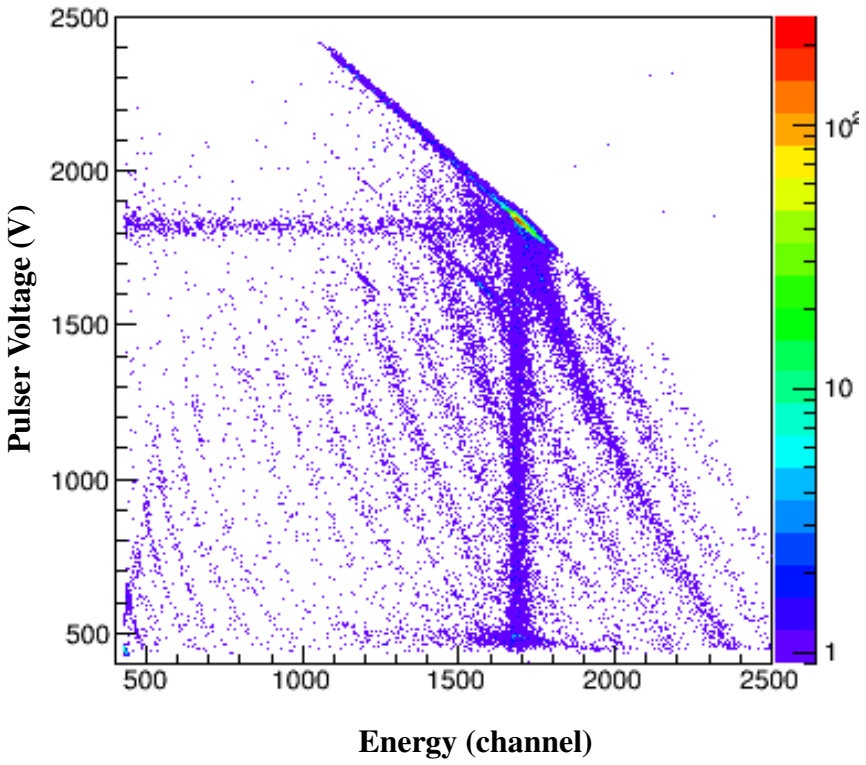

Figure 6.6: E vs. ΔE for a Ring 2/3 detector. The band at constant total energy above the elastic scattering point is consistent with channeling effects.

Channeling occurs in materials with symmetric atomic structures. In the case of silicon, the crystal structure of silicon is FCC, as shown in Figure 6.7 [14]. When an incident particle passes through the silicon at a small angle relative to a crystalline plane, the particle will scatter at small

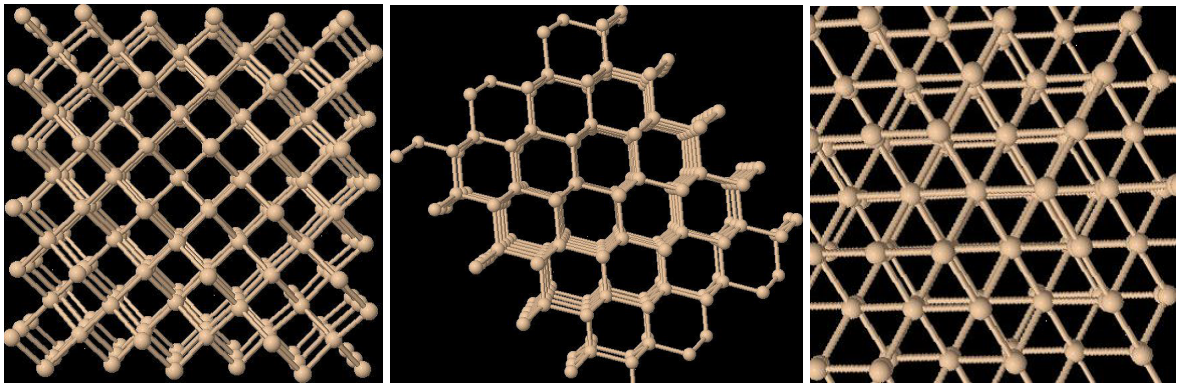

(a) 100 lattice structure (b) 110 lattice structure (c) 111 lattice structure

Figure 6.7: 100, 110 and 111 FCC lattice structures of silicon. Drawings taken from [14].

angles and be guided through an open crystal channel. Consequently, the number of interactions with electrons will be less, reducing the energy loss as a function of distance [63].

Signs of channeling exist when examining the silicon energy deposited in each detector in Figure 6.6. A hot spot is seen at (x∼1700, y∼1800) in channels corresponding to the elastic beam spot (^{40}Ar at 25 MeV/nucleon). If no channeling effects were present, only one small, narrow spot should be present. However, there is a long tail present at constant total energy (E+ΔE). The tail is only present for values of decreasing ΔE, which is consistent with channeling effects. The bands at constant *x*- and *y*-values correspond to incomplete charge collection.

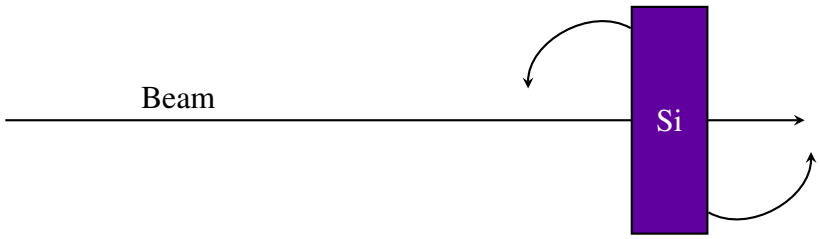

Figure 6.8: Schematic of how the Si detector was rotated relative to the beam.

To characterize the channeling effects present in the Si detectors purchased from Micron [15], one of the new 140 μm or 300 μm thick detector was placed in front of a 5 cm × 5 cm, 1 mm

thick position sensitive, 16-strip Si detector. The first Si detector was placed on a platform, which rotated the detector up-down relative to the beam axis, as demonstrated in Figure 6.8. A mono-energetic ^{22}Ne beam at 19 MeV/nuc was used in the K150 SEE line. The first detector acted as a transmittance detector and the second one as the residual energy detector. The test was performed for all new detectors, which consisted of 6 140 μm detectors in Ring 2/3, 6 300 μm detectors in Ring 2/3, and 2 140 μm ones in Ring 4/5 and Ring 6/7. The energy of the first detector was plotted in channel space and a Gaussian fit was applied. The full-width half-maximum (FWHM) sigma value from the fit was plotted in Figure 6.9. The 0° value starts at approx. 8% FWHM. As the angle increased, the width of the energy peak decreases until it reaches a minima at approx. 4% FWHM. For θ_H >5°, the width of the energy distribution increases again. The platform was only capable of being rotated up to θ_H=8°. The energy resolution values are higher than within the NIMROD experiment due to a lack of emphasis placed on fighting noise and the lack of optimization of the set up for energy resolution testing. The dependence of the energy resolution on the incident angle indicates channeling effects are present.

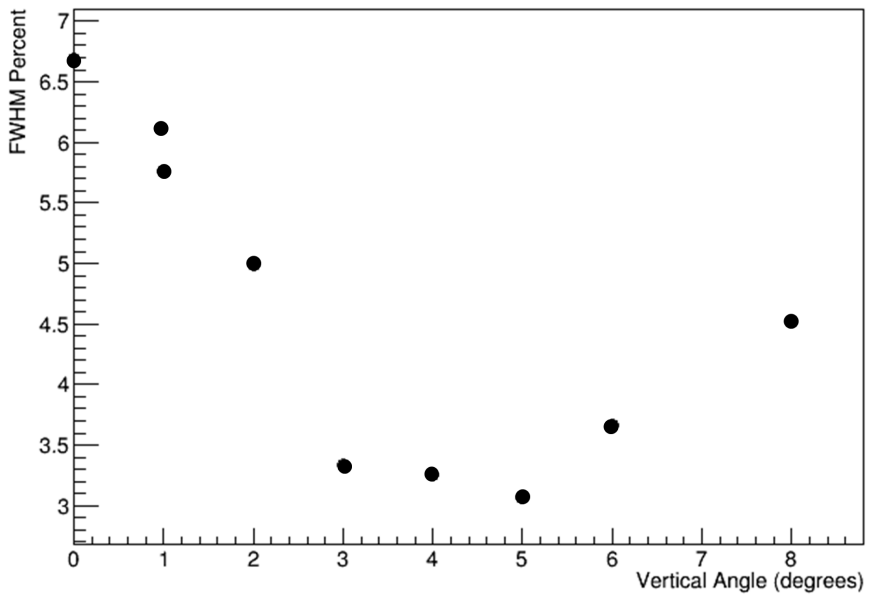

Figure 6.9: FWHM Energy resolution plotted as a function of rotation angle, θ_H. The energy resolution was minimized for 3° < θ_H <5°.

The trend shown in Figure 6.9 was consistent for all 10 new 140 μm and 6 new 300 μm detectors purchased. Results were not available for the 500 μm thick detectors because the energy of the beam particles was too low to punch through. The channeling should not have an effect on the energy resolution for the residual energy detector as long as the particle stops within the detector.

The same test was performed for the Eurisys Mesures [85] detectors. Results for the energy resolution showed a flat distribution at approx. 4% FWHM for all angles of rotation. The results indicate the energy resolution of the previously purchased detectors is independent of the incident angle within the angles tested, implying channeling effects are not present.

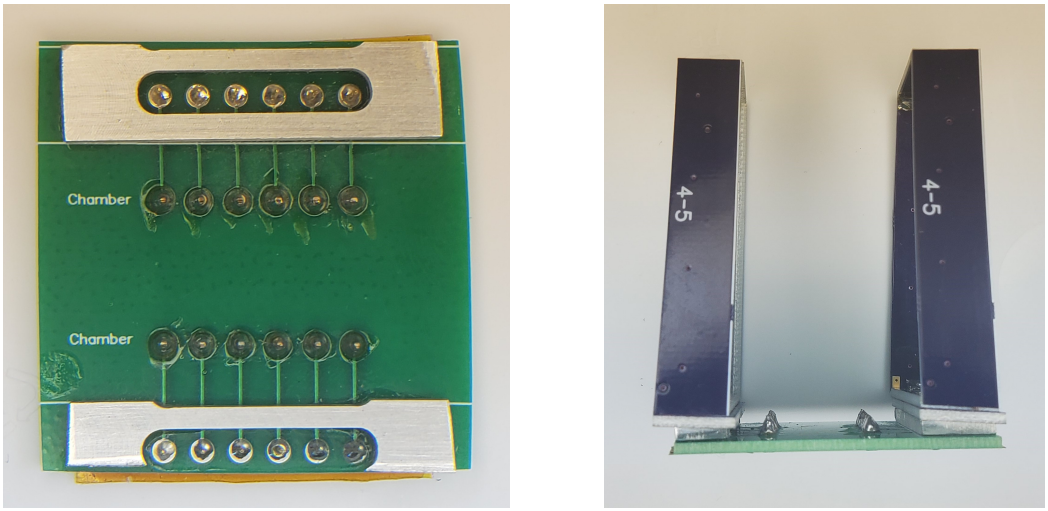

(a) (b)

Figure 6.10: Picture of the PCB tilters used to rotate the Si detectors purchased from Micron [15] by θ=4°. The left panel shows a bird's eye view of the tilter without Si detectors attached. The middle two sets of pins attach to the pins corresponding to the original position in NIMROD. The outer pins are where the new Si detectors are positioned and the metal bars are the tilting mechanism that was used to rotate the Si detectors. The right panel shows a side view of the tilters with Si detectors attached.

To minimize the effects of the channeling for the newly purchased detectors, circuit board connectors were designed to rotate the first and second Si detector by 4°. Figure 6.10a shows the "tilters" and Figure 6.10b shows the tilters with Si frames placed on them. The tilters are designed to be placed on the original pins holding the Si detectors. The location of the new supertelescope detectors is forward of the original position for the first, thinner Si detector and behind for the

second Si detector. The tilters for the telescopes were designed to hold the Si detector between the original two sets of pins. Because the modules are at a slight angle relative to the target, the forward Si does not perfectly fit in the first position. Therefore, the tilters were designed to be slightly offset to maximize the angular coverage of the supertelescopes.

Results from the implementation of the tilters and AC coupling the signals restored a large amount of isotopic resolution, and will be further discussed in Section 6.4.

6.3 New Electronics Configuration

The objective of the electronic modules within the NIMROD array was to convert the analog signals from the detectors (silicon, Cesium Iodide and neutron ball) to digital signals. The digital signals were collected by the data acquisition software (DAQ). Substantial changes have been made to the electronics configuration. The changes include new modules and a new electronic trigger. The new electronic diagrams are shown in Figures 6.12-6.19. The trigger for this experiment was the back-plane of the silicons in Ring 2-9. A short description and abbreviations of all the modules is shown in Figure 6.3.

One significant difference is the omission of Indiana Silicon Sphere. Previous experiments [65, 10, 34] have found very low multiplicities of particles detected in the Indiana Silicon Sphere. The particles detected have low charges (Z=1-2), which is not of essential importance for the original objective of the proposed studies.

For the silicon detectors, two different electronic configurations were used. The diagrams for the Ring 2-9 Si fronts and the Ring 10-11 Si were seen in the top half of Figure 6.12. The diagram for the Ring 2-9 backs was in the bottom half of Figure 6.12. For Ring 2-9, custom motherboards were designed to fit directly outside the chamber for signal collection. The motherboards functioned to hold the Zeptosystem preamps [60], provide ±12 V, and provide bias to each detector. The 1.8 mV/MeV gain preamps were used in for the 300 μm and 500 μm Si detectors. 5 mV/MeV gain preamps were used for the 150 μm thick detectors. Additionally, new motherboards were designed to collect the signals for Ring 10-11, and the Ring 12-15 Si and PDs. The new boards can be seen in Figure 6.11 (a) and Figure 6.11 (b), respectively. The Ring 10-11 motherboards housed 7.5 mV/MeV preamps, while the Ring 12-15 motherboards had 15 mV/MeV preamps for the Si signals and 45 mV/MeV preamps for the CsI PD signals.

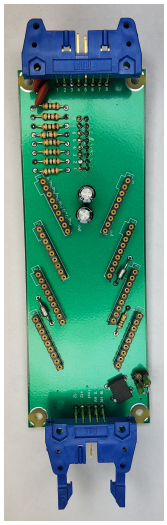

(a) Ring 10/11 Motherboard

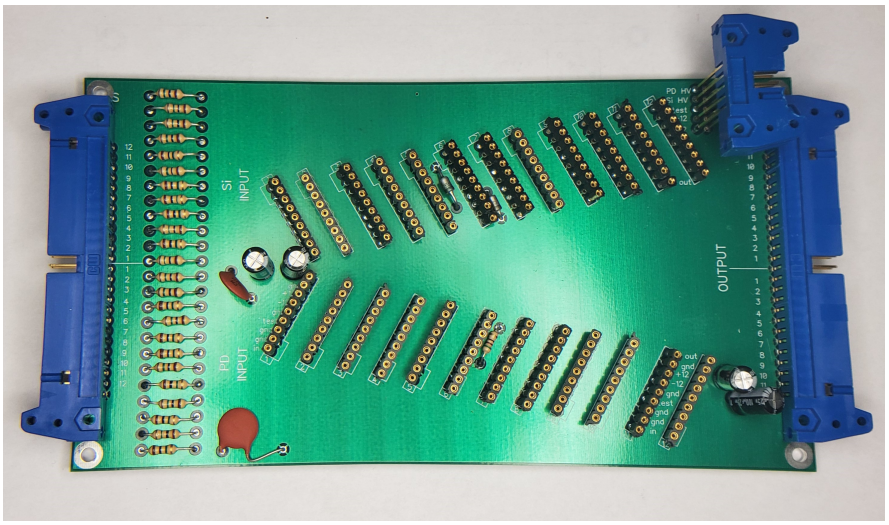

(b) Indiana Si Sphere Motherboard

Figure 6.11: Picture of the motherboards for collecting signals from Ring 10/11 Si signals (left) and Indiana Silicon Sphere Si and PD signals (right).

Module Name	Abbrev.	Function	Examples
Leading Edge Discriminator	LED	Creates a logic signal after a signal crosses thresholds	LeCroy 623B
Constant Fraction Discriminator	CFD	Creates a logic signal when a signal reaches a constant fraction of its peak	EG&G CF8000 CAEN 812
Peak-Sensing Analog to Digital Converter	PS-ADC	Converts the peak of an analog signal to a digital signal	CAEN 785
Charge to Digital Converter	QDC	Integrates the current and converts to a digital signal	CAEN 965
Waveform Digitizers ("Flash" Analog to Digital Converters)	FADC	Takes in the waveform and allows for integration and triggering of the signal	SIS 3316
Fast Amplifier	FA	Amplifies a signal with a short rise and fall time	Phillips 777
Shaping Amplifier	-	Integrates, amplifies and shapes a signal from the preamp	CAEN N1068
Timing Fast Amplifier	TFA	Amplifies the fast component of a signal used for timing purposes	Tennelec TC 248
Charge-Sensitive Pre-Amplifier	preamp	Integrates and amplifies the charge from a detector	Zeptosystems Pre-Amplifier
Signal digitizer	XLM	Convert multiplexed analog signals to digital	XLMXXV
Logic Fan In Fan Out	FI/FO	Creates a logic signal from one or more inputs	LeCroy 429A CAEN N454
Linear Fan In Fan Out	FI/FO	Makes a linear sum of all signals	LeCroy 428F

Table 6.3: List of common electronic modules, abbreviations, functions and examples modules used in the experiment

Module Name	Abbrev.	Function	Examples
Dual 4-Fold Logic Unit	FLU	Creates a logic signal when selected requirements are met	LeCroy 365AL
Coincidence	-	Creates a logic signal when selected signals come in coincidence	Phillips 756
Bit Register	-	Registers a bit corresponding to with trigger fired	CAEN 259
Gate Generator	-	Makes a logic signal of changeable width	LeCroy 222 Phillips 794
Scaler	-	Counts number of signals registered	SIS 3820
Prescaler (Divider)	-	Allows for triggering from multiple sources and divides the trigger based on set values	SIS 3802

Table 6.3: Continued

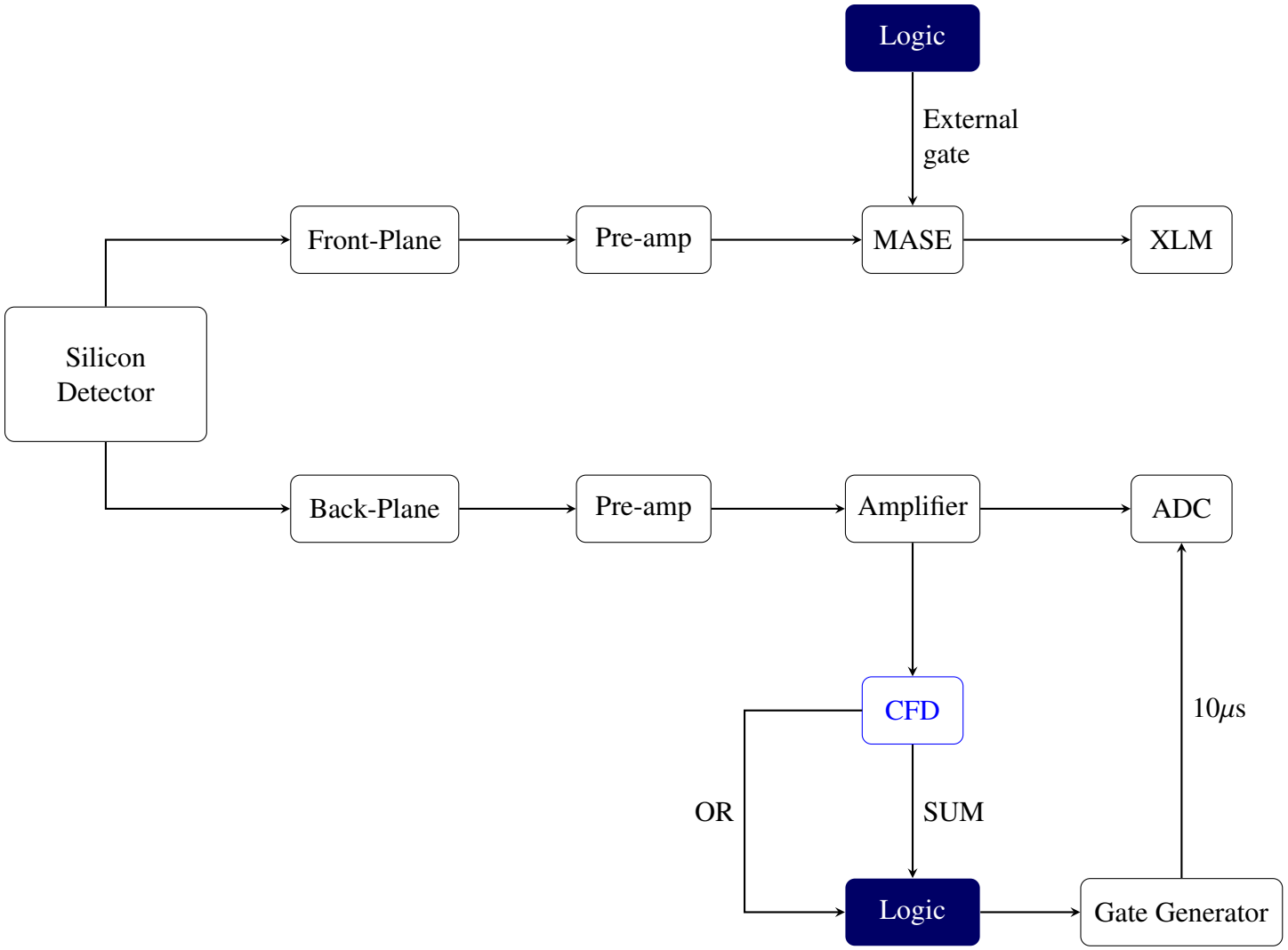

Figure 6.12: Electronics diagram for the front-panel (top) and back-panel (bottom) of Si detectors for Ring 2-11 and Ring 2-9, respectively.

All detectors were biased using the Wiener MPod Voltage Supply modules [89], which differs from the previous configuration. The Wiener MPod was implemented for biasing Si detectors in the Fall 2009 and one CsI module was implemented in Spring 2010. The current experimental campaign implemented the remaining modules to bias all detectors with only the Wiener MPod. The ±12V power supply for the Ring 2-11 preamps was supplied using a Topward Dual-Channel DC Voltage Supply, which was consistent with the previous configuration. The Si front-plane signals were collected with the Multiplexed Analog Shaping Electronics (MASE) [16], allowing signal processing of the analog signals and multiplexing the digital output, reducing the number of electronics required. MASE replaces the CAMAC Pico systems [61] Shaping Amplifiers and CAMAC Phillips peak sensing ADCs previously used.

On a basic level, MASE has three build-in modular functions per channelboard: a shaping amplifier, a LED and an ADC. The electronics diagram for a single signal firing in MASE can be seen in Figure 6.13. For an input signal coming from a preamp, the signal was first amplified with a shaping time of 1.1 μs and a >1kΩ impedance. The shaped signal can be seen in Figure 6.14 (a). The input signal can be amplified using both the high and low gain setting, however in this experiment only the low gain settings were used. The low gain settings cover an amplification factor of approx. 0.4-7 times the input signal amplitude.

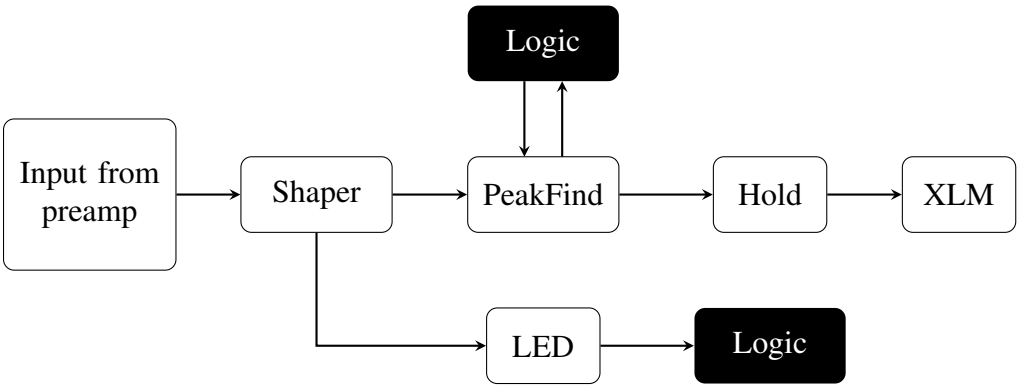

Figure 6.13: Electronics diagram for a single channel of MASE firing as shown in Ref. [16]. See the main text for a discussion.

The bipolar output signal was split with one path going to the LED and the other to the analog

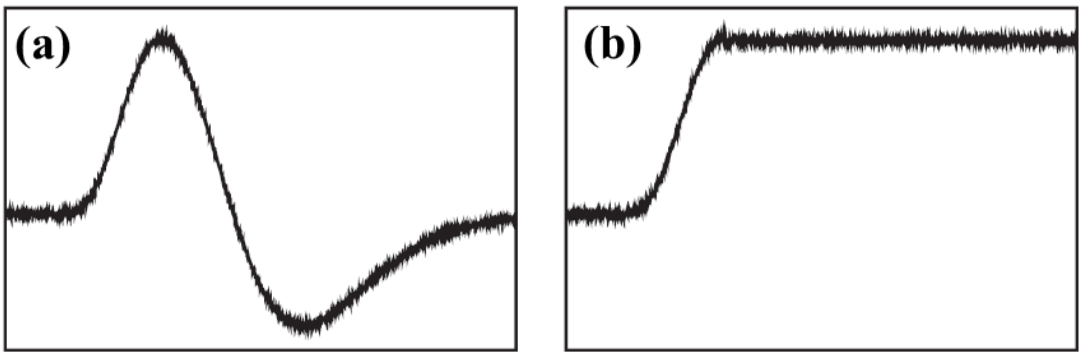

Figure 6.14: Panel (a) shows the shaped MASE signal from a pre-amp with a 1.1 μs shaping time. Panel (b) shows the held signals. The held signal for each channel gets converted to a voltage, collected and send to the XLM via a train. The small notch corresponds to the start of the holding circuitry. Reprinted with permission from Ref. [16].

peak finding circuit (Peak Finder). If the signal passes the LED threshold, a logic signal was created. The first logic signal opens up the "threshold time out" window, which corresponds to the time allocated for other signals to fire the discriminator. Only a signal that crosses the threshold within the threshold time out window opens its corresponding peak finding circuit. An example of this can be seen in Figure 6.15. Signal 1 from the first channel starts the threshold time out window (yellow), since it was the first signal to cross the set threshold. The timing corresponding to when signal 2 reaches the set threshold was within the window and that signal will be analyzed. However, signal 3 does not fall within this window, therefore it will not be analyzed.

One downside to the MASE configuration is each channelboard operates independently. As a result, the threshold timeout value for each channelboard is set by the first signal received in each channelboard, regardless of what event it came in. For example, an event can generate 3 particles that are detected in three separate silicon detectors on three different channelboards. Each channelboard would open up the threshold timeout window as soon as the LED threshold is crossed. If a second event came within the next few milliseconds generating four signals on four other channelboards, the threshold timeout window would be opened on each corresponding channelboard for the second event. This can lead to misidentification of the events. To avoid this issue, an external trigger was used. The external trigger, which is generated from the silicon backs and will be discussed shortly, is inputted to each channelboard via the controller board. The external trigger acts as the start for the threshold timeout window.

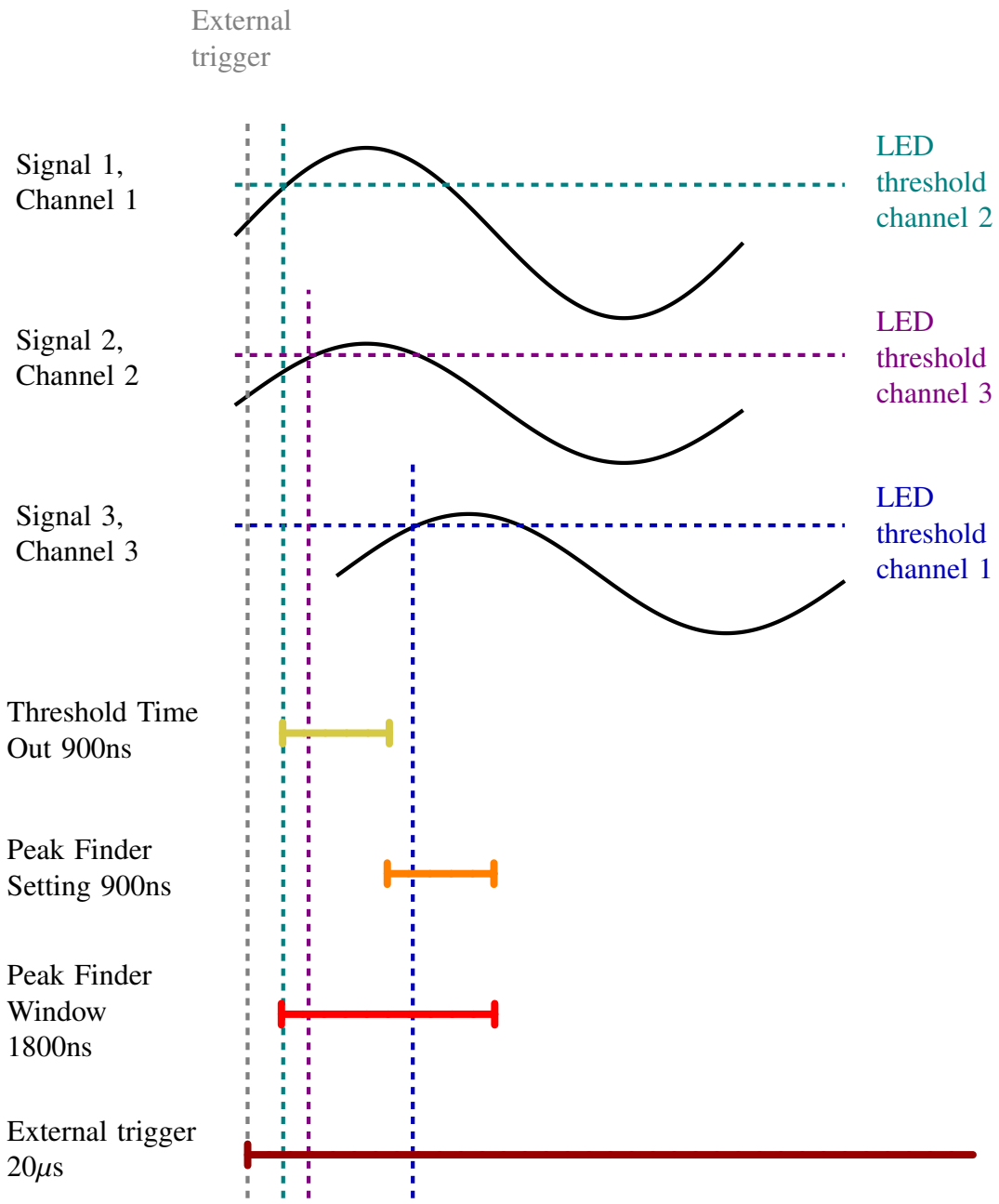

Figure 6.15: Schematic of how the trigger and peak finding setting work within MASE. The grey line corresponds to the external trigger generated from the Si back. The teal line represents the value where the first signal surpasses the LED threshold. The purple and blue lines correspond to the LED threshold value for the 2nd and 3rd signals, respectively. The yellow, orange and red lines correspond to the various threshold settings (labeled accordingly on the left) in MASE.

The first logic signal also opens up the peak finder window. The peak finder window corresponds to the sum of the threshold time out and the peak finder settings. The peak finder works

similarly to a PS-ADC. The maximum value within the peak finder window was stored and held, as long as the signal overturns. In other words, if the peak was still rising when the peak finder window ends, the maximum value will not be held, and a null value will be returned. The held signal, seen in Figure 6.14, was within a few millivolts of the shaped signal. The held signals were supplied to a 32-channel multiplexer (16 high gain and 16 low gain channels).

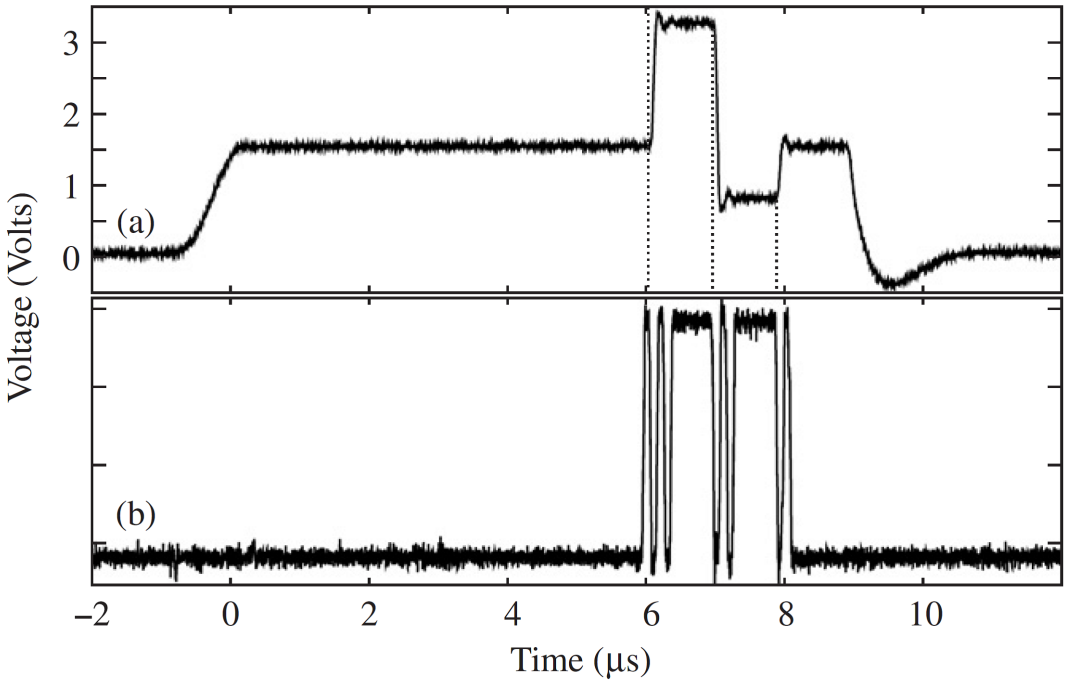

Figure 6.16: Panel (a) shows the multiplexed analog energy signal train in voltage sent to the XLM for analysis. Panel (b) shows the change in voltage from the XLM indicating the signal has been received indicating the "hand-shaking" in the readout. Reprinted with permission from Ref. [16].

MASE has the capability to provide a timing and energy signal, however only the energy signal was analyzed in this experiment. MASE does not have the capabilities to be directly read into the data acquisition (DAQ) system. The read-out was done through the XLMXXV VME module [90], which acts as a hand-shaking module. The signals were converted to three output pulse trains. The address was read first through a low voltage differential signaling (LVDS) cable. The energy and timing were each read-out, respectively, through a dual-pin lemo connector. Each train was equal

in length and has a 1.5 μs offset governed by the 1.1 μs shaping time. An example of the energy pulse train was shown in Figure 6.16.

Results from MASE testing, and comparison between the previous configuration and current one will be discussed in the next two subsections (Subsection 6.3.1 and 6.3.2).

The back-plane signals for Ring 2-9 were collected using the CAEN Shaping Amplifiers. The gains were adjusted on the shaping amplifiers and the shaping time was set to the 3 μs setting. Two of the CAEN shaping amplifiers were configured so the fast amplification output was opposite in polarity from the slow amplification. For the other two modules, linear inverters were used to flip the polarity of the fast output of the signals. The slow amplified signals was converted to digital signals using CAEN peak-sensing ADCs. The fast amplified signal was sent to the CAEN CFDs, which provide both an OR and SUM signal for triggering.

The Ring 2-11 CsI PMT detectors were biased through upgraded bases. The bases were designed to distribute the correct voltage to each dynode of the PMT. The new active-component bases were designed in 2011 and tested in 2012. The active-base configuration allows for control of the current flow. As a result, the voltage is more stable and the gain drift is lower. In order to reduce the gain drifts, the previous passive bases were run at a high current of approx. 1-2mA. The active base design decreased the current to approx. 230 μA. The active bases were tested in 2012 and results concluded the active bases were at least as effective at biasing the CsI PMTs. A bonus feature was the reduction in heat production, which helped keep the temperature of the electronics within the neutron ball lower, reducing the gain drifts from the preamps.

For the CsI PMT detectors in Ring 2-11, the signals were collected using the SIS 3316 waveform digitizers (FADC). The FADCs reduced the number of electronic components from six to one. The electronics diagram was seen in Figure 6.17.

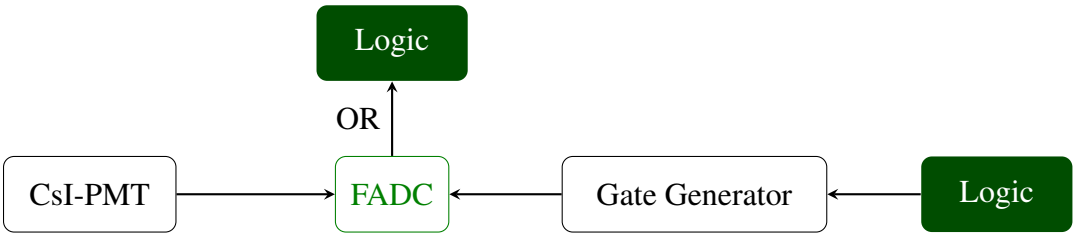

Figure 6.17: Electronics diagram for Ring 2-11 CsI detectors.

First, the trigger settings were set to enable all signals have the same start. Figure 6.18 shows a diagram of the internal triggering. The discriminator works by setting the "peak" and "gap" times, so that the modified signal was trapezoidal in shape. A "moving average" (MA) or a discreet gate was opened up as the peak comes in. The average of the MA was plotted as the gate moves across the signal (Figure 6.18 (b)). The length of the MA was the "peak" time and was proportional to the rise time of the signal. The peak time was set to 5, which corresponds to 20 ns. The MA was duplicated and delayed. The delay between the peak of the MA and the start of the delayed MA was the "gap" time (Figure 6.18 (c)). The gap value was adjusted until the peak start jitter was within the 4 ns timing resolution of the FADC. The gap time was set to 60 or 240 ns. The delay MA was subtracted to the original MA to produce the final moving average window, which was mostly trapezoidal in shape (Figure 6.18 (d)). A logic signal was generated when the MAW falls below 50% of the maximum value. This configuration was consistent with the zero crossing from a CFD, allowing for triggering independent of input signal amplitude.

Accumulators were set to allow for fast and slow components of the CsI signals to be collected. The first accumulator was set to be 400 ns wide, extending from the start of the signal rise to include past the peak encapsulating the fast component. A 1 μs wide accumulator gate starting 1 μs after the signal start was implemented to collect the slow component. Unlike the previous configuration, the FADC can be configured up to collect up to 8 accumulator settings. The 400 ns and 1 μs gates were chosen to maximize the isotopic resolution from pulse-shape discrimination [11].

The FADC does not have a fast clear. As a result, even though each module was vetoed by the computer busy, the module stores up events until the computer logic opens up again. Uncorrelated events were all taken in without an unique timestamp, making event matching impossible. To avoid this, a 400 ns gate generated from the trigger logic start was send to each FADC. The length was set based on the difference between the start of the trigger and the trigger out from the FADC. Only events within the 400 ns window were stored.

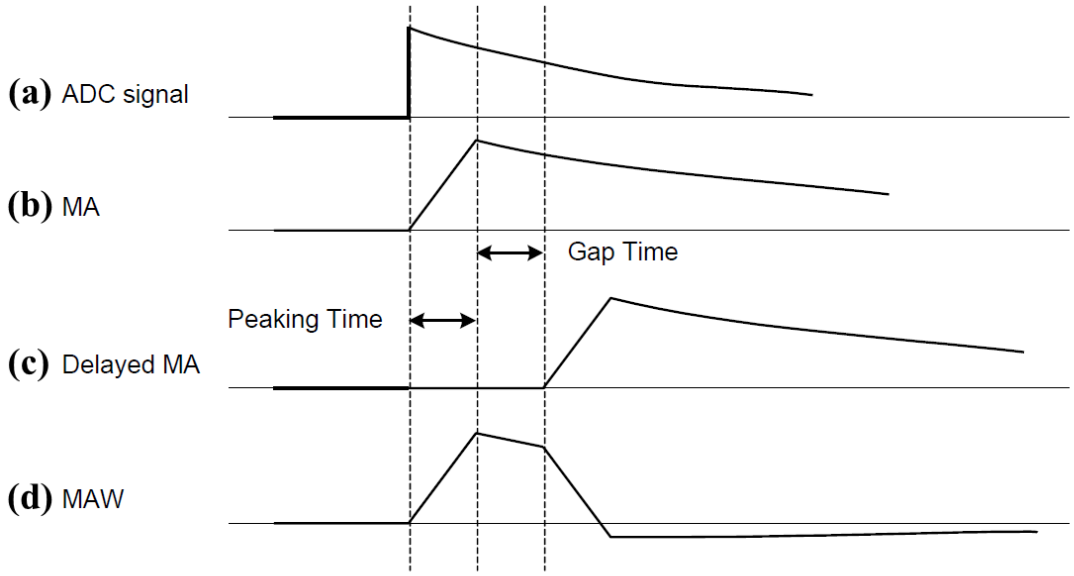

Figure 6.18: Schematic showing the trigger logic for the SIS3316. Panel (a) shows the input signal from the CsI. Panel (b) shows the transformed signal after it has been averaged over the moving average was set. The moving average is set by the peak time parameter. Panel (c) is the delayed signal, which is determined by the combination of the peak and gap time. Finally, panel (d) shows the final signal after the delayed MA (panel c) is subtracted from the MA (panel b). The trigger logic signal is produced when the transformed signal drops to 50% of the maximum. Reprinted from Ref. [17].

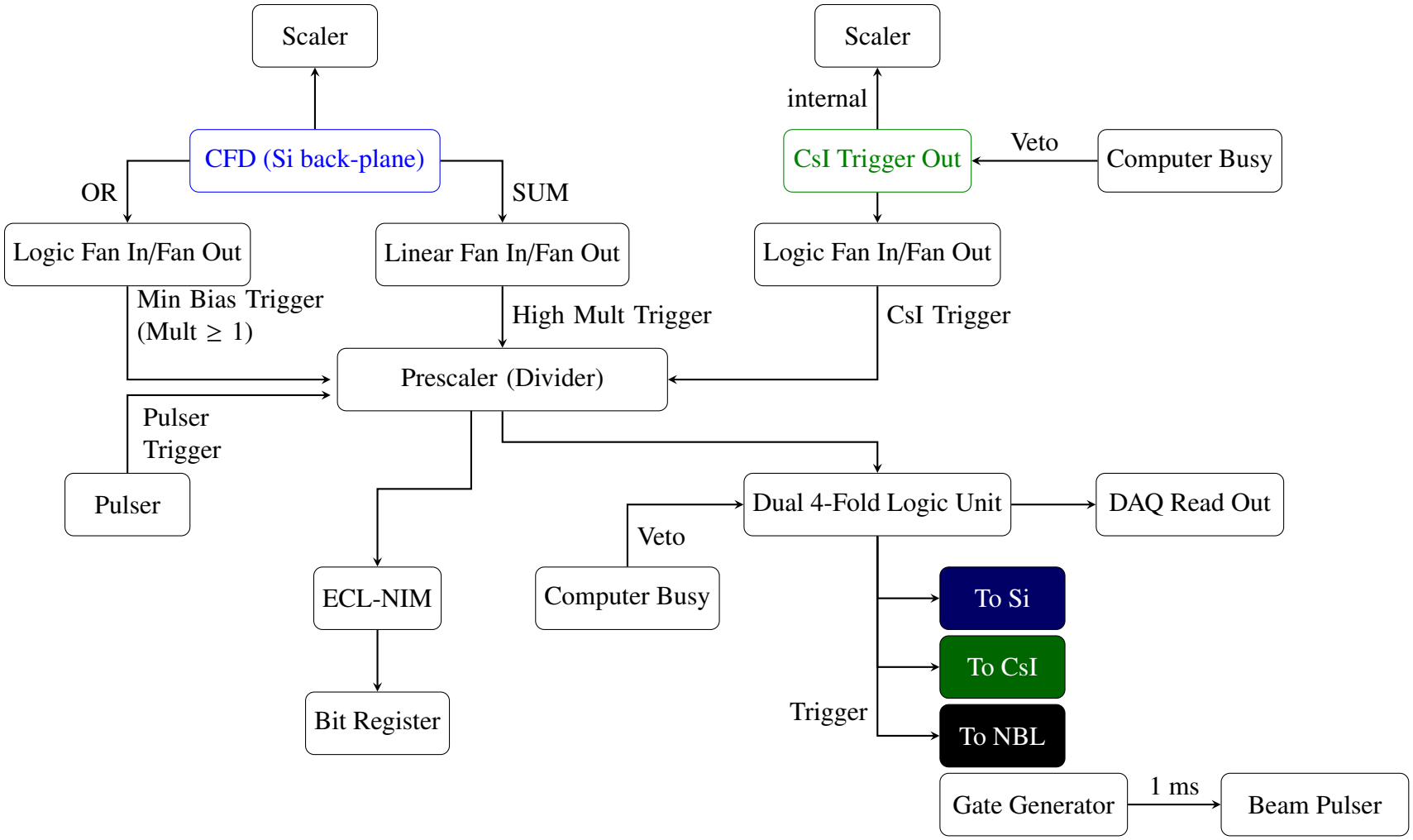

Figure 6.19: Electronics diagram for the logic. The trigger start are indicated in the colored outlined boxes. The trigger signals from the other electronics diagrams are shown in the colored boxes.

Each of the above electronics diagrams (Figures 6.12- 6.19) has a common requirement of a trigger signal, including the neutron ball which will be discussed in Section 6.5.4. The electronic diagram for the trigger logic is shown in Figure 6.19. The triggering of events was provided by the Si back-plane signals from Ring 2-9. VME CFDs were used to produce SUM and OR logic signals above threshold.

Four different event types were collected: minimum bias, high multiplicity, CsI and pulser events. A minimum bias trigger means an event was collected when at least one Si back triggered. These events were independent of multiplicity and should be triangular in impact parameter distribution. The min bias was achieved by taking the OR of each CFD and combining them into a logic FI/FO. A high multiplicity trigger means a multiplicity of at least 2 was implemented. The multiplicity only included the first Si detectors and not the second Si detectors from the supertelescope configuration. The SUM output from each CFD was added in a linear FI/FO module. The output of the linear FI/FO was amplified using a timing fast amplifier and passed through a LED. The threshold of the LED was set to only give a logic signal when at least two Si back-plane fired. The CsI trigger corresponds to at least one CsI firing. For each FADC module, a "trigger out" logic signal was generated when a CsI fires. Each trigger out was combined in a logic FI/FO. The last event trigger was the pulser trigger, which was used to trigger non-beam events. The pulser trigger can be used to examine the background of the neutron ball and to help characterize potential electronic gain drifts.

Each event trigger was send to a different channel in the prescaler VME module. The prescaler module allows one to choose which trigger can be incorporated and to scale down each trigger. The min bias trigger was downscaled by 10 and the pulser trigger was downscaled by 100. The pulser trigger came in at about a rate of 1 event/sec. Therefore, only every tenth minimum bias or 100th pulser event was accepted. All high multiplicity events were accepted. The CsI trigger was not used in the main experiment, however it was incorporated for diagnostic purposes. The output logic signal of the prescaler was sent to a dual 4-fold logic unit, which sends a trigger to the computer. Unfortunately, the trigger module does not have a means to track which event fired the DAQ. In order to know which event fired the DAQ, the signals were passed through a ECL-NIM converter and the output was sent to a bit register.

The dual 4-fold logic unit was chosen to trigger the computer, or Data Aquisition (DAQ), due

to its abilities to be vetoed. The logic signal from the prescaler was inputted into the top module. The output of the top module was sent to the bottom module and to a scaler. The scaler was used to measure the "raw" data rate. The bottom module was vetoed using the computer busy. The dead time was on the order of 3ms. The output from the bottom module was used to start the DAQ and to measure the "live" data rate with the scaler. Hence, events were only triggered if the computer was not busy.

The trigger signal starts the CsI, Si and neutron ball electronics, as shown in Figure 6.12-6.19. The trigger signal was used to generate an external trigger for MASE and an external gate for starting the FADCs, ADCs and scalers. A gate was also generated from the trigger signal and sent to the DAQ to start read in the XLM, FADC, ADC and scaler modules. Lastly, the trigger was used to stop the beam from the cyclotron utilizing the beam pulser. Turning off the beam minimizes the background in the neutron ball. However, the beam turns off approx. 50 μs after the trigger was sent.

Finally, a SIS3802 was used to read out the trigger from each individual CFD channel corresponding to the front Si detectors in Ring 2-9. The internal scalers in the FADCs was implemented to monitor the CsI hit rate.

6.3.1 Comparing Configurations: MASE Vs. Picoshapers

In the previous NIMROD campaigns, silicon front and back signals were collected using picoshapers [61] from Washington Univeristy in St. Louis. Picoshapers are ideal modules to use for arrays consisting of hundreds of channels of electronics. Each picoshaper has 16 channel inputs and up to 21 picoshapers can fit into each CAMAC crate. The CAMAC crate provides the power to the modules and interfaces between the modules and the computer via a controller. However, the picoshapers are no longer a feasible solution. With the increase in channels from the new Si detectors implemented into NIMROD, the number of channels needed has exceeded the number of available picoshaper channels. In addition, both the picoshapers and the CAMAC crates are no longer in production.

MASE has been implemented to overcome some of the above mentioned obstacles. Each MASE board also has 16 channels. However each crate only holds 16 boards, for a total of 256 channels. For the proposed configuration, 228 channels of Si front electronics were required (or

15 boards).

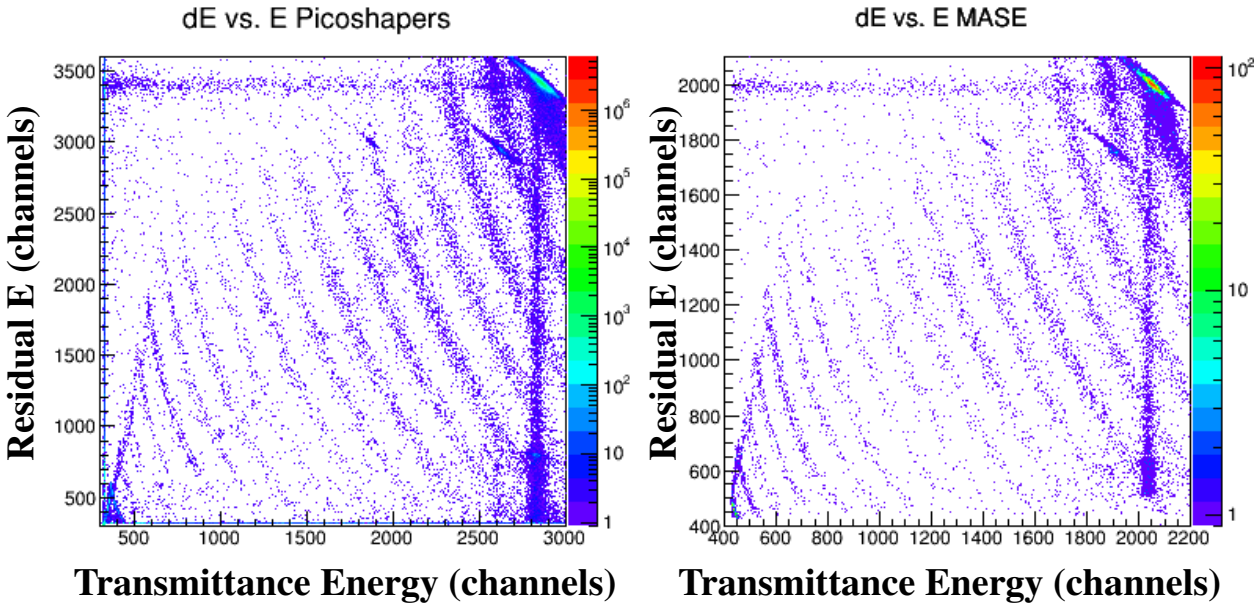

Figure 6.20: Residual energy versus transmittance energy in a Si supertelescope from Ring 4/5. The data in the left-hand panel was taken using the Picoshapers, which are the shapers used in the previous NIMROD campaigns. Data taken with the new shapers used (MASE) is in the right-hand panel.

During a May 2019 test experiment, signals from the Si detectors in a Ring 4/5 super-telescope were compared. The signals for two sets of boards (32 channels) were taken in using the Picoshapers for several hours. The input was changed over to MASE and the test was repeated. Figure 6.20 shows a side by side comparison of the two modules. The left panel shows the Picoshaper results and the right one shows the MASE results. The triggering for the Picoshapers came from the MASE OR, since all but 32 channels of signals were still being taken in using MASE. For the MASE signals, the internal trigger was implemented.

The results indicate MASE is performing comparably to the Picoshaper configuration. However, due to the lack of isotopic resolution present in the results, definitive results for the resolution are not available.

6.3.2 MASE Testing

Although MASE was designed and implemented into experiments starting in 2005, the extent of the implementation was smaller than the current application within NIMROD. In addition, several modifications had been made to the FPGA code to make the interface more user-friendly. While these modifications had been tested on a small scale, multi-event testing was limited. Several tests had been performed to access the capabilities of MASE. Specifically, the testing involved determining external versus internal triggering, and what the functions and settings of the threshold timeout and peak finder were.

In initial testing, the internal trigger from MASE was used to trigger the data acquisition (DAQ). However, when the Si signals were plotted against either other, results showed a "haze" on the left side of the punch-through line as shown in the left-hand panel of Figure 6.21. In discussion with S. Hudan [91], the triggering for MASE was noted to be independent for each channelboard. As a result, the OR signal used to trigger the DAQ came from the first signal on the first channelboard that fired. Because the dead time from the DAQ is several milliseconds long, another event can occur during this time triggering another channelboard. Since MASE cannot be vetoed, the event will be send to the XLMXVV to be read causing event mixing. An external trigger originating from the Si back signals was implemented. The external triggering mode in MASE prevented an OR signal from being produced for self-triggering purposes. The results from the external trigger are shown on the right-hand panel of Figure 6.21. The "haze" left of the punch-through line was significantly minimized as well as the noise between the lines.

As discussed in Section 6.3, MASE has a set shaping time of 1.1 μs. However, the setting used to hold the shaped signals, which allows the signals to be converted to a digital signal, are adjustable. These parameters are the "threshold out" (TO) gate and the "peak finder" (PF) gate. The TO gate is defined as the time after either the first signal triggers each board in internal triggering mode or the external trigger starts the gate. The PF gate is the time allotted for the shaped peak to be found and held. Only peaks that have reached their global maxima are held and hence read out through the XLMXXV.

Initially, the peak finding gate was believed to start right after the TO gate. Therefore, if the TO was set to a value greater than zero and the PF was set to zero, no data should be read into the

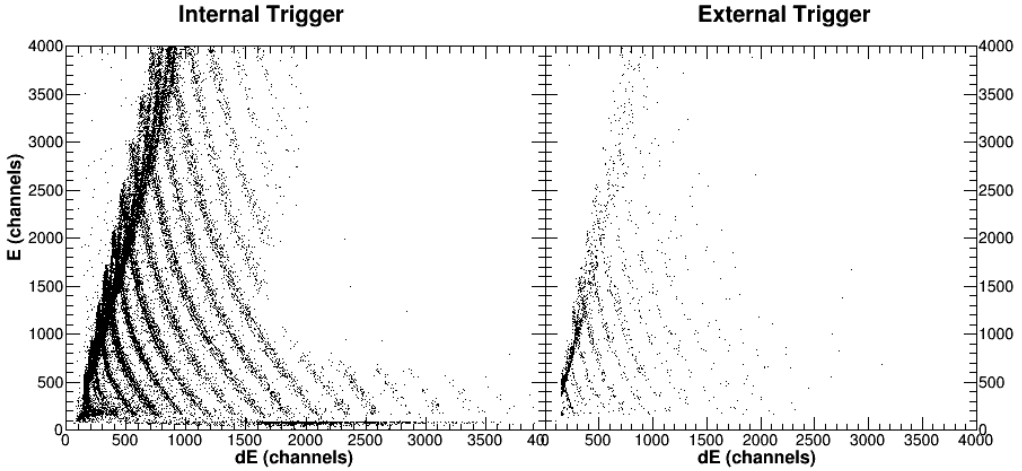

Figure 6.21: Residual energy versus transmittance energy in a Si supertelescope from Ring 4/5. The data in the left-hand panel was triggered using an internal trigger and the data in the right-hand panel was triggered using an external trigger. The internal trigger showed a larger amount of data missing for larger charged particles.

DAQ. However, when this simple test was performed, data results came into the DAQ. When the same test was performed for TO = 0 ns and PF > 0 ns, no signals were seen in the DAQ. These simple tests indicate that the TO is independent of the PF and does correspond to the window for the triggers from adjacent signals to be analyzed.

It was also noted that for a small TO value (TO < 900 ns) and a zero PF value, the right portion of the Si vs. Si spectrum was cut off similar to the left panel of Figure 6.21. The extent to which the right side was cut off was proportional to the LED values. This phenomenon is due to the LED feature within MASE. Since the signal is proportional to the mass and charge of the incident particle, a smaller particle (for example an alpha particle) will reach the threshold value closer in time to the shaped signal peak than larger particles. In addition, the signal from the second Si detector is more likely to fall within the time window allotted to analyze the signal. The results further indicate that the peak finding window is dependent on the TO setting.

Lastly, to show the peak finding window is dependent on the TO setting, the values for the TO and PF were changed while keeping the TO + PF constant and greater than the shaping time of 1.1 μs. Results showed that, as long as the TO setting was long enough to allow the trigger from the second Si detector to fall within the triggering window, all the signals were shaped and held. The

same test was performed for a constant TO + PF value smaller than the 1.1 μs shaping time. The same portion of the Si vs. Si spectrum was filled each time. If the PF setting was independent of the TO setting, only a small portion of the Si vs. Si spectrum should be filled for small TO values. However, since the same portion of the Si vs. Si spectrum was filled each time, the conclusion was reached the peak finding window was equal to the sum of the PF setting and the TO setting.

6.4 Particle Identification

Details regarding the use of the ΔE-E method for analyzing CsI and Si detector signal was discussed in Section 2.6. To avoid repeating the same information, this section will focus on showing examples of the particle identification (PID), the linearization results, and a short comparison and discussion of the results to previous data.

6.4.1 CsI Slow Versus Fast, CsI Versus Si and Si Versus Si Results

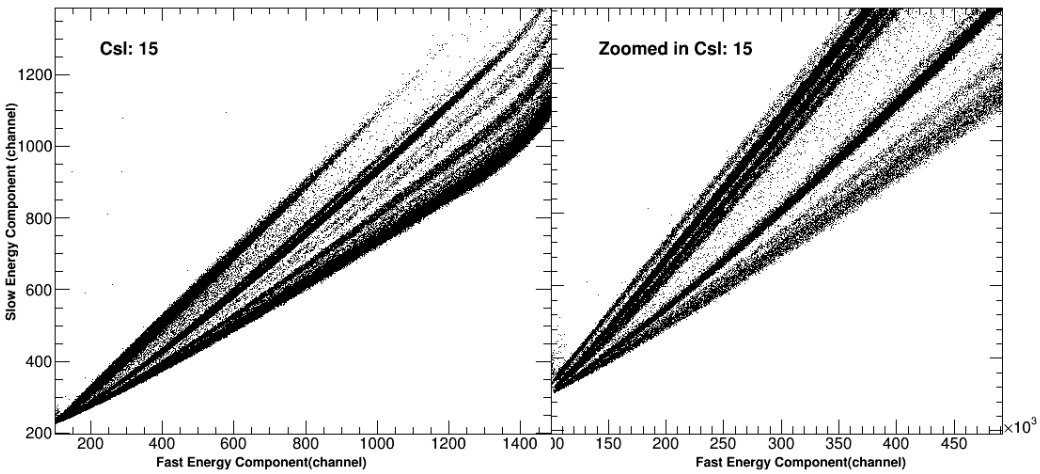

Figure 6.22: Slow vs. fast light output component of the CsI-PMT. The left-hand panel is the entire range of both the x- and y-axis. The right-hand panel is a zoomed-in version of the same plot. The lines correspond to protons, deuterons, tritons, ^{3}He, alpha, ^{6}He, double alpha, Li isotopes, Be isotopes and beam particles.

Figure 6.22 shows the overall isotopic resolution for an example CsI detector. The fast component of the CsI is plotted on the x-axis and the slow component is plotted on the y-axis. The

left panel shows the entire detection range of the FADC, and the right panel shows a zoomed-in version of the same plot. Great isotopic range is seen for p, d, t, ^{3}He, α and Li isotopes (left to right).

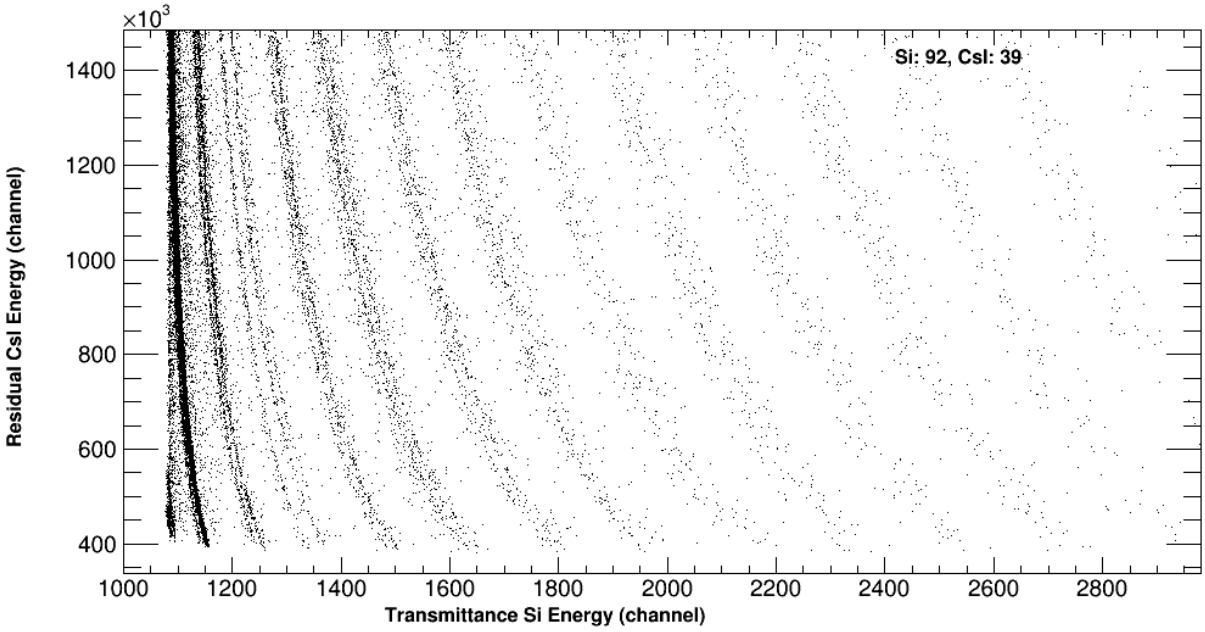

Figure 6.23: CsI total energy from the residual detector versus the Si signals from the transmittance detector in channel space. The broad lines correspond to the atomic number and the lines within the broader lines correspond to the respective isotopes.

For the CsI vs. Si, Figure 6.23 shows the total CsI energy in channels versus the Si energy in channels for a Ring 4 detector. The Si signals were corrected for gain drifts, details of which will be discussed in Section 6.4.2. Good isotopic resolution is seen up through Z=10, although the statistics are fairly low. The energy for the CsI did exceed the limits of the FADC.

Lastly, the Si energy in the residual detector is plotted vs. the transmittance Si detector energy. Both of the Si signals were also gain drift corrected. Results show isotopic resolution up through Z=10 for a Ring 7 detector.

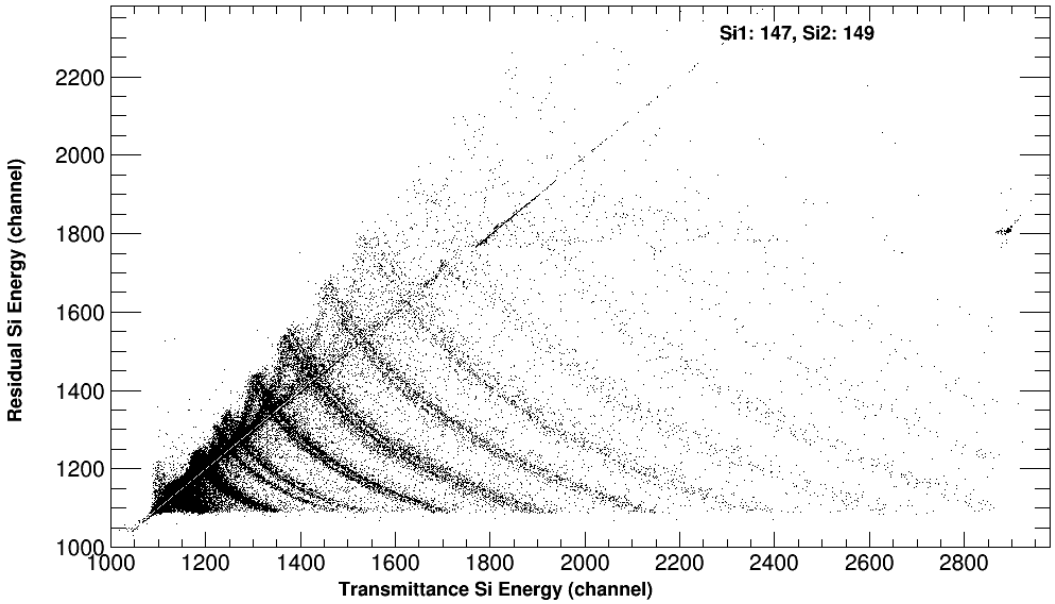

Figure 6.24: Si signals from the residual detector plotted against the Si signals from the transmittance detector in channel space. The broad lines correspond to the atomic number and the lines within the broader lines correspond to the respective isotopes.

6.4.2 Silicon Signal Correction

The amplitude of Si signals tend to drift in gain over time due to a variety of reasons, such as fluctuations in temperature affecting electronics and detectors, changes in leakage current and internal drifts in electronics [63]. In order to quantify the gain drifts, two pulsers were used. The lower voltage pulser was set to produce a signal with an amplitude consistent with a 6 MeV ^{241}Am alpha source (0.9 V). The second pulser was set at 1.1 V consistent with a signal from a higher charged particle. The pulser was triggered using a self-looping gate generator producing a logic signal with a frequency of 100 Hz. The signal was sent through a divider box, which was set to produce a signal every 1 s and 2 s.

Figure 6.25 shows the results for pulser amplitude as a function of time in hours for Si detector #2, which is representative of the effects seen throughout the array. The pink and blue points represent the two pulsers used. The pulser was accidentally turned off during 9 runs, which explains the absence of points between approx. 5-10 h. The gain for both pulsers is constant until approx. 18 h, at which point the value decreases by 4 channels (or approx. 0.35%) in both pulsers. To

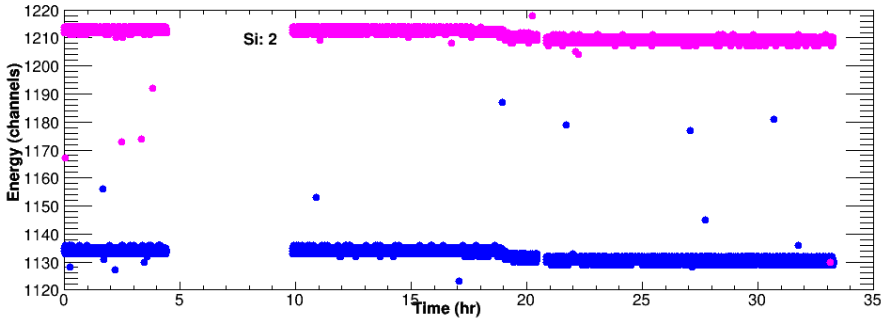

Figure 6.25: Pulser energy in channels plotted as a function of time. The pink points correspond to the higher voltage pulser and the blue points correspond to the lower voltage pulser.

compensate for this effect, a run by run correction to the gain was applied.

First, the mode was calculated for each individual run ($mode_i$) and the summed runs ($mode_{tot}$). The ratio of $\frac{mode_i}{mode_{tot}}$ was calculated on a run to run basis and used a multiplication factor. The results did improve the resolution of the detectors.

6.4.3 Linearizations

Data was linearized for one set of CsI Slow vs. Fast, CsI vs. Si and Si vs. Si histograms per ring in NIMROD. An example of the linearization steps for each PID method will be presented first followed by the 1-D results for all the detectors linearized.

For the CsI detector, an example of the points picked is shown in Figure 6.26. The points picked were for the protons, tritons, α, ^{6}Li and beam particles. The beam particles were selected to better separate the ^{6}Li from the α, ^{6}He and double α particles. The inclusion of the beam particles straightens the linearizations. The points also extended past the limit of the protons and tritons to provide a more accurate linearization of the high energy higher charged particles. The spline fit for the selected isotopes is shown in blue.

Figure 6.27 shows an example for the Si vs CsI point picking. Only the most common isotope of each element was selected and a spline fit was applied as shown in blue.

The point picking example for Si vs. Si is shown in Figure 6.28. Similar to the CsI vs. Si, the most common isotope for each element was picked.

The results for the linearized slow vs. fast data is shown in Figure 6.29. The colored lines show

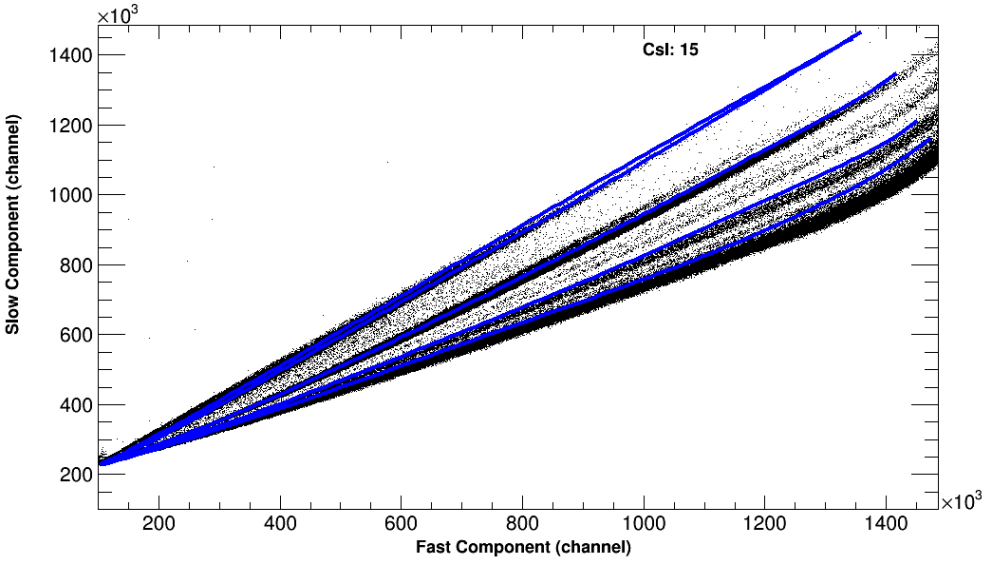

Figure 6.26: Slow vs. fast light output component of the CsI-PMT with the linearization fits. The fits were only applied for protons, tritons, alpha, ^{6}Li, and beam particles.

the limits for each isotope. The maximum and minimum value for each color represent the upper and lower limit for each isotope to the right of said line. The results show good separation between p, d, t, ^{3}He, α, ^{6}He, double α and ^{6}Li particles. The results for the beam particles (furthest line to the) exhibit non-linear behavior. However, this behavior is acceptable since particle identification of those heavier fragments in not done in the slow vs. fast, but in the CsI vs. Si.

Figure 6.30 shows the linearized results for a CsI vs. Si spectra. The left and right, and upper and lower limits for each isotope are represented by the colored lines. The lines for Z=2 are shown despite not being used in the final PID for the fragments. The linearizations go out to Z=9.

Figure 6.31 shows the linearized results for a Si vs. Si spectra. The colored lines show the left and right limits for each isotope, as well as the upper and lower limits for the isotope to the right of the line. The linearization is shown out to Z=9 and includes Z=2. Similar to the CsI vs. Si linearized spectra (Figure 6.30), the Z=2 particles are not identified through the Si vs. Si method.

The linearized results are projected onto the x-axis. The results are shown in Figure 6.32 for the CsI slow vs. fast results, Figure 6.33 for the CsI vs. Si results and Figure 6.34 for the Si vs. Si results. The results for the CsI slow vs. fast show good separation between the p, d, t and

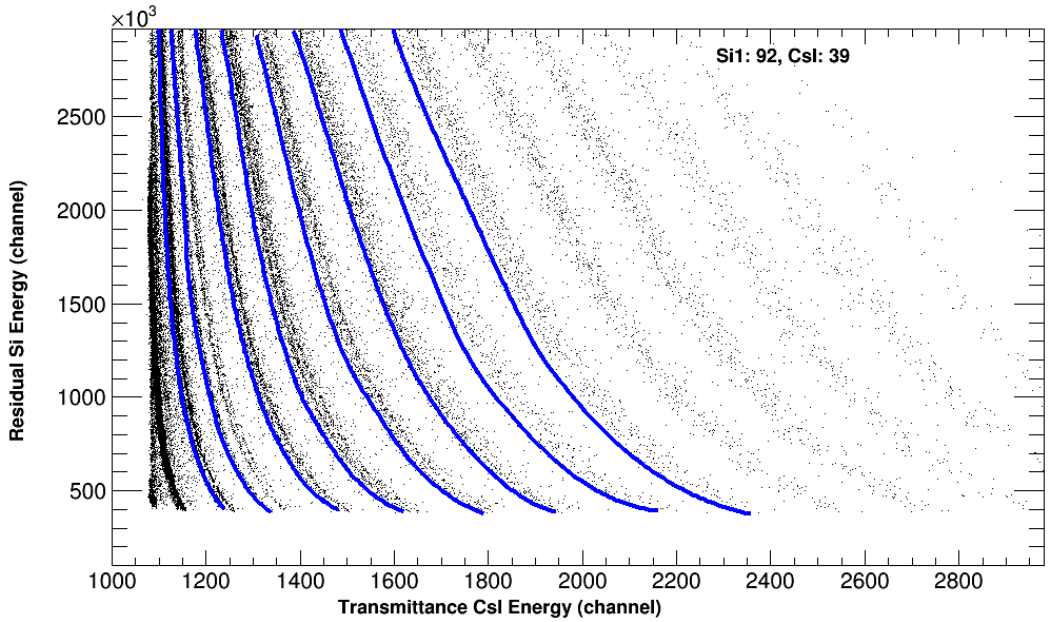

Figure 6.27: CsI total energy from the residual detector versus the Si signals from the transmittance detector in channel space. The fit lines are shown in blue. The most common isotope was fitted for each element.

the He isotopes. The He isotopic separation (^{3}He, α, ^{6}He and double α) is not as good as the p, d, t separation. However, the isotopes are still clearly present. As the ring θ increases (top, left to bottom, right), the α particle yield decreases relative to the Z=1 yield. The change in yield is consistent with previous work, which shows an increase in the relative Z=1 yield at larger angles in θ.

The results for the Si vs. CsI linearization shows good isotopic separation for the Ring 4-6 detectors up through Z=8. The isotopic separation is not as good for Ring 2-3. A large portion of detectors in Ring 2-3 had issues with leakage currents, causing the energy resolution to decrease. For Ring 7-9, the statistics for large Z fragments are very low, limiting the isotopic range shown.

The Si vs. Si linearization results show fairly good isotopic separation for Ring 4-6 detectors. The linearization gave isotopic resolution up to Z=8 in most of the detectors. The Ring 2-3 detectors did not have as good isotopic resolution. This is believed to be due to the detector issues for the new Micron detectors previously discussion in Section 6.2.2. Results for Ring 8-9 were not presented due to dead detectors.

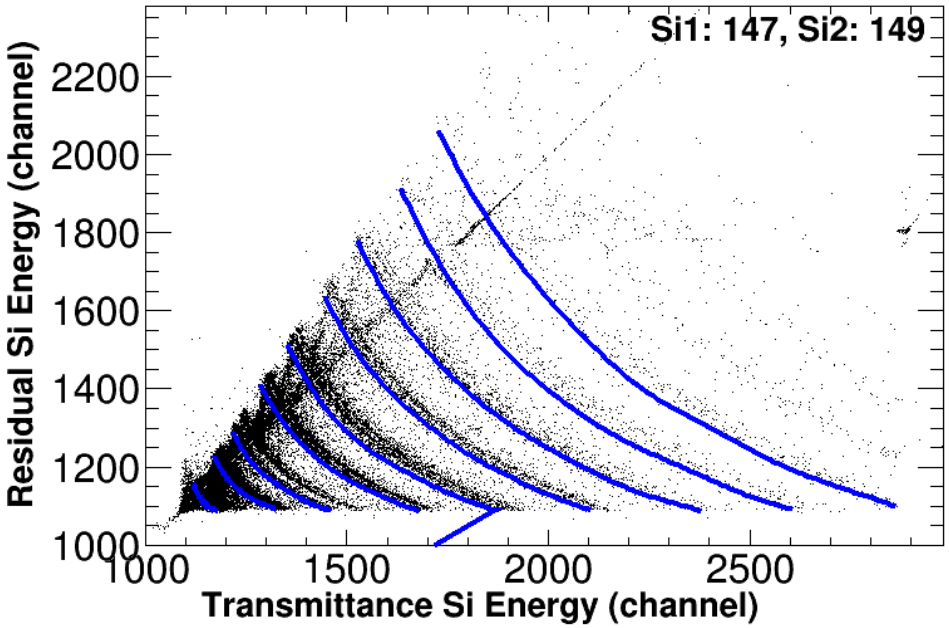

Figure 6.28: Si signals from the residual detector plotted against the Si signals from the transmittance detector in channel space. The most common isotope was fitted for each element and are shown in blue.

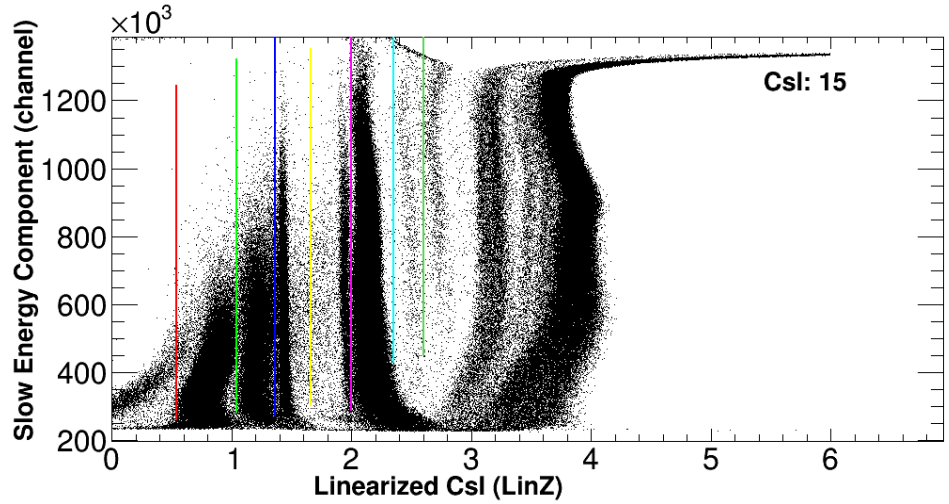

Figure 6.29: Linearized data for the detector shown in Figure 6.26. The colored lines represent the left, right and upper, lower limits for each isotope. Isotopic identification is assigned using CsI slow vs. fast for Z=1,2.

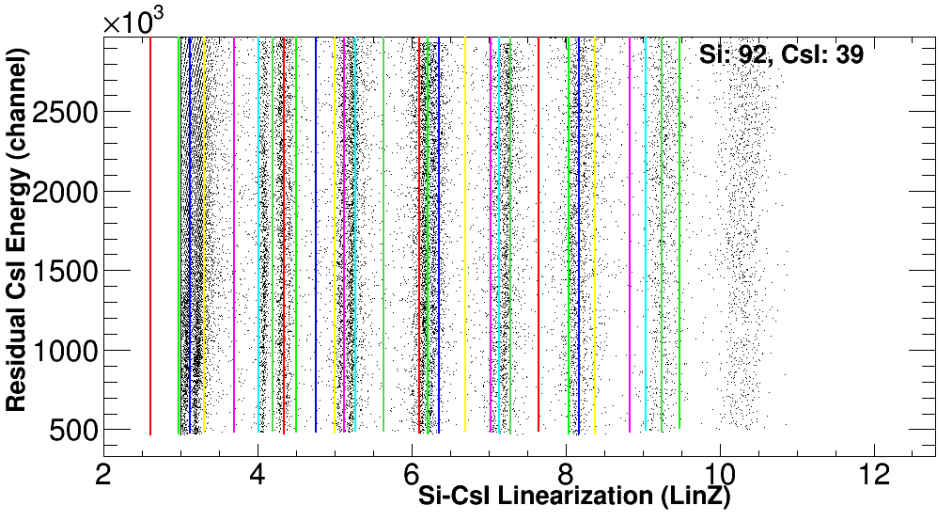

Figure 6.30: Linearized data for the detector shown in Figure 6.27. The colored lines represent the left and right limits of for each isotope. The height of each line corresponds to the upper and lower linearization limit for each isotope that is plotted on the right-hand side of said line. Isotopic identification is assigned using CsI vs. Si for Z≥3.

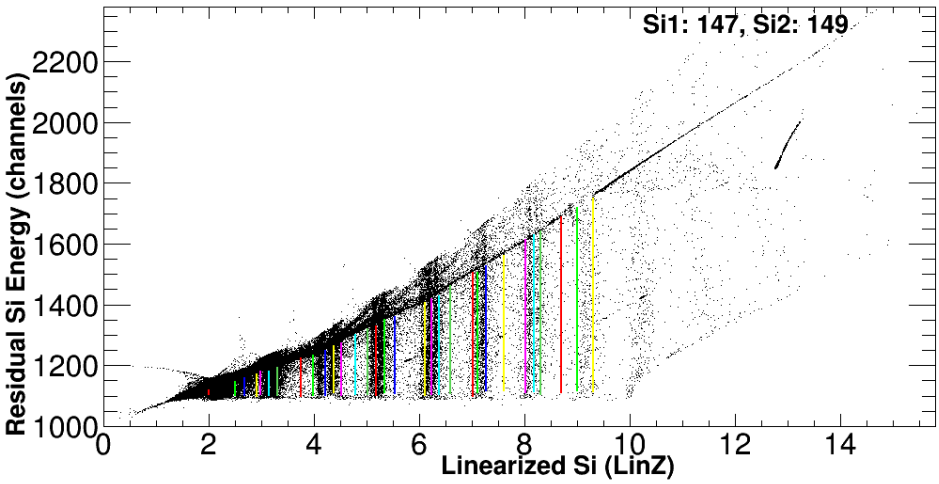

Figure 6.31: Linearized data for the detector shown in Figure 6.28. The colored lines represent the left and right limits of for each isotope. The extent of the lines vertically corresponds to the upper and lower limits the isotope right of each line. Isotopic identification is assigned using Si vs. Si for Z>3 for particles that stop in the 2nd Si detector.

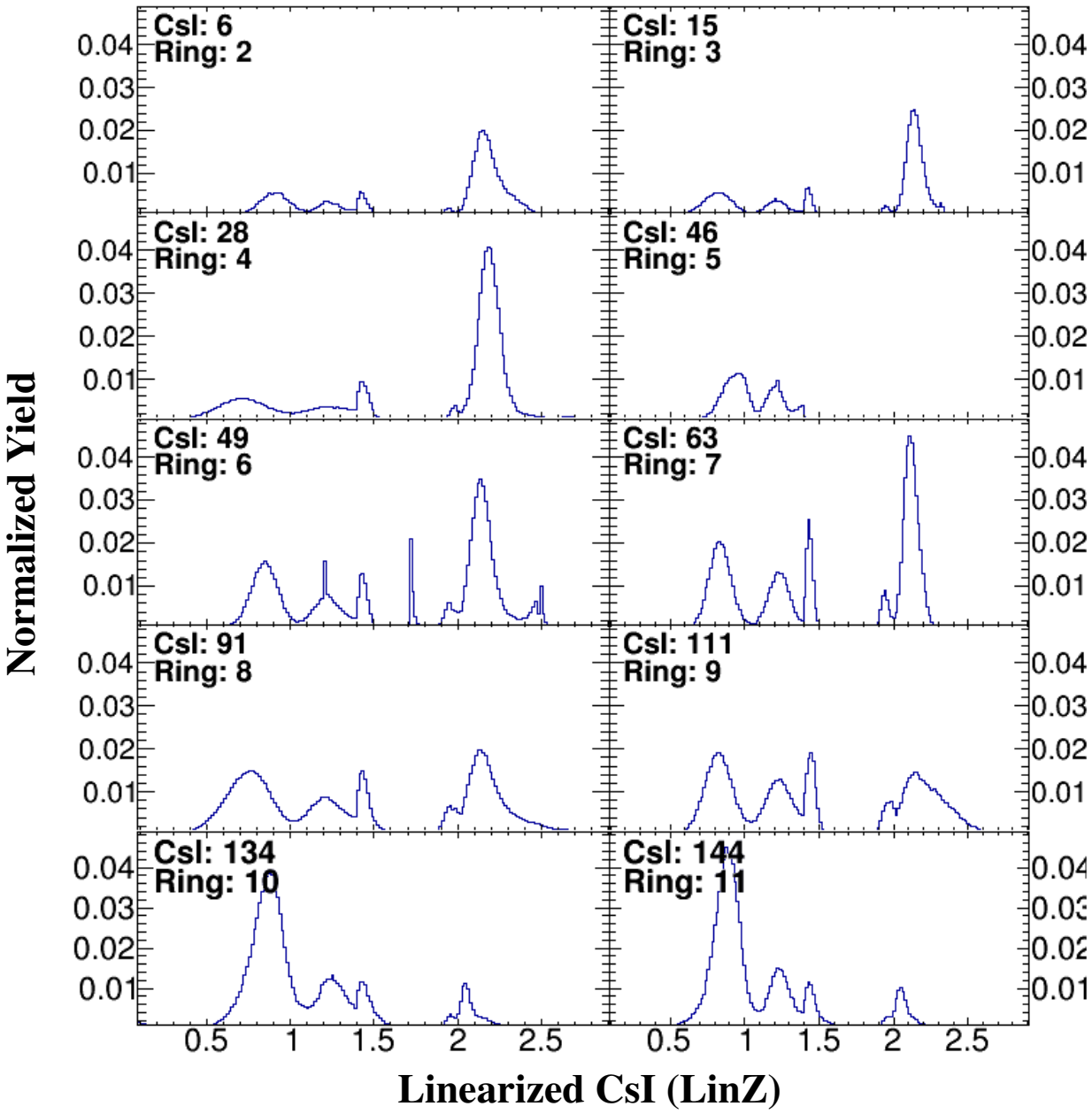

Figure 6.32: 1-D projections of the CsI slow vs. fast data for the best detector in each ring between Ring 2-11. Great isotopic resolution is seen up for p, d, t, ^{3}He, α, ^{6}He and double α.

6.4.4 Comparison to Previous Results and Discussion of the Results

The linearized results show the isotopic resolution for the previous campaign is better than the current campaign. Previous isotopic resolution extended up to Z=20 in some supertelescopes,

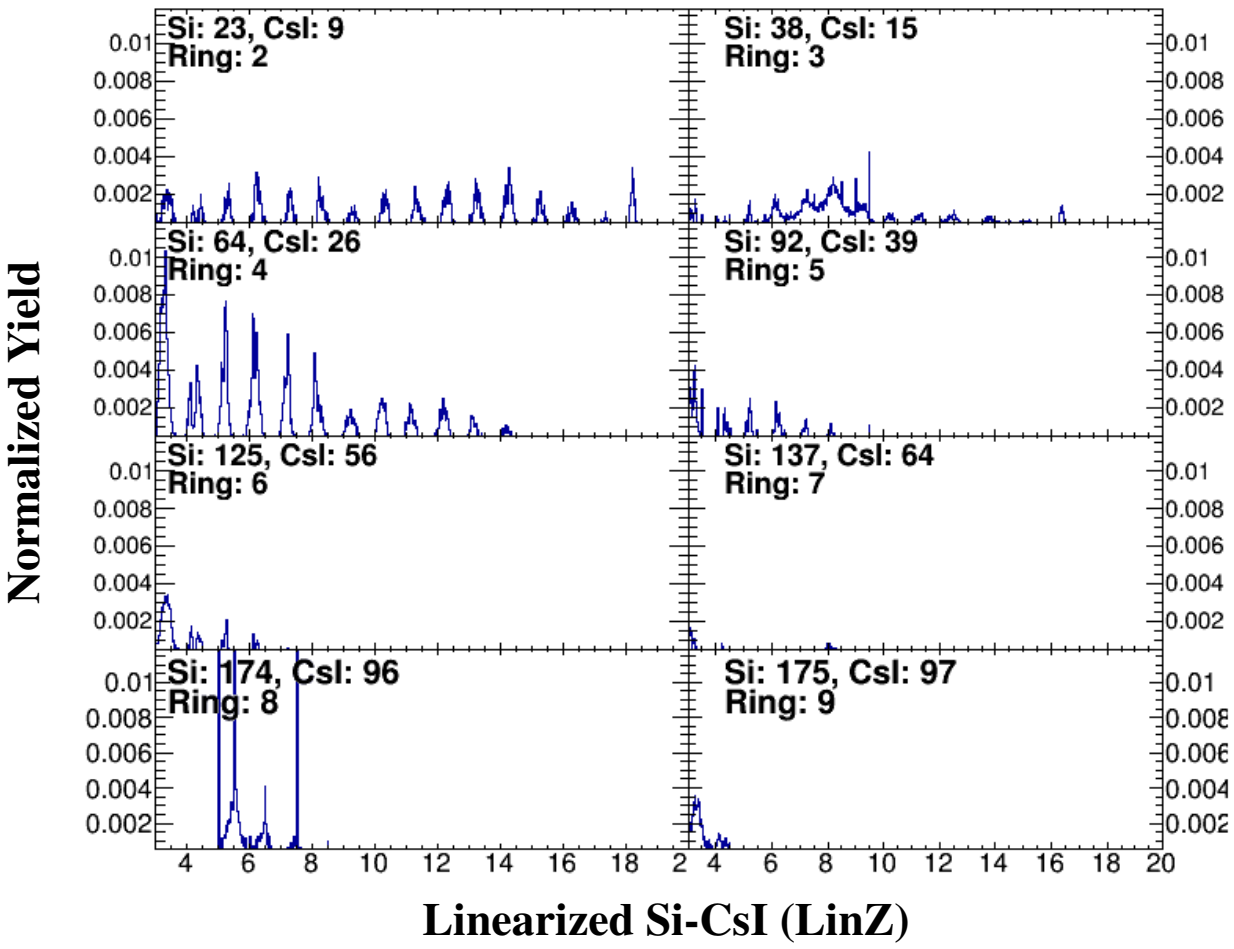

Figure 6.33: 1-D projections of the CsI vs Si data for the best detector in each ring between Ring 2-9. The isotopic resolution is seen up through Z=9 for the best detectors.

where as current resolution does not surpass Z=10 in the supertelescopes. Several reasons could explain the lack of isotopic resolution in the new configuration. Most notably, the isotopic resolution is very sensitive to the signal to noise ratio, and since the preamps have very low gain (1.8 mV/MeV or 5 mV/MeV), the baseline noise level needs to be minimized to under 5 mV. The NIMROD configuration was designed to minimize the noise contribution. For example, all detector ground were connected to the chamber ground and NIMROD ground was isolated from the beam lines.

The elephant in the room is the new electronics and detector configuration. Results from Section 6.2.2 show the channeling effects present in the new detectors, which affects the energy res-

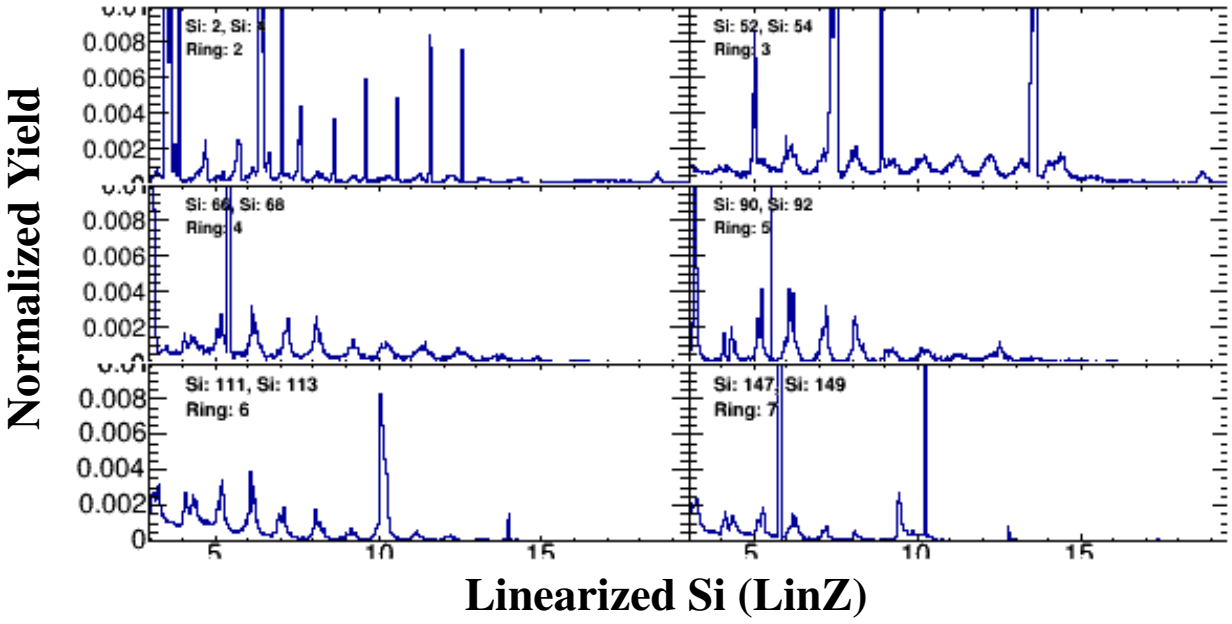

Figure 6.34: 1-D projections of the Si vs Si data for the best detector in each ring between Ring 2-7. The isotopic resolution is seen up through Z=9 for the best detectors.

olution of the each detector. The new tilters implemented did help improve the energy resolution slightly. However, the peak-to-peak difference in the sinusoidal baseline noise level increased from approx. 2-5 mV to 5-10 mV. The increase in baseline noise could be due to enhancement of the RF pickup or enhancement due to bad circuitry. In addition, the new detectors exhibited issues retaining the voltage on the detector. The leakage current on approx. a third of the new detectors were high ($> 5\mu$A). Two leakage current effects were present. First, the detectors were somehow damaged and had large leakage currents that were independent of whether the beam was on target or not. In the other case, the leakage current would start off relatively low (usually $< 1\mu$A), and increase slowly and linearly until the voltage was turned off when the leakage current exceeded 5 μA. When the voltage was applied again after the detectors had rested for at least several hours, the leakage currents would return to approx. the value before the leakage current ran away. Enough Si-Si detector pairings had at least one detector with leakage current issues that the isotopic resolution of the ΔE-E spectra was very poor in Rings 2/3 and 4/5. Unfortunately, the issues discussed with the new detectors do not explain the poor energy resolution seen in the previously used detec-

tors. The previously used Si detectors in Ring 6-9 started to exhibit poorer energy resolution and increasing leakage currents at the end of Campaign II [92].

For the new electronics, extensive testing to understand the operation of MASE was performed and discussed in Section 6.3.2. Signals were shaped using both MASE and the picoshapers (details are found in subsection 6.3.1). If MASE was injecting noise into the system, the energy resolution should be improved using the picoshapers. However, the results showed good agreement between the two shaper electronics. It is worth noting, the results were obtained before the final noise fighting efforts had been implemented. Although MASE is not suspected to have significantly introduced noise, it cannot be ruled out completely.

Lastly, efforts were made to reduce the baseline noise. The signals were initially DC-coupled. However, the voltage supply source (Wiener MPod) introduced large periodic noise. The noise from the Wiener MPod was proportional to the voltage applied. The motherboards also did not have a smoothing capacitor between the bias supply and the detectors. The design could not be modified due to the limited physical area on the motherboards. PC boards were designed to AC-couple the signals. The frequency of the sinusoidal noise was 100 Hz. Using Ohm's law, a capacitor value of 0.1μF was chosen such that sinusoidal noise could not drive through the capacitor, but the signal could. The new AC-coupled signals shown in Figure 6.35 reduced the sinusoidal baseline noise deviation from 5-10 mV to 2-5 mV across all detectors. The new baseline noise level is consistent with previous NIMROD experiments in Campaign II [92, 93].

For the experiment, the pin on the voltage ladder was accidentally torn off. The voltage was designed to reduce the number of electrons transferred to the PLF*. The electrons can "muddy" the signals leading to worse resolution. However, the Mylar foils installed on the ionization chambers were still present. Results from Ref. [10, 65] show the Mylar foils were critical to achieving great isotopic resolution.

Based on the discussion of the noise presented, the isotopic resolution should have been closer to the results from the previous campaigns. Further studies need to be performed to quantify other potential sources of noise.

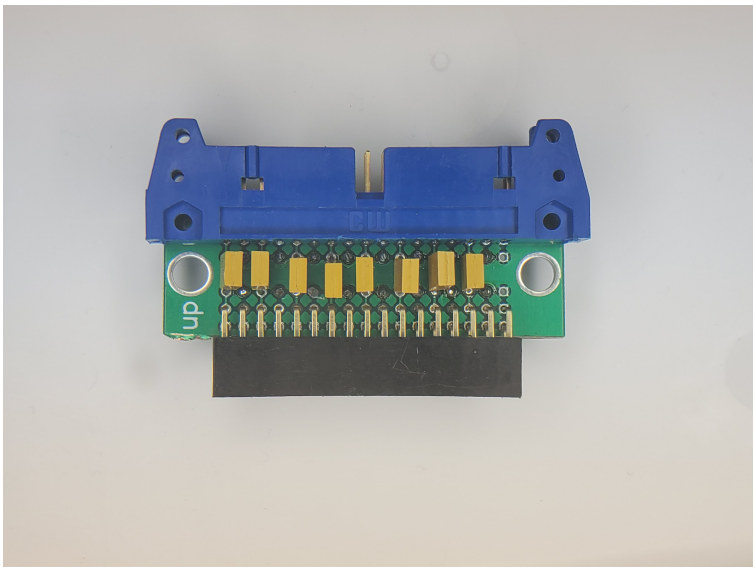

Figure 6.35: PC board designed to AC-couple silicon detector signals. The capacitors are 0.1 pF and, due to physical space issues, the capacitors are placed in every other set of soldering holes on each side. The AC-couplers were designed to fit onto the input of MASE.

6.5 Neutron Ball Reconfiguration

Several experiments were performed at the Cyclotron Institute at Texas A&M University. The neutron ball detector was used to measure the free neutron multiplicity. The neutron ball is part of the NIMROD array and sits outside the charged particle portion.

The neutron multiplicity plays an important role in understanding the reaction dynamics of a collision between a target and projectile in heavy ion experiments. An overview of the the neutron ball is discussed in Section 6.5.1. Due to changes in the neutron ball and cave configurations, discussed in Section 6.5.2 and 6.5.3 respectively, the neutron ball background has changed. The background needs to be characterized in order to determine the effect the reconfiguration can have on the neutron distribution.

The electronic configuration will be discussed in Section 6.5.4. The results and comparison to previous data are found in Section 6.5.5.

6.5.1 Overview of the Neutron Ball Detector

The neutron ball (NBL) was installed at the Texas A&M Cyclotron Institute in the 1980s. Initally, the NBL consisted of two hemispheres with four PMTS each in a hamburger configuration.

In the mid-1990s, four middle quarter-cylinders were added with three PMTs each encompassing the outside of the charged-particle portion of the NIMROD array. The four quarter-cylinders made up the middle segment of the NBL and each segment has 3 PMTs. The initial hemispheres were rotated 90° to cover the upstream (top) and downstream (bottom) portions of the NIMROD array. The NBL now sits in a hoagie configuration. The top, middle and bottom segments were placed on tracks and can be moved independently, which enables access to the charged-particle array. A schematic of the NBL is shown in Figure 6.36.

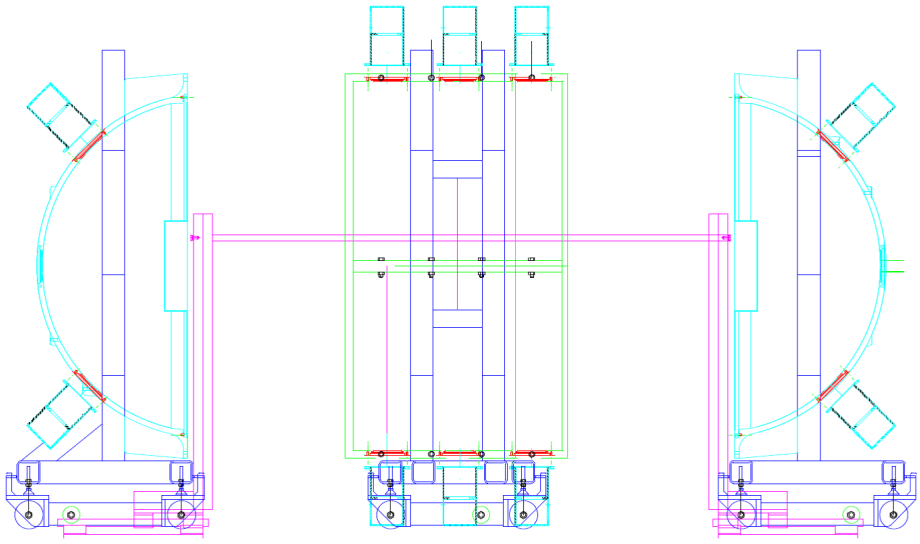

Figure 6.36: CAD drawing of the neutron ball from the side. The upstream and downstream segments are shown in blue. The green section is the four middle segments. The neutron ball surrounds NIMROD.

The NBL is used as a neutron calorimeter. The outside consists of thin aluminum walls. On the inside was a pseudocumene liquid scintillator, which was doped with 0.3% wt Gd. After a nuclear collision, a gamma flash is immediately released producing a large, sharp signal after interaction with the scintillator. After the gamma flash, free neutrons are collected. The neutrons entering the NBL interact with the pseudocumene. Through neutron-proton collisions, the fast neutrons are thermalized. The thermalized neutrons are captured by the Gd, which released on average three

gamma rays totaling approx. 8 MeV [58, 59]. The Gd was chosen due to its high neutron capture cross-section [58]. The gamma rays knock out electrons in the pseudocumene causing the liquid to scintillate, and the light output is captured by the PMTs. Two sources of background contamination exist: background neutrons and cosmic particles. The background neutrons can also be captured by the Gd. The gamma rays produced from the reaction neutrons, background neutrons and cosmic particles cannot be distinguished by the NBL. Therefore, the gamma rays from all three sources can cause the pseudocumene to scintillate, producing a light output in the PMTs. The neutrons take a fairly long period of time to capture. Therefore, a 100 μs gate is required to detect the vast majority of the free neutrons. The details of the neutron detection will be discussed in Section 6.5.4.

The NBL is used to tune the beam in NIMROD. The beam diagnostics within the beam consist of a beam viewer just behind the upstream quadrupole magnets (approx. 5 m upstream of the target position) and a beam viewer about a meter upstream from the beam dump (approx. 10 m behind the target position). There are no beam diagnostics at the target position. To determine if the beam spot is centered on target, a blank frame is placed at the target position. The beam is tuned through the frame, minimizing the background NBL rate. Testing was to conducted to see the effect of tuning the beam onto a phosphor on the NBL rate. Results are discussed in Appendix F.

6.5.2 Neutron Ball Configuration

In 2016, the NBL was reconfigured by the LLNL NuStars collaboration [59]. The 4512/B Hamamatsu PMTs were replaced with R1250 Hamamatsu PMTs. The new PMTs were approximately 2" shorter in height. As a result, the lower quarter-cylinder in the middle section was lowered by 1.5" and the other quarter-cylinders were raised 0.5". The motivation was to maximize the space between the NBL quarter-cylinders and the charged-particle array. The preamps on the motherboards sitting on the outside of the charged-particle array sit within millimeters of the lower quarter-cylinder of the NBL middle segment. The new configuration reduces the likelihood of breaking preamps and unplugging flat cables transporting signals from the motherboards to the electronic modules.

The EJ-331 pseudocumene liquid scintillator was also replaced with EJ-335. The new mixture includes mineral oil, which increases the flash point of the scintillator from 44°C to 64°C [94].

The increase in the flash point assures the volatility of the liquid is outside the temperature range achievable in the experimental cave. The Gd concentration was decreased to be 0.25% wt from 0.3% wt.

The new liquid scintillator has a different neutron capture time distribution, which can affect the width of the gate used in the electronics to measure the free neutrons (Section 6.5.4). The neutron capture time for this experiment is defined as the average length of time for 90% of neutrons produced to be captured. The neutron capture time distribution was measured using a SIS3316 and a ^{252}Cf-source. The ^{252}Cf-source has an average neutron multiplicity of 3.76 for fission decays, which has a branching ratio of 0.03. The source was placed next to an Ortec surface barrier Si detector inside a small chamber placed right next to the upstream section of the NBL. The neutron capture time distribution was measured using only the upstream section.

The SIS3316 was configured to take in logic signals from the NBL within a 200 μs window, which is the timing limit of the SIS3316. The computer logic was triggered by a signal in the Si detector from the ^{252}Cf source. The ^{252}Cf signals were collected using a spectroscopy amplifier and a Mesytec PS-ADC to ensure only fission events were analyzed. The NBL signals were added together and the distribution was fit with an exponential fit of the form

$$P(t) \propto \exp^{-\lambda t}\left[(\beta - \lambda)t - 1)\right] + \exp^{-\beta t}; \tag{6.1}$$

where P(t) is the neutron capture time distribution, λ represents the properties of the scintillator, β is proportional to the Gd concentration [58].

Figure 6.37 shows the results for the neutron distribution in blue and the exponential fit in red. The mean capture time extracted from the fit is 18.9 μs. For the experimental configuration, capturing the majority of neutrons is essential. Therefore, the value corresponding to when 90% of neutrons have been captured is used as the neutron capture time. The neutron capture time was approx. 36 μs.

The results are comparable to previous measurements [58]. The distribution was measured using a TAC, which was triggered by a prompt γ-ray corresponding to the γ-flash. The TAC was stopped when a delayed flash from the PMT was detected. The resulting distribution quotes a capture time distribution of approx. 20 μs for a Gd concentration of 0.4% wt and approx. 40 μs for

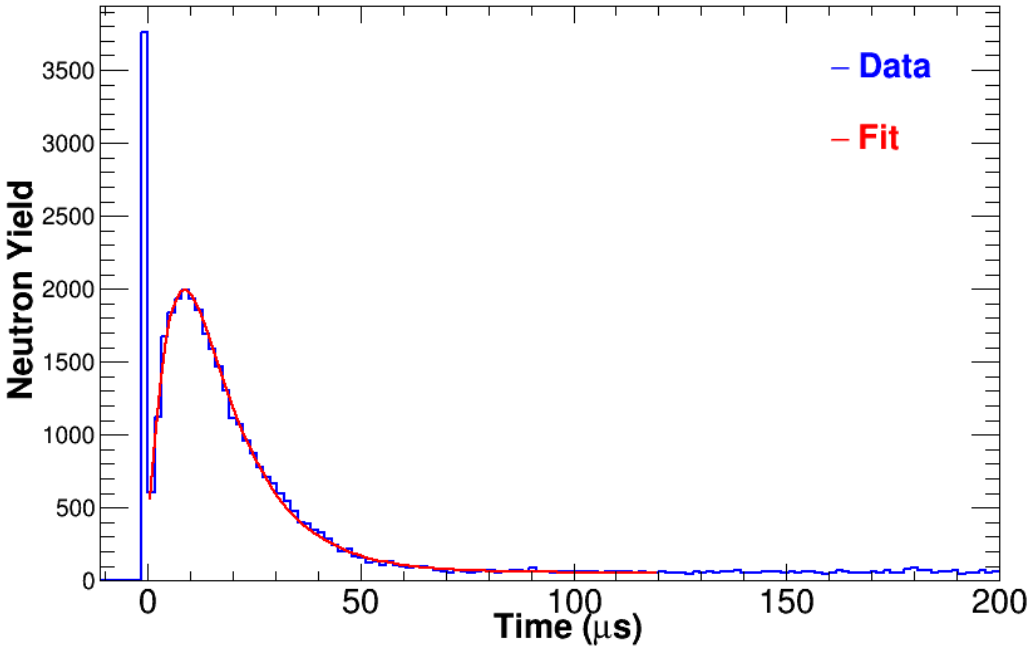

Figure 6.37: Neutron yield as a function of time in μs. The maximum time plotted is the same as the timing limit of the SIS3316. The first peak corresponds to the gamma flash and occurs right after the electronics are triggered. The yield rises quickly over approx. $5\mu s$ and then falls off exponentially with a mean capture time of $18.9\mu s$. The results are consistent with the majority of neutrons being captured within the 100μs gate.

a Gd concentration of 0.2% wt. The new measurement is consistent with a Gd concentration closer to 0.4% wt. Although the results vary, both values are still within the 100 μs gate implemented in NIMROD to measure the neutron multiplicity.

6.5.3 Experimental Cave Configuration

In addition to the changes within the NBL detector array, the experimental cave was also re-configured to accompany the addition of the AGGIE separator and relocation of HYPERION. In the previous configuration, a concrete half-wall was located right behind the NBL and concrete shielding was placed around the beam dump. The location of these are seen with the dotted black lines downstream of NIMROD in Figure 6.38. The concrete blocks acts to thermalize and capture the fast neutrons, and reflect the neutrons away from the NBL. Because the concrete bricks have a large fraction of water present in them, the water acts as a neutron absorber due to the two hydrogen atoms per oxygen atom. The hydrogen atoms have a high neutron capture cross-section.

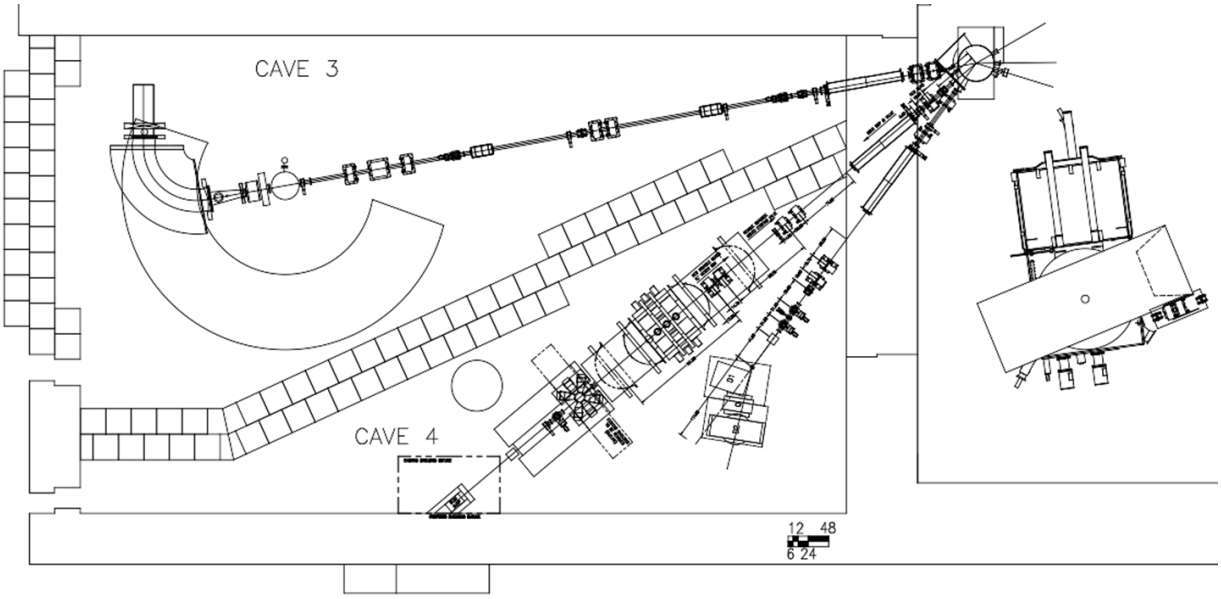

Figure 6.38: Depiction of the new cave 4 configuration. The dotted lines correspond to where the concrete half wall and NIMROD beam dump shielding were located in the old configuration. Figure courtesy of S. Molitor.

To study the effect of the half-wall and the beam dump shielding on the neutron ball background rate, GEANT3 simulations were run by Guoqiang Zhang in collaboration with Dr. Roy Wada. Figure 6.39 shows the shielding effect of just the beam dump shielding (left panels), and the combination of half-wall and beam dump shielding (right panels). The neutron was treated as a point source starting at the beam dump with an energy of 1 MeV (top panels) and 10 MeV (bottom panels). Figure 6.40 shows the simulations from GEANT3, left to right, for 1 eV, 1 keV, 1 MeV and 10 MeV neutron from a point source. The results show both the half-wall and the beam dump shielding were very effective in shielding the NBL from fast neutrons produced from reactions in the beam dump.

In the new experimental cave configuration, the half-wall and shielding around the beam dump were removed. A new beam dump was designed by G. Zhang in collaboration with R. Wada and implemented by S. Molitor. The new beam dump is 30" and contains a Faraday Cup at the end to monitor the beam current. The beam dump is surrounded by 4 layers of green board, followed by stacked concrete blocks. The green board consists of 5% borated polyethylene. Boron has a high neutron capture cross-section, which helps absorb neutrons after they are produced in collisions

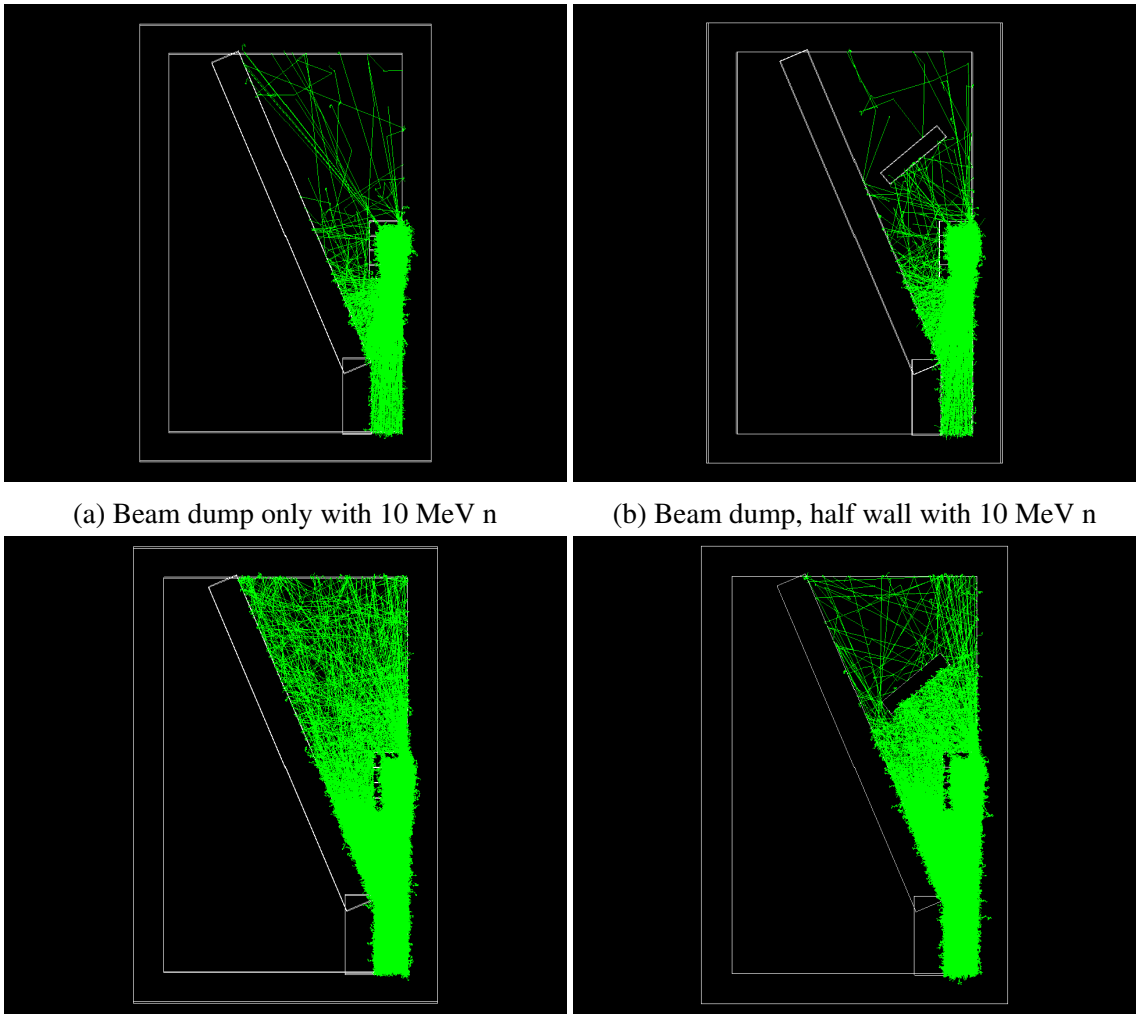

(a) Beam dump only with 10 MeV n

(b) Beam dump, half wall with 10 MeV n

(c) Beam dump only with 1 MeV n

(d) Beam dump, half wall with 1 MeV n

Figure 6.39: GEANT simulations comparing addition and removal of the concrete half-wall utilizing the old beam dump. The removal of the concrete half-wall is shown on the left panel and the addition is in the right panels. The top panels correspond to a neutron energy of 1 MeV and the bottom panels correspond to a neutron energy of 10 MeV. The neutrons are treated as a point source in the beam dump.

in the beam dump and thermalized. The outside concrete bricks were added to help thermalize the neutrons and reflect the neutrons back towards the green board. The results showed the beam dump should work comparably as well at shielding the NBL as the previous configuration.

Experimental results will be discussed in Section 6.5.5.

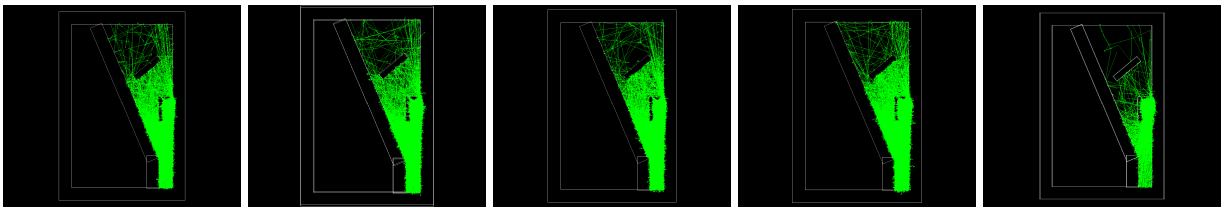

(a) 0.1 eV n (b) 1 eV n (c) 1 keV n (d) 1 MeV n (e) 10 MeV n

Figure 6.40: Results for the GEANT simulations with the beam dump shielding and half-wall for 0.1 ev, 1 eV, 1 keV, 1 MeV and 10 MeV neutron point source. Each panel is labelled with the energy of the neutron underneath, with "n" standing for neutrons. The neutron point source was placed inside the beam dump.

6.5.4 NBL Electronics

To achieve the free neutron multiplicity, gates were generated to count the neutron event plus background and background multiplicities. By subtracting the background multiplicity from the neutron event plus background multiplicity, a "true" neutron multiplicity can be calculated.

Figure 6.41 shows the electronics diagrams for the NBL. The signal from each PMT was sent to a fast amplifier and then a CFD. The gains of the fast amplifiers and the thresholds of the CFDs were set so that the neutron ball efficiency from a ^{252}Cf source matched the NIMROD GEANT-3/GCALOR simulation efficiency of approx. 70% [11, 67].

The logic OR signal from each CFD produced when a neutron reached threshold was sent to a logic Fan In/Fan Out (FI/FO). The OR from the FI/FO was sent to two coincidence modules. The OR was utilized since each logic signal corresponds to a neutron regardless of the number of PMTs that fire. When the experimental logic was triggered, a 100 μs gate was opened. The 100 μs gate was sent to the first coincidence module, which was set to two. Therefore, any OR signal from the logic FI/FO that came in coincidence with the 100 μs gate was sent to a scaler.

Although the scaler counts all thermalized and captured neutrons from a reaction, it counts all background neutrons that were also thermalized and captured within the 100 μs window. To estimate the background, a second 100 μs gate was opened to measure the neutron background. The delay from the first 100 μs gate was used to start the second 100 μs gate, and that gate was sent to the second coincidence module. The coincidence from the FI/FO OR logic signal and the second 100 μs gate was also sent to the scaler. The lengths of the two gates was chosen based on the neutron capture time distribution. Details were shown in Section 6.5.2. A 40 ns delay,

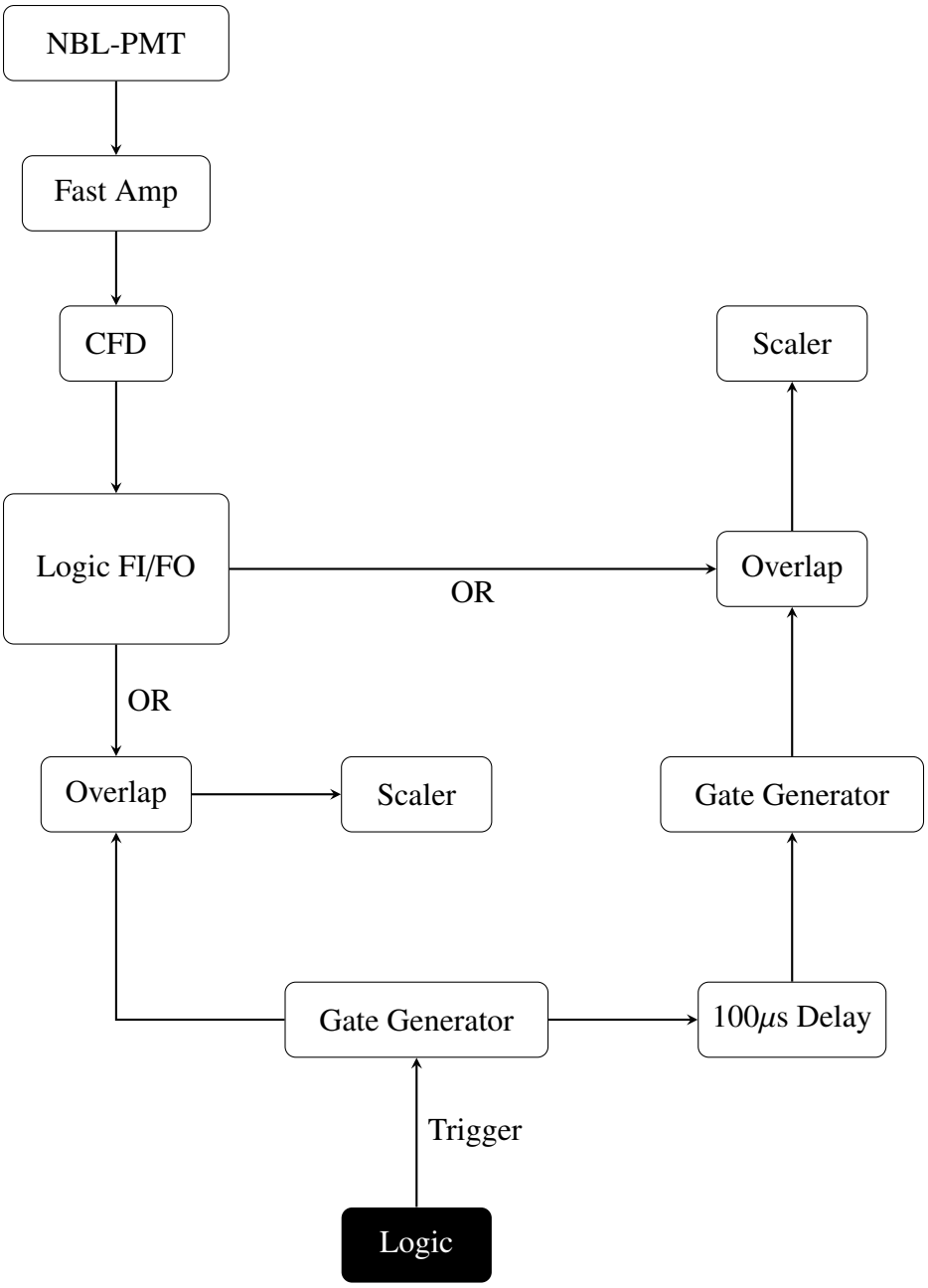

Figure 6.41: Electronics diagram for the NBL electronics.

generated from the prescaler module in the trigger logic, was applied. The delay ensures the neutrons measured did not correspond to the large gamma flash in the neutron ball, which occurs right after the reaction.

6.5.5 Results and Comparison toPrevious Experiments

Several experiments were run to characterize the NBL. The 1st series of experiments were performed in July and September of 2018 using the K150 at the Texas A&M Cyclotron Institute. The objective was to understand the neutron background with beam on and beam off before and after the experimental cave reconfiguration. In both experiments, the NuStars chamber seen in Figure 6.42 was used, which also illustrates the location of the experimental components. The electronics trigger came from an Ortec surface barrier silicon detector placed approx. 45° from the beam axis. Both experiments were performed with a ^{22}Ne beam at 19 MeV/nuc. The efficiency of the NBL was 10% using a ^{252}Cf source. Unlike the K500, the K150 did not have a beam pulser or phase shifter, therefore a mechanism to turn the beam off was rigged together. Further details of this beam pulser are discussed in Appendix D.

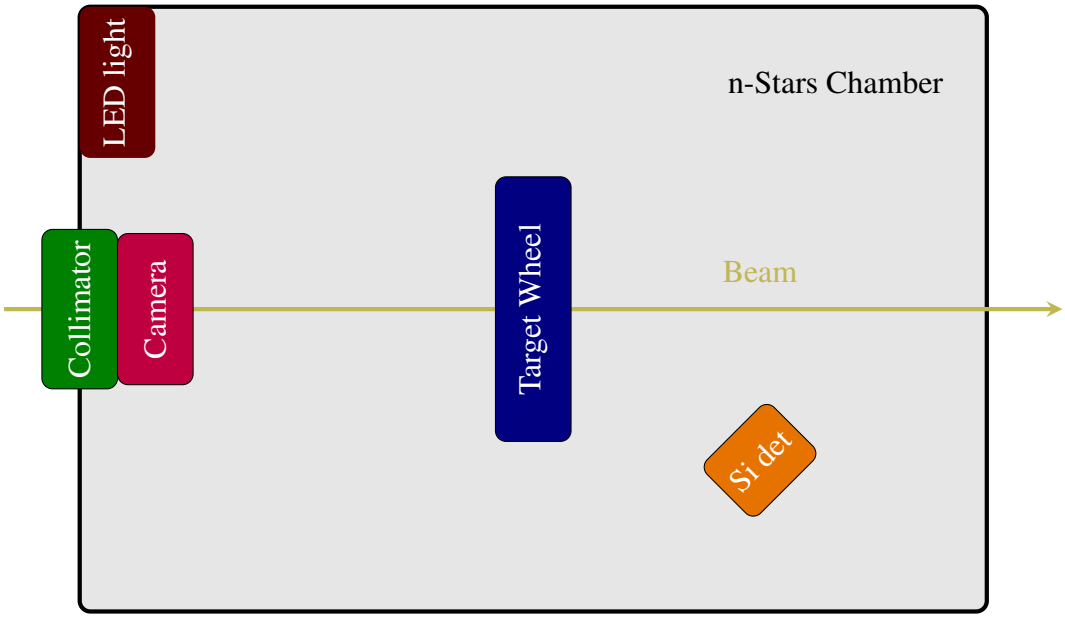

Figure 6.42: Schematic of the NuStars chamber configuration

For the July experiment, the background was 1000 counts/sec without beam. Upon tuning the beam through a blank target, the background rate increased to 2000 counts/sec. Results from a 5.0 mg/cm^2 ^{nat}Sn target showed a rate of 60,000 counts/sec. For this experiment, six 100 μs gates were set up in sequence. The results for each gate are seen in Figure 6.43. The results indicate the

average neutron multiplicity decreases rapidly over the first 3 100 μs gates. However, the average neutron multiplicity for those gates was above background indicating excess neutron yield in the cave after the beam had been turned off.

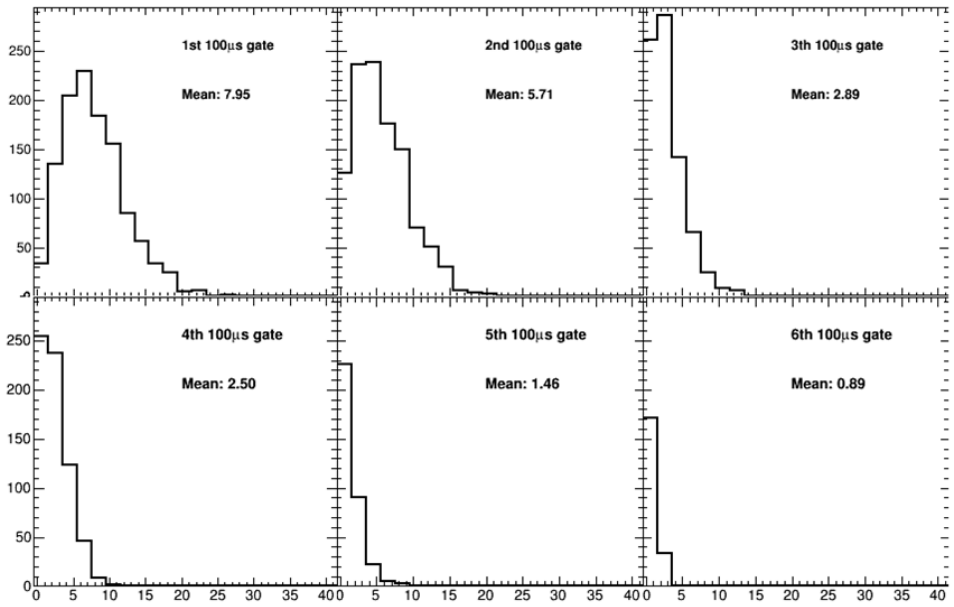

Figure 6.43: The neutron multiplicity distribution and average in each of the six consecutive 100 μs gates is plotted from top left to bottom right. The average multiplicity decreases rapidly between the 1st, 2nd and 3rd gate. However, the multiplicity does not decrease to be consistent with the background in the 2nd window. This effect is consistent with a large background rate due to the large dispersion in the x-direction on the K150. The beam is partially grazing off the beam pipe, producing extra background neutrons.

In September, the experiment was repeated with the new configuration consisting of the new beam dump and the removal of the half-wall behind the neutron ball. The background rate without beam was still 1000 counts/sec. The beam was tuned through the blank target, and the beam-on background rate was 6000 counts/sec. The ^{nat}Sn target produced a rate of 200,000 counts/sec with 0.3 enA on FC02. When the beam viewer was placed in the beam line, right upstream of the beam dump, it was concluded the dispersion in the x-direction was larger than the beam viewer and, hence the width of the beam line. The dispersion in the y-direction was minimal covering approx. 0.5" above and below the beam viewer center. The beam viewer was moved upstream to where the half-wall used to be. The beam in the x-direction covered the majority of the beam viewer, but did

not exceed it. The beam was retuned onto the beam dump without a target in the target position to achieve a straighter tune. The beam-on background rate was 1500 counts/sec before the retune, and 2400 counts/sec after the retune. A ^{70}Zn target was used and a rate of 3000 counts/sec was observed.

The x-dispersion problem is a well-known issue with the K150. Because of the two Dee design, the beam that exits the K150 is much wider in the x-direction. While several sets of dipole and quadrupole magnets exist upstream of the NBL, the beam cannot be tuned to minimize the x-dispersion along the approx. 10m long path between the last set of steering magnets and the beam dump. The beam when entering the last set of steering magnets is approx. 2" in diameter. Optically speaking, if the objective is to tune the beam to approx. 1mm wide point at the target position approx. 2m downstream of the steering magnets, the beam will widen again downstream from the NBL. The beam will widen to greater than the 4" beam pipe causing activation and neutron scattering. The half-wall was not preventing the neutron scattering effect, which is why the neutron multiplicities for the July experiment were higher than background in the first 3 100μs gates. However, the half-wall did do a good job suppressing a majority of the neutrons from scattering back towards to NBL. This explains why the neutron count rate for the September experiment was much higher than the July experiment.

Attenuation	1st window	2nd window	3rd window	4th window	5th window	6th window	Δ=(x_1-($\overline{x_{2-6}}$)
1×10^{-2}	10.96±0.15	2.35±0.09	2.13±0.08	2.00±0.08	1.91±0.08	2.16±0.10	8.85±0.17
1×10^{-2} bp off	11.02±0.11	4.39±0.11	4.36±0.11	4.22±0.11	3.90±0.09	4.18±0.11	6.81±0.14
3×10^{-3}	9.63±0.24	1.77±0.12	1.84±0.16	2.29±0.22	2.00±0.18	1.91±0.19	7.67±0.30
1×10^{-3}	10.96±0.15	2.35±0.09	2.13±0.08	2.00±0.08	1.91±0.08	2.16±0.10	8.85±0.17
3×10^{-4}	8.56±0.24	1.76±0.17	2.14±0.22	1.97±0.27	1.84±0.17	1.82±0.20	6.65±0.32

Table 6.4: Neutron count in six consecutive 100 μs gates triggered by an event in a silicon detector. The second row corresponds to the same attenuation as the first row. However, the second row results are for when the beam pulser was removed and the beam was not turned off. All other rows correspond to the beam pulser turned on. Results show a large initial neutron rate followed by a large asymptotic drop off. The last column is the difference between the 1st window and the average of the following 5 windows.

Beam Shielding	1st window	2nd window
No shielding	8.86 ± 0.13	2.89 ± 0.16
1 layer of green board bags	8.76 ± 0.07	2.63 ± 0.07
2nd layer of bags and 1 layer upstream	8.67 ± 0.12	2.35 ± 0.10
2nd layer of bags upstream	8.48 ± 0.11	2.58 ± 0.12
Lead brick wall upstream of bags	8.80 ± 0.08	2.61 ± 0.09

Table 6.5: Results for beam shielding added to the beam pipe upstream of the beam dump. The 1st column shows the different beam shielding applied. The 2nd column corresponds to the 1st 100μs window, which is the average neutron event count and background. The 3rd column is the 2nd 100μs window corresponding to the average background count. Additional beam shielding decreased the average neutron event count with the exception of the leak brick wall.

The K500 was used to further test the beam dump due to the less dispersive nature of the beam. The beam viewer was again used to diagnose the width of the beam. The beam was within the area of the beam viewer right upstream of the beam dump, indicating the majority of the beam was entering the beam dump. The background measurement without beam was 8,000 counts/sec at a 55% efficiency (using the ^{252}Cf source) and the beam-on background rate was 10,000 counts/sec with 600 enA on the beam dump. The neutron count was measured in six 100 μs gates. The results are seen in Table 6.4. Each row corresponds to a different attenuation setting with no attenuation corresponding to 600 enA. Two measurements were taken for the 1×10^{-2} attenuation setting, corresponding to the phase shifter being turned off and on.

For the above experiments, the beam was turned off with the phase shifter using the silicon detector logic signal. The objective was to mitigate the effect of the beam on the background measurement However, for the thesis experiment, the beam pulser was used. An experiment was performed to compare the beam pulser and phase shifter. Further discussion is found in Appendix E.

Beam shielding studies were performed looking at the effect of adding bags of green board shavings around the beam pipe right upstream of the beam dump. Table 6.5 shows the results in the first two 100 is gates. The results shown are for no shielding, one layer (3 bags) of green board shavings, 2nd layer around initial layer and a layer upstream, a 2nd layer around the more upstream

layer, and a lead brick wall. The lead wall was placed right upstream from the 2nd layer of green board shavings. The results indicate adding layers of green board shavings decreases the neutron rate slightly. The addition of a lead wall did increase the rate in the 1st 100 μs gate, which does not rule out the possibility that the beam is hitting the pipe upstream of the wall. It is believed that the increase in neutron count after implementing the lead brick indicates gamma rays produced from neutron capture is not a large contributor in the neutron ball background rate.

The neutron ball background rate was characterized for the new experimental cave configuration and beam shielding studies were conducted. The results indicate that the beam dump is successful at thermalizing and capturing neutrons. However, the neutron rates indicate that the beam is hitting the beam pipe, creating a larger background rate than the previous configuration.

Quadruple magnets (quads) were installed right behind the NBL where the half-wall used to be. Tests in December 2018 were performed with the K150 to see the effects of tuning the beam into the beam dump using the quads. Initially, the beam was tuned onto the beam viewer about a meter upstream from the beam dump. The beam viewer was removed and the quads were fine-tuned to try to minimize the NBL rate. This process was repeated for the beam passing through the blank target and through a 500μg/cm^2 ^{58}Ni target. While using the quadrupole magnets showed an increase in the beam current on the Faraday cup in the beam dump for both targets, neither target showed a change in the NBL rate.

The lack of change in the NBL rate is understood when examining the charge distribution and the energy distribution of the beam after passing through the target. The $^{22}Ne^{+10}$ beam is fully stripped of electrons before it passes though the target. However, the target has a neutral charge. While most of the beam passes through the target without interaction, some of the beam can interact with the target and pick up electrons. In addition, the beam can also Coulomb deflect. The deflected beam is harder to tune since the quads direct particles based on the mass to charge ratio (m/q). The m/q of the deflected particles is different enough from the non-deflected particles that they cannot be tuned into the beam dump using the quads behind the NBL. As a result, the deflected beam interacts with the beam pipe made of stainless steel, producing and scattering neutrons.

The tests were repeated in September 2019 using a 35 MeV/nuc ^{78}Kr beam on the 500 μg/cm^2 ^{58}Ni target from the K500 cyclotron. Results indicated the quads did not have an impact on the NBL rate. However, the background rate for the K500 beam was lower due to the x-dispersion

properties previously discussed. The size of the spot was also monitored on the beam viewer as the quad settings were changed and showed no significant changes.

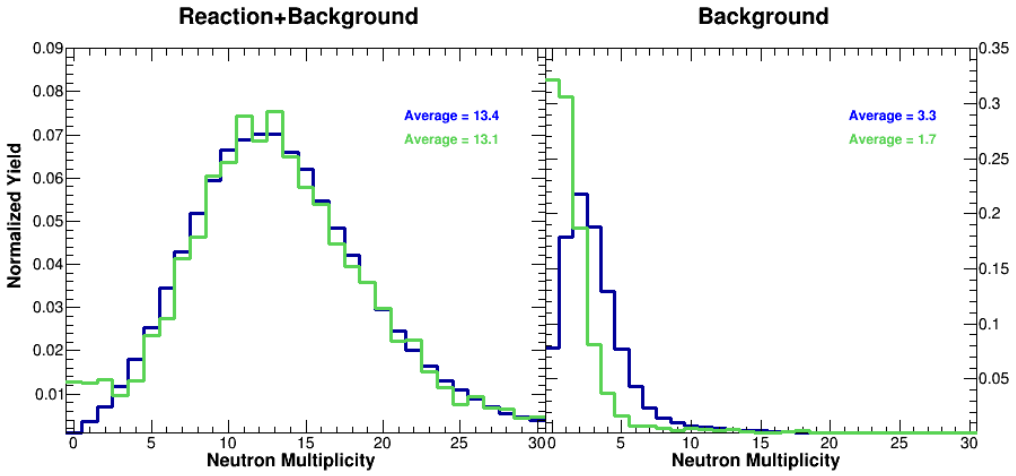

Figure 6.44: The multiplicity distribution for the current and previous cave configuration. The current distribution is shown in green and the previous configuration in blue. Results are plotted for the total multiplicity, or combination of reaction and background, (left panel) and the multiplicity distribution of the background (right). The average multiplicity for the total is 13.4 neutrons for the previous configuration and 13.1 neutrons for the new one. The background average multiplicity is 3.3 and 1.7 neutrons for the previous and new configuration, respectively. The average neutron multiplicity per reaction for the previous and new configurations are 10.1 and 11.4 neutrons, respectively.

In the same September 2019 experiment, the background and the neutron rate were characterized for the new cave configuration by directly comparing the results to the ones from S. Wuenschel's thesis [65]. The reaction system was ^{78}Kr on ^{58}Ni at 35 MeV/nuc. Figure 6.44 shows the results for the total rate (left panel) and background rate (right panel). The results for the previous cave configuration are plotted in blue and the new ones are in green. The results indicate the average neutron multiplicity for the total (reaction and background) window is approximately 13 neutrons for both experiments. However, the background is approximately 1.5 neutron higher for the new configuration than the old one. The effect can be attributed to the new beam dump. As previously mentioned, the vast majority of the beam ends up in the beam dump due to the tight beam spot produced from the K500 cyclotron. The beam dump is designed to thermalize and capture neutrons on the boron as they disperse from the core. The outside of the beam dump is covered

in concrete blocks, which acts as both a reflector for the fast neutrons and a means to capture the neutrons onto the hydrogen in the water.

The concrete half-wall behind the NBL from the previous configuration did a sufficient job at deflecting the neutrons away from the NBL. However, the concrete is not as good at absorbing the neutrons as the borated polyethylene. The results indicate that the neutrons from the the beam dump in the new configuration are more likely to be absorbed in comparison to the previous configuration. The neutrons in the previous configuration were more likely to be deflected away from the NBL using the concrete half-wall, bounce off the walls in the cave and eventually end up in the NBL compared to the new configuration.

7. CONCLUSIONS

Constraining the density dependence of asymmetry energy is an important goal to further quantify the nuclear equation of state. It is crucial to understanding astrophysical phenomena such as the neutron star skin thickness and heavy element formation in supernova explosions. Many probes have been used to help constrain the asymmetry energy term. The one focused on in this dissertation is neutron-proton (NZ) equilibration in ^{70}Zn+^{70}Zn, ^{64}Zn+^{64}Zn and ^{64}Ni+^{64}Ni at 35 MeV/nuc. The composition of the two heaviest fragments originating from the excited projectile-like fragment (PLF*) were examined as a function of angle of rotation. The results were compared to simulations performed using Anti-symmetrized Molecular Dynamics (AMD) and Constrained Molecular Dynamics (COMD) model.

The neutron-proton equilibration was examined as a function of the charge of the heaviest fragment (**HF**) and lighter fragment (**LF**). The velocity of the fragments was plotted and the results showed an average velocity of both **HF** and **LF** above mid-velocity. The velocity of the **HF** was greater than the **LF**. The results are consistent with both fragments originating from the PLF*, with the **HF** originating from the PLF end and the **LF** coming from the neck region.

The angular distribution exhibited a large enhancement in the yield for **HF** decay forward of the **LF** over an isotropic background. The bi-modal feature is consistent with the dynamical and statistical decay mechanism seen in previous results [5, 41].

The experimental results for the composition ($\Delta = \frac{(N-Z)}{A}$) showed an exponential decrease in the average composition of the **LF** as the rotational angle (α) increased. The results are consistent and expand upon the work from Hudan *et al*. [7, 72] and Brown *et al*. [8]. The **HF** composition showed a mirroring effect, where the composition started off relatively neutron-poor and evolved to be more neutron-rich. The increase in composition is consistent with the simulated predictions from Stiefel *et al*. [9] The exponential change in concentration was approximately equal for the **HF** and **LF**, and follows first-order kinetics.

The Δ vs. α results were fit with an exponential. The extracted rate constant was converted to time assuming a monotonic and linear correlation between the rotational angle and time. The results showed a mean equilibration time of τ_H=0.3$\pm^{0.5}_{0.3}$ zs and τ_L=0.3$\pm^{0.3}_{0.2}$ zs for ^{70}Zn+^{70}Zn reac-

tion system, τ_L=0.3$\pm^{0.4}_{0.2}$ zs and τ_H=0.3$\pm^{0.3}_{0.2}$ zs for ^{64}Zn+^{64}Zn reaction system, and τ_L=0.3$\pm^{0.4}_{0.2}$ zs and τ_H=0.3$\pm^{0.3}_{0.2}$ zs for ^{64}Ni+^{64}Ni reaction system. The results were compared to previous work [48, 49, 77, 6] and were consistent within error bars.

The NZ equilibration results illustrate a highly-deformed PLF* with a small, neutron-rich component coming from the neck region and a larger projectile-like component (PLF). The PLF is more neutron-proton symmetric. If the fragments break up immediately after formation, the difference in the neutron content of each component is preserved. The equilibration is governed by the contact time as well as the force driving the equilibration, which can be directly related back to the nuclear equation of state. The first-order kinetics behavior and the equivalent mean equilibration lifetimes between the **HF** and the **LF** indicate the equilibration is only dependent on the difference in the chemical potential of the **HF** and **LF** and not secondary effects.

The COMD and AMD results were passed through a software filter of the NIMROD array to simulate the experimental conditions. Results from COMD and AMD showed an exponential decrease in the composition of the **LF** as a function of atomic number. The rate constants were extracted in per degrees and results showed good agreement with the experimental data for the soft AMD and COMD interaction. The stiff COMD interaction also showed agreement with the experimental results. However, the COMD super-stiff interaction over-predicted the rate of equilibration and the stiff AMD interaction under-predicted the rate. GEMINI was applied and results washed out the exponential effect for the AMD results. The exponential behavior was preserved for the COMD systems, and the rate constants were shown to be consistent with the pre-GEMINI results.

The results for the **HF** only reproduced the exponential trend observed experimentally for the soft AMD interaction. A linear increase in the composition as a function of α was seen for the COMD soft and stiff interaction, which the greatest extent of equilibration seen for the soft interaction. The stiff AMD and super-stiff COMD reproduced no difference in the initial and final compositions. The super-stiff COMD interaction produced a flat distribution, whereas the stiff AMD interaction produced a V-shaped interaction. The results were analyzed after GEMINI was applied and the results produced inverse effects. The composition was becoming more neutron-rich as the rotational angle increased, due to the most neutron-rich fragments being furthest from the line of stability and hence de-excited more. A mean equilibration lifetime for the soft AMD results was extracted to be k_H=0.03±0.01 per degree.

Lastly, the NIMROD array was recommission and upgraded to include additional Si-Si-CsI (supertelescope) stacks and new electronic modules. The thickness uniformity of the new purchased detectors was tested and the thickness across the detectors were within ±1%. Channeling effects were seen and quantified. The channeling effects were minimized between $3^\circ \leq \theta_H \leq 5^\circ$. The results from the CsI slow vs. fast particle identification method are consistent with the previous experimental campaign. The Si-Si and CsI-Si isotopic identification range is much lower than previous results due to a combination of new electronics, detector resolution issues and white noise. The neutron ball and the cave it is housed in was also reconfigured. Results showed the average neutron ball multiplicity is equivalent in the first 100μs measured, but the average background rate is approximately 1.5 neutrons lower than the previous configuration.

In summary, NZ equilibration is observed between the two heaviest fragments originating from the PLF* in ^{70}Zn+^{70}Zn, ^{64}Zn+^{64}Zn and ^{64}Ni+^{64}Ni at 35 MeV/nucleon. An average mean equilibration lifetime of 0.3 zs was observed for **HF** and **LF** for all three reaction systems. Most signatures were observed for an AMD and COMD soft interaction and the COMD stiff interaction. The super-stiff COMD and stiff AMD interactions were not consistent with the examined observables.

REFERENCES

[1] A. Jedele, A. B. McIntosh, K. Hagel, M. Huang, L. Heilborn, Z. Kohley, L. W. May, E. McCleskey, M. Youngs, A. Zarrella, and S. J. Yennello, Phys. Rev. Lett. **118**, 062501 (2017).

[2] G. Audi, A. Wapstra, and C. Thibault, Nuclear Physics A **729**, 337 (2003), the 2003 NUBASE and Atomic Mass Evaluations.

[3] A. Poulsen, "Neutron-proton equilibration drawings," oxidantshappen-comics.wordpress.com, accessed Oct. 14, 2020.

[4] A. Rodriguez Manso, A. B. McIntosh, A. Jedele, K. Hagel, L. Heilborn, Z. Kohley, L. W. May, A. Zarrella, and S. J. Yennello, Phys. Rev. C **95**, 044604 (2017).

[5] G. Casini, P. G. Bizzeti, P. R. Maurenzig, A. Olmi, A. A. Stefanini, J. P. Wessels, R. J. Charity, R. Freifelder, A. Gobbi, N. Herrmann, K. D. Hildenbrand, and H. Stelzer, Phys. Rev. Lett. **71**, 2567 (1993).

[6] M. B. Tsang, T. X. Liu, L. Shi, P. Danielewicz, C. K. Gelbke, X. D. Liu, W. G. Lynch, W. P. Tan, G. Verde, A. Wagner, H. S. Xu, W. A. Friedman, L. Beaulieu, B. Davin, R. T. de Souza, Y. Larochelle, T. Lefort, R. Yanez, V. E. Viola, R. J. Charity, and L. G. Sobotka, Phys. Rev. Lett. **92**, 062701 (2004).

[7] S. Hudan, A. B. McIntosh, R. T. de Souza, S. Bianchin, J. Black, A. Chbihi, M. Famiano, M. O. Frégeau, J. Gauthier, D. Mercier, J. Moisan, C. J. Metelko, R. Roy, C. Schwarz, W. Trautmann, and R. Yanez, Phys. Rev. C **86**, 021603 (2012).

[8] K. Brown, S. Hudan, R. T. deSouza, J. Gauthier, R. Roy, D. V. Shetty, G. A. Souliotis, and S. J. Yennello, Phys. Rev. C **87**, 061601 (2013).

[9] K. Stiefel, Z. Kohley, R. T. deSouza, S. Hudan, and K. Hammerton, Phys. Rev. C **90**, 061605 (2014).

[10] Z. Kohley, *Transverse collective flow and emission order of mid-rapidity fragments in Fermi-Energy Heavy Ion Collisions*, Ph.D. thesis, Texas A&M University (2010).

[11] S. Wuenschel, K. Hagel, R. Wada, J. Natowitz, S. Yennello, Z. Kohley, C. Bottosso, L. May, W. Smith, D. Shetty, B. Stein, S. Soisson, and G. Prete, Nuclear Instruments and Methods in Physics Research Section A: Accelerators, Spectrometers, Detectors and Associated

Equipment **604**, 578 (2009).

[12] S. Piantelli, G. Casini, A. Ono, G. Poggi, G. Pastore, S. Barlini, A. Boiano, E. Bonnet, B. Borderie, R. Bougault, M. Bruno, A. Buccola, A. Camaiani, A. Chbihi, M. Cicerchia, M. Cinausero, M. D'Agostino, M. Degerlier, J. A. Dueñas, Q. Fable, D. Fabris, J. D. Frankland, C. Frosin, F. Gramegna, D. Gruyer, M. Henri, A. Kordyasz, T. Kozik, N. Le Neindre, I. Lombardo, O. Lopez, G. Mantovani, T. Marchi, L. Morelli, A. Olmi, P. Ottanelli, M. Pârlog, G. Pasquali, A. A. Stefanini, G. Tortone, S. Upadhyaya, S. Valdré, G. Verde, E. Vient, M. Vigilante, R. Alba, and C. Maiolino, Phys. Rev. C **101**, 034613 (2020).

[13] C. J. Horowitz, E. F. Brown, Y. Kim, W. G. Lynch, R. Michaels, A. Ono, J. Piekarewicz, M. B. Tsang, and H. H. Wolter, Journal of Physics G: Nuclear and Particle Physics **41**, 093001 (2014).

[14] L. Bardelli, "Study of channeling effects in silicon detectors for pulse-shape applications," (2007), iWM.

[15] "Micron semiconductor, ltd," www.micronsemiconductor.co.uk, accessed Oct. 14, 2020.

[16] C. Metelko, A. Alexander, S. Hudan, J. Poehlman, and R. de Souza, Nuclear Instruments and Methods in Physics Research Section A: Accelerators, Spectrometers, Detectors and Associated Equipment **569**, 815 (2006).

[17] S. I. Systeme, *SIS3316 16 Channel VME Digitizer User Manual*, Struck Innovative Systeme (2015).

[18] A. Steiner, M. Prakash, J. Lattimer, and P. Ellis, Physics Reports **411**, 325 (2005).

[19] P. Demorest, T. Pennucci, S. M. Ransom, M. S. E. Roberts, and J. W. T. Hessels, Nature **467**, 1081 (2010).

[20] J. M. Lattimer and M. Prakash, The Astrophysical Journal **550**, 426 (2001).

[21] J. M. Lattimer and M. Prakash, Science **304**, 536 (2004), https://science.sciencemag.org/content/304/5670/536.full.pdf .

[22] M. B. Tsang, J. R. Stone, F. Camera, P. Danielewicz, S. Gandolfi, K. Hebeler, C. J. Horowitz, J. Lee, W. G. Lynch, Z. Kohley, R. Lemmon, P. Möller, T. Murakami, S. Riordan, X. Roca-Maza, F. Sammarruca, A. W. Steiner, I. Vidaña, and S. J. Yennello, Phys. Rev. C **86**, 015803 (2012).

[23] C. F. v. Weizsäcker, Zeitschrift für Physik **96**, 431 (1935).

[24] V. Baran, M. Colonna, V. Greco, and M. D. Toro, Physics Reports **410**, 335 (2005).

[25] M. A. Famiano, T. Liu, W. G. Lynch, M. Mocko, A. M. Rogers, M. B. Tsang, M. S. Wallace, R. J. Charity, S. Komarov, D. G. Sarantites, L. G. Sobotka, and G. Verde, Phys. Rev. Lett. **97**, 052701 (2006).

[26] M. B. Tsang, Y. Zhang, P. Danielewicz, M. Famiano, Z. Li, W. G. Lynch, and A. W. Steiner, Phys. Rev. Lett. **102**, 122701 (2009).

[27] H.-l. Liu, G.-C. Yong, and D.-H. Wen, Phys. Rev. C **91**, 044609 (2015).

[28] M. B. Tsang, C. K. Gelbke, X. D. Liu, W. G. Lynch, W. P. Tan, G. Verde, H. S. Xu, W. A. Friedman, R. Donangelo, S. R. Souza, C. B. Das, S. Das Gupta, and D. Zhabinsky, Phys. Rev. C **64**, 054615 (2001).

[29] G. A. Souliotis, D. V. Shetty, A. Keksis, E. Bell, M. Jandel, M. Veselsky, and S. J. Yennello, Phys. Rev. C **73**, 024606 (2006).

[30] S. Galanopoulos, G. Souliotis, A. Keksis, M. Veselsky, Z. Kohley, L. May, D. Shetty, S. Soisson, B. Stein, S. Wuenschel, and S. Yennello, Nuclear Physics A **837**, 145 (2010).

[31] G. A. Souliotis, P. N. Fountas, M. Veselsky, S. Galanopoulos, Z. Kohley, A. McIntosh, S. J. Yennello, and A. Bonasera, Phys. Rev. C **90**, 064612 (2014).

[32] M. Veselsky, G. A. Souliotis, and M. Jandel, Phys. Rev. C **69**, 044607 (2004).

[33] S. Wuenschel, R. Dienhoffer, G. A. Souliotis, S. Galanopoulos, Z. Kohley, K. Hagel, D. V. Shetty, K. Huseman, L. W. May, S. N. Soisson, B. C. Stein, A. L. Caraley, and S. J. Yennello, Phys. Rev. C **79**, 061602 (2009).

[34] L. May, *Isospin Equilibration in Fermi-Energy Heavy-Ion Nuclear Collisions*, Ph.D. thesis, Texas A&M University (2015).

[35] A. W. Steiner and B.-A. Li, Phys. Rev. C **72**, 041601 (2005).

[36] V. Baran, M. Colonna, and M. D. Toro, Nuclear Physics A **730**, 329 (2004).

[37] Z. Y. Sun, M. B. Tsang, W. G. Lynch, G. Verde, F. Amorini, L. Andronenko, M. Andronenko, G. Cardella, M. Chatterje, P. Danielewicz, E. De Filippo, P. Dinh, E. Galichet, E. Geraci, H. Hua, E. La Guidara, G. Lanzalone, H. Liu, F. Lu, S. Lukyanov, C. Maiolino, A. Pagano, S. Piantelli, M. Papa, S. Pirrone, G. Politi, F. Porto, F. Rizzo, P. Russotto, D. Santonocito, and Y. X. Zhang, Phys. Rev. C **82**, 051603 (2010).

[38] C. P. Montoya, W. G. Lynch, D. R. Bowman, G. F. Peaslee, N. Carlin, R. T. de Souza,

C. K. Gelbke, W. G. Gong, Y. D. Kim, M. A. Lisa, L. Phair, M. B. Tsang, J. B. Webster, C. Williams, N. Colonna, K. Hanold, M. A. McMahan, G. J. Wozniak, and L. G. Moretto, Phys. Rev. Lett. **73**, 3070 (1994).

[39] F. Bocage, J. Colin, M. Louvel, G. Auger, C. Bacri, N. Bellaize, B. Borderie, R. Bougault, R. Brou, P. Buchet, J. Charvet, A. Chbihi, D. Cussol, R. Dayras, N. D. Cesare, A. Demeyer, D. DorÃl', D. Durand, J. Frankland, E. Galichet, E. Genouin-Duhamel, E. Gerlic, D. Guinet, P. Lautesse, J. Laville, J. Lecolley, R. Legrain, N. L. Neindre, O. Lopez, A. Maskay, L. Nalpas, A. Nguyen, M. PÃćrlog, J. PÃl'ter, E. Plagnol, M. Rivet, E. Rosato, F. Saint-Laurent, S. Salou, J. Steckmeyer, M. Stern, G. TÄČbÄČcaru, B. Tamain, O. Tirel, L. Tassan-Got, E. Vient, M. Vigilante, C. Volant, J. Wieleczko, C. L. Brun, A. Genoux-Lubain, G. Rudolf, and L. StuttgÃl', Nuclear Physics A **676**, 391 (2000).

[40] B. Davin, R. Alfaro, H. Xu, L. Beaulieu, Y. Larochelle, T. Lefort, R. Yanez, S. Hudan, A. L. Caraley, R. T. de Souza, T. X. Liu, X. D. Liu, W. G. Lynch, R. Shomin, W. P. Tan, M. B. Tsang, A. Vander Molen, A. Wagner, H. F. Xi, C. K. Gelbke, R. J. Charity, and L. G. Sobotka, Phys. Rev. C **65**, 064614 (2002).

[41] J. Colin, D. Cussol, J. Normand, N. Bellaize, R. Bougault, A. M. Buta, D. Durand, O. Lopez, L. Manduci, J. Marie, J. C. Steckmeyer, B. Tamain, A. Van Lauwe, E. Vient, B. Borderie, F. Lavaud, N. Le Neindre, P. Pawłowski, E. Plagnol, M. F. Rivet, B. Bouriquet, A. Chbihi, J. D. Frankland, D. Guinet, B. Guiot, S. Hudan, J. P. Wieleczko, J. L. Charvet, R. Dayras, E. Galichet, P. Lautesse, L. Nalpas, M. Pârlog, E. Rosato, R. Roy, M. Vigilante, and C. Volant (INDRA Collaboration), Phys. Rev. C **67**, 064603 (2003).

[42] E. D. Filippo, A. Pagano, E. Piasecki, F. Amorini, A. Anzalone, L. Auditore, V. Baran, I. Berceanu, J. Blicharska, J. Brzychczyk, A. Bonasera, B. Borderie, R. Bougault, M. Bruno, G. Cardella, S. Cavallaro, M. B. Chatterjee, A. Chbihi, M. Colonna, M. D'Agostino, R. Dayras, M. D. Toro, J. Frankland, E. Galichet, W. Gawlikowicz, E. Geraci, F. Giustolisi, A. Grzeszczuk, P. Guazzoni, D. Guinet, M. Iacono-Manno, S. Kowalski, E. L. Guidara, G. Lanzanó, G. Lanzalone, N. L. Neindre, S. Li, S. L. Nigro, C. Maiolino, Z. Majka, M. Papa, M. Petrovici, S. Pirrone, R. Płaneta, G. Politi, A. Pop, F. Porto, M. F. Rivet, E. Rosato, F. Rizzo, S. Russo, P. Russotto, M. Sassi, K. Schmidt, K. Siwek-Wilczyńska, I. Skwira, M. L. Sperduto, J. C. Steckmeyer, L. Świderski, A. Trifirò, M. Trimarchi, G. Vannini, M. Vigilante,

J. P. Wieleczko, J. Wilczyński, H. Wu, Z. Xiao, L. Zetta, and W. Zipper (REVERSE Collaboration), Phys. Rev. C **71**, 064604 (2005).

[43] A. B. McIntosh, S. Hudan, J. Black, D. Mercier, C. J. Metelko, R. Yanez, R. T. de Souza, A. Chbihi, M. Famiano, M. O. Frégeau, J. Gauthier, J. Moisan, R. Roy, S. Bianchin, C. Schwarz, and W. Trautmann, Phys. Rev. C **81**, 034603 (2010).

[44] S. Hudan, R. Alfaro, L. Beaulieu, B. Davin, Y. Larochelle, T. Lefort, V. E. Viola, H. Xu, R. Yanez, R. T. de Souza, R. J. Charity, L. G. Sobotka, T. X. Liu, X. D. Liu, W. G. Lynch, R. Shomin, W. P. Tan, M. B. Tsang, A. Vander Molen, A. Wagner, and H. F. Xi, Phys. Rev. C **70**, 031601 (2004).

[45] E. De Filippo, A. Pagano, P. Russotto, F. Amorini, A. Anzalone, L. Auditore, V. Baran, I. Berceanu, B. Borderie, R. Bougault, M. Bruno, T. Cap, G. Cardella, S. Cavallaro, M. B. Chatterjee, A. Chbihi, M. Colonna, M. D'Agostino, R. Dayras, M. Di Toro, J. Frankland, E. Galichet, W. Gawlikowicz, E. Geraci, A. Grzeszczuk, P. Guazzoni, S. Kowalski, E. La Guidara, G. Lanzalone, G. Lanzanò, N. Le Neindre, I. Lombardo, C. Maiolino, M. Papa, E. Piasecki, S. Pirrone, R. Płaneta, G. Politi, A. Pop, F. Porto, M. F. Rivet, F. Rizzo, E. Rosato, K. Schmidt, K. Siwek-Wilczyńska, I. Skwira-Chalot, A. Trifirò, M. Trimarchi, G. Verde, M. Vigilante, J. P. Wieleczko, J. Wilczyński, L. Zetta, and W. Zipper, Phys. Rev. C **86**, 014610 (2012).

[46] D. Thériault, J. Gauthier, F. Grenier, F. Moisan, C. St-Pierre, R. Roy, B. Davin, S. Hudan, T. Paduszynski, R. T. d. Souza, E. Bell, J. Garey, J. Iglio, A. L. Keksis, S. Parketon, C. Richers, D. V. Shetty, S. N. Soisson, G. A. Souliotis, B. C. Stein, and S. J. Yennello, Phys. Rev. C **74**, 051602 (2006).

[47] J. Wilczyński and K. Siwek-Wilczyńska, Physics Letters B **55**, 270 (1975).

[48] L. G. Moretto and R. P. Schmitt, Reports on Progress in Physics **44**, 533 (1981).

[49] J. Galin, B. Gatty, D. Guerreau, M. Lefort, X. Tarrago, R. Babinet, B. Cauvin, J. Girard, and H. Nifenecker, Zeitschrift für Physik A Atoms and Nuclei **278**, 347 (1976).

[50] B. Gatty, D. Guerreau, M. Lefort, X. Tarrago, J. Galin, B. Cauvin, J. Girard, and H. Nifenecker, Nuclear Physics A **253**, 511 (1975).

[51] J. B. Natowitz, M. N. Namboodiri, P. Kasiraj, R. Eggers, L. Adler, P. Gonthier, C. Cerruti, and T. Alleman, Phys. Rev. Lett. **40**, 751 (1978).

[52] P. Glässel, R. S. Simon, R. M. Diamond, R. C. Jared, I. Y. Lee, L. G. Moretto, J. O. Newton, R. Schmitt, and F. S. Stephens, Phys. Rev. Lett. **38**, 331 (1977).

[53] G. Wozniak, G. Mathews, R. Schmitt, R. Regimbart, H. HÃijbel, R. Diamond, and L. Moretto, Nuclear Physics A **402**, 322 (1983).

[54] E. Hernandez, W. Myers, J. Randrup, and B. Remaud, Nuclear Physics A **361**, 483 (1981).

[55] G. Casini, A. A. Stefanini, M. Bini, P. R. Maurenzig, A. Olmi, G. Poggi, R. J. Charity, R. Freifelder, A. Gobbi, K. D. Hildenbrand, M. H. Tanaka, and J. P. Wessels, Phys. Rev. Lett. **67**, 3364 (1991).

[56] A. A. Stefanini, G. Casini, P. R. Maurenzig, A. Olmi, R. Charity, R. Freifelder, A. Gobbi, N. Herrmann, K. D. Hildenbrand, M. Petrovici, F. Rami, H. Stelzer, J. Wessels, M. Gnirs, D. Pelte, J. Galin, D. Guerreau, U. Jahnke, A. Peghaire, J. Adloff, B. Bilwes, R. Bilwes, and G. Rudolf, Z. Physik A - Hadrons and Nuclei **351**, 167 (1995).

[57] E. Bell, *N/Z Equilibration*, Ph.D. thesis, Texas A&M University (2005).

[58] R. Schmitt, L. Cooke, G. Derrig, D. Fabris, B. Hurst, J. Natowitz, G. Nebbia, D. O'Kelly, B. Srivastava, W. Turmel, D. Utley, H. Utsunomiya, and R. Wada, Nuclear Instruments and Methods in Physics Research Section A: Accelerators, Spectrometers, Detectors and Associated Equipment **354**, 487 (1995).

[59] O. Akindele, R. Casperson, B. Wang, J. Burke, R. Hughes, S. Fisher, A. Saastamoinen, and E. Norman, Nuclear Instruments and Methods in Physics Research Section A: Accelerators, Spectrometers, Detectors and Associated Equipment **872**, 112 (2017).

[60] B. Davin, R. de Souza, R. Yanez, Y. Larochelle, R. Alfaro, H. Xu, A. Alexander, K. Bastin, L. Beaulieu, J. Dorsett, G. Fleener, L. Gelovani, T. Lefort, J. Poehlman, R. Charity, L. Sobotka, J. Elson, A. Wagner, T. Liu, X. Liu, W. Lynch, L. Morris, R. Shomin, W. Tan, M. Tsang, G. Verde, and J. Yurkon, Nuclear Instruments and Methods in Physics Research Section A: Accelerators, Spectrometers, Detectors and Associated Equipment **473**, 302 (2001).

[61] J. Elson, "Pico systems, inc." https://pico-systems.com/, accessed Oct. 14, 2020.

[62] K. Kwiatkowski, D. Bracken, K. Morley, J. Brzychczyk, E. R. Foxford], K. Komisarcik, V. Viola, N. Yoder, J. Dorsett, J. Poehlman, N. Madden, and J. Ottarson, Nuclear Instruments and Methods in Physics Research Section A: Accelerators, Spectrometers, Detectors and

Associated Equipment **360**, 571 (1995).

[63] W. Leo, *Techniques for Nuclear and Particle Physics Experiments* (Spring-Verlag, 1994).

[64] G. F. Knoll, *Radiation Detection and Measurements* (John Wiley & Sons, 2000).

[65] S. Wuenschel, *Temperature and Scaling Studies from Projectile Fragmentation of* ^{86,78}*Kr*+^{64,58}*Ni at 35 MeV/A*, Ph.D. thesis, Texas A&M University (2009).

[66] F. Hubert, R. Bimbot, and H. Gauvin, Atomic Data and Nuclear Data Tables **46**, 1 (1990).

[67] R. Wada, T. Keutgen, K. Hagel, Y. G. Ma, J. Wang, M. Murray, L. Qin, P. Smith, J. B. Natowitz, R. Alfarro, J. Cibor, M. Cinausero, Y. E. Masri, D. Fabris, E. Fioretto, A. Keksis, S. Kowalski, M. Lunardon, A. Makeev, N. Marie, E. Martin, Z. Majka, A. Martinez-Davalos, A. Menchaca-Rocha, G. Nebbia, G. Prete, V. Rizzi, A. Ruangma, D. V. Shetty, G. Souliotis, P. Staszel, M. Veselsky, G. Viesti, E. M. Winchester, S. J. Yennello, W. Zipper, and A. Ono (NIMROD Collaboration), Phys. Rev. C **69**, 044610 (2004).

[68] L. Tassan-Got, Nuclear Instruments and Methods in Physics Research Section B: Beam Interactions with Materials and Atoms **194**, 503 (2002).

[69] R. Charity, M. McMahan, G. Wozniak, R. McDonald, L. Moretto, D. Sarantites, L. Sobotka, G. Guarino, A. Pantaleo, L. Fiore, A. Gobbi, and K. Hildenbrand, Nuclear Physics A **483**, 371 (1988).

[70] R. J. Charity, Phys. Rev. C **58**, 1073 (1998).

[71] "code gemini++," www.chemistry.wustl.edu/rc/gemini++/, accessed Oct. 14, 2020.

[72] Hudan, S. and deSouza, R. T., Eur. Phys. J. A **50**, 36 (2014).

[73] N. Carjan and M. Kaplan, Phys. Rev. C **45**, 2185 (1992).

[74] R. Vandenbosch and J. Huizenga, *Nuclear Fission* (Academic Press, New York, 1973).

[75] A. Artukh, G. Gridnev, V. Mikheev, V. Volkov, and J. Wilczyński, Nuclear Physics A **215**, 91 (1973).

[76] J. Galin, D. Guerreau, M. Lefort, J. Peter, X. Tarrago, and R. Basile, Nuclear Physics A **159**, 461 (1970).

[77] P. Russo, R. Schmitt, G. Wozniak, R. Jared, P. Glässel, B. Cauvin, J. Sventek, and L. Moretto, Nuclear Physics A **281**, 509 (1977).

[78] M. Papa, T. Maruyama, and A. Bonasera, Phys. Rev. C **64**, 024612 (2001).

[79] M. Papa, G. Giuliani, and A. Bonasera, Journal of Computational Physics **208**, 403 (2005).

[80] B. Harvey, M. Youngs, A. McIntosh, A. Jedele, A. Abbott, J. Gauthier, K. Hagel, A. Hannaman, K. Krieble, Y. Lui, L. McIntosh, A. Rodriguez Manso, M. Sorensen, Z. Tobin, R. Wada, A. Zarrella, and S. Yennello, "Time dependence of angular alignment in heavy ion collisions," (2020), manuscript to be submitted.

[81] A. Ono and H. Horiuchi, Progress in Particle and Nuclear Physics **53**, 501 (2004).

[82] X. Roca-Maza, M. Brenna, G. Colò, M. Centelles, X. Viñas, B. K. Agrawal, N. Paar, D. Vretenar, and J. Piekarewicz, Phys. Rev. C **88**, 024316 (2013).

[83] A. Tamii, I. Poltoratska, P. von Neumann-Cosel, Y. Fujita, T. Adachi, C. A. Bertulani, J. Carter, M. Dozono, H. Fujita, K. Fujita, K. Hatanaka, D. Ishikawa, M. Itoh, T. Kawabata, Y. Kalmykov, A. M. Krumbholz, E. Litvinova, H. Matsubara, K. Nakanishi, R. Neveling, H. Okamura, H. J. Ong, B. Özel-Tashenov, V. Y. Ponomarev, A. Richter, B. Rubio, H. Sakaguchi, Y. Sakemi, Y. Sasamoto, Y. Shimbara, Y. Shimizu, F. D. Smit, T. Suzuki, Y. Tameshige, J. Wambach, R. Yamada, M. Yosoi, and J. Zenihiro, Phys. Rev. Lett. **107**, 062502 (2011).

[84] P. Danielewicz and J. Lee, Nuclear Physics A **922**, 1 (2014).

[85] "Eurisys mesures," (defunct).

[86] A. Zarrella, *Pionic Fusion of* $^4He+^{12}C$, Ph.D. thesis, Texas A&M University (2018).

[87] J. F. Ziegler, M. Ziegler, and J. Biersack, Nuclear Instruments and Methods in Physics Research Section B: Beam Interactions with Materials and Atoms **268**, 1818 (2010), 19th International Conference on Ion Beam Analysis.

[88] D. Bazin, O. Tarasov, M. Lewitowicz, and O. Sorlin, Nuclear Instruments and Methods in Physics Research Section A: Accelerators, Spectrometers, Detectors and Associated Equipment **482**, 307 (2002).

[89] "W-ie-ne-r," http://www.wiener-d.com/sc/power-supplies/mpod–lvhv/, accessed Oct. 14, 2020.

[90] J. Toke and I. Toke, "Jtec instruments," http://www.jtec-instruments.com, accessed Oct. 14, 2020.

[91] S. Hudan, Private Communication (2018).

[92] K. Hagel, Private Communication (2018).

[93] R. Wada, Private Communication (2018).

[94] “Eljen technology,” https://eljentechnology.com, accessed Oct. 14, 2020.

APPENDIX A

SCHEMATIC OF THE NIMROD ARRAY RINGS

The schematics in this appendix show the location of each silicon and CsI detector within the NIMROD array. Each top and bottom slice, defined by the dark black lines, corresponds to a detector module. The detector module ID is labeled on the outside. The numbering of the silicon and CsI detectors corresponds to the MASE and SIS3316 channels. For the silicon detectors in the supertelescope configuration, the front segments are labeled in red and the back segments are labeled in green. The CsI detectors are labeled according to the location on the motherboard through which the signal is transmitted. The inner rings are labeled CsIB. For the outer rings with one CsI crystal, the signal are patched out through CsIR, and for Rings 7 and 9, CsIL and CsIR was used for the left and right CsI crystals, respectively.

For orientation purposes, the top of the schematic corresponds to 90° in the lab. The point of view for each ring is relative to the target position. Rings 2-11 correspond to the beam traveling into the page and Ring 12-15 correspond to the beam traveling out of the page.

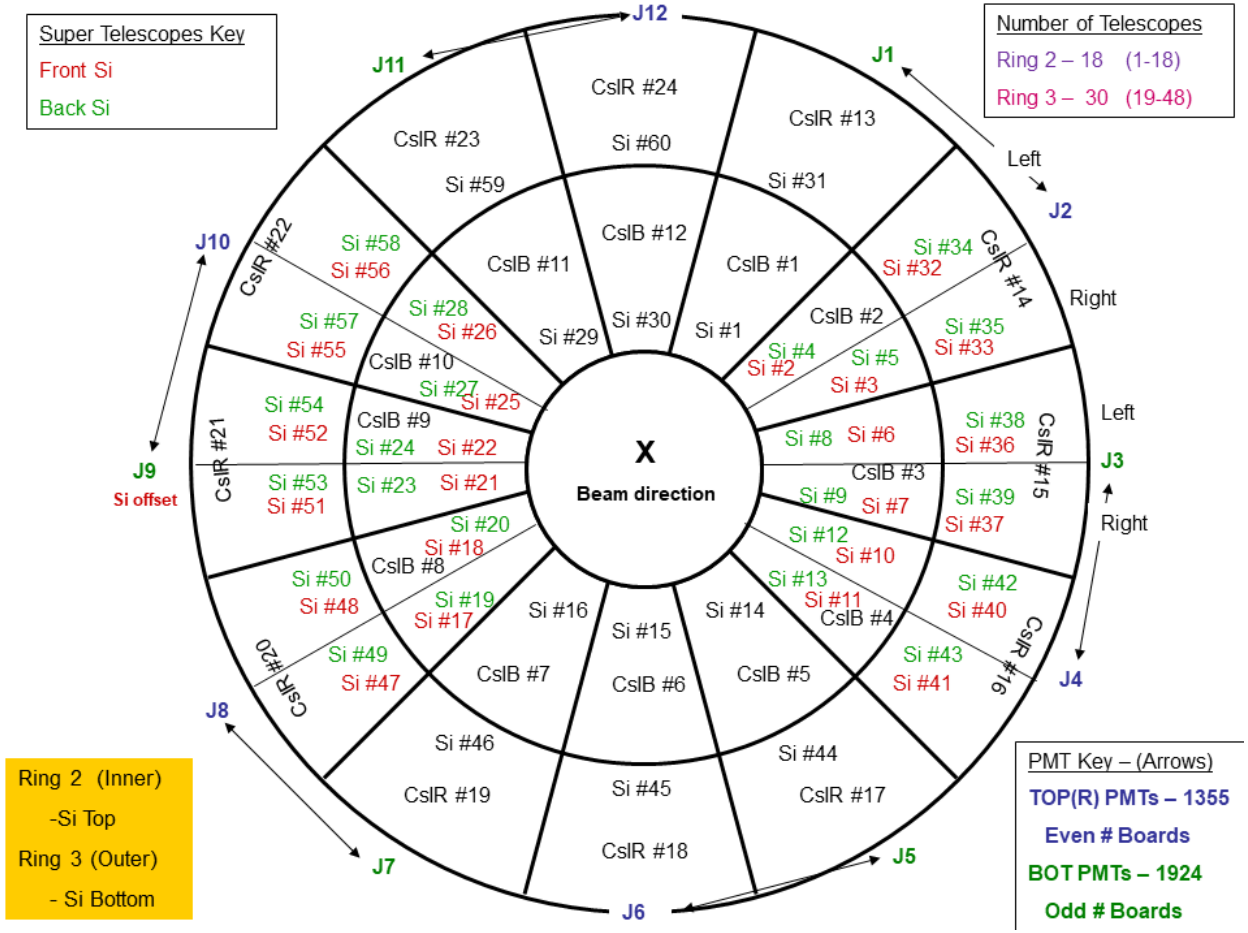

Figure A.1: CsI and Si detector numbering and assignment in Ring 2/3.

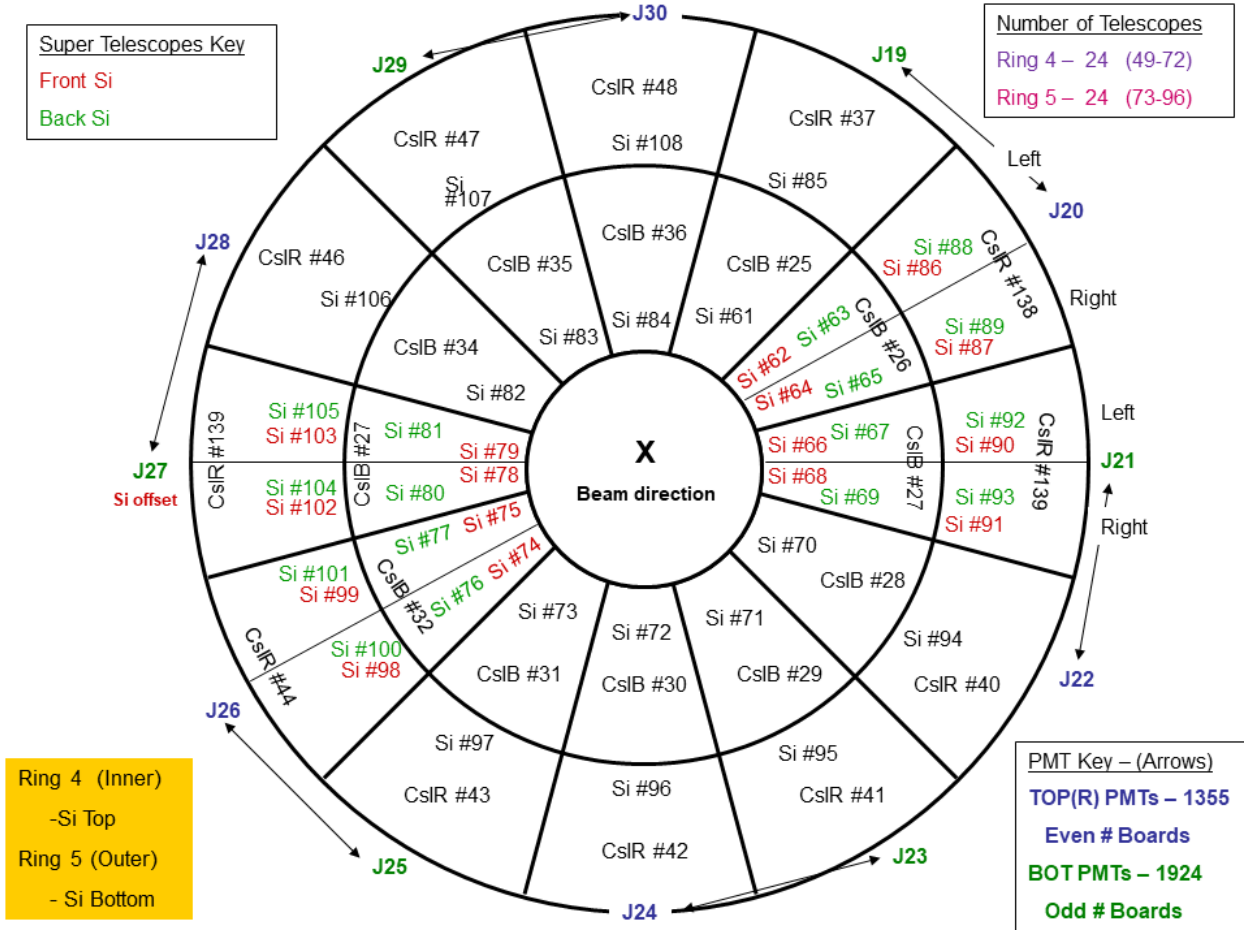

Figure A.2: CsI and Si detector numbering and assignment in Ring 4/5.

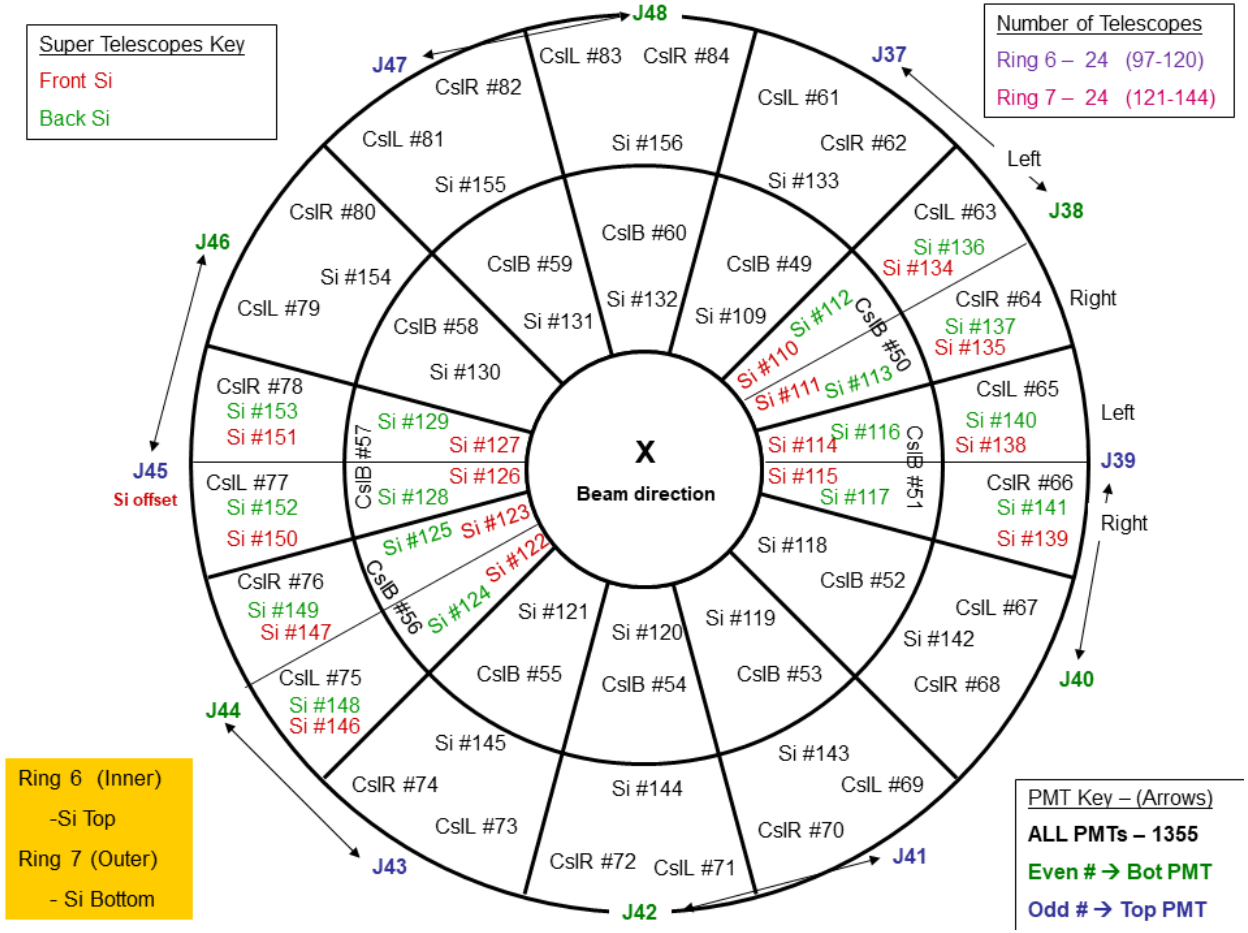

Figure A.3: CsI and Si detector numbering and assignment in Ring 6/7.

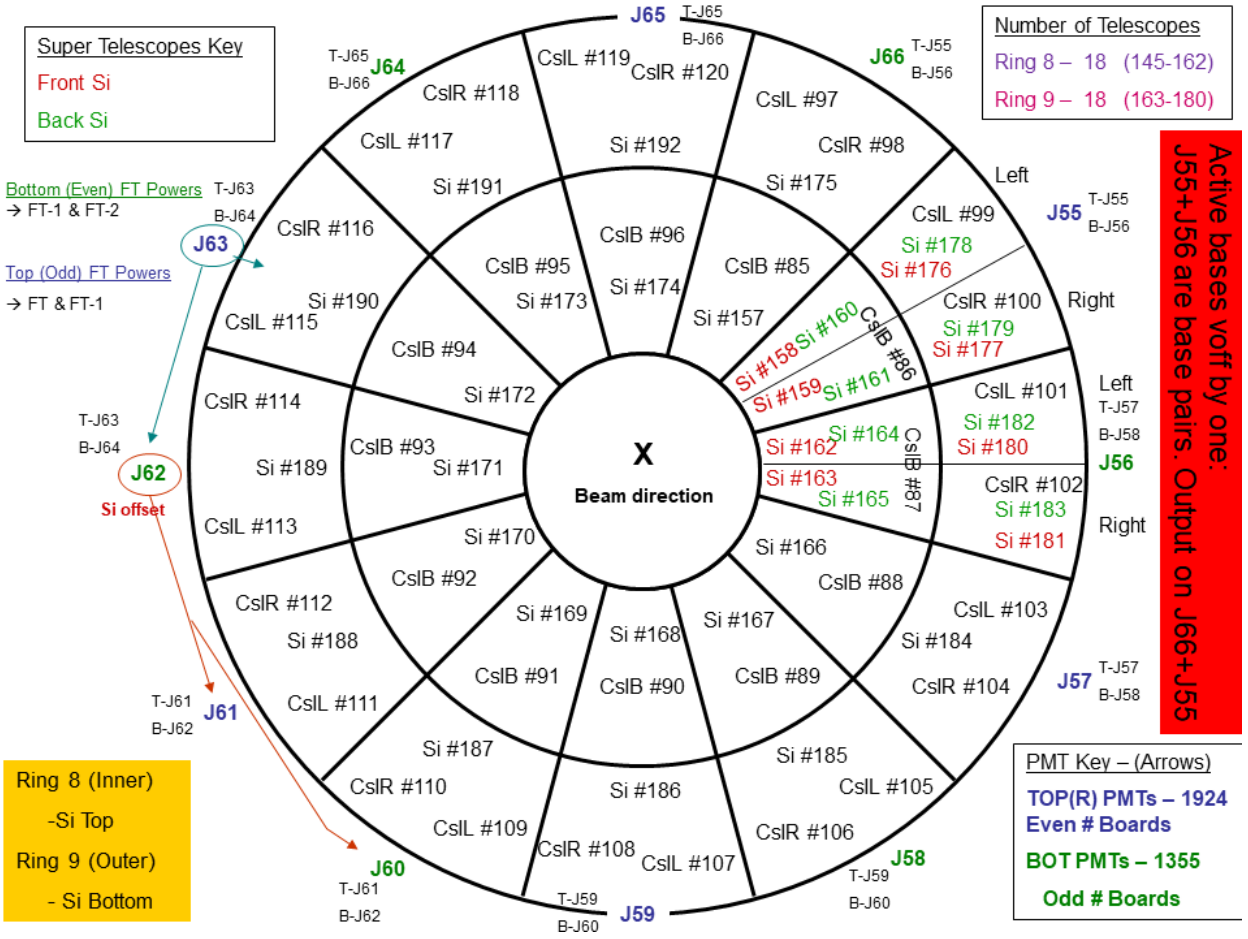

Figure A.4: CsI and Si detector numbering and assignment in Ring 8/9.

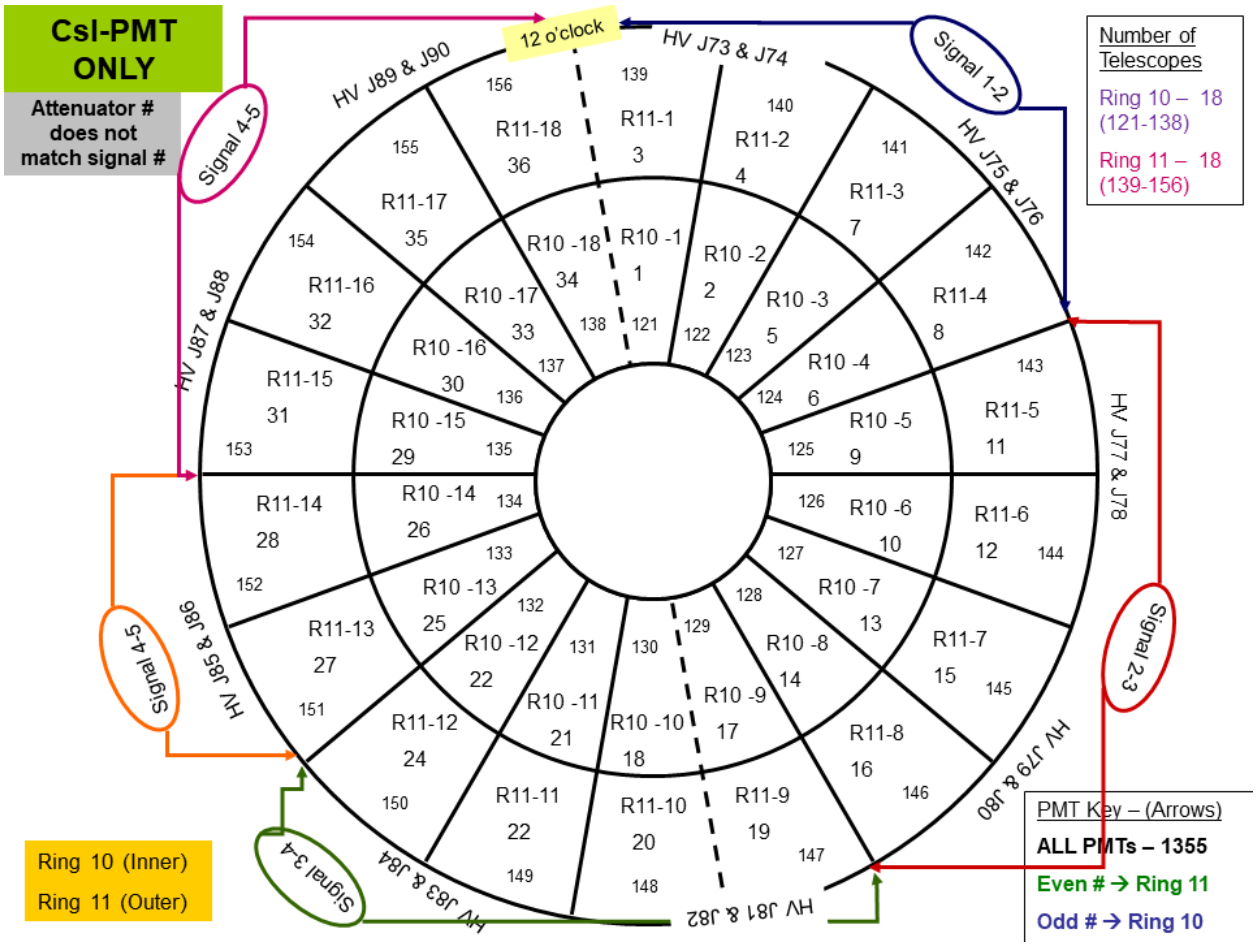

Figure A.5: CsI detector numbering and assignment in Ring 10/11.

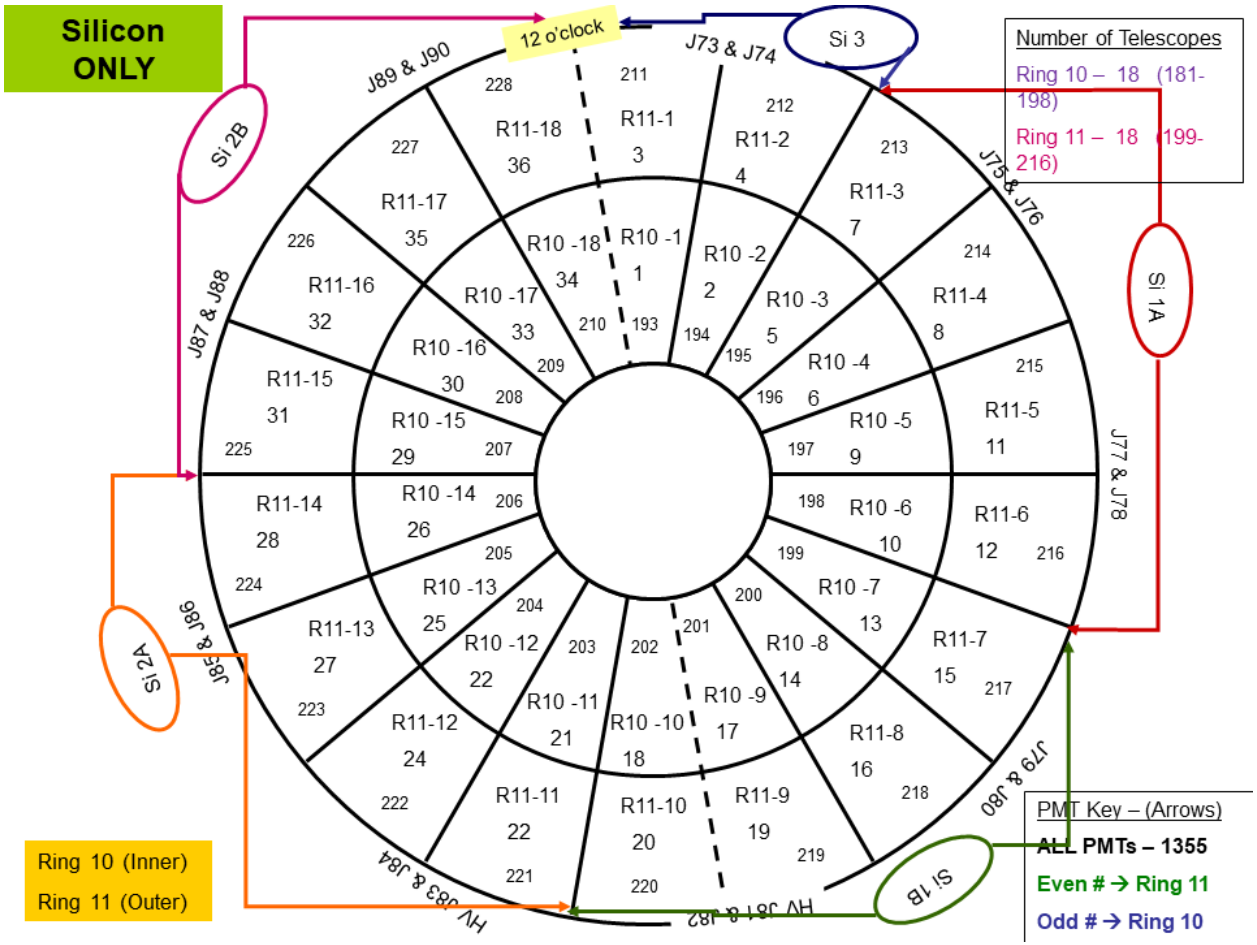

Figure A.6: Si detector numbering and assignment in Ring 10/11.

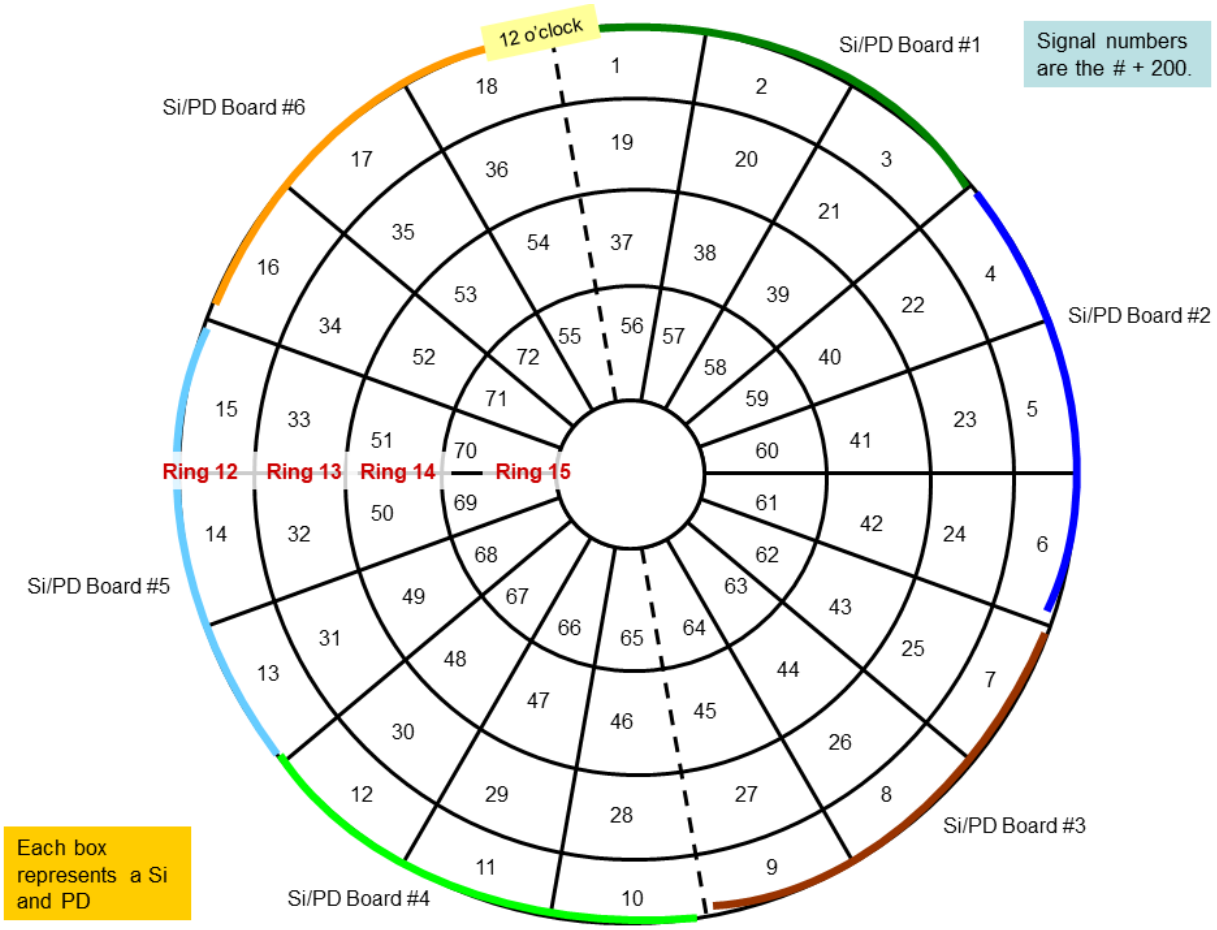

Figure A.7: CsI and Si detector numbering and assignment in Ring 12-15.

APPENDIX B

SCHEMATIC OF THE CSI-PMT LOCATIONS IN NIMROD

The schematics in this appendix show the exterior location corresponding to each CsI-PMT pairing in NIMROD. Each active base powers two CsI in the same ring, with the exception of Ring 7 and 9, which powers 4. There are two different kinds of PMTs used: Hamamatsu 1355s and 1924s. The PMTs have different pin diagrams or assignments of voltage to the PMT. Currently, there are two copies of the original CAD drawing, which has been lost. This appendix serves as a permanent reference.

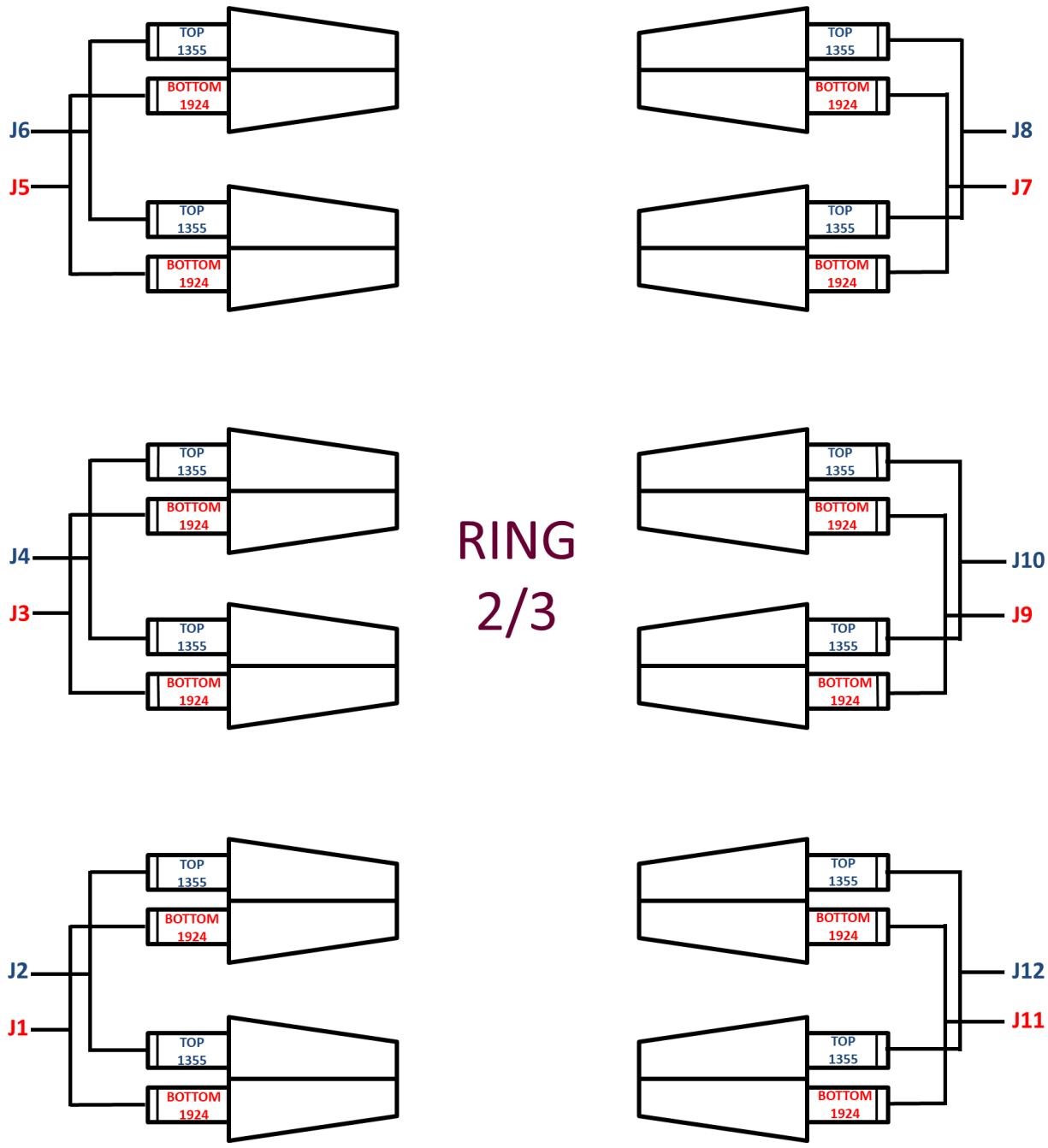

Figure B.1: PMT location of Ring 2/3 CsI detectors.

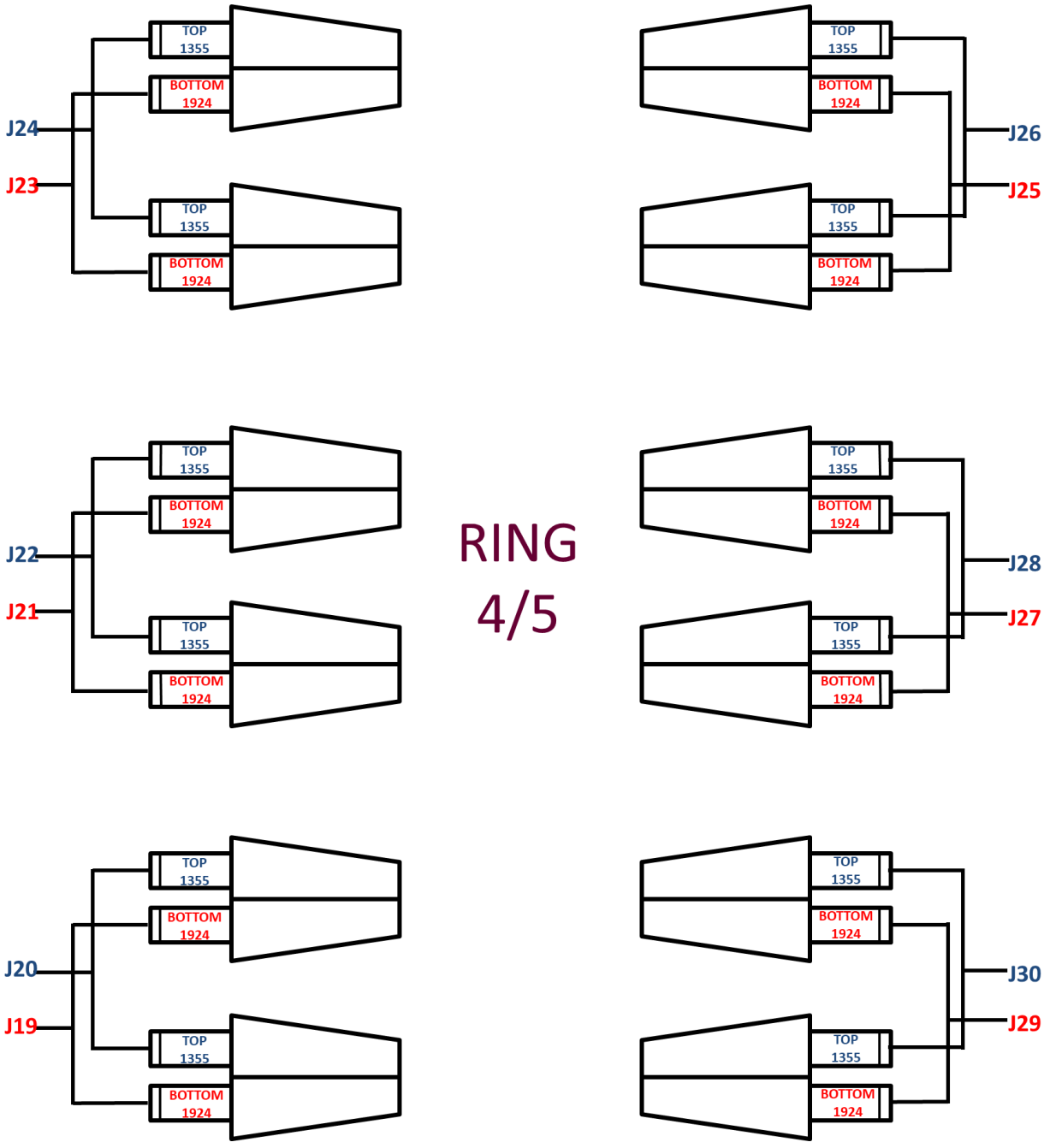

Figure B.2: PMT location of Ring 4/5 CsI detectors.

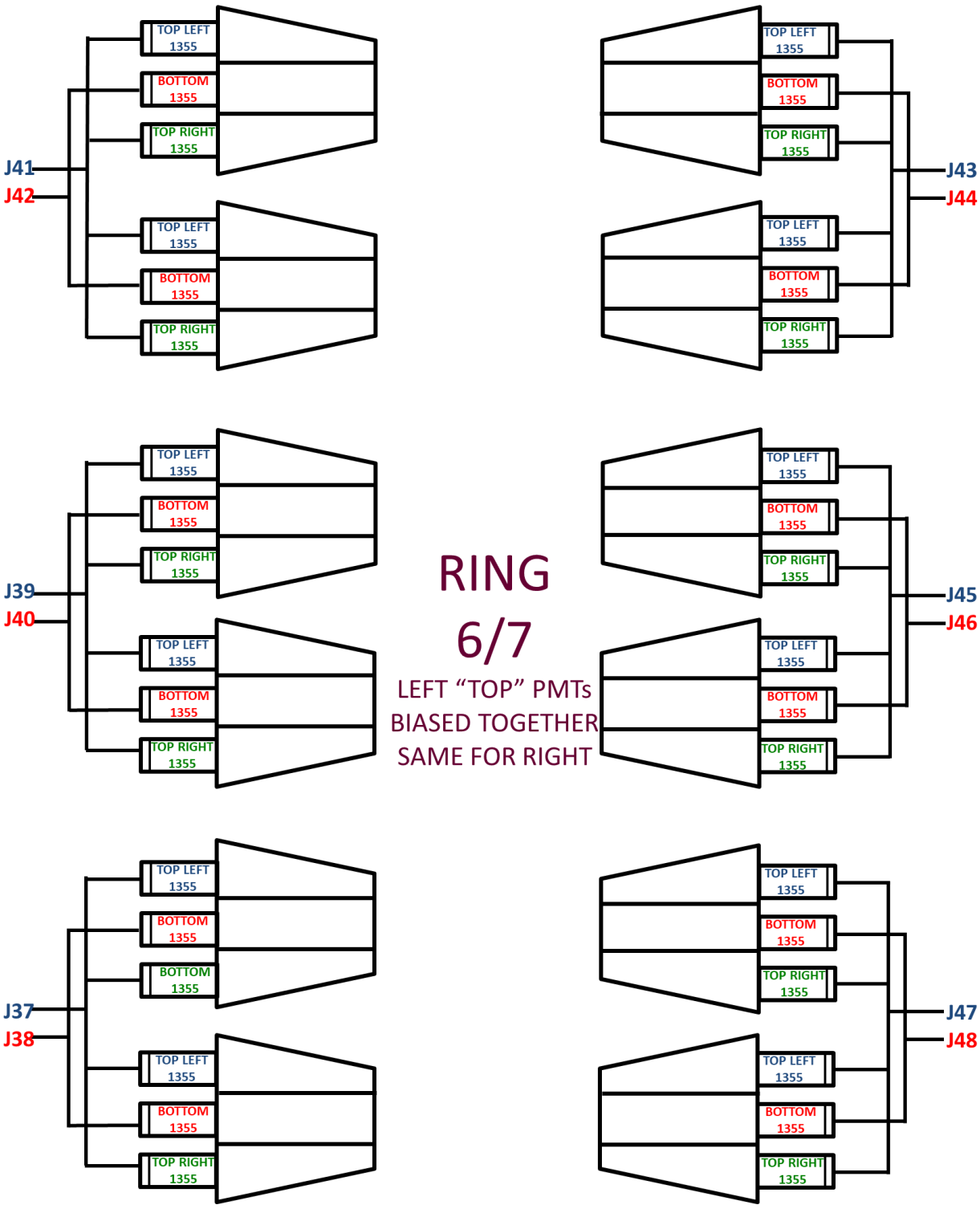

Figure B.3: PMT location of Ring 6/7 CsI detectors.

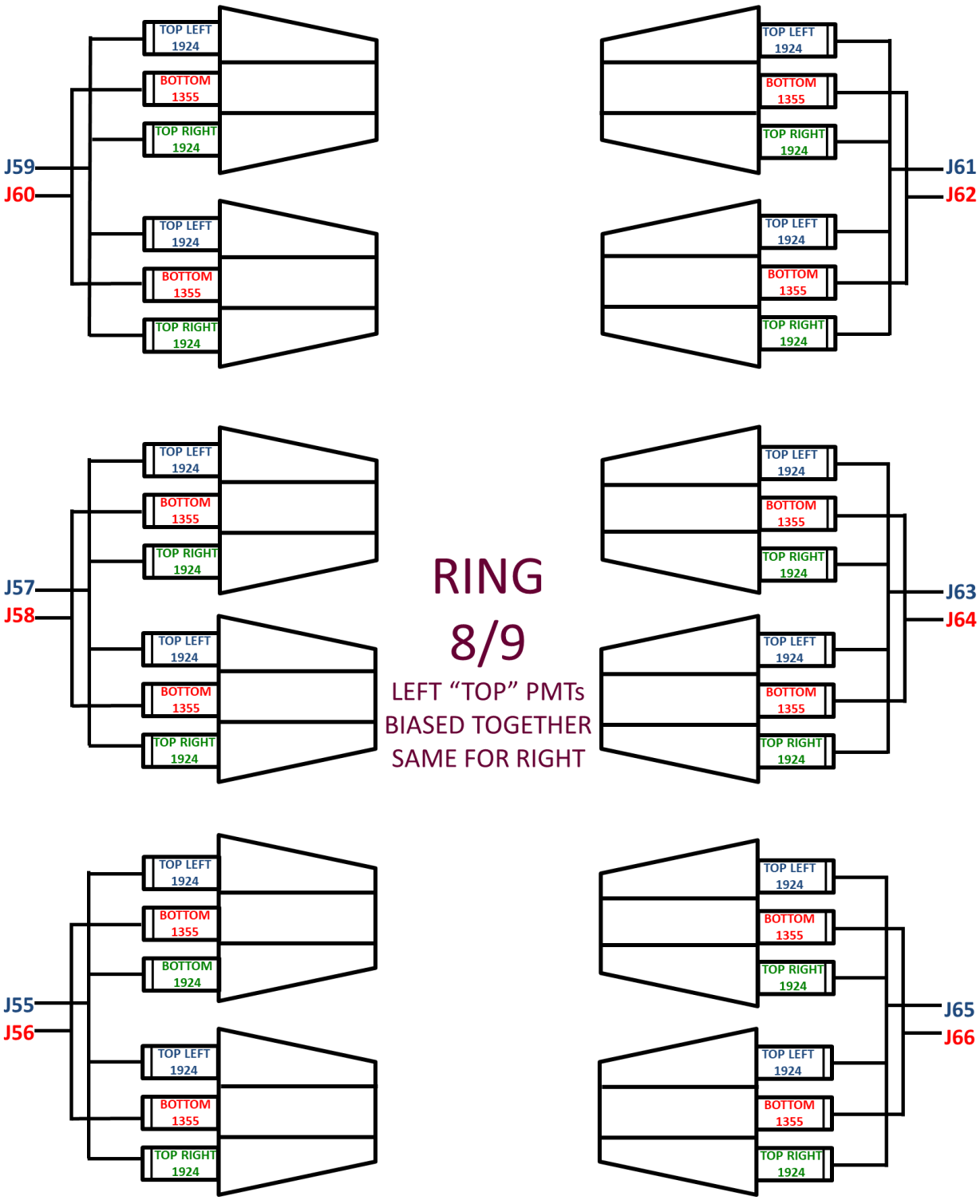

Figure B.4: PMT location of Ring 8/9 CsI detectors.

APPENDIX C

EFFECTS OF THE MIXED EVENT ANALYSIS

One method to test whether or not the effects observed are due to experimental constraints is to do a mixed events analysis. The mixed events analysis was applied to the four Z_H, Z_L pairings shown throughout this work. For each Z_H, Z_L pairing, an ascii file was generated with the Z, A, p_x, p_y and p_z of the **HF** and **LF** in the event. The α value was recalculated for all **HF** and **LF** combinations where **HF** and **LF** came from a different event. The first 10,000 events in the ascii file were used for this calculation. The α distribution is shown in Figure C.1, where the purple line shows the mixed event distribution and the pink distribution is for the non-mixed events. The mixed event α distribution is consistent with the non-mixed event analysis.

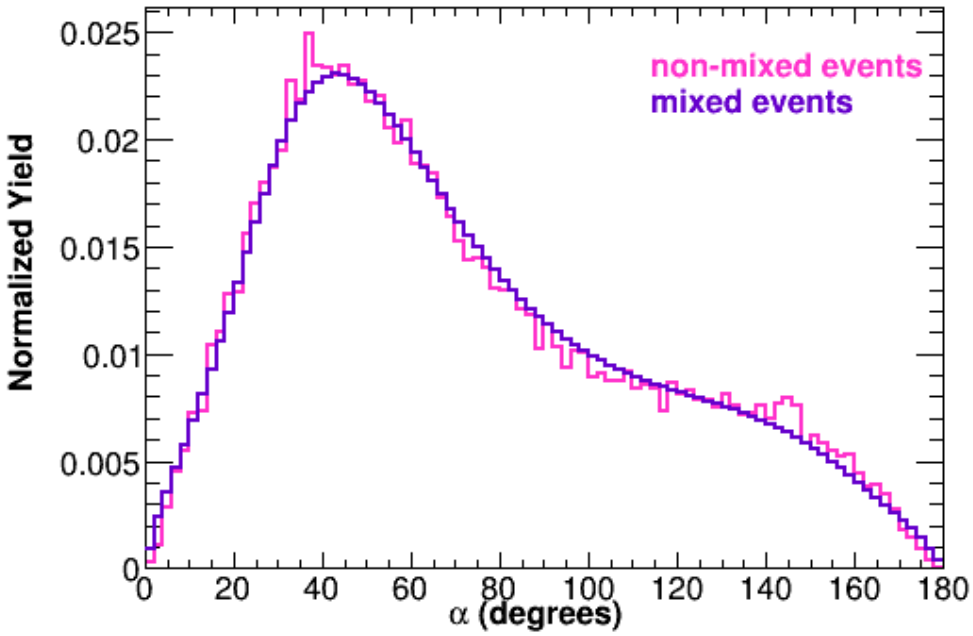

Figure C.1: α distribution for Z_H=12 and Z_L=7 for mixed and non-mixed events. The mixed events are plotted in purple and the non-mixed ones are plotted in pink. The distributions are consistent with each other and are representative of all other pairings.

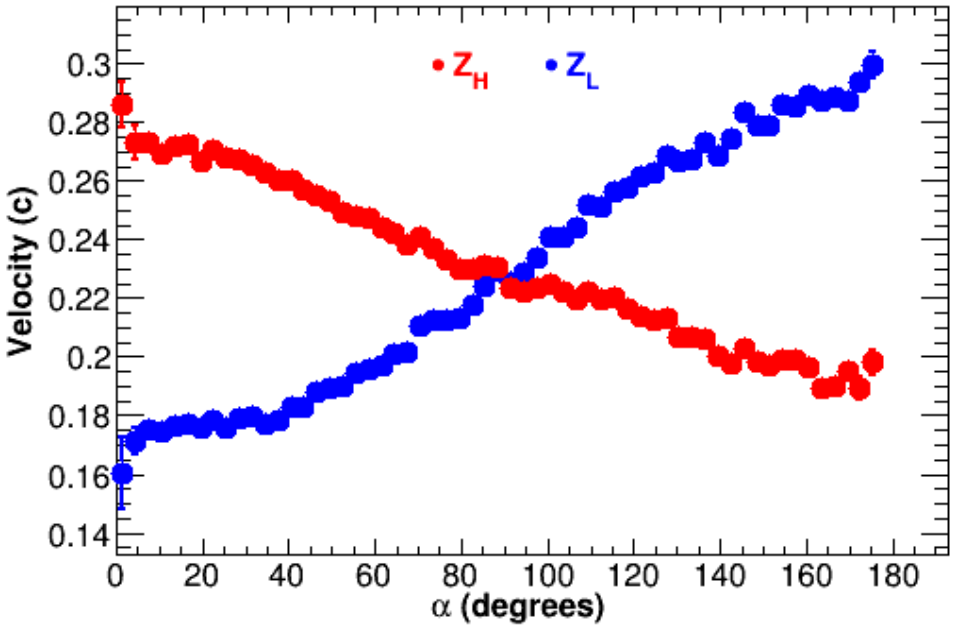

Figure C.2: average velocity in the beam direction (v_z) versus α. A direct relationship is seen for v_z of the **LF** and α. An invrese relationship is seen for v_z of the **HF** and α. The average velocity is the same at approx 90°. The relationship indicates the alignment of the **HF** relative to **LF** is governed largely by the velocity ordering of the two fragments.

The consistency in the mixed and non-mixed α distribution can be explained by examining the α calculation. The first step in calculating the α value is to calculate the $\vec{v}_{REL}$ and $\vec{v}_{CM}$. When breaking down the v_x, v_y, v_z components, the v_z, or velocity in the beam direction, is the largest component of the total velocity. In cases where the v_z of the **HF** ($v_{z,ZH}$) and the v_z of the **LF** ($v_{z,ZL}$) is much different, the α calculation is governed by the dot product of the z-component of the $\vec{v}_{REL}$ and $\vec{v}_{CM}$. As $v_{z,ZH}$ and $v_{z,ZL}$ approach an equivalent value, the z-component of the $\vec{v}_{REL}$ approaches zero, and, hence, the $cos(\alpha)$ approaches zero too. This is further verified when plotting the $\langle v_z \rangle$ vs. α, as shown in Figure C.2. There is an inverse relationship between the $\langle v_{z,ZH} \rangle$ and α, and there is a direct relationship between the $\langle v_{z,ZL} \rangle$ and α. At α=0° and α=180°, the greatest difference in the average v_z is seen for the **HF** and **LF**. The $\langle v_{z,ZH} \rangle$ crosses $\langle v_{z,ZL} \rangle$ at α=90°, further verifying the importance of the v_z component of the total velocity on the α calculation.

The relationship between v_z and α can be further explained by the reaction dynamics. In the case of dynamical decay, the PLF* decays shortly after the TLF* and PLF* break apart. The **LF**

comes from the neck region and should have a velocity closer to the mid-velocity of the reaction system (v_{beam}=0.27c). The **HF** comes from the PLF region resulting in a velocity more consistent with v_{beam}. The longer the PLF* stays intact before decaying, the more momentum is transferred and the more similar the $p_{z,ZH}$ and $p_{z,ZL}$ are. For statistical decay, the neck region is reabsorbed into the PLF* becoming spherical before decaying into the **HF** and **LF**.

The composition of the mixed and non-mixed events was plotted as a function of α and the results are shown in Figure C.3. The non-mixed events are plotted in the same color scheme as shown previously in Figure 3.6 in Chapter 3.3. The red points correspond to the non-mixed event **HF** compositions and the blue points correspond to the non-mixed event **LF** compositions. The respective fits are shown in black. The mixed event **HF** compositions are shown in orange and the mixed event **LF** compositions are shown in cyan. The gray fits correspond to the mixed event fits.

The results for the mixed-event analysis show a decrease in **LF** composition and an increase in the **HF** composition similar to the effects seen in the non-mixed events. However, the evolution of the composition is much flatter. Figure C.4 shows the rate constants extracted from the exponential fits in per degrees. The coloring is the same as the one shown in Figure C.3. The general trend seen is a decrease in the rate constant between the mixed and the non-mixed events.

While the preservation of the trends seen in the mixed events relative to the non-mixed events would suggest the exponential trend is fabricated, an examination of the reaction mechanism can give insight into the correlations between $\langle\Delta\rangle$ and α. The most neutron-rich **LF** compositions for the non-mixed events are seen at very small α and small v_z values. When mixing a very neutron-rich, slow **LF** with a slow, relatively neutron-rich **HF**, the neutron-rich **LF** will appear at a larger α value. However, the α value does not change considerably due to the differences in v_z as previously discussed. For every combination of a slow, neutron-rich **LF** with a slow, relatively neutron-rich **HF**, there is a slow, neutron-rich **LF** paired with a fast, relatively neutron-poor **HF**, therefore the effects of the pairing selection on the composition should average out. Only in regions where the dynamical and statistical contributions is changed will the composition vary.

The first notable region where the composition is different between the $\langle\Delta_L\rangle$ of the mixed and non-mixed events is at small α (α <30°). In this region, the dynamical mechanism is dominant and any contribution from a statistically decaying **LF** paired with a fast **HF** will decrease the $\langle\Delta_L\rangle$ for the mixed events relative to the non-mixed events. The second region of interest is between

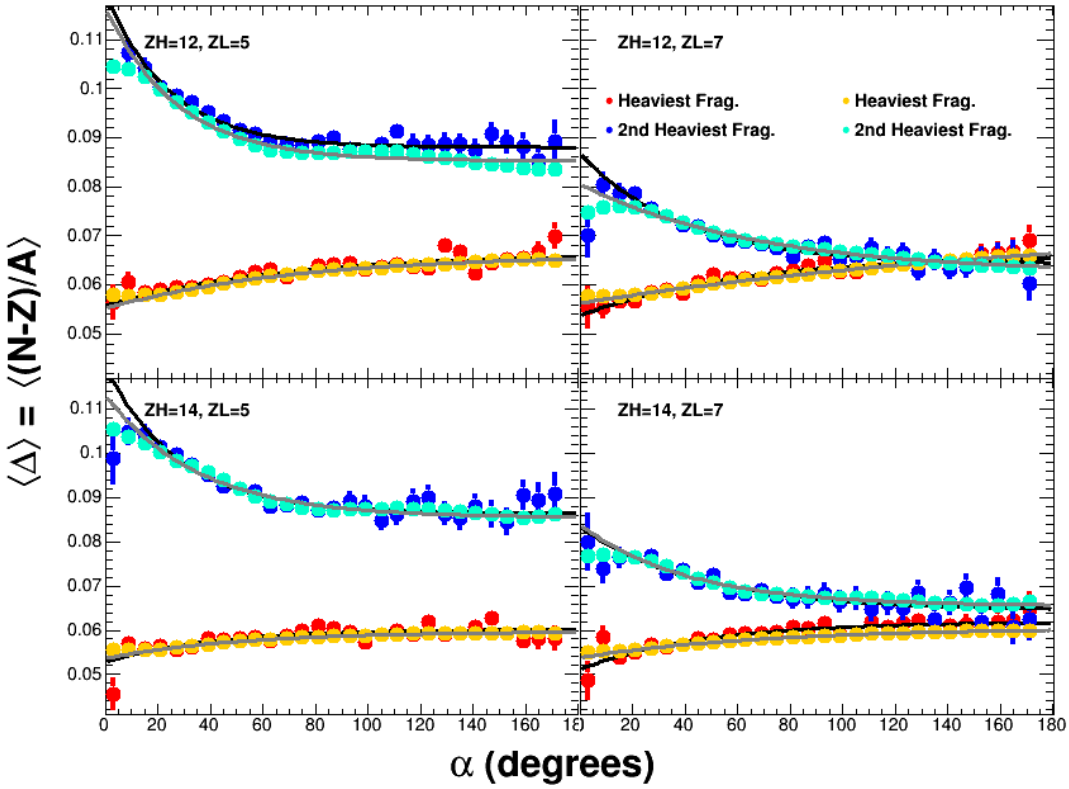

Figure C.3: Composition of the **HF** and **LF** for the combinations of Z_H=12,14 and Z_L=5,7 for the mixed and non-mixed events analysis. The blue and red results are for the non-mixed event **LF** and **HF**, respectively, and the black lines are the corresponding exponential fits. The cyan and orange points are the mixed-event **LF** and **HF**, respectively, and the gray lines are the corresponding exponential fits. In all cases, the exponential behavior is observed. However, in the trend was flatter for the mixed events.

40° < α <100°. In this region, a mix of contribution from the dynamically-decayed, neutron-rich **LF** and the statistically-decayed, neutron-poor **LF** is present. While the dynamical decay is still dominant as shown in Figure C.1, the statistical contribution at approx. α=40°, will lower the average neutron content of the **LF**. As the distribution moves from α=40° to α=100°, very neutron-rich **LF** contribute to the $\langle\Delta_L\rangle$, raising the average neutron composition. Therefore, the average composition as a function of α is flatter than for the non-mixed events. A similar, mirroring effect is also seen for the $\langle\Delta_H\rangle$ as a function of α.

The presence of the flattened exponential trend of the $\langle\Delta_H\rangle$ and $\langle\Delta_L\rangle$ further verifies the picture of dynamical and statistical decay mechanism. The relationship between α and v_z is consistent with work from Ref. [5, 38, 39, 40, 41]. The neutron enhancement in the neck region is also consistent

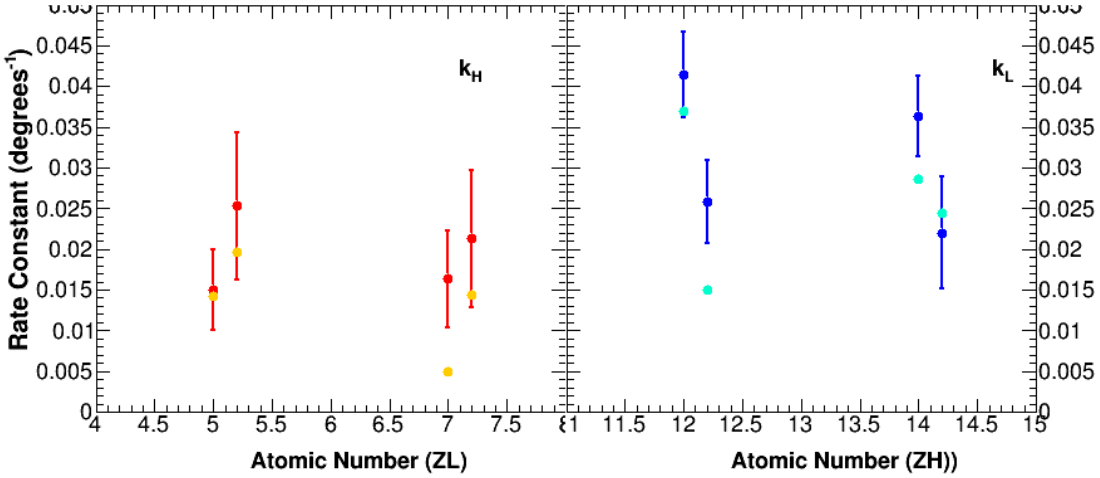

Figure C.4: Rate constants for the mixed and non-mixed analysis for **HF** (left) as a function Z_L and **LF** (right) as a function of Z_H. The red and blue points correspond to the non-mixed event **HF** and **LF** results, respectively. The orange and cyan results are for the mixed event **HF** and **LF** rate constants, respectively. The results indicate the rate constant is much lower for the mixed-events compared to the non-mixed events.

with previous work as discussed in Ref. [42, 45, 46, 7, 8]. The work presented in this dissertation further connects the effects previous studies.

APPENDIX D

BEAM PULSER IN THE K150

Unlike the K500, the K150 does not have a beam pulser or phase shifter. A phase shifter is not possible in the K150 due to the two Dee design. The beam pulser design, which utilizes two plates and an electric field to deflect the beam in the injection line, was not implemented on the K150 until early 2020. Instead, for the experiments performed using the K150, a signal is sent to the RF control for the cyclotron. The signal engages the mechanism to clamp the RF when the voltage on the Dee runs too high. The clamping mechanism turns off fairly quickly, however the length of time between beam bursts, or for the Dee voltage to ramp back up, was not known. Tests were performed changing the length of time between each beam burst. Figure D.1 shows the Dee voltage does not fully ramp back up for approximately 3s.

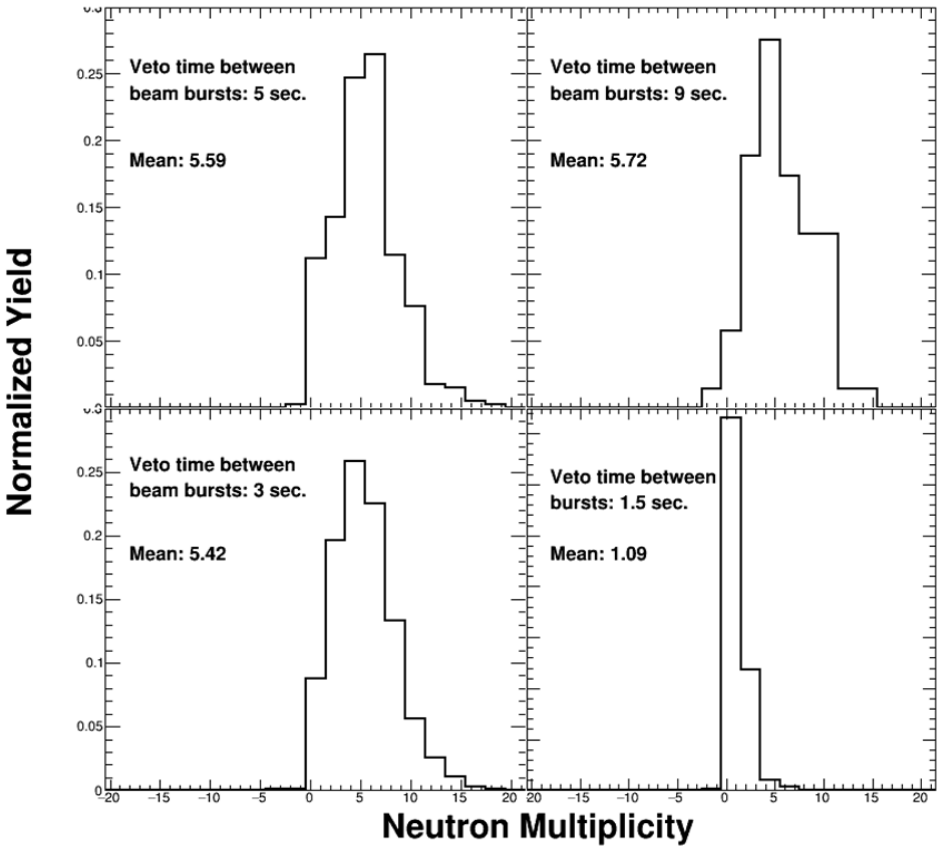

Figure D.1: The neutron multiplicity distribution for each length of time between RF clamps. For each length of time between RF clamps, the neutron multiplicity is approximately the same except for the 1.5 s window. The 3 s length was chosen for the experiment.

APPENDIX E

COMPARISON OF THE BEAM PULSER AND THE PHASE SHIFTER

Currently, there are two methods to turn off the beam on the K500. The beam pulser consists of two plates located on the injection line right after the ECR. An electrical field is applied to divert the beam from the cyclotron. The time of the beam pulser is limited by the timing it takes for the remaining beam to travel through the beam line, cycle through the cyclotron and exit to the cave. The phase shifter changes the phase of the cyclotron, causing the beam to be stopped within the cyclotron. The limiting factor is the time needed to change the phase of the cyclotron.

The timing to turn off the beam is of great concern for NIMROD experiments. The free neutron multiplicity is measured using the neutron ball detector [58, 59] through neutron capture on Gd. Scalers are used to measure the rate within 2 consecutive 100μs gates. As soon as the data acquisition is triggered, the beam is turned off to mitigate the background rate. The beam must be turned off as quickly as possible to ensure an accurate free neutron multiplicity measurement.

The Si detector was placed at 0° upstream of the target position in the NuStars chamber. The beam was turned on for 30ms and then turned off for 30ms. During the beam off time, the computer was triggered using the Si signal. The radiofrequency of the cyclotron was sent into a scaler, which was cleared as soon as the beam was turned off, and the frequency was multiplied by the scaler value to obtain the timing.

The results are shown in Figure E.1. The beam pulser (left side) turns off within 50μs and the phase shifter (right) turns off within 100μs. The first peak comes in at 20μs due to VME timing, which correlates to the last peak coming 20μs later than the actual value. Most of the beam is turning off within 40μs for the beam pulser with some beam coming in up to 10μs later. The phase shifter turns off within 80μs with some coming through up to 100μs. The 7μs spacing between peaks is due to VME read-out timing. The percentage of beam leaking through after the beam has been completely turned off was not tested in this experiment due to threshold changes between measurements and the amount of noise was not quantified.

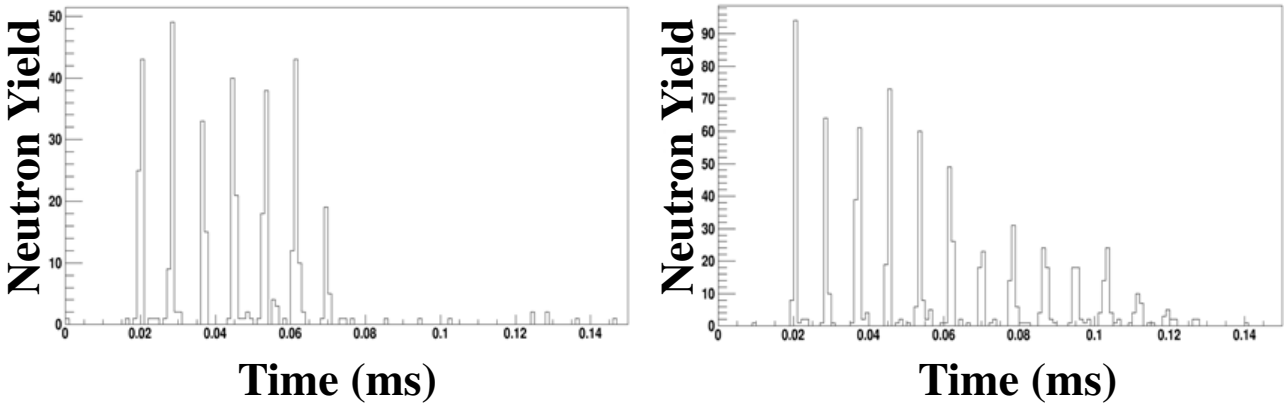

Figure E.1: Timing of the beam pulser (left) and the phase shifter (right). The timing is plotted in microseconds. The beam pulser turns off in 40μs with some beam leaking through up to 50μs. The phase shifter turns out within 100μs with most turning off within 80μs. In both cases, a very small amount of beam creeps in throughout the distribution due to noise in the system and inability to completely turn the beam off in the case of the beam pulser. The first peak comes in 20μs late due to VME dead times. The 7μs interval between peaks also corresponds to VME read out time.

APPENDIX F

IMPLEMENTATION OF A PHOSPHUR IN THE NBL FOR USE IN NIMROD

Historically, the beam tune for NIMROD was done with a combination of the neutron ball, a blank target and the Faraday cup in the beam dump. The beam was passed through the blank target onto the Faraday cup. The beam was tuned to minimized the NBL background and maximize the the Faraday cup reading. However, a more accurate tuning could be achieved by using a phosphor in the target position and a camera. There have been concerns in the past regarding activating the NBL if a phosphor was used.

To test this, a phosphor was placed in the target position of the LLNL setup during the K150 testing in July 2018. Further details are in Section 6.5. The beam attentuation was changed from a factor of 10^3 down to no attenuation by factors of 10. The beam current without attenuation was measured to be 88 enA on FC02. The phosphor was irradiated for a minute and then the beam was turned off. After that, the neutron rate was measured as a function of event number, which is a surrogate for time. Results are shown in Figure F.1. For a factor of 10^3 and 10^2 (top panels), the neutron rate was constant across the entire range. The red line corresponds to the average background rate measured using a ratemeter. There is a slight enhancement seen at low event number (<10000) for an attenuation of 10 (bottom, left panel). For no attenuation, there is a larger enhancement seen up to 7 neutrons initially, followed by the fast, exponential decay back to background. These results indicate that the neutron ball is only slightly activated for a beam current greater than 10 enA, which is several orders of magnitude greater than the 200-700 epA typically run through NIMROD.

Lastly, an extreme test was performed. In this case, the phosphor was irradiated for 10 min with a direct beam. The beam current was 95 enA. Results are shown in Figure F.2. The NBL is initially highly activated before decaying exponentially with a small spike in the rate seen at approx. 50×10^3. The decay time is greater for the 10 min irradiation. However, the conditions applied are extreme conditions that would not be applied while tuning a beam.

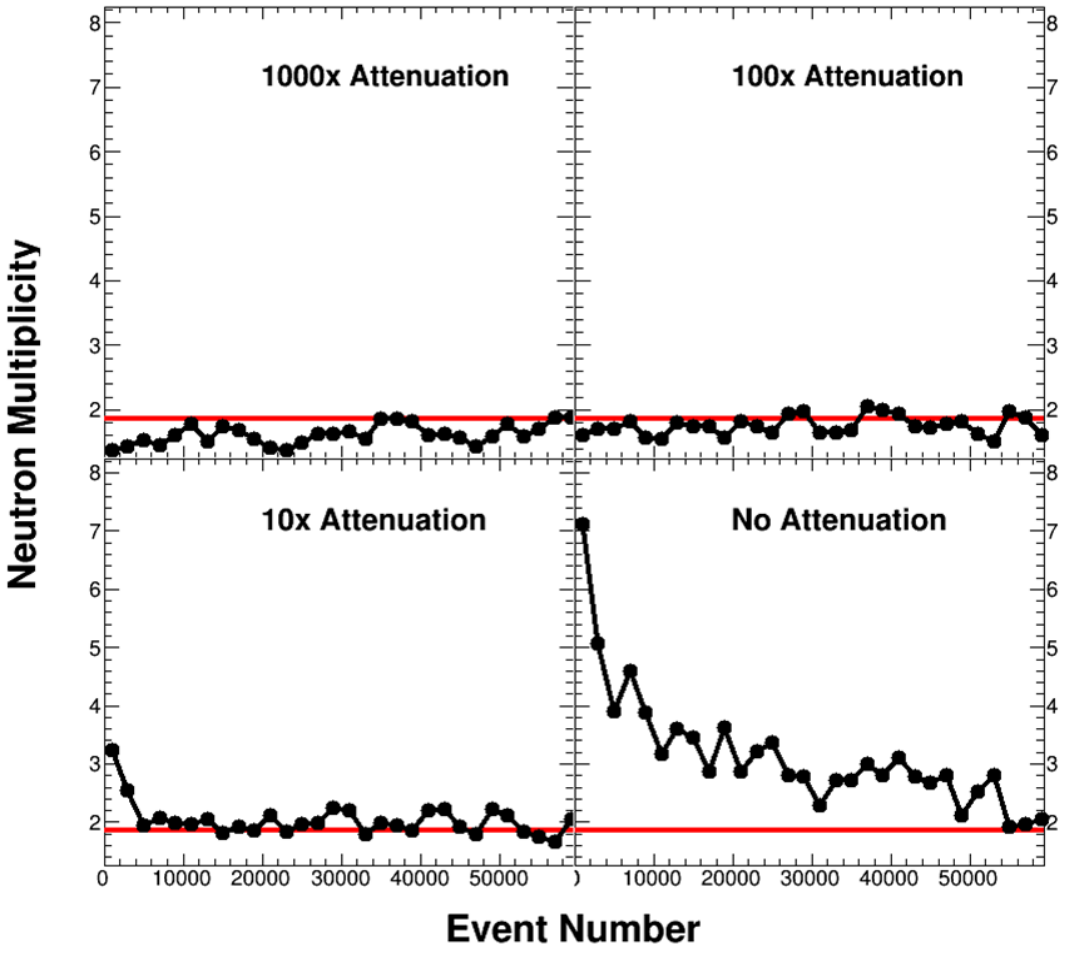

Figure F.1: Neutron count as function of event number, which is a surrogate for time. The range corresponds to approx. 1 min. In each case, the phosphor had been irraditated for 1 min. The panels from top, left to bottom, right represent an increase in the beam current on target. The red line corresponds to the average background rate. For an attenuation factor of 100 and 1000, the rate is constant throughout the distribution. An enhancement in the neutron count is seen initial for an attenuation of 10, however the distribution returns to background quickly. The largest enhancement is seen for no attenuation with quick fall off back to baseline. The latter two cases are not consistent with beam tuning conditions.

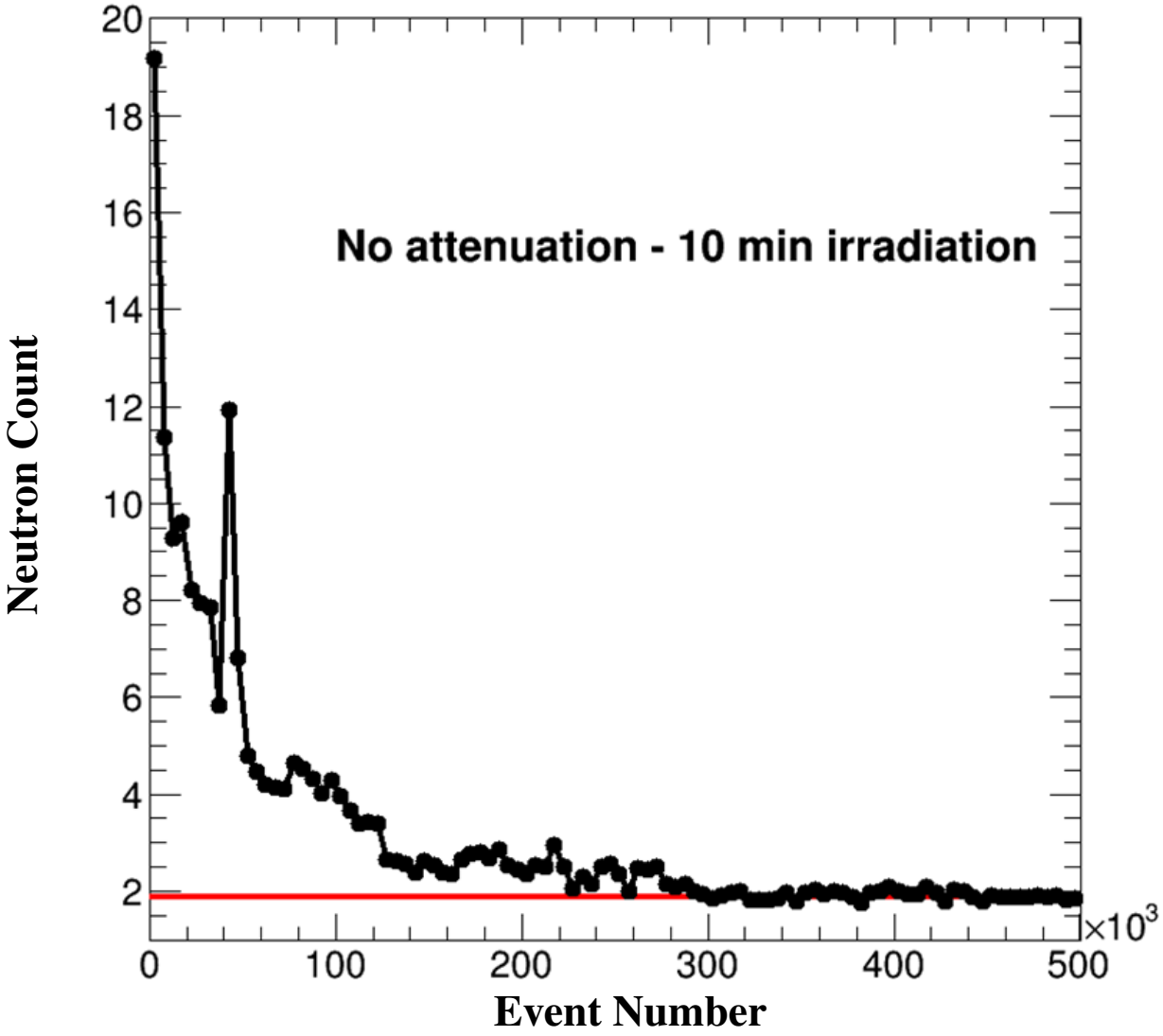

Figure F.2: The neutron count as a function of time for an extreme case where the phosphur was irradiated for 10 min with no attenuation. Initially, there is a large neutron count over background. The distribution falls off very quickly, eventually reaching background within a few seconds. The conditions run to produce this Figure are not consistent with beam tuning conditions.